博士論文

Evaluation of mechanical properties of sand subjected to piping effect

（内部侵食により連続空隙を有する砂質土供試体の力学特性）

楊 陽

論文の内容の要旨
Thesis Summary

Evaluation of mechanical properties of sand subjected to piping effect

（内部侵食により連続空隙を有する砂質土供試体の力学特性）

楊 陽

Internal erosion of soil resulted from piping, seepage or overtopping is the main cause of landslide, dam and levee failures. Internal Erosion refers to the detachment of soil particles from the main soil structure due to the mechanical or the chemical action of a fluid flow. Compare with surface erosion, internal erosion is less studied and harder to quantify, for the reason that only subtle evidence could be observed externally even when severe migration of soil particles has already taken place. Thus, how to predict failure due to internal erosion has become one of the most difficult challenges to both geotechnical engineers and hydraulic engineers.

“Piping” used in this thesis actually refers to a specific internal erosion mechanism, which has been attributed as a cause of approximately half of all dam failures. Piping occurs when water flows through a cavity, crack or other continuous void within the soil. Apparently, the propagation of such internal pipe subject to hydraulic action will directly influence the soil behavior.

Recently, landslides due to piping have occurred frequently in rainy season, such as the disasters in Izu Oshima and Hiroshima in the last two years. Chains of connected macropores, developing nearly parallel to the soil surface, are commonly observed. According to previous studies, such soil pipes is one of the important storm runoff

mechanisms on vegetated slope, which has significant impact on the effective hydraulic conductivity and strongly contribute to sediment movement on slopes as well as landslide initiation.

Although it has been identified by many researchers that concentrated leaks (piping) loosens the soil structure and reduces the soil's shear strength, piping effect on soil behaviour has not been quantitatively studied in laboratory by element experiment.

In order to obtain a better understanding of piping effect, an attempt was made in this research to create artificial piping by dissolving water soluble material (glucose) in uniform fine (Toyoura) sand. Plastic straws with different diameters were used to form the regular shape of glucose pipes both in vertical and horizontal. Piping effect was generated when water was infiltrated and drained out through the specimen, leaving loosened sand around the initial pipe. Thus, a new methodology is offered to gain a better insight to the piping phenomenon through mechanical experiments.

The main objective of this research is to evaluate the mechanical properties of sandy soil subjected to localized disturbance. Due to the continuous defect of glucose pipe which forms an erodible flow path, another "inherent anisotropy" appeared in soil. As it is known that anisotropy acts an important role in modelling the shear behavior of sands, in this study, influence of piping-induced anisotropy would be another important issue.

Piping effect is a sophisticated phenomenon as it deals with reformed soil particles with unpredictable structure. With artificially created piping in sand, both the triaxial test and the hollow cylindrical torsional shear tests were conducted. Details about the experiments are introduced as follows.

1. Triaxial compression test

   Quantitative evaluation on mechanical properties of soil subjected to piping effect was achieved by a series of triaxial test for Toyoura sand and Edosaki sand respectively. While the pipe direction was kept as vertical, influence of density, confining pressure, number of pipes was studied. Variation of axial strain, radial strain and volumetric strain during the piping propagation was obtained by LDT and CGs. Young's modulus and Poisson's ratio were evaluated under small cyclic loading before and after loosening. In addition, shear strength variation among specimen with and without pipes were investigated by conducting monotonic compression.

2. Hollow cylindrical torsional shear test

In order to study the piping-induced anisotropy in more detail, torsional shear tests were conducted both for vertical-pipe-specimen and horizontal-pipe-specimen. With different combination of vertical stress, circumferential stress (equal to radial stress in this study) and shear stress, inclination of the direction of the major principal stress to vertical (α) could be changed continuously. Shear modulus was evaluated with the help of gap sensor under small torsional cyclic loadings, which were applied at initial dry state, after the piping formation, and during the rotation of major principal stress. Moreover, by shearing the specimen under different fixed direction of major principal stress, failure behavior of specimen subjected to piping effect was studied.

Based on the above experimental study, it was found that smaller density samples (initial relative density around 45%) showed larger volumetric strain increment than samples with initial relative density around 75% during the first water infiltration, indicating that loose sand is more vulnerable to progressive deformation during piping formation. For specimens with the initial relative density around 75% in the current research, piping induced volumetric variation was found to be 30%~40% of the initial glucose volume for most cases, which is also influenced by the confining pressure level. A slight larger increase was found in specimen under smaller confining pressure.

The role of fines in piping effect could be clarified to some extent by comparing the results from Toyoura sand and Edosaki sand. In Toyoura sand, piping plane existed as a region where voids with different sizes aligned around the initial glucose pipe in general; while for Edosaki sand, these voids were filled with fines during the water infiltration and the piping plane could be taken as an area with concentrated fines. As a result, different behavior was found in these two sands after piping was formed. Voids in Toyoura sand introduced a new structure with unpredictable properties, especially when checked locally. On the other hand, the rearranged particles in Edosaki sand did not show much piping-induced anisotropy because of the disturbed structure was still uniform in general.

The test results showed that Young's modulus tended to decrease and Poisson's ratio showed a tendency of increase in most specimens with internal pipes after the first water cycle for Toyoura sand. Especially, reduction of shear modulus caused by piping effect showed more dependency on the volume of influenced area compared, in regardless of piping direction.

During the rotation of the major principal direction (α), piping effect was found to have a more obvious influence under $\alpha = 90°$, in which the reduction of shear modulus show smaller dependency on the variation of normal stresses. For complete rotated α, reductions of G was found in specimen with internal pipes, where a more unstable soil structure was found by the fluctuation of G value against α.

In both triaxial test and torsional shear test, specimen subjected to piping effect showed lower resistance against shear in Toyoura sand. For vertical-pipe-specimen, piping effect in the shear strength was found to be small, possibly due to the end restraint by the top cap and pedestal during the formation of shear band. For horizontal-pipe-specimen, in which the piping plane is coincided with the bedding plane, piping effect on shear strength was more obvious. Existence of piping plane on the development of shear band was also observed in specimen with horizontal pipe, which in turn influenced the shear behavior of the sand.

Surficial failure caused by piping and other factors including poor compaction, saturation, low overburden stress put a great risk on the slope stability. Once soil was detached under the seepage force, global failure might be induced. Since the piping direction in reality always goes with the direction of strata, results obtained from horizontal pipes would be important in predicting the failure of slope or embankment. It is expected that when the potential slip surface directions coincide with the piping planes, a lower strengths would appear. While in this study, a special case of $\alpha = 90°$ was found to be the weakest because of the extreme narrow cross section area in the horizontal direction due to the existence of piping. Therefore, future attention is supposed to be paid on the proper specimen dimension in simulating piping effect.

Keywords: Internal erosion; piping; torsional shear; shear modulus; shear strength; anisotropy.

ACKNOWLEDGEMENTS

First, I would like to extend my deepest gratitude to my supervisor, Professor Reiko Kuwano, Institute of Industrial Science, The University of Tokyo, for her constant support, kindhearted guidance, valuable suggestions and encouragement during my study. Without her help and attention, this achievement would not have been a reality. All the efforts she devoted in my past three years of study not only in research but also in day to day life have been of great value to me.

I sincerely acknowledge Professor Junichi Koseki, Geotechnical engineering laboratory, The University of Tokyo, for dedicating his valuable time and effort in offering valuable comments, constructive criticisms and suggestions for my research. It is really a privilege for me to study under the guidance of such a distinguished professor in the field of geotechnical engineering.

I am also deeply grateful to Professor Ikuo Towhata, Associate Professor Taro Uchimura (Geotechnical Engineering Laboratory), Associate Professor Takashi Kiyota (Institute of Industrial Science) and Professor Tomoyoshi Nishimura (Ashikaga Institute of Technology) for their encouragement, criticisms and suggestions for my study.

My special appreciation goes to the laboratory technician Mr. Takeshi Sato for teaching me the basic procedures of testing, assembling the apparatus and advising on trouble shooting. I felt fortunate to have the opportunity to learn from him. His knowledge, experience, patience and optimistic attitude always encourage me. It is a great fun to chatting with him, which grew on me an everlasting love to laboratory testing.

I am grateful to Ms. Yukika Miyashita for her highly cooperative support in the software and computer code. Her helps were essential for the smooth progress of my academic activities. Without her it would be impossible for me to complete my research.

I am also very much grateful to Ms. Satoko Kichibayashi for her kind support in handling the administrative aspects during my study. Her cheerful attitude and warmhearted care is highly appreciated.

My sincere appreciation is forwarded to Dr. Laxmi Suwal and Mr. Biruk Adane for teaching me about soil testing in the very beginning. Dr. Wang Hailong, who was senior student of Koseki labotory, taught me a lot about the apparatuses. Dr. Chiaro Gabriele,

Dr. Seto Wahyudi and Dr. Usama Juniansyah Fauzi, they all sheared their knowledge and valuable experience in performing torsional shear test, which inspired me a lot. Thanks to Mr. Mao Wuwei, my classmate in Tongji University, forwarded helping hands whenever I was in trouble. Thanks to Dr. Sato Mari, who sheared valuable experience in many ways, I still remember the days when we were in Kyoto and Perth. Thanks to Mr. Tsubasa Sasaki, Ms. Nguyen Duyen, Mr. Avilash Pokharel, Mr. Suzuki and Mr. Horiuchi for being kind to me all the time and made my laboratory life enjoyable. In addition, I would like to thank all the members in Koseki & Kuwano Laboratory, Hongo Geotechnical Laboratory, and Kiyota Laboratory. Ms. Wang Feier, Ms. Luisa, Ms. Dayani, Ms. Leah, Mr. Geinfranco Fivalta, Mr. Ryuchiro Hoshino, Mr. Jaylord Tan, Mr. Yudai Aoyagi, Dr. Rama Mohan Pokhrel, Mr. Wu, Ms. Mary Roxanne, Mr. Satoru Hagino, Ms. Yuki Umehara, Mr. Umar Muhammad, Mr. Naveed Ahmad, Mr. Zhao Chuang, Mr. Motonao Funaki, Mr. Mitutaka Hirano and Mr. Nikolay Milev, we had so many good experience in the summer trip, ski tour and lab parties. I will treasure these memories forever.

Without the dedication of me father, mother and other family members, most of my ambitions may not be fulfilled. My special gratitude is directed to them for their continuous support and encouragement during my three years journey in Japan.

Finally, I wish to express my special gratitude for the China Scholarship Council, for providing me the necessary financial assistance during my studies in Japan.

Yang Yang
August 2015
Tokyo, Japan

TABLE OF CONTENTS

List of Figure

List of Table

Chapter 1 Introduction

1.1 Background

Internal erosion, including piping and suffusion, presents great risk on the hydraulic structures including levees, dikes and embankment dams. In the previous literature related to failures of embankments (Fry et al., 1997; Foster et al., 2000), internal erosion has been considered as one of the most common causes responsible for those catastrophic consequences.

The term “internal erosion” usually refers to the detachment of soil particles from the main soil structure due to the mechanical or the chemical action of a fluid flow. Due to the existence of subsurface defects, in which concentrated leakage is likely to appear, soil particles would be flushed away and a continuous tunnel would be formed. This aggravates the erosion in turn.

Customarily, there are two classifications of internal erosion phenomenon, which refers to “suffusion” and “piping”. In suffusion, the fine particles migrate through the voids between the coarse particles under the seepage flow, leaving behind the coarse skeleton. In piping, progressive transportation of soil particles are washed out by water flows through the continuous channels within the soil. Suffusion and piping are always coupled phenomenon, and would lead to obvious changes in porosity, increase in hydraulic conductivity and reduction in soil strength.

Naturally existing water flow paths network is called “soil pipes”, which is quite common in most natural slopes. According to Sidle et al. (1995), soil pipes are a chain of connected macropores, developing nearly parallel to the soil surface. Some common causes related to soil pipes are: subsurface hydraulic erosion, large decayed root channels, animal burrows, desiccation, tension cracks and dissolution.

Soil pipes have significant impact on the effective hydraulic conductivity and strongly contribute to sediment movement on slopes as well as landslide initiation. Recently, landslides due to piping have also drawn much attention among geotechnical engineers. Chains of connected macropores, developing nearly parallel to the soil surface, are commonly observed in slopes. According to previous studies, such soil pipes is one of the important storm runoff

mechanisms on vegetated slopes (Uchida *et al*., 2001), and are often found in the scars of shallow landslides occurred during heavy rainfalls.

For the widespread landslides on the western slopes of Izu Oshima island on 16 Oct. 2013, triggered by the heavy rainfall with the total amount of 824mm in 24 hours, immense damage has been caused and 36 people were killed.

Another landslide occurred in August in Hiroshima last year. The landslides happened after the equivalent of a month's rain fell in the 24 hours. Dozens of homes in a residential area close to a mountain on the outskirts of Hiroshima were buried.

Fig. 1.1 ~ Fig. 1.4 shows the landslide surface in Izu Oshima and Hiroshima respectively. In both of the above disasters, piping holes along the main scarp in the filed were observed and considered as one important reason for the hazard which caused severe casualties (Wakai et al. 2014; Inagaki, 2014; Ueno, 2014; Yang, 2014).

Fig. 1.1 Landslide in Izu Oshima (2013.10)

Fig. 1.2 Soil pipe along the porous layer

Fig. 1.3 Landslide in Hiroshima (2014.08)

Fig. 1.4 Piping holes in the topsoil layer

It has been suggested by many researchers that soil pipes might play an important role in landslide initiation (Tsukamoto et al., 1982; Pierson, 1983; McDonnell, 1990; Mizuyama et al., 1994). However, effects of soil pipe on landslide initiation have not been understood sufficiently. Information about mechanism of runoff and erosion by piping flow is still limited. Compare with surface erosion, subsurface erosion is less studied and harder to quantify, for the reason that only subtle evidence could be observed externally even when severe migration of soil particles has already taken place. Thus, how to predict failure due to

internal erosion has become one of the most difficult challenges to both geotechnical engineers and hydraulic engineers.

In the previous study on erosion, plenty of research was conducted on gap-graded cohesionless soil, which is especially vulnerable to internal erosion due to its deficiency in particle size. Primary concerns are the critical hydraulic gradient and hydraulic conductivity, as well as the loss in fine particles. Other than Moffat and Fannin (2006) and Aberg (1993), very little recent work has been done with respect to piping in cohesionless soils.

Even in spite of the number of advances in our understanding of piping phenomena, there are still a large number of incidents that occur due to concentrated leakage in embankment dams and slopes. This reflects a need for increased attention to find the mechanism in these potential failure modes.

1.2 Objectives of this study

Given the widely investigation on hydrological mechanism of internal erosion, there is little study on the mechanical properties of soil subjected to piping erosion through element experiment. The difficulties lie in the proper simulation of erosion in laboratory. Thus, the primal intention of this research is to find a way to generate internal erosion in laboratory in order to obtain a better understanding of the behavior of sandy soils subjected to piping effect, which will be achieved by dissolving water soluble materials in the specimen which is placed in advance.

The first concern is the propagation characteristics of piping in sandy soil. Deformation properties of subsurface piping is of great importance as it directly related with the degree of ground loosening, which brings vital influence on the behaviour of soil. Since quantitatively investigation on exact how the soil deforms when given the pre-existed erodible path has not been studied before, the current study would focus on identifying the parameters which are affecting the piping expansion and propagation towards the exit.

The second issue will be focused is the mechanical properties including Young's modulus, Poisson's ratio and small strain stiffness of piping influenced soil. Since the elastic properties of soils play an important part in deformation prediction of ground, knowledge of piping effect on sandy soil should be clarified. It has been known that soils formed under gravity are anisotropic in terms of strength and stiffness. Such anisotropy could be divided into the inherent anisotropy (Arthur and Menzies, 1972) and induced anisotropy (Wong and Arthur,

1985). Piping, acting as a weak plane, induces another anisotropy in soil structure, which would have significant influence on the behaviour of soil. Previous laboratory study on shear band formation has focused on the anisotropy caused by bedding plane or rotation of principal stress (Tatsuoka et al., 1990; Han et al., 1993; Yoshida et al., 1994). However, there is little research about piping-induced anisotropy.

In addition, special attention would be paid on the failure behavior of sand with internal piping plane. It has been identified by many researchers that concentrated leaks loosens the soil structure and reduces the soil's shear strength. Still, little research has discussed the piping-induced anisotropy in related with the deformation of shear band. As it is known that anisotropy acts an important role in modelling the shear behavior of sands, in this study, under the combined influence of bedding plane, piping plane and the major principal direction, complicated failure behaviour could be expected.

The present study concerns piping in pre-existing erodible path and should not be confused with backward erosion piping in cohesionless soils whose mechanics are completely different. A particular emphasis is put on the effect of piping on some important mechanical parameters and piping propagation characteristics.

1.3 Scope of this study

The idea of simulating piping in laboratory experiments was inspired by the previous study done in Kuwano lab (IIS, the University of Tokyo) by Samanthi Renuka, in which glucose block was used to form the cavity in sand. Similarly, dissolving glucose in a pipe shape was attempted and proved to be a new method to represent piping effect, which allows quantitative analysis of piping-influenced soil.

In the present study, the drained deformation characteristics as well as small strain stiffness of sand which possesses an anisotropic fabric formed by the specimen preparation together with the internal erosion under piping effect, were examined in detail.

Two types of experiment were carried out in this study:

1. Triaxial compression test

   Quantitative evaluation on mechanical properties of soil subjected to piping effect was achieved by a series of triaxial test for Toyoura sand. While the pipe direction was kept as vertical, influence of density, confining pressure, number of pipes was

studied. Variation of axial strain, radial strain and volumetric strain during the piping propagation was obtained by LDTs and CGs. Young's modulus and Poisson's ratio were also evaluated under small cyclic loading before and after loosening. In order to observe the influence of fines during piping formation, Edosaki sand was also used.

2. Hollow cylindrical torsional shear test

   In order to study the role of principal stress rotation in a more detailed way, torsional shear tests were conducted both for specimen with vertical pipe and horizontal pipe. With different combination of vertical stress, circumferential stress (equal to radial stress in this study) and shear stress, inclination of the direction of the major principal stress to vertical (α) could be changed continuously.

   Shear modulus was evaluated with the help of gap sensor under small torsional cyclic loadings, which were applied at initial dry state, after the piping formation, and during the rotation of major principal stress. A complete rotation of σ_1 from 0^o to 180^o was achieved and piping induced anisotropy on shear modulus was obtained.

   Moreover, by shearing the specimen under fixed angle of major principal stress, failure behavior of sand with piping plane was checked. Since the piping direction in reality always goes with the direction of strata, results obtained from horizontal pipes would be important in predicting the failure of slope or embankment.

1.4 Structure of the dissertation

There are seven chapters in this thesis in total. Description on content of each chapter is briefly introduced below.

Chapter 1 Introduction

In this chapter, background of the proposed research is introduced. Significance of this study and genera plan with regard to experimental purpose is discussed.

Chapter 2 Previous research on piping erosion and soil anisotropy

Previous studies on internal erosion and soil anisotropy are reviewed. Some recent experimental studies of piping simulation are introduced. Soil anisotropy caused by bedding plane inclination and stress rotation was explained.

Chapter 3 Material, apparatus and test procedure

Test material in this study is identified and its properties were introduced. Then the test apparatuses consisting triaxial apparatus and torsional shear apparatus, both developed at the Institute of Industrial Science, University of Tokyo, are described in detail, together with the measurement devices employed. Subsequently, specimen preparation and loading procedure are described.

Chapter 4 Formulation of stresses and strains

After the general theories of soil mechanics, formulations of stresses and strains both in triaxial apparatus on cylindrical specimen and torsional shear apparatus on hollow cylindrical specimen were presented.

Chapter 5 Results and discussion – Triaxial test

Results from the investigations on the effect of piping on the drained behaviour of Toyoura sand and Edosaki sand were analysed. Volumetric strain during piping formation, effects of piping on Young's modulus and Poisson's ratio, failure characteristics and so on, are discussed in order to have a comprehensive understanding of the piping effect.

Chapter 6 Results and discussion – Torsional shear test

Piping-induced anisotropy on the small strain stiffness and failure behaviour of Toyoura sand are presented. Sand deformation during piping propagation, shear modulus variation against rotation of the major principal stress, failure behaviours and the mode of development of shear strain during shearing are discussed to understand the role of piping on the behaviour of Toyoura sand.

Chapter 7 Conclusions and recommendations

In the last chapter, conclusions of this study are presented. Recommendations for the future studies are also suggested.

1.5 Reference

1. Aberg, B. (1993). Washout of grains from filtered sand and gravel materials. ASCE J Geotech Eng, 119(1), 36-53.
2. Arthur, J.R.F. and Menzied, B.K. (1972). Inherent anisotropy in a sand, Geotechnique, 22(1), 115-128.
3. Foster, M., Fell, R., Spannagle, M. (2000). The statistics of embankment dam failures and accidents.
4. Fry, J.J., Degoutte, G., & Goubet, A. (1997). L'érosion interne: typologie, détection et réparation. Can. Geotech. J. Volume 37, 1000-1024.
5. Han, C., and Drescher, A. (1993). Shear bands in biaxial tests on dry coarse sand, Soils and foundations, 33(1), 118-132.
6. Inagaki H. (2014). Mechanism of landslides occurrence. Investigation report of Izu Oshima landslide caused by Typhoon No. 26 in October 2013, 74-77.
7. McDonnell, J.J. (1990). The influence of macropores on debris flow initiation, Quart. J. Eng. Geol., 23, 325-331.
8. Mizuyama, T. Kosugi, K. Sato, I and Kobashi, S. (1994). Runoff through underground pipes in hollows. Proc. International Symposium on Forest Hydrology, 233-240.
9. Moffat RA, Fannin RJ. (2006). A large permeameter for study of internal stability in cohesionless soils. Geotech Test J 29(4), 273-279.
10. Pierson, T.C. (1983). Soil pipes and slope stability, Quart. J. Eng. Geol., 16, 1-11.
11. Renuka, I.H.S. (2012). Evaluation of ground loosening behavior and mechanical properties of loosened sand associated with underground cavities. Master dissertation, Department of Civil engineering, University of Tokyo.
12. Sidle R.C., Kitahara H. and Terajima T., Nakai Y. (1995). Experimental studies on the effects of pipeflow on through flow partitioning, Journal of Hydrology 165, 207-219.
13. Tatsuoka, F., Nakamura, S., Huang, C. C., and Tani, K. (1990). Strength anisotropy and shear band direction in plane strain tests of sand, Soils and foundations, 30(1), 35-54.
14. Tsukamoto, Y., Ohta, T. and Noguchi, H. (1982). Hydrogeological and geomorphological studies of debris slides on forested hillslopes in Japan, *IAHS Publ.*, 137, 89-98.

15. Uchida, T., Kosugi, K. Mizuyama, T. (2001). Effect of pipeflow on hydrological process and its relation to landslide: a review of pipeflow studies in forested headwater catchments, Hydrol. Process., 15, 2151-2174.

16. Ueno S. (2014). Groundwater. Investigation report of Izu Oshima landslide caused by Typhoon No. 26 in October 2013, 19.

17. Wakai A, Uchimura T, Araki K, Inagaki H, Goto S. (2014). Geotechnical characters of soil. Investigation report of Izu Oshima landslide caused by Typhoon No. 26 in October 2013, 35-39.

18. Wong, R.K.S and Arthue, J.R.F. (1985). Induced and inherent anisotropy in sand, Geotechnique, 35(4), 471-481.

19. Yang H.F., (2014). Report of field trip to Shobara, Hiroshima.

20. Yoshida, T., Tatsuoka, F., Kamegai, Y., Siddiquee, M. S. A., Park, C. S. (1994). Shear banding in sands observed in plane strain compression, Proc. 3rd Int. Workshop on Localization and Bifurcation Theory for Soils and Rocks, Balkema, Rotterdam, The Netherlands, 165-179.

Chapter 2 Previous research on internal erosion and soil anisotropy

In this chapter, previous research on internal erosion and experimental study on soil anisotropy are described in detail. A review of piping literature and methods currently available for the evaluation of piping related problems are provide.

2.1 Internal erosion and soil piping phenomena

Internal erosion, inadequate filter design and improper maintenance are found to be responsible for a larger number of cases according to the statistics of dam failures. Among which, piping has been considered as one of the most common reason attributed to such disasters.

Soil erosion due to piping could be found in plenty of reports related with dam and levee failures (Foster et al., 2000), landslides and debris flows (Uchida et al., 2001), stream bank failures (Wilson et al., 2007), gully erosion (Faulkner, 2006), and ephemeral gully erosion (Wilson, 2011). Foster et al. (2000) found that 46% of dam failures were caused at least in part by piping. Jones et al. (1997) surveyed 74 basins in Britain and found that 30% were susceptible to piping. Pierson (1983) reported the propensity of landslide scarps to contain a soil pipe, suggesting a cause-and-effect relationship. Pipe collapses on landscapes provided evidence that internal erosion by pipeflow had been occurring below ground (Verachtert et al., 2010; Zhang and Wilson, 2012).

In addition, based on data of dam piping failures taken from Jones (1981) and Lane (1934), four broad categories related with piping cases are divided by K.S. Richards and K.R. Reddy (2007).

(1) Foundation related piping failures.

(2) Conduit and internal erosion piping failures.

(3) Possible backwards erosion and suffusion piping failures.

(4) Piping failures induced by biological activity.

Among them, nearly one-third (31.1%) of all piping failures could be associated with the classic backwards erosion model of piping or suffusion.

It should be noted that such classification of piping failure is quite difficult since when dams fail by piping the evidence is often washed away with the dam. Also, embankments that are undercut by seepage erosion may have internal erosion occurring due to pipeflow, without being visible from the soil surface. It was proposed that sudden collapse might be triggered by a mature gully forming undetected during internal erosion by Swanson et al. (1989) and Faulkner (2006).

Hence, compared with the surface erosion, soil pipe underground is more dangerous due to the lack of information about the soil structure as well as real time detection during heavy rainfall.

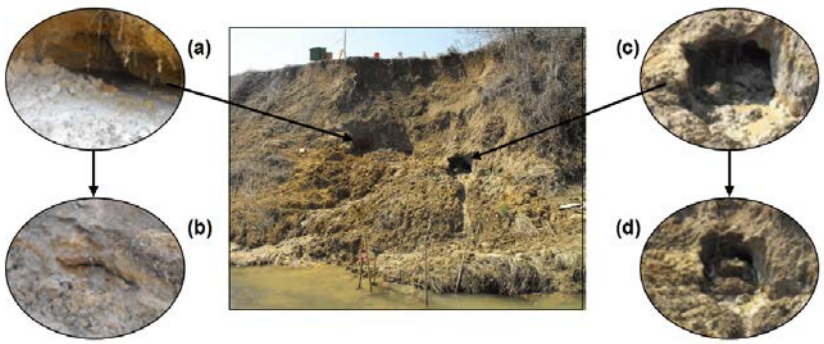

Fig. 2.1 Seepage erosion in streambank (Midgley et al. 2012)

Fig. 2.2 Piping holes observation after the heavy rain in Kagoshima (1993)

In some cases, slope failure could even be initiated due to the sudden increase of pressure in those closure pipes, according to Pierson (1983); Brand et al. (1986); Uchida et al. (2001);

and Kosugi et al. (2004). Pierson (1983) pointed out that if the transmission rate of water through a soil pipe is less than the rate of water entry into the pipe, an increase in pore water pressure will occur that could trigger a landslide.

Evidence that pipe flow had occurred below ground could be found by the collapses macropores and along the landscapes. Here, soli pipes are used to refer such connected macropores, which usually developed nearly parallel to the soil surface, ranging from subarctic wetland (Woo and diCenzo, 1988) and boreal forest (Roberge and Plamondon, 1987) to tropical rain forest (Elsenbeer and Lack, 1996) and semiarid land (Newman et al., 1998).

As shown in Table. 2.1, soil pipe outlets were often found in the scars of shallow landslides which occurred during heavy rainfalls in Japan (Uchida, 2001). In scars of various magnitude landslide, geological condition and slope gradient, soil pipes could be observed.

Table 2.1 Summary of soil pipe outlet observation[a]

Site		Diameter (cm)	Density[b] (pipes/m^2)	Pipe location			Flow type	References
				Soil profile	Topography	Material		
Forest								
Yakeyamagawa	Japan	0·1–9·1	6·3	ts	hillslope	brown forest soil	pe	Kitahara (1994)
Jozankai	Japan	0·8–2·1	9·7	ls	hillslope	brown forest soil	ep	Kitahara and Nakai (1992)
Hitachi Ohta	Japan	0·2–4	3·8	ts/ls	valley head	brown forest soil	ep	Tsuboyama *et al.* (1994)
Hayano	Japan	8, 10	—	ls	valley head	clay loam	ep	Yasuhara *et al.* (1984)
Hakyuchi 1	Japan	5	—	ls	valley head	clay loam	ep	Shindo (1983)
Hakyuchi 2	Japan	1–50	11·6	ts/ls	valley head	clay loam	ep	Tsukamoto and Ohta (1988)
Hakyuchi 3	Japan	1·5–30	2·3	ls	valley head	clay loam	pe	Tanaka *et al.* (1984)
Hakyuchi 4	Japan	−10	15·5	ts	hillslope	clay loam	—	Tsukamoto *et al.* (1988)
Hakyuchi 5	Japan	−10	3·4	ts/ls	valley head	clay loam	—	Tsukamoto *et al.* (1988)
Nozasa	Japan	20	—	—	valley head	decomposed granite	ep	Ogawa (1997)
Obara	Japan	3	—	ls	hillslope	decomposed granite	—	Onda (1994)
Akatsu	Japan	25–60	—	ls	valley head	decomposed granite	ep	Terajima and Sakura (1993)

[a]Abbreviations: ts, topsoil; ls, lower soil; br, bedrock; pe, perennial; ep, ephemeral.

[b]The density of soil pipes at excavated trenches.

Jones et al. (1997) pointed out that the soil pipe primarily formed in soils of low permeability in upland regions, through the investigation of soil pipes distribution in UK. It was reported that 70% of soil pipes were found in moorland catchment covered by peats or podzols.

Tsukamoto (1997) surveyed two piped slopes including Hakyuchi (clay loam) and Nishimikawa (decomposed granite) to investigate the effects of soil properties on the formation of soil pipe. It was suggested that the rate of pipe developing in clay loam was lower than that in the sandy soil, due to the greater cohesion of the clay loam than the sandy soil.

Dunne (1990) and Onda et al. (1996) also demonstrated that the resistance of the soil to erosion under subsurface flow is influenced by its cohesion.

By corroborating with the previous observation, it was suggested by Tsukamoto (1997) that the sediment yields from the soil pipes were commonly greater in forested hillslopes covered by decomposed granites (Terajima and Sakura, 1993; Sonoda, 1993; Onda, 1994; Ogawa, 1997).

Moreover, Tsukamoto (1997) stated that once soil pipes were generated, compared with sandy soil, soil pipes in the clay loam showed relatively rich sustenance agents determined by soil hardness, which indicated that periods from the initiation of the specific soil pipe to the disappearance in the clay loam may be longer than those in the sandy soil (Tsukamoto, 1997).

These investigations indicated that soil properties including permeability, cohesion and hardness, had great influence on the soil pipe formation.

2.2 Experimental study about erosion

Numerous field observations has been the focus on piping formation process, but very limited mechanistic experimental work has been done. Questions still exist as to the situations under which preferential flow through soil pipes would lead to internal erosion.

The initial systematical experimental investigations on hydrological mechanism of internal erosion consisted of base soil and filter compatibility studies (Terzaghi and Peck, 1948, Kenney and Lau, 1985 and Kenney and Lau, 1986; among others). By recognizing the effective particle size ratio between the base soil and the filter, plenty of empirical methods were proposed to prevent soil erosion and to allow for water seepage. Because of the internal erosion of fine particles, the base soil or the filter which satisfied the geometrical criteria,

could still come to fail, which call on a demand of the soil internal instability studies (Skempton and Brogan, 1994, Tomlinson and Vaid, 2000 and Moffat and Fannin, 2006; among others).

With the advent of modern soil mechanics, research related with internal erosion has been conducted to study the erodibility of soil, such as the Crumb test (Emerson, 1964, 1967) and Pinhole test (Sherard et al., 1976).

In recent decades significant progress has been made in assessing internal erosion quantitatively by developing different improved methods like the rotating cylinder test (Arulanandan et al., 1975), the flume test (Arulanandan et al.,1980), the drill hole test (Lefebvre et al.,1985; Rohan et al.,1986), the erosion function apparatus EFA (Briaud et al.,2001), the triaxial erosion test (Bendahmane et al.,2006), the flow pump test (Reddi et al.,2000) and the jet erosion test (Hanson et al.,1991, 2004).

In these experimental investigations, not only the geometric characteristics of the soil, but also the influence of other factors such as flow velocity, flow direction and the hydraulic gradient have been considered.

Wan and Fell (2002, 2004a, b) developed hole Erosion Test (HET) recently, which allows simulating of the erosion phenomenon in open cracks. Similar apparatuses are also used and modified by Benahmed and Bonelli (2007, 2012) to measure the erosion properties of soils. According to their result, both erosion threshold and erosion rate are critical when evaluating the erodibility of soil.

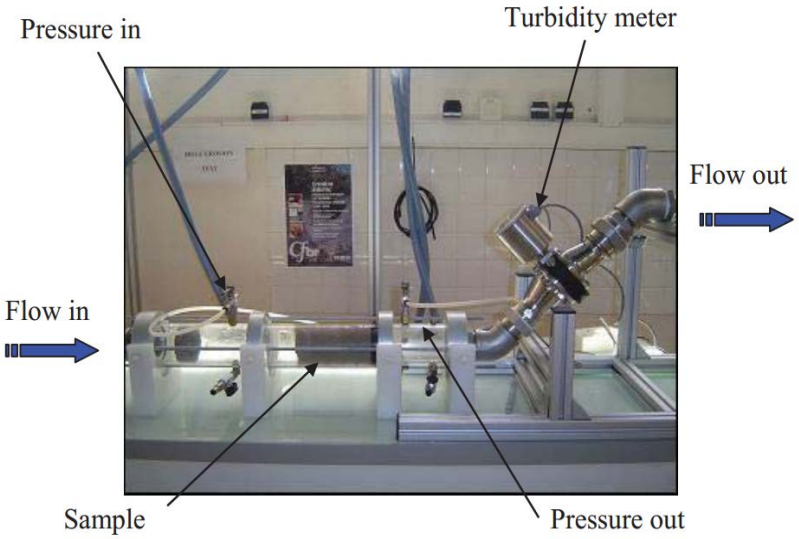

Fig. 2.3 Hole erosion test apparatus developed by Benahmed and Bonelli (2012)

According to the experimental study of piping erosion by Wan (2006), internal erosion occurs if the following criteria are satisfied: (a) the size of the fine particles is smaller than the size of the voids between the coarse particles, which form the skeleton of the soil, and the amount of fine particles is less than enough to fill the voids between the coarse particles (geometrical criteria) and (b) the hydraulic gradient is large enough to move the fine soil particles through the voids between the coarse particles (hydraulic criterion).

Lin Ke and Akihiri Takahashi (2012) conducted a series of one-dimensional upward seepage tests in a mixed soil sample, aiming to study the influence of fines content on the maximum imposed hydraulic gradient on the specimen. They also checked the mechanical consequences of the internal erosion by cone penetration tests and conclude that loss of fine particles would cause change in the void ratio and increase in hydraulic conductivity, resulting in a decrease in the soil strength.

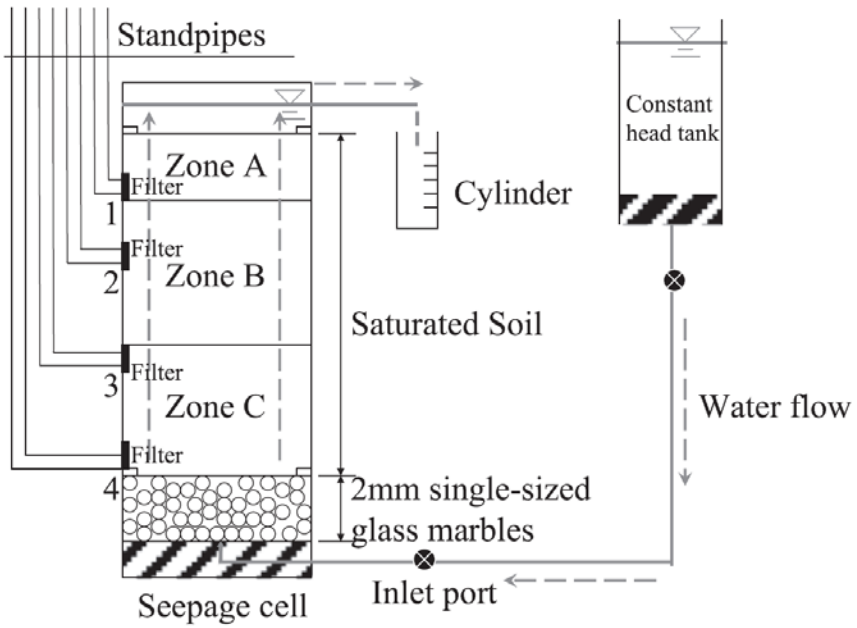

Fig. 2.4 One dimensional upward seepage flow test on Silica sand (Lin Ke, et al., 2012)

An overview of the research work on the erodibility of soils is presented in Fell and Fry (2007).

The nature and state of soils determine their vulnerability to erosion and govern their rate of erosion. However, the relationship between the erosion parameters and the geotechnical properties of soils subjected to erosion still remains in the research stage and is not yet fully understood.

In a series model tests simulating underground cavity formation, quantitative analysis on loosened ground was investigated by Renuka, S. (2012). Glucose block with different size was used to generate loosening effect in Toyoura sand. It was concluded that loosened region expands at least twice of cavity height, and the propagation of loosening was mainly spreading in vertical direction than lateral. Ground density, location of cavity (shallow or deep ground), ground compaction effort, rate and frequency of ground water fluctuations have significant influence on cavity expansion and propagation of loosening.

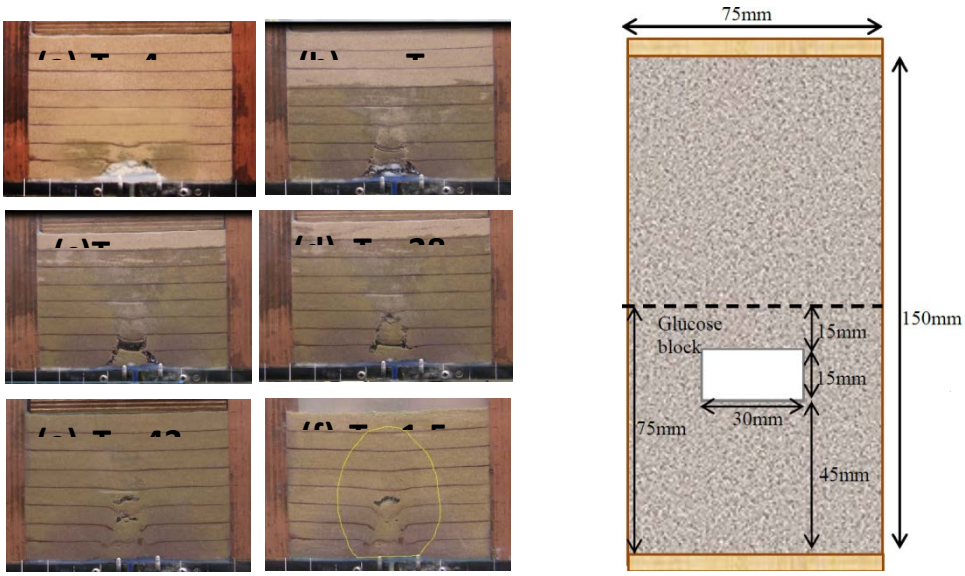

Fig. 2.5 Cavity simulation by glucose block in model test and triaxial test (Renuka, S., 2012)

In addition, in a series of triaxial test with the modified pedestal with holes conducted by Sato Mari (2014) (Fig. 2.6), internal erosion was caused under the drained condition. It was suggested that very small amounts of fines removal can cause decrease in soil stiffness, even if the density is not significantly changed.

Fig. 2.6 Suffusion simulation through modified pedestal in triaxial apparatus (Sato. M, 2014)

2.3 Previous study of soil anisotropy

Many natural and manmade materials like soils, rocks, and many artificial composites exhibit some degree of anisotropy, i.e., their response differs when loaded in different directions. Anisotropy can be distinguished into two types. The first is due to the initial fabric of the particle which is referred to as inherent anisotropy. The other is a result of loading and plastic deformation and can develop in originally isotropic material.

As for the inherent anisotropy, it was found that a cross-anisotropy fabric would be created when natural sand or even perfectly round spheres was deposited under gravity. An uneven distribution of the contacts among particles with preferred orientation in the direction of deposition was considered as the major reason for this anisotropy (Arthur, Menzies, 1972). Besides that, particle long axis orientation also has significant influence on the granular soils behavior (Ochiai, Lade, 1983).

Oda et al. (1978) found out that as much as 34% variation in the bearing capacity of two model strip foundations on sand was caused due to the loading direction.

A number of researchers experimentally investigated the effect of the initial anisotropy on the failure behavior of soils by using series of true triaxial tests to obtain the three-dimensional behavior (Lewin et al. 1982; Ochiai and Lade. 1983; Krikgard and Lade. 1991, 1993). It was shown that soil deformation and peak shear resistance were largely controlled by the initial anisotropic fabric when the monotonic loading coincided with the deposition directions without rotation of the principal stresses.

Lam and Tastuoka (1988) conducted comprehensive tests on Toyoura sand with different angles of bedding plane and different b values to study the inherent anisotropy. And they concluded that the peak angle of internal friction is affected by the b value as well as the bedding plane angle in a complicated manner (Fig. 2.7).

However, due to a tendency for developing an S-shaped specimen for α different from 0° and 90°, non-uniform stresses might be caused when using triaxial specimens with inclined bedding planes (Saada, 1970). A better experimental approach to study the directional strength variation may be achieved by a torsion shear apparatus, in which the bedding planes remain the same and the major principal stress direction changes.

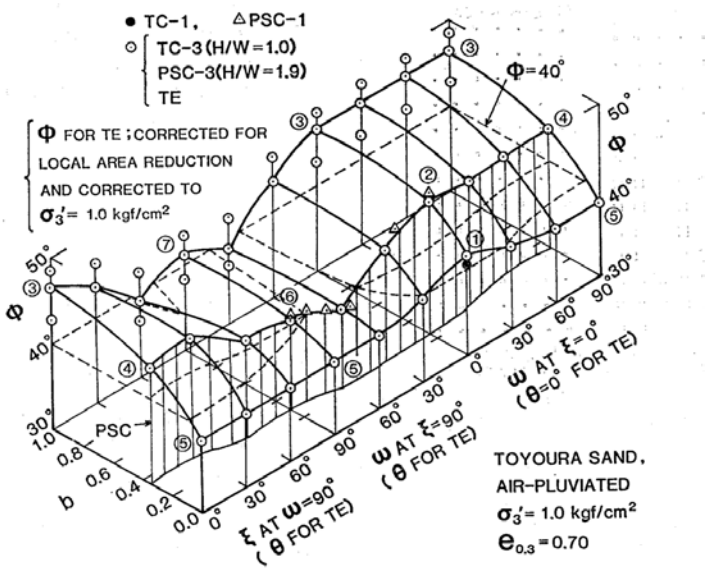

Fig. 2.7 Peak angle of internal friction of Toyoura sand with different angles of bedding plane and b values

On the other hand, as a common feature in many geotechnical engineering problems, rotation of principal stress directions has a considerable effect on the behavior of soils. The importance of such stress induced anisotropy of soil has been recognized in geotechnical engineering for a long time.

The first study about the influence of principal stress rotation on the soil strength using the hollow cylinder apparatus was conducted by Broms and Casbarian (1965). It was pointed out that the continuous rotation of principal stress axes would increase the rate of pore water pressure and reduce the undrained strength of cohesive soil.

Similarly, Saada and Zamini (1969) found that the effective stress path as well as the effective friction angles was the functions of the inclination of the principal stresses for Kaolin clay.

Arthur et al. (1980) used the specially designed apparatus called “directional shear cell” with flexible boundary to investigate the cyclic rotation of principal stress on the drained strength of cohesionless soil. It was revealed that during cyclic loading, strains accumulate steadily even when only half of the static shear strength was mobilized when the principal stress rotated through a large angle for dense sand.

Ishihara and Towhata (1983) conducted a series of cyclic undrained tests on saturated loose sand on a triaxial torsional shear apparatus to simulate the complete rotation of principal stress. According to their results, dependency of deformability and pore water pressure development on the rotation of principal stress axes was clarified. In addition, it was demonstrated that the resistance value of saturated sand against liquefaction would be decreased due to the rotation of principal stress for a wide range of density.

Zdravkovic et al. (2002) simulated a full-scale embankment test with an anisotropic constitutive model successfully. Interactions among strength anisotropy, embankment geometry, ground movements and collapse heights were explored.

Lin and Penumadu (2005) presented the effective friction angles, undrained shear strength, pore water pressure, stress-strain relationship and stress path as a function of the angle of principal stress.

Lade et al. (2008) conducted a series of stress rotation experiments torsional shear apparatus with Santa Monica beach sand, and pointed out that the strength parameters were affected by the cross-anisotropic behavior of sand as well as shear band.

In another experimental program carried out by Lade et al. (2014), shear strength variation of cross-anisotropic deposits of fine Nevada sand was studied. The experiments were performed on large hollow cylinder specimens deposited by dry pluviation and the failure surface of the specimen is presented with discrete combinations of α and intermediate principal stress.

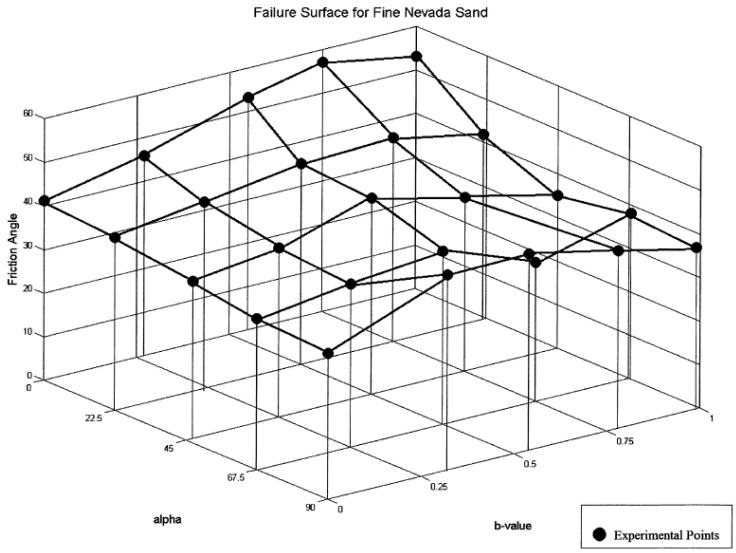

Fig. 2.8 3D surface for dense fine Nevada sand by Lade et al. (2014)

Piping, acting as a weak plane, induces another anisotropy in soil structure, which would have significant influence on the failure behaviour of soil. Given the rich study on the anisotropy caused by bedding plane or rotation of principal stress, there is little research about piping-induced anisotropy. As a sophisticated phenomenon dealing with reformed soil particles with unpredictable structure, special attention should be paid to gain a better understanding of the piping-influenced soil.

2.4 Reference

1. Arthur, J. R. F., Menzies, B. K. (1972). Inherent anisotropy in a sand. Geotechnique, 22(1), 115-128.
2. Arthur, J.R.F., Chua, K.S., Dunstan, T., Rodriguez del C.J.I. (1980). Principal stress rotation: A missing parameter. Proc., ASCE, Vol. 106, GT4, 419-433.
3. Arulanandan, K., Loganathan, P., Krone, R.B. (1975). Pore and eroding fluid influences on surface erosion of soils. Journal of the Geotech. Eng. Div., ASCE, Volume101, 51-66.
4. Bendahmane F., Marot D., Rosquoët F., Alexis A. (2006). Characterization of internal erosion in sand kaolin soils. European Journal of Environmental and Civil Engineering, 4(10), 505-520.
5. Benahmed N., & Bonelli S. (2012). Investigating concentrated leak erosion behaviour of cohesive soils by performing Hole Erosion Test. European Journal of Environmental and Civil Engineering, 16(1), 43-58.
6. Boardman and J. Poesen, eds. Chichester, U.K.: John Wiley and Sons, Ltd.
7. Bonelli S., Benahmed N. (2011). Piping flow erosion in water retaining structures. International Journal on Hydropower and Dams, Volume18, 94-99.
8. Brand, E. W., M. J. Dale, and J. M. Nash. 1986. Soil pipes and slope stability in Hong Kong. *Qtly. J. Eng. Geol. and Hydrogeol*. 19(3), 301-303.
9. Briaud, J. L., Ting, F. C. K., Chen, H. C., Cao, Y., Han, S. W., & Kwak, K. W. (2001). Erosion function apparatus for scour rate predictions. Journal of Geotechnical and Geoenvironmental Engineering, No. 2, Volume 127, 105-113.
10. Broms, B.B. and Casbarian, A.O. (1965). Effects of rotation of the principal stress axes and of the intermediate principal stress on the shear strength. Proceedings of the 6th ICSMFE, Montreal, Vol.1, 179-183.
11. Dunne T. 1990. Hydrology, mechanics, and geomorphic implications of erosion by subsurface flow. Geological Society of America: Boulder, CO; 1-28.
12. Elsenbeer H, Lack A, Cassel K. (1995). Chemical fingerprints of hydrological compartments and flow paths at La Cuenca, western Amazonia. Water Resources Research, 31, 3051-3058.
13. Emerson, W. W. (1946). The Slaking of Soil Crumbs as Influenced by Day Mineral Composition. Journal of Soil Research, Volume 2:211-217.
14. Emerson, W. W. (1967). A Dassification of Soil Aggregates Based on Their Coherence in Water. Australian Journal of Soil Research, Volume 5, 47-57
15. Faulkner, H. (2006). Piping hazard on collapsible and dispersive soils in Europe. Soil Erosion in Europe, 537-562.

15. Fell R, & Fry J.J (2007). Internal Erosion of Dams and Their Foundations. Aussois, France, 25-27 April 2005.
16. Foster, M., Fell, R., & Spannagle, M. (2000). The statistics of embankment dam failures and accidents. Can. Geotech. J. Volume 37:1000-1024.
17. Foster, M. A., R. Fell, and M. Spannangle. (2000). The statistics of embankment dam failures and accidents. *Canadian Geotech. J.* 37(5): 1000-1024.
18. Hanson G. J. (1991). Development of a jet index to characterize erosion resistance of soils in earthen spillways. Transactions of the ASAE, 5(34), 2015-2020.
19. Ishihara. K., Towhata, I. (1983). Sand response to cyclic rotation of principal stress directions as induced by wave loads. Soils and Foundations, 23(4), 11-26.
20. Jones, J. A. A. (1981). The Nature of Soil Piping: A Review of Research. BGRG Research Monograph 3. Norwich, U.K.: Geo Books.
21. Jones J. A. A. (1997a). Pipeflow contribution areas and runoff response. Hydrological Processes 11: 35-41.
22. Jones J. A. A. (1997b). The role of natural pipeflow in hillslope drainage and erosion: extrapolating from the Maesnant data. Physics and Chemistry of the Earth 22: 303-308.
23. Jones, J. A. A, J. M. Richardson, H. J. Jacobs. (1997). Factors controlling the distribution of piping in Britain: A reconnaissance. Geomorphology 20(3-4): 289-306.
24. K. Terzaghi, R.B. Peck. 1948. Soil Mechanics in Engineering Practice. John Wiley and Sons, New York.
25. Kevin S. Richards, Krishna R. Reddy. (2007). Critical appraisal of piping phenomena in earth dams. Bull Eng. Geol. Environ. 66:381-402.
26. Kirkgard, M. M., Lade, P. V. (1991). Anisotropy of normally consolidated San Francisco bay mud. Geotechnical Test, 14(3), 231-246.
27. Kirkgard, M. M., Lade, P. V. (1993). Anisotropic three-dimensional behavior of a normally consolidated clay. Can. Geotech. J., 30, 848-858.
28. Kosugi, K. (1996). Lognormal distribution model for unsaturated soil hydraulic properties. Water Resour. Res. 32(9): 2697-2703.
29. Lade, P. V., Nam, J., Hong, W. P. (2008). Shear banding and cross-anisotropic behavior observed in laboratory sand tests with stress rotation. Canadian Geotechnical Journal, 45, 74-84.
30. Lade, P. V., Nina, M., Eugene, J. (2014). Effects of principal stress directions on 3D failure conditions in cross-anisotropic sand. J. Geotech. Geoenviron. Eng. 140(2), 04013001.
31. Lefebvre, G., Karol, R., & Douville, S. (1985). Erosivity of naturel intact structured clay : Evaluation. Can. Geotech. J. Volume 22:508-517.

32. Lewin, P. I., Yamada, Y., Ishihara, K. (1982). Correlated drained and undrained 3D tests on loose sand. IUTAM Conf., Deformation and Failure of Granular Materials, Delft, 419-429, Balkema, Rotterdam.
33. Lin, H., Penumadu, D. (2002). Interpretation of combined axial-torsional test for 3D constitutive behavior of geomaterials. 15th ASCE Engineering Mechanics conference, 1-8.
34. Newman BD, Campbell AR, Wilcox BP. (1998). Lateral subsurface flow pathways in a semiarid ponderosa pine hillslope. Water Resources Research 34: 3485-3496.
35. Ochiai, H., and Lade, P. V. (1983). Three-dimensional behavior of sand with anisotropic fabric. Geotech. Eng., 109(10), 1313-1328.
36. Oda, M., Koishikawa, I., Higuchi, T. (1978). Experimental study of anisotropic shear strength of sand by plane strain test. Soils and Foundations. 18(1), 25-38.
37. Ogawa K. (1997). Study of profile patterns and moisture variations in surface soil layers on slopes of a mountain region. Research Bulletin of Hokkaido University Forest 54: 87-141.
38. Onda Y. (1994). Seepage erosion and its implication to the formation of amphitheater valley head: a case study at Obara, Japan. Earth Surface Processes and Landforms 19: 627-640.
39. Onda Y, Okunishi K, Iida T, Tsujimura M. (1996). The Interaction of Hydrological and Geologic Processes. Kokonshoin, Tokyo, 267.
40. Pierson, T. C. (1983). Soil pipes and slope stability. Qtly. J. Eng.Geol. and Hydrogeol. 16(1): 1-11.
41. R.A. Moffat, R.J. Fannin. (2006). A large permeameter for study of internal stability in cohesionless soils.Geotechnical Testing Journal, 29 (4), 273-279.
42. Reddi, L.N., Lee, I., Bonala, M.V.S. (2000). Comparison of internal and surface erosion using flow pump test on a sand-kaolinite mixture. Geotechnical Testing Journal, No. 1 Volume 23,116-122.
43. Renuka, S. (2012). Evaluation of ground loosening behavior and mechanical properties of loosend sand associated with underground cavities. Master of Engineering thesis, the University of Tokyo.
44. Roberge J, Plamondon AP. (1987). Snowmelt runoff pathway in a boreal forest hillslope, the role of pipe throughflow. Journal of Hydrology 95, 39-54.
45. Rohan K., Lefebvre G., Douville S., J. P. & Milette J. P. (1986). A new technique to evaluate erosivity of cohesive material. Geotech. Test. J., No. 2, Volume 9, 87-92.
46. Saada, A.S., Zamani, K.K. (1969). The mechanical behavior of cross anisotropic clays. Proceedings of the 7th ICSMFE, Mexico, Vol.1, 351-359.

47. Saada, A. S. (1970). Testing of anisotropic clay soils. J. Soil Mech. and Found. Div., 96(5), 1847-1852.
48. Sato, M. (2014). Study on progress of internal erosion and its effects on mechanical properties. PhD thesis, Department of Civil Engineering, The University of Tokyo, Japan.
49. Sherard, J.-L., Dunnigan, L.-P., Decker, R.S. (1976). Identification and nature of dispersive soils. Journal of the Geotech. Eng. Div., ASCE, No GT4, Volume 102:287-301.
50. Sonoda M. (1993). Seasonal change of sediment discharge in a forested small basin in Japan. Transactions, Japanese Geomorphological Union 14: 53-70.
51. S.S. Tomlinson, Y.P. Vaid. (2000). Seepage forces and confining pressure effects on piping erosion. Canadian Geotechnical Journal, 37, 1-13.
52. Swanson, M. L., G. M. Kondolf, P. J. Boison. 1989. An example of rapid gully initiation and extension by subsurface erosion: Coastal San Mateo County, California. *Geomorphology* 2(4): 393-403.
53. T.C. Kenney, D. Lau. (1985). Internal stability of granular filters. Canadian Geotechnical Journal, 22, 215-225.
54. T.C. Kenney, D. Lau. (1986). Internal stability of granular filters. Canadian Geotechnical Journal, 23, 420-423.
55. Terajima T, Sakura Y. (1993). Effect of subsurface flow on a topographic change at a valley head of granitic mountains. Transactions, Japanese Geomorphological Union 14: 365-384.
56. Tsukamoto Y. (1997). In Conservation of Forest, Water and Soil . Asakurashoten: Tokyo; 134.
57. Uchida, T., K. Kosugi, and T. Mizuyama. (2001). Effects of pipeflow on hydrological process and its relation to landslide: A review of pipeflow studies in forested headwater catchments. *Hydrol. Proc.* 15(11): 2151-2174.
58. Verachtert, E., M. Van Den Eeckhaut, J. Poesen, and J. Deckers. (2010). Factors controlling the spatial distribution of soil piping erosion on loess-derived soils: A case study from central Belgium. Geomorphology 118(3-4): 339-348.
59. Wan C.F., Fell R. (2002). Investigation of internal erosion and piping of soils in embankment dams by the slot erosion test and the hole erosion test. UNICIV Report, no. R-412, July 2002.
60. Wan C.F., Fell R. (2004a). Investigation of rate of erosion of soils in embankment dams. Journal of Geotechnical and Geoenvironmental Engineering, No.4, Volume 30:373-380.
61. Wan C.F., Fell R. (2004b). Laboratory Tests on the Rate of Piping Erosion of Soils in Embankment Dams. Journal of Geotechnical Testing Journal, No.3, Volume 27:295-303.

62. Wan, C.F., (2006). Experimental Investigations of Piping Erosion and Suffusion of Soils in Embankment Dams and Their Foundations. Ph.D. Thesis. School of Civil and Environmental Engineering, University of New South Wales.
63. Wilson, G. V., R. K. Periketi, G. A. Fox, S. Dabney, F. D. Shields, and R. F. Cullum. (2007). Soil properties controlling seepage erosion contributions to streambank failure. Earth Surface Proc. and Landforms 32(3): 447-459.
64. W.K.Lam., F. Tatsuoka. (1988). Effects of initial anisotropic fabric and σ_2 on strength and deformation characteristics of sand. Soils and Foundations, 28(1), 89-106.
65. Woo M, diCenzo P. 1988. Pipe flow in James Bay coastal wetlands. Canadian Journal of Earth Science 25: 625-629.
66. Zdravkovic, L., Potts, D. M., Height, D. W. (2002). The effect of strength anisotropy on the behavior of embankments on soft ground. Geotechenique, 52(6), 447-457.
67. Zhang, T., and G. V. Wilson. (2012). Spatial distribution of collapsed pipes in Goodwin Creek watershed, Mississippi. J. Hydrol. Proc.

Chapter 3 Material, Apparatus and test procedures

3.1 Introduction

In this chapter, the methodology of this study is explained by introducing the apparatus and the test procedures in detail.

As the ultimate objective of this research is to evaluate the mechanical properties of sand subjected to piping effect, the methodology has been developed by considering the following key issues.

1. Making specimen which contains internal pipes.

The method to artificially form the soil piping came from previous study about cavity in Kuwano lab by Renuka. S. (2012), in which glucose block was used to generate the underground loosening effect. Compared with sugar, salt and some other water soluble materials, glucose was found to be the fastest dissolved and selected as the suitable material to represent cavities (Renuka, S., Kuwano. R.2011). Thus, in this study, glucose was used to simulate piping effect, which is, by dissolving glucose pipes in the specimen, sand around the pipes would be loosened and voids along the pipes would be created.

2. Performing experiments which could clarify the behavior of soil subjected to piping effect.

As for the mechanical properties of soil, small strain stiffness and shear strength are the major concern in this study. To achieve this objective, both triaxial test and hollow cylindrical torsional shear test were performed. In triaxial test, specimen with vertical pipes was examined. After that, torsional shear tests were conducted on specimens with internal pipes both in horizontal and vertical, and anisotropy of soil due to piping effect was studied in a more detail way by changing the principal stress direction.

In this chapter, first the testing material is identified. Then the triaxial test apparatus and torsional shear apparatus developed at the Institute of Industrial Science, University of Tokyo, is introduced respectively. In addition, transducers employed to obtain the local deformation of specimens are described in detail. Finally, test procedures are illustrated.

3.2 Test material

3.2.1 Toyoura sand

Toyoura sand originated from Toyoura Beach area of Yamaguchi prefecture in Japan was used for most cases in triaxial tests and all cases in the torsional shear tests. As an uniform sand with negligible fines content, Toyoura sand is the most employed sand for laboratory experiments in Japan. It is mostly sub-angular in shape and consisting mainly of quartz and limestone. In this research, Toyoura sand from batch "J" was used (Fig.3.2). The properties and grain size distribution curve of Toyoura sand are shown in Table 3.1 and Fig. 3.1.

3.2.2 Edosaki sand

In order to check the influence of fines, several cases are conducted in Triaxial apparatus with Edosika sand, which is fine uniform sand having ocher color. Table 3.2 shows the physical properties of Edosaki sand. Particle distribution is shown in Fig.3.3.

Table 3.1 Properties of Toyoura sand

Material	Specific gravity G_s	Mean particle diameter D_{50}(mm)	Maximum void ratio e_{max}	Minimum void ratio e_{min}	Coefficient of uniformity C_U	Fines content F_c
Toyoura sand	2.642	0.19	0.992	0.679	0.146	1.2

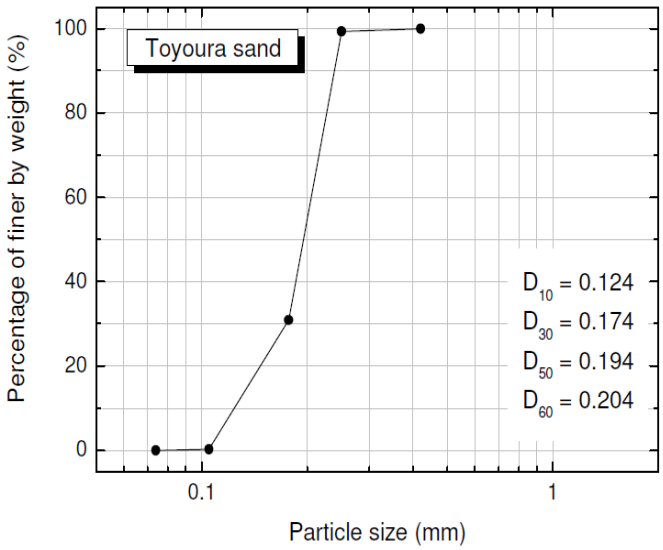

Fig. 3.1 Grain distribution curve of Toyoura sand (Batch J)

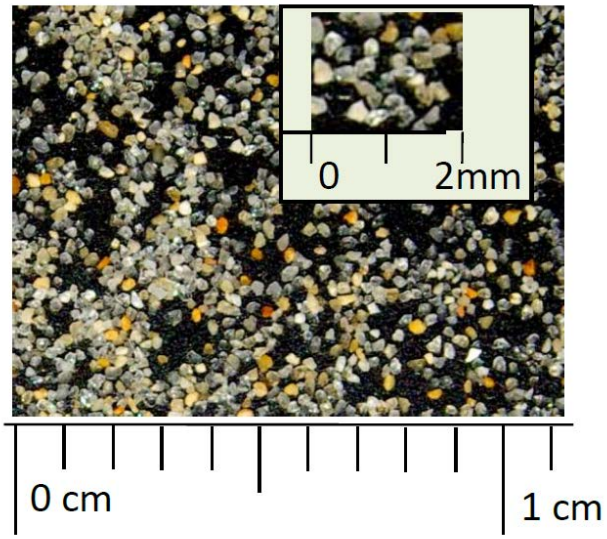

Fig. 3.2 Toyoura sand

Table 3.2 Properties of Edosaki sand

Material	Specific gravity G_s	Maximum dry density ρ_{dmax}(g/cm^3)	Maximum void ratio e_{max}	Minimum void ratio e_{min}	Optimal water content W_{opt} (%)	Fines content F_c
Edosaki sand	2.705	1.76	1.383	0.868	14.2	23.5

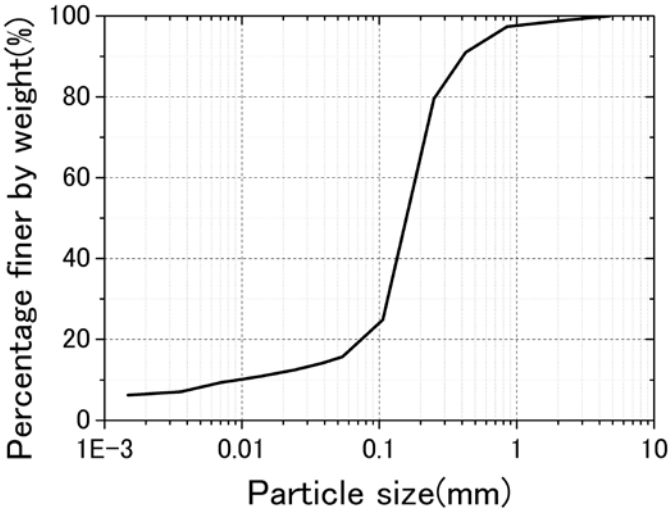

Fig. 3.3 Grain distribution curve of Edosaki sand

3.2.3 Glucose

Glucose ($C_6H_{12}O_6$) is used in this research to create loosening effect in sand. The idea is to dissolve preplaced glucose by inserting water into the specimen, as is shown in Fig.3.4. Such idea was confirmed by R. Samanthi in the study of underground cavity (R. Samanthi, 2012). With the help of glucose block, cavity was simulated successfully and loosening effect was observed through voids around the initial glucose block. Compared with other water soluble material such as sugar or salt, glucose was found to be dissolved fastest. Thus, it was chosen to reproduce piping in this research.

The attempt is made to create both vertical and horizontal pipes in the specimen with glucose powder. For vertical one, plastic straw (7mm in outer diameter for triaxial specimen and 4.5mm for hollow cylinder specimen) is placed into the mould in advance. After completing the sand pluviation, dry glucose powder is filled into the straw with a small funnel. Finally, the straw was removed, left glucose pipes inside the specimen. The horizontal pipe was casted by compacting glucose paste which was made by mixing the powder with nearly 5% of water in a hollow steel pipe with 4.5 mm in diameter and 100mm in length. And then, the pipe was cut by 1 cm and placed at mid-height of specimen in a circle during pouring of sand. The number of glucose pipes varies according to the purpose of the trials. Fig. 3.5 and Fig. 3.6 show the specimen with internal glucose pipes.

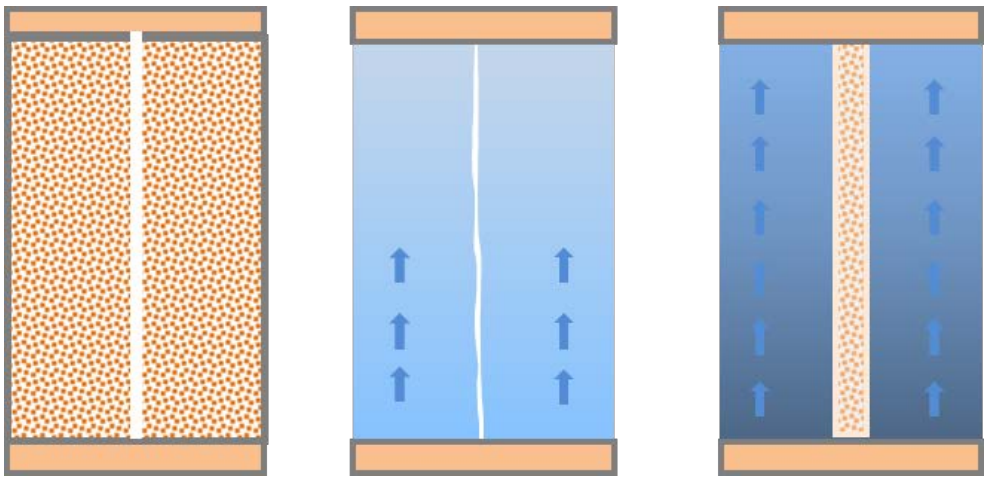

Fig. 3.4 Formation of piping effect in triaxial apparatus

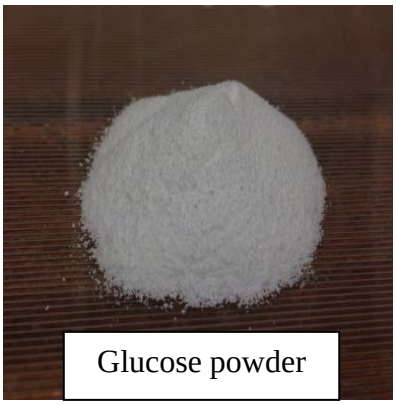

Fig. 3.5 Vertical glucose pipe in triaxial apparatus

Fig. 3.6 Vertical & horizontal glucose pipe in torsional shear apparatus

3.3 Column model test

In order to observe the piping formation and progression visually, column test with was conducted by preparing the specimen in a transparent cylinder in triaxial apparatus, seen in Fig. 3.7. For Toyoura sand, the specimen was prepared by air pluvation, while for Edosaki sand, moisture tamping method was employed under water content around 6% (Fig. 3.8). No extra pressure was applied to the specimen. Porous stones were put at both sides, and de-aired water was allowed to enter the specimen through the bottom pedestal and came out from the top cap. Glucose pipe was placed close to the wall of the cylinder, so that the development of piping could be seen easily.

The amount of water coming in and out of the specimen was measured by the load cells connected with the upper and lower water tank. Upper water tank was open to atmosphere, and by changing the height of the tank, the water inflow rate could be controlled. Here the

speed was set to 14~16ml/min in order to dissolve the glucose in a gentle manner. As is shown in Fig. 3.9, after around 300 ml water was infiltrated, water started to come out from the top cap to the lower tank. When 1400ml water was filled into the specimen, glucose was dissolved completely.

Fig. 3.10 showed the piping development in Toyoura sand and Edosaki sand, respectively. Compared with Toyoura sand, area influenced by piping effect was larger in Edosaki sand, for the reason that fine particles kept flushed into the voids caused by the loss of glucose. During the dissolving of glucose, sand upon the wet part kept dropping down into the voids. And those voids gradually rose to the top part of the specimen. Sand more than two times of the initial glucose size was loosened. Distribution of voids with different sizes was left in the specimen, indicating that piping effect was generated successfully.

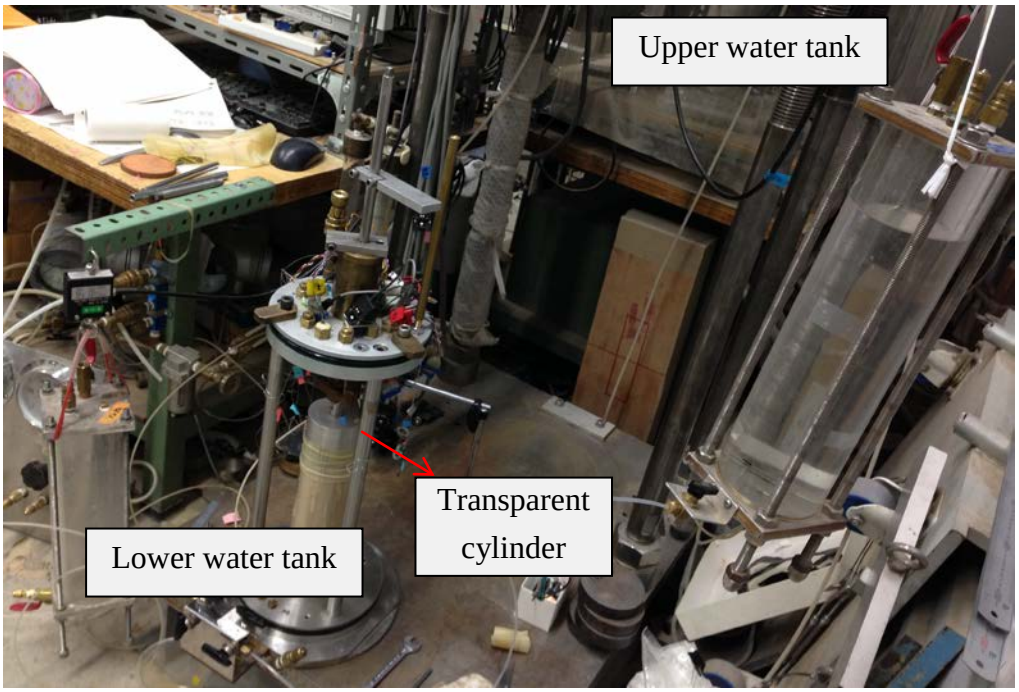

Fig. 3.7 Column test in transparent cylinder mould

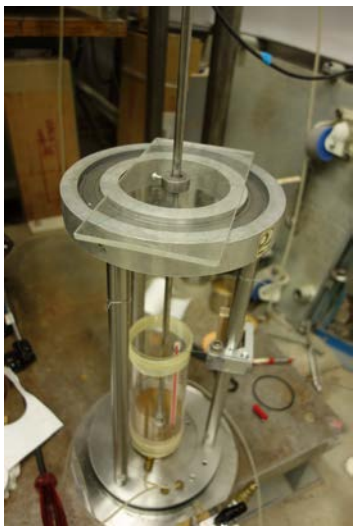

Fig. 3.8 Specimen preparation of Edosaki sand by moisture tamping

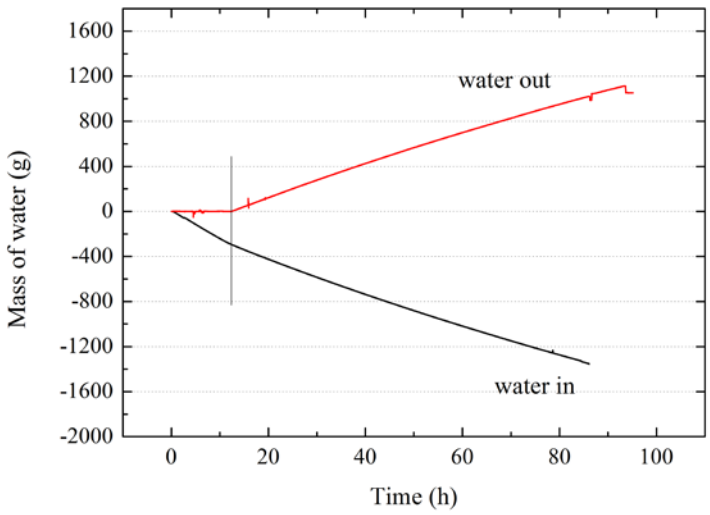

Fig. 3.9 Water infiltration

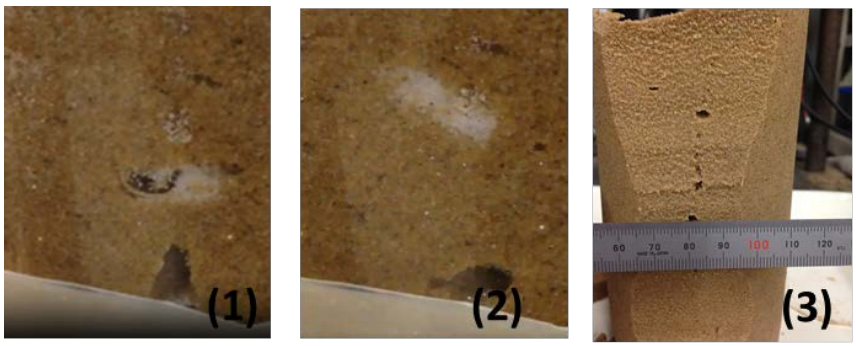

Fig. 3.10 (a) Piping propagation in Toyoura sand

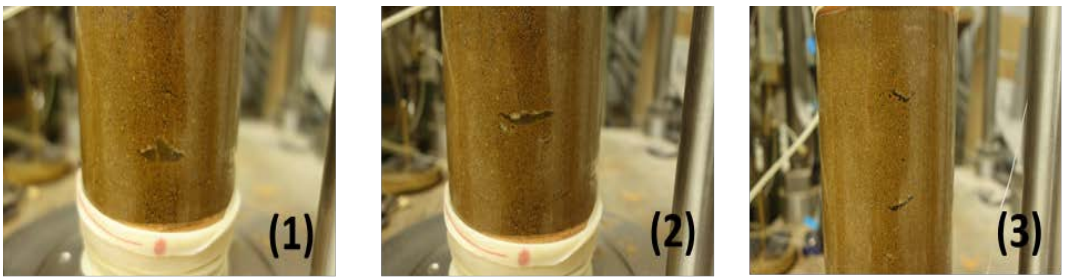

Fig. 3.10(b) Piping propagation in Edosaki sand

3.4 Apparatus and testing procedure-Triaxial compression test

Fig.3.11 shows the triaxial apparatus which is employed in this study. This apparatus mainly consists of vertical loading system, the cell, measurement devices and the computer. Fig. 3.12 and Fig. 3.13 show the schematic diagram of the apparatus and loading systems.

3.4.1 Loading systems

The axial loading system consists of an AC servomotor, a reduction gear system, electromagnetic clutches and brakes. The axial load is applied on the cylindrical specimen via servo-motors at constant strain rates. Through an electro-magnetic clutch, loading direction could be reversed instantly. Stress and strains are controlled automatically in the program named “Digit Show Basic” in computer, where required value is given as an input to the software and converted into the voltage signals and then to analog signals by DA (digital to Analog) board. The calibration result for motor speed is shown in Fig. 3.28.

3.4.2 Cell pressure

During the specimen set-up period, cell pressure is adjusted by a regulator, with the positive pressure from the main source. After that, control of cell pressure is fully computerized through an electro-pneumatic transducer (E/P) with a capacity of 1000 kPa. E/P receives the analog signal corresponds to the required cell pressure which is converted from D/A board.

3.4.3 Measurement devices

As for the data acquisition system, different transducers are employed as introduced below. These transducers will generate small voltages, and the voltages will be amplified by amplifiers. Then the analog signals would be converted into a digital electronic signal by two 16-bit AD converter board. Thus, output files including voltage and physical results calculated by calibration factors will be saved automatically.

11 amplifiers were employed in this study, corresponding to 11 channels: load cell, External Displacement Transducer (EDT), High Capacity Differential Pressure Transducer (HCDPT), Local Displacement Transducer (4 channels), Clip Gauges (3 channels), upper water tank, lower water tank.

✧ *Load cell*

A load cell with a capacity of 2 kN was used in this apparatus, which was fixed upon the top cap. Four electronic resistant strain gauges are fixed on the copper block with one pair at compression side and the other pair on the tension side. It was calibrated by knows weights and the voltage in amplifier varies from 0 to 5 in 100kg. The photo of load cell and its calibration result are shown in Fig. 3.14.

✧ *High Capacity Differential Pressure Transducer (HCDPT)*

HCDPT is the device for measuring the effective stress by the difference in pressures between cell pressure and the pore water pressure. The chamber in HCDPT is divided by a thin membrane into two parts, with the positive side connected to the cell pressure and negative one to the top and bottom drainage tubes of the specimen. The central membrane will be bended if the pressure difference between two chambers is detected, which would be reflected by a voltage difference. In this research, sand was tested under drained condition and the negative terminal of HCDPT is open to atmosphere, i.e. back pressure is kept as 0. Calibration curve for HCDPT is given in Fig. 3.15.

✧ *External Displacement Transducer (EDT)*

As illustrated in Fig. 3.16, EDT which is externally fixed on a horizontal plate connected with the loading piston, is employed to measure the axial deformation of the specimen. EDT used in this study has a capacity of 20mm along the loading shaft, calibrated by measuring the voltage output corresponding to known heights from 1mm to 20mm (seen in Fig.3.16).

✧ *Local deformation transducer (LDT)*

LDT is commonly used in this laboratory for its simplicity and precise measurements. Compare with EDT, LDT shows its advantage in measuring very small strain between 10^{-6} and 10^{-2}. It is made of a thin and flexible phosphor bronze strip, with a pair of strain gauges attached on. These gauges could catch bending deformations of LDT caused by axial compression or extension.

In this study, four LDTs with 70 mm in length, 3 mm in width, and 0.2 mm in thickness are used. In order to obtain the axial strain of sand along the glucose pipe locally, two pair of LDTs is fixed at the upper and lower half of the specimen separately at opposite side. The calibration of LDT is carried out on a micrometer, which can apply known displacements by 0.1mm. The calibration results of four LTDs are shown in Fig. 3.17 - Fig. 3.20.

✧ *Clip gauges (CG)*

Each clip gage has a transducer made from a phosphor bronze strip on which four strain gages, of the same type as mentioned in case of LDT, are arranged (two on the compression side and two on the tension side) forming a Wheatstone bridge. The sensitivity and the working principle of the transducer is exactly the same as the LDT. The maximum measurable radial deformation is about 3 mm. For the calibration, it was fixed on a table with micrometer in the same way as it was attached to the soil specimen during the test. Then a known increment of deformation was applied and the resulting voltage was recorded, and the results are shown in Fig. 3.22 – Fig. 3.24.

✧ *Water tanks*

Water infiltration during the dissolving of glucose pipes is controlled by the load cell connected with water tank. Upper water tank is hung at higher elevation and the water comes into the specimen under gravity. On the other hand, lower water tank is set at lower elevation referred to the specimen and water was drained out from the top cap to the tank. Capacity of the two load cells for water tank is 10 kg (Fig. 3.25), and the calibration curves are shown inFig. 3.26 and Fig. 3.27.

Fig. 3.11 Triaxial apparatus

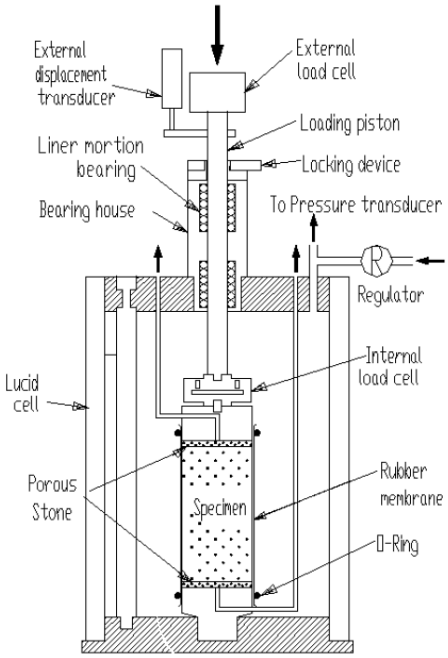

Fig. 3.12 Schematic diagram of triaxial apparatus-cell and transducers

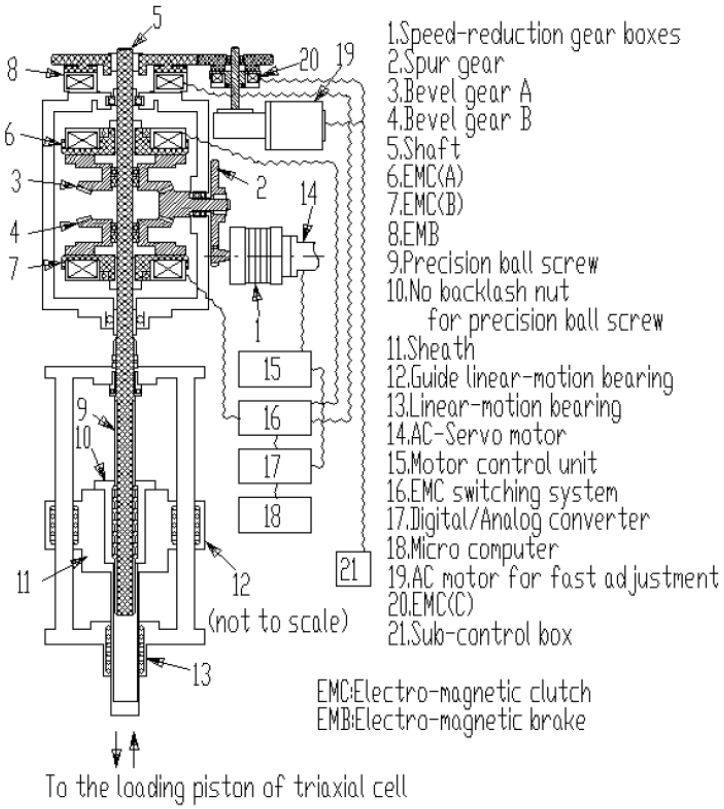

Fig. 3.13 Schematic diagram of triaxial apparatus - axial loading system

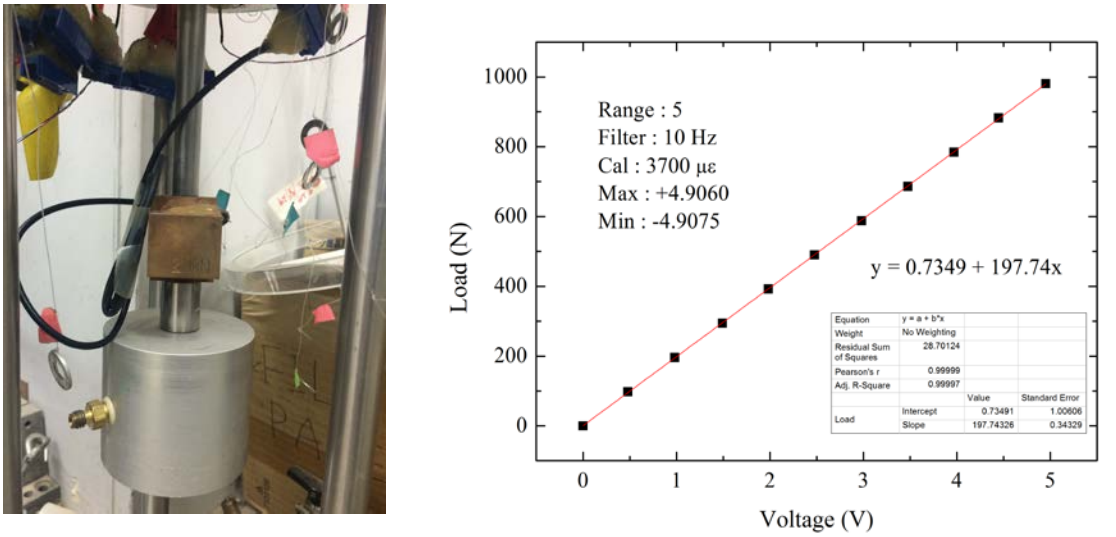

Fig. 3.14 Load cell and its calibration

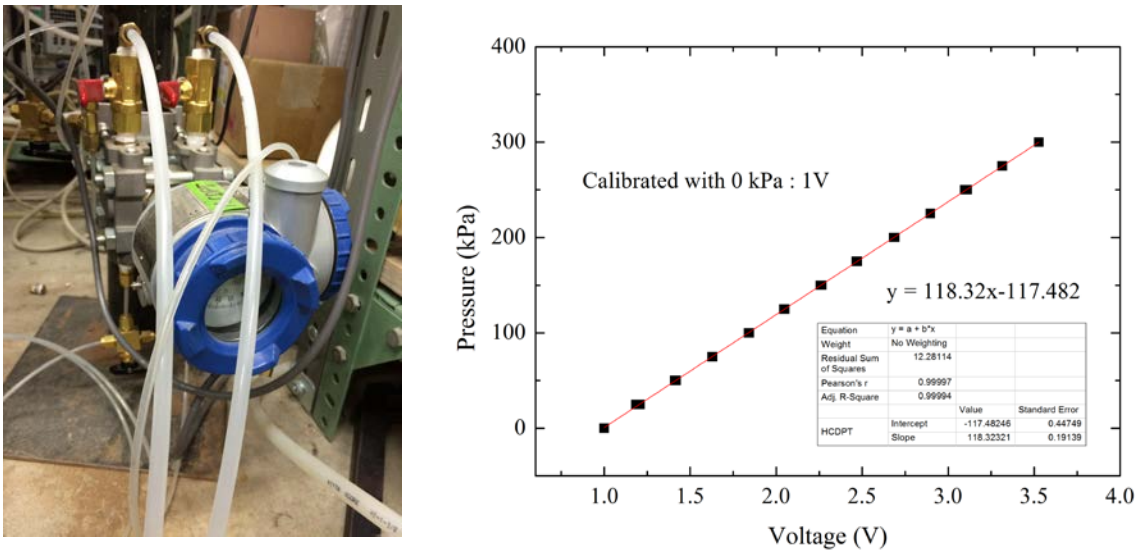

Fig. 3.15 HCDPT and its calibration

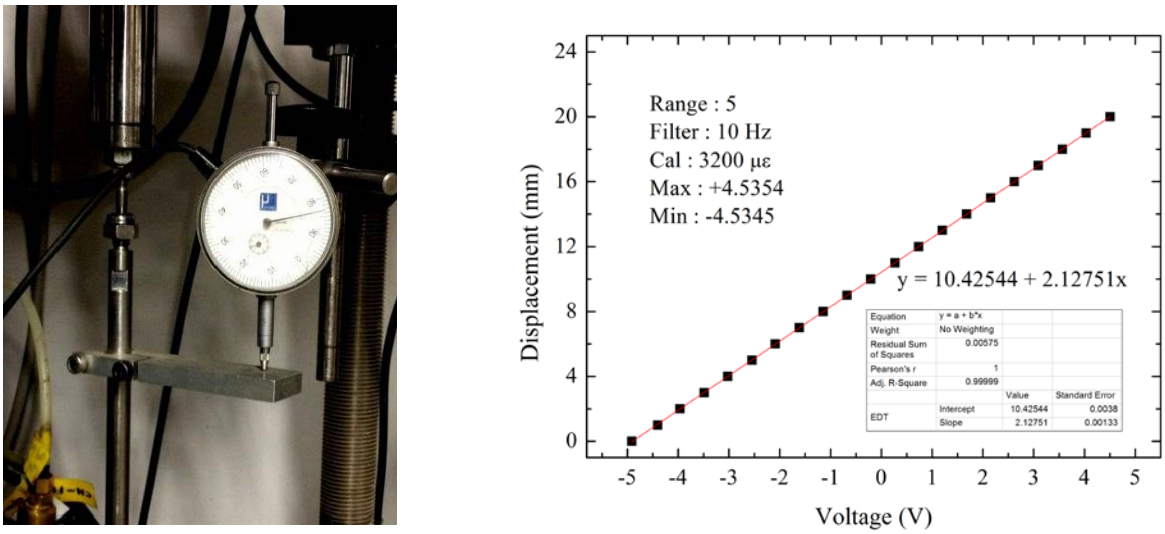

Fig. 3.16 EDT and its calibration

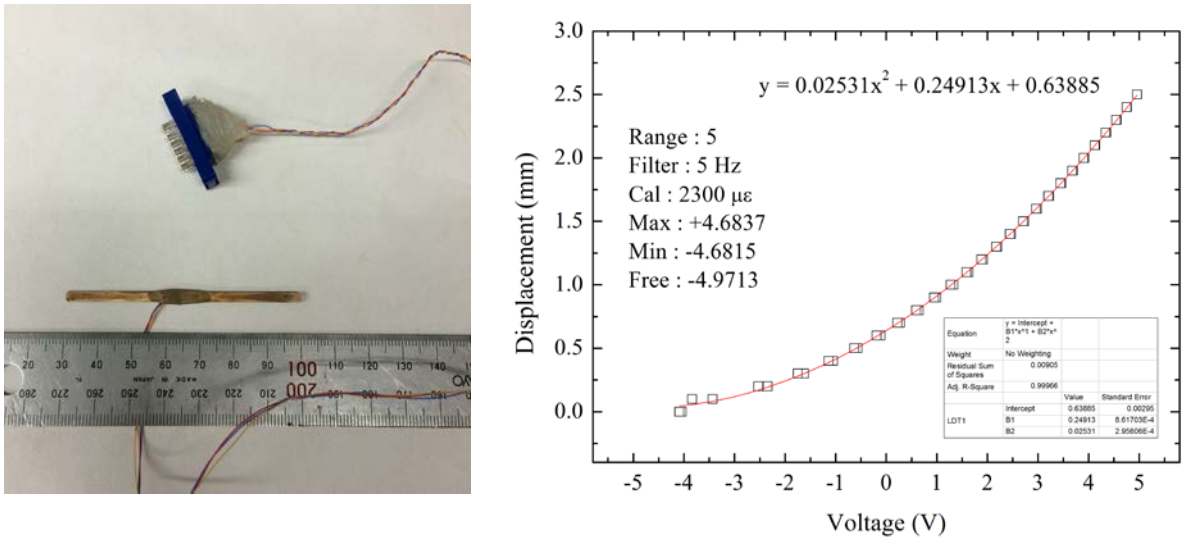

Fig. 3.17 LDT and its calibration (LDT1)

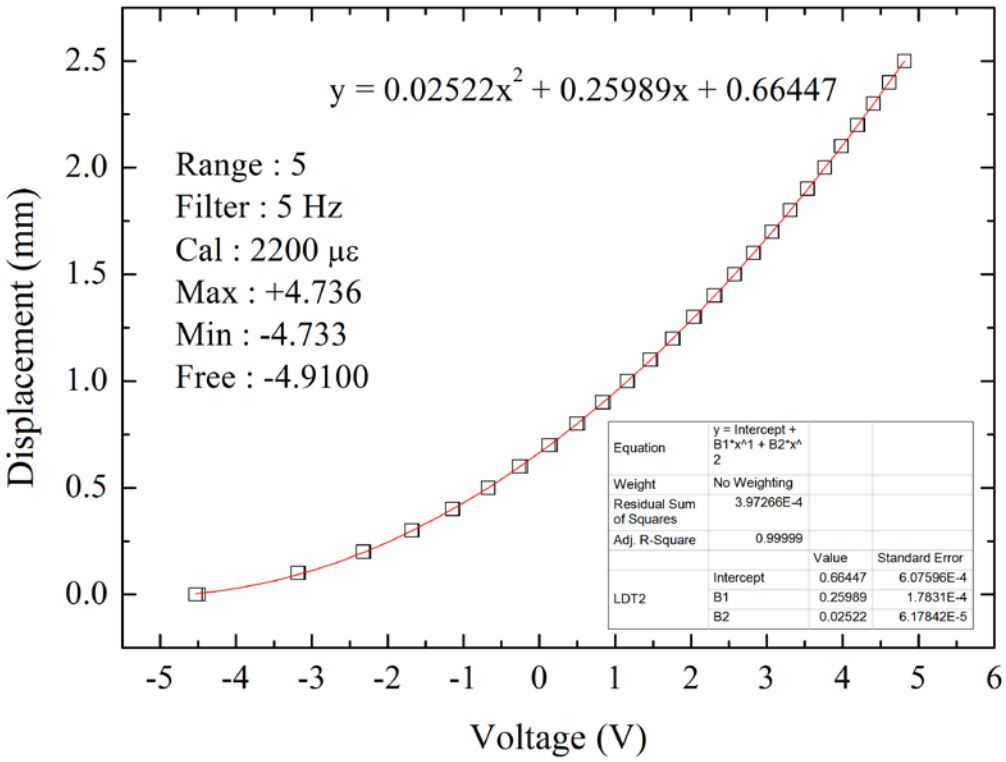

Fig. 3.18 Calibration of LDT2

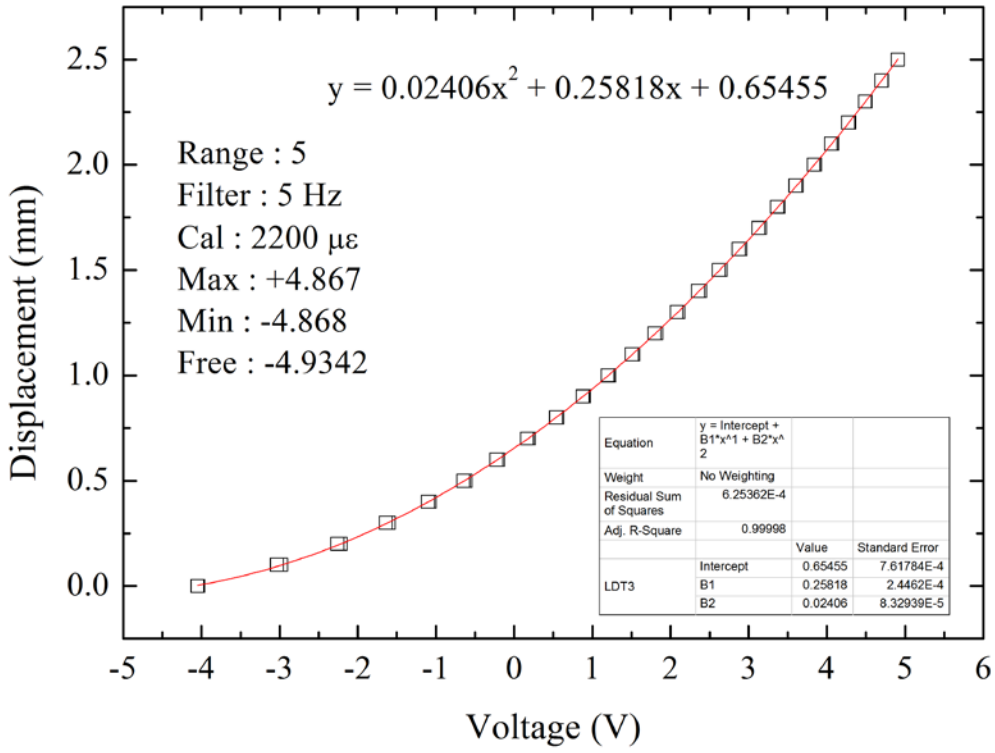

Fig. 3.19 Calibration of LDT3

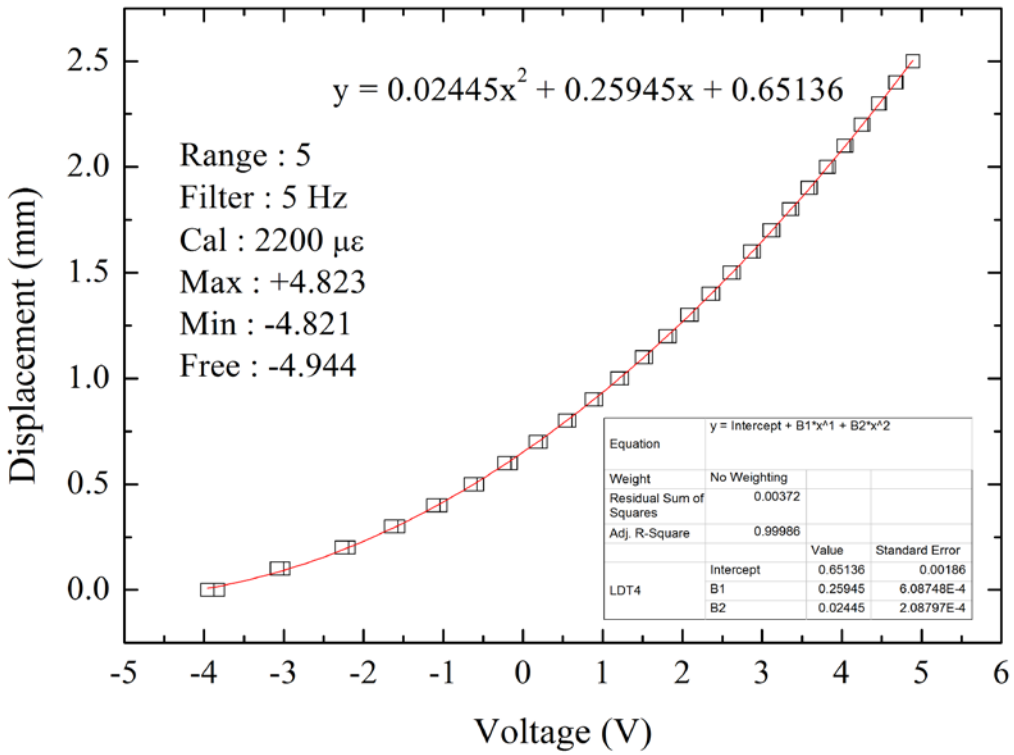

Fig. 3.20 Calibration of LDT4

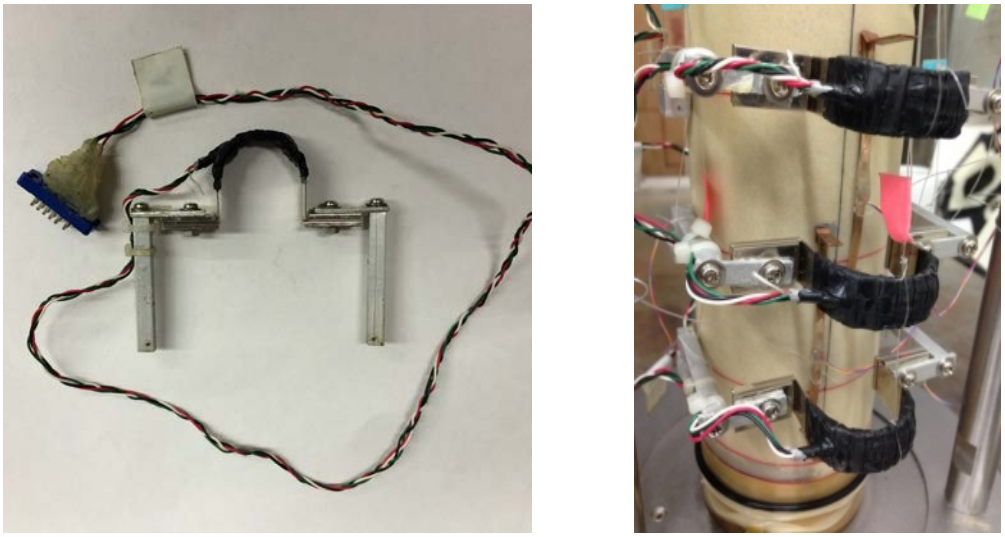

Fig. 3.21 Clip Gauges

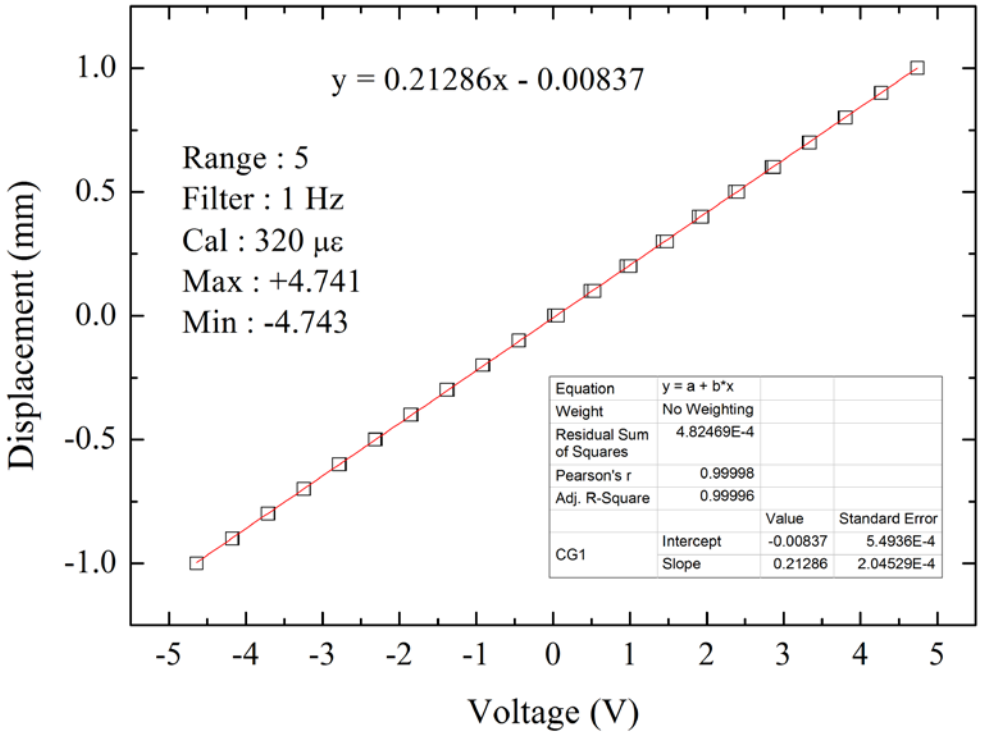

Fig. 3.22 Calibration of CG1

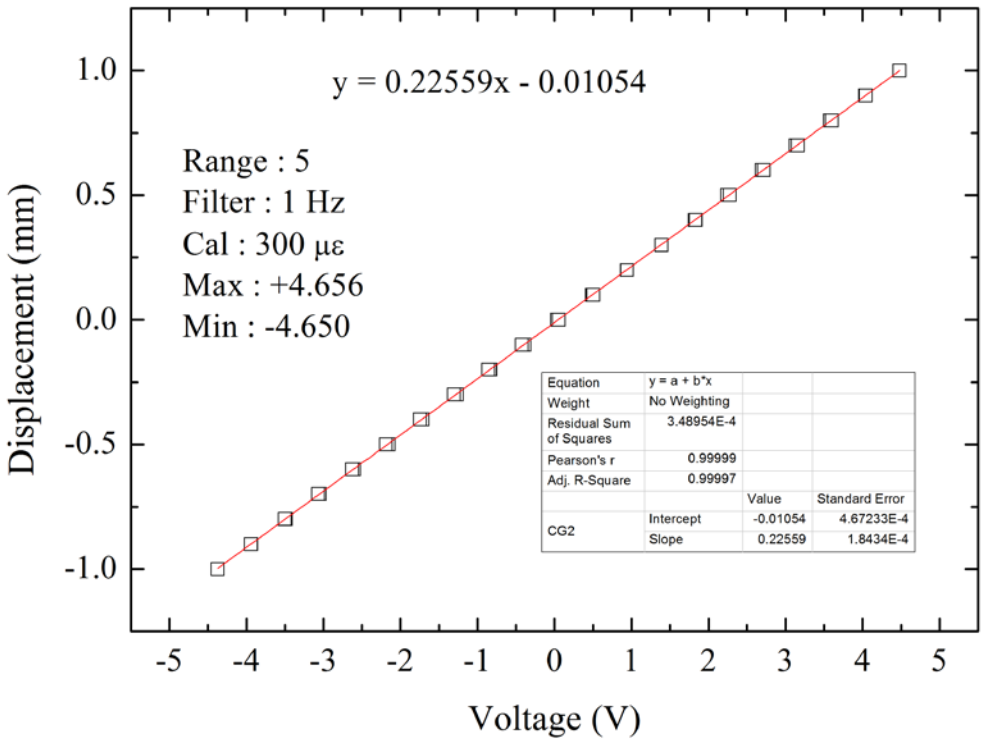

Fig. 3.23 Calibration of CG2

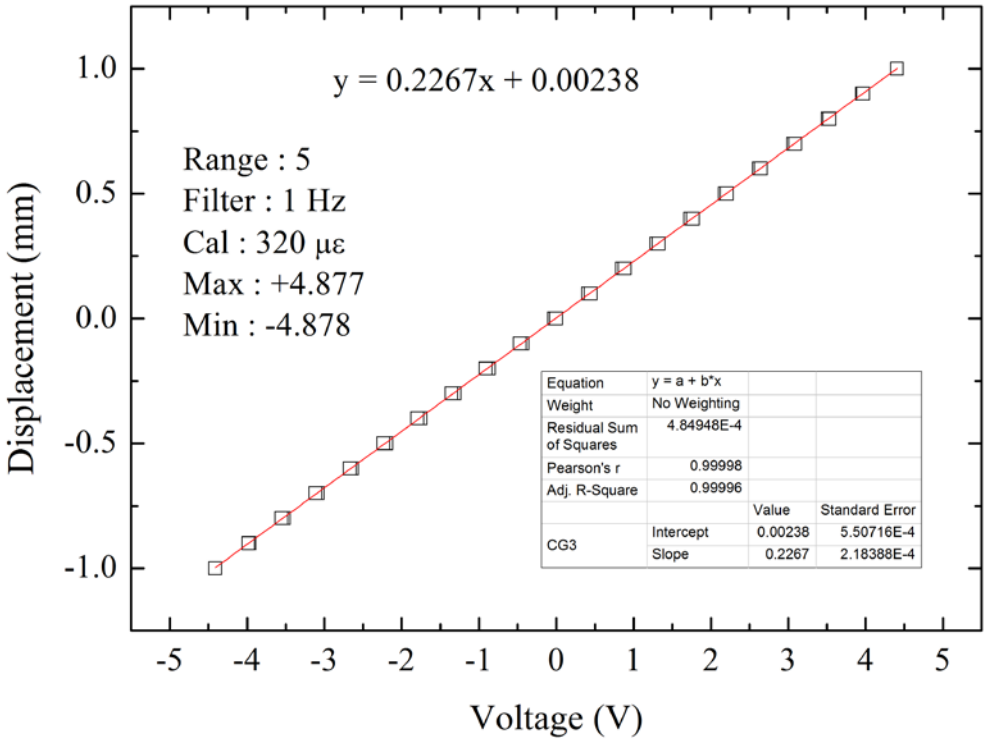

Fig. 3.24 Calibration of CG3

Fig. 3.25 Load cell for water tank

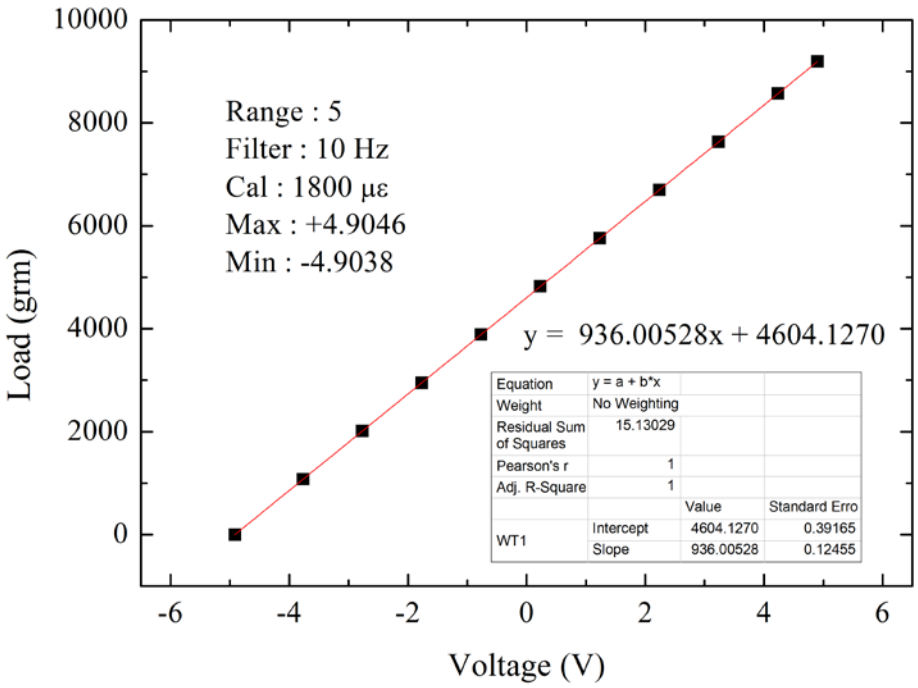

Equation	y = a + b*x		
Weight	No Weighting		
Residual Sum of Squares	15.13029		
Pearson's r	1		
Adj. R-Square	1		
		Value	Standard Erro
WT1	Intercept	4604.1270	0.39165
	Slope	936.00528	0.12455

Fig. 3.26 Calibration of water tank 1

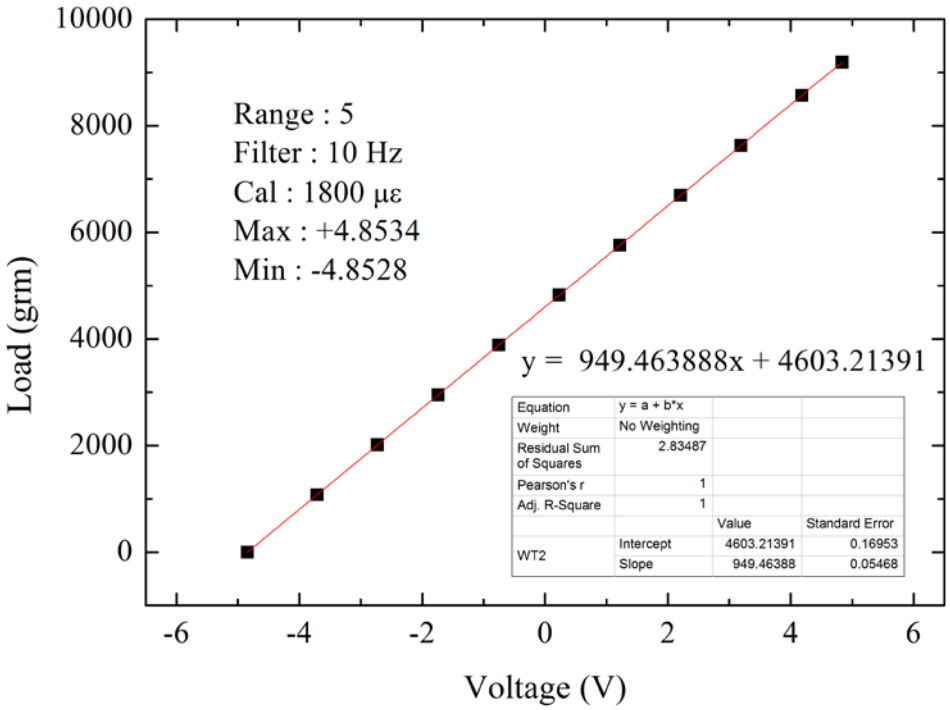

Equation	y = a + b*x		
Weight	No Weighting		
Residual Sum of Squares	2.83487		
Pearson's r	1		
Adj. R-Square	1		
		Value	Standard Error
WT2	Intercept	4603.21391	0.16953
	Slope	949.46388	0.05468

Fig. 3.27 Calibration of water tank 2

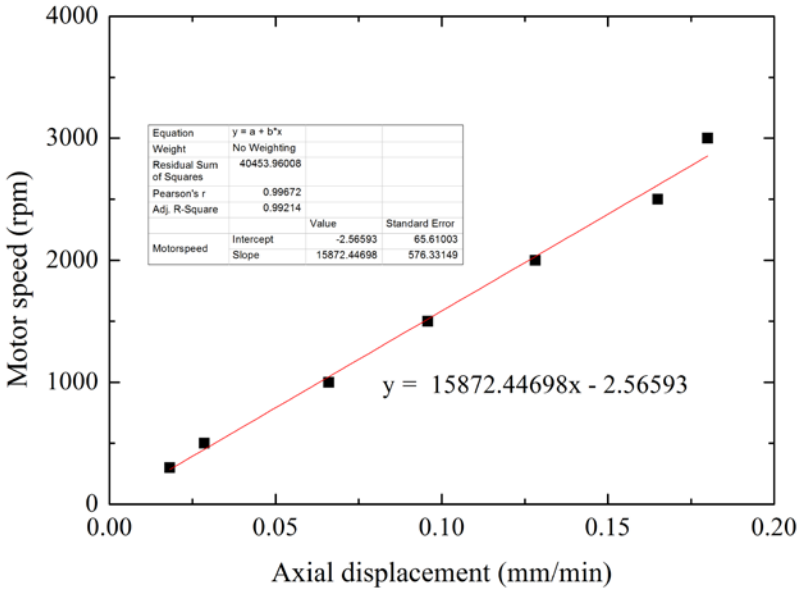

Fig. 3.28 Calibration of motor speed

3.4.4 Preparation of the specimen and test procedure

3.4.4.1 Specimen preparation

- First, the membrane was cut into the proper size, by considering the specimen size in this test is 75 mm in diameter and 150 mm in height. The locations of sensors such as LDTs and CGs should be marked in advance.
- After grease was applied around the pedestal, two rubber bands as well as O-ring were inserted. Then the membrane of 0.3 mm thickness was placed over the pedestal with a porous stone on it.
- Outer mould consists two symmetrical metal parts was fixed and tightened together, so as to avoid vacuum leakage. A small amount of grease should be applied long the edges of the mould before fixing it.
- Membrane was put over the mould, and a partial vacuum of 40 kPa was applied between the membrane and mould to make it perfectly sealed.
- The specimen was prepared by the air pluviation method by using a funnel with appropriate opening. The falling height was decided by the desired densities, and the same height was supposed to be maintained from the funnel opening to the sand surface. In order to make a uniform specimen, pouring direction was changed from clockwise to

anti-clockwise circumferentially. The extra sand which was flowing away during the pluviation was collected in the manually made collector laid around the mould.

For the cases with internal glucose pipe, a plastic pipe of 7mm in diameter and 0.15mm in thickness was placed in advance. Glucose powder was poured into the pipe after all the sand was placed into the mould. Then, the pipe was removed by hand carefully, with the glucose left inside.

- After completing the pluviation, top surface of the specimen was leveled horizontally by a metal strip. Then the upper porous stone was placed on the top of sand. Waste sand was then collected and weighted.
- Top cap was placed and fixed by screws. Then the top cap is balanced using the counter weight. Adjusted the amplifier of load cell to 0 voltage, and set the value of axial pressure as 0 kN as well.
- Before moving down the top cap to the specimen, drainage tubes connection should be finished both at the pedestal and the top cap. After that, top cap was placed carefully over the specimen until it touched the top porous stone. The clamp was then fixed, and the membrane was pulled gently over the top cap. The specimen was perfectly sealed by rubber bands.
- The counter balance was applied again and the clamp was unlocked. Then vacuum pressure around 25 kPa was applied to the specimen, while decreasing the vacuum between the membrane and the mould. Finally, the mould was removed carefully.
- The height and diameter were measured at three locations. The average result was inputted into the program.
- Before fixing the local sensors on the specimen, they were placed at freely with no deformation and strain at this state was considered as 0. Then four LDTs and three CGs were fixed on the specimen with the support of the hinges and aluminum blocks glued outside the membrane, as is shown in Fig. 3.21. Since large deformation would happen near the glucose side, the initial values of the sensors were supposed to be set around -1 in voltage for LDTs and +1 for CGs. In addition, in order to protect the sensors during shearing, detachment was allowed by pulling a thin thread (fishing line) with one end connected to the sensor and the other end outside the cell through the top cover of the cell chamber.
- After all the connections and conditions of sensor were checked, top cap was locked and the counter balance system was removed. Then the specimen was covered with the cell carefully since even small disturbance might cause detachment of the sensors.

- Counter balance was then applied again, and connection with HCDPT was set.
- The cell pressure was increased gradually up to 25 kPa, while reducing the vacuum pressure in the specimen down to the atmospheric pressure. During this process, the effective stress acting on the specimen was maintained constant as 25 kPa. The load cell value should also be kept as 0 by adjusting the counter balance.
- External Displacement Transducer was fixed with the tip touching to the rigid palte which is connected to the loading piston, and the initial value was set as 0.

For Edosaki sand, specimen was prepared by moisture tamping method. 15 layers with the height of 1 cm for one layer were tamped from the bottom to the top gradually. The water content was around 6%.

3.4.4.2 Test procedures

Fig. 3.29 shows the stress path in the triaxial compression test.

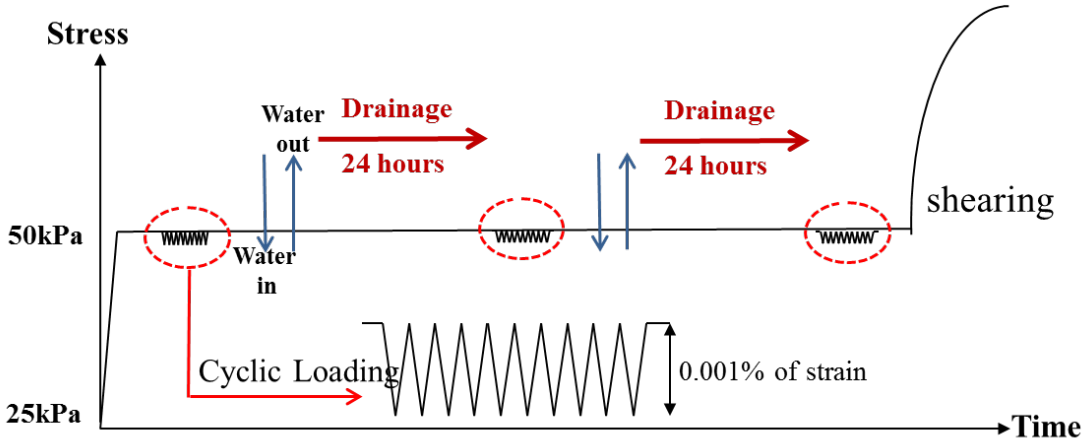

Fig. 3.29 Stress path for triaxial compression test

Step 1 Confining pressure was increased to 50 kPa, and then isotropic consolidation was kept around 12 hours to dissipate the creep effect.

Step 2 Eleven cycles of small cyclic loading was applied axially with peak to peak strain amplitude of 0.01% for the dry sand.

Step 3 The first water cycle started. About 1500 ml of de-aired water was infiltrated from the pedestal with the rate of 14~16 ml/min, and drained out from the top cap to the lower water tank. After all the water in infiltrated in, water input valve was closed for nearly 10 minutes, and then drainage was allowed again.

Step 4 Second small cyclic loading was conducted after 20 hours from the last step.

Step 5 In order to check the influence of repetitive water flow on the behavior of soil with internal pipes, a second water cycle of 300 ml was applied.

Step 6 Third small cyclic loading was conducted after 20 hours, following the second water cycle.

Step 7 Local sensors were removed from the specimen, and shearing started with strain rate of 0.1%/min.

3.5 Apparatus and testing procedure-Torsional shear test

As is shown in Fig. 3.30, newly developed high capacity medium size hollow cylinder apparatus at Institute of Industrial Science, the University of Tokyo, is employed in this study. With triaxial apparatus, piping effect is evaluated by examining the variation of Young's modulus, Possion's ratio and shear strength of the sand. In order to clarify the relationship between piping orientation and major principal stress direction, torsional shear test is conducted on the sand both with glucose pipes vertically and horizontally.

3.5.1 Vertical and torsional loading systems

The hollow cylinder apparatus is schematically shown in Fig. 3.31 and Fig. 3.32, in which the specimen size is 100 mm in outer diameter, 60 mm in inner diameter and 100 mm in height.

The axial loading system is similar with the one in triaxial apparatus, which consists of an AC servo-motor, a reduction gear system with two gears, electro magnetic clutches, brakes, and a ball screw with a pre-pressured nut. The motor always drives in one direction. Simultaneously, the upper gear is rotating in one direction and the lower gear is rotating in the opposite direction. Thus, the loading direction from downward to upward could be achieved without any backlash by the electric clutches.

The torsional loading system also consists of similar devices. Torque is transmitted to the loading shaft by means of a metal band. Both vertical and torsional loading systems are designed to have nearly zero backlashes.

3.5.2 Cell pressure

As illustrated in Fig. 3.31, cell pressure which is applied through E/P is kept as the same with the pressure in the inner hollow of the specimen by connecting the cell with the bullet of Low Capacity Differential Pressure Transducer (LCDPT). The inner hollow of the specimen is fully filled with de-aired water, and through LCDPT, the volume change could be obtained. The working principal of LCDPT is introduced in the next part.

3.5.3 Measurement devices

14 channels were used in this study in total, which are: two channels for load cell (axial load and torque), two channel for HCDPT and LCDPT, one channel for LVDT, two channel for potentiometers, three channel for CGs, two channel for water tanks and two channel for gap sensors.

Since some of these devices have been explained in triaxial apparatus already, the following illustration mainly focus on the devices and sensors used only in this apparatus.

✧ *Two-component Load cell*

A two-component load cell with a capacity of 15 kN for vertical load and 0.3 kN·m for torque was used in this apparatus as shown in Fig. 3.34. As described by Tatsuoka (1988), such load cells has a negligible coupling effect. The axial load and torque are applied simultaneously and independently on the hollow cylindrical specimen via two servo-motors at constant strain rates.

✧ *Low Capacity Differential Pressure Transducer (LCDPT)*

LCDPT (Fig.3.35) was employed to measure the volumetric change in the torsional test. As illustrated schematically in Fig. 3.33, LCDPT consists of two options of measurement burettes with inner diameters of 36.70 mm and 21.70 mm for large and small volumetric changes, respectively. The third burette is the reference burette with the inner diameter of 21.70 mm. The capacity of the small burette is about 65 cm^3, which is enough for the measurement during monotonic shear.

✧ *Potentiometers*

Fig. 3.36 shows the two potentiometers with the diameter of 30 mm and 50 mm used in this study to detect shear strain during shearing. The bigger one (POT1) was attached to the loading shaft, which could measure large shear strain; while the smaller one (POT2) was attached to the top cap inside the cell to obtain an accurate rotational angle during the beginning of shearing.

✧ *Gap sensor*

As shown in Fig. 3.37, two gap sensors were employed to detect the shear strain during the small cyclic torsional loadings, which were fixed upon the top cap and could be rotated by a knob outside the cell. The effective range of these Gap sensors is -4 mm ~ 4mm, which enable to measure very small shear strain less than 10^{-5}.

Calibration results for all the devices and sensors in this apparatus are shown in Fig. 3.38 – Fig. 3.51.

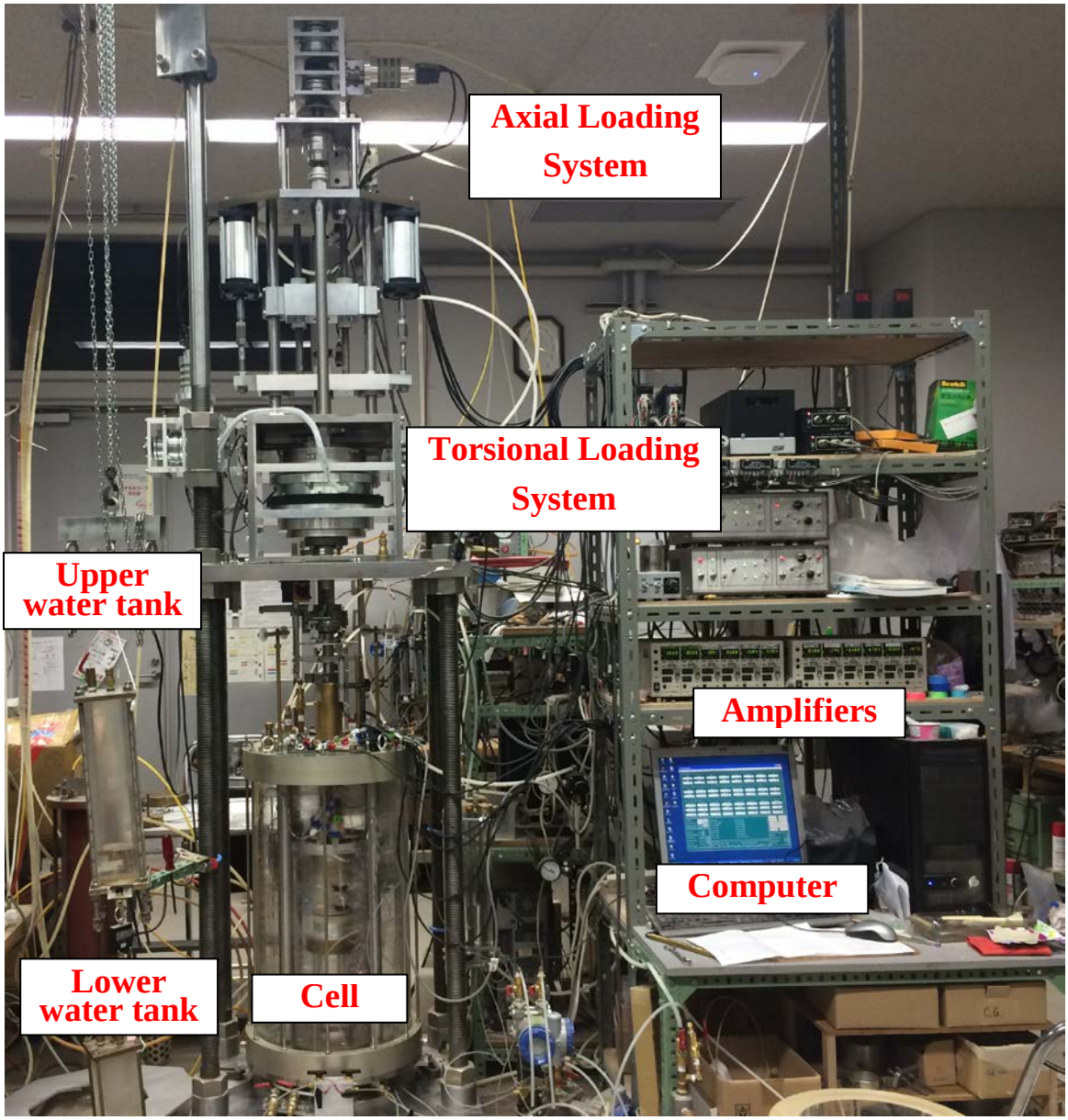

Fig. 3.30 Hollow cylindrical torsional shear apparatus

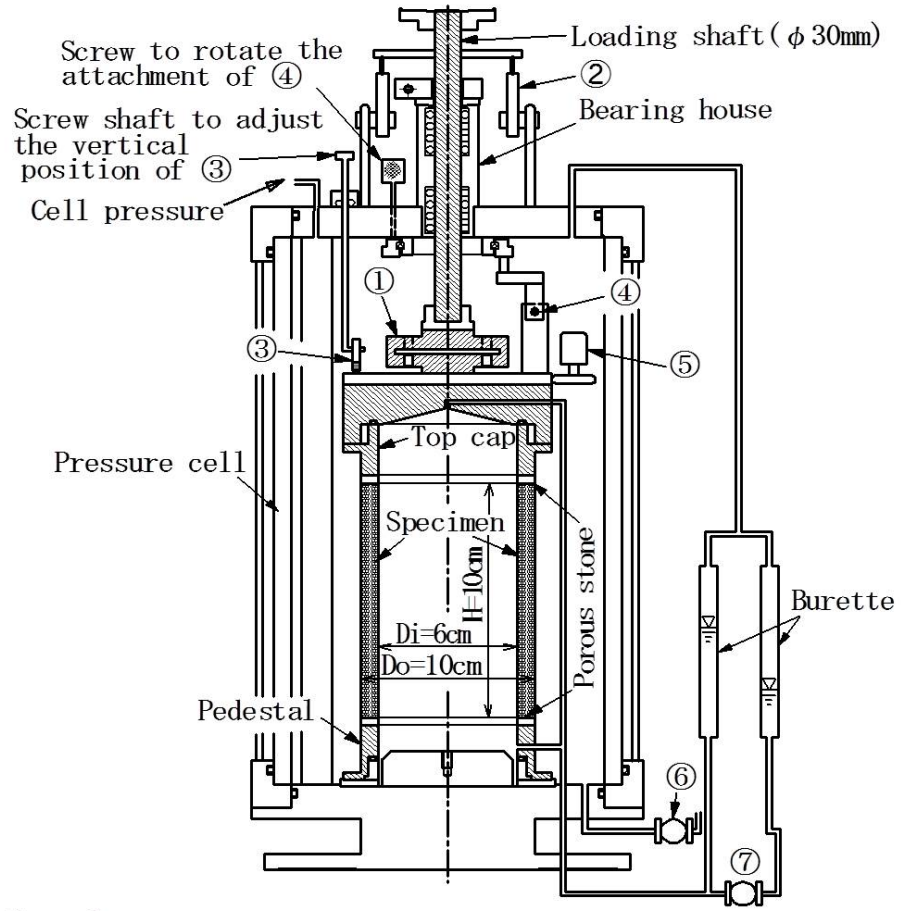

Fig. 3.31 Triaxial cell and transducers for hollow cylinder torsional shear apparatus

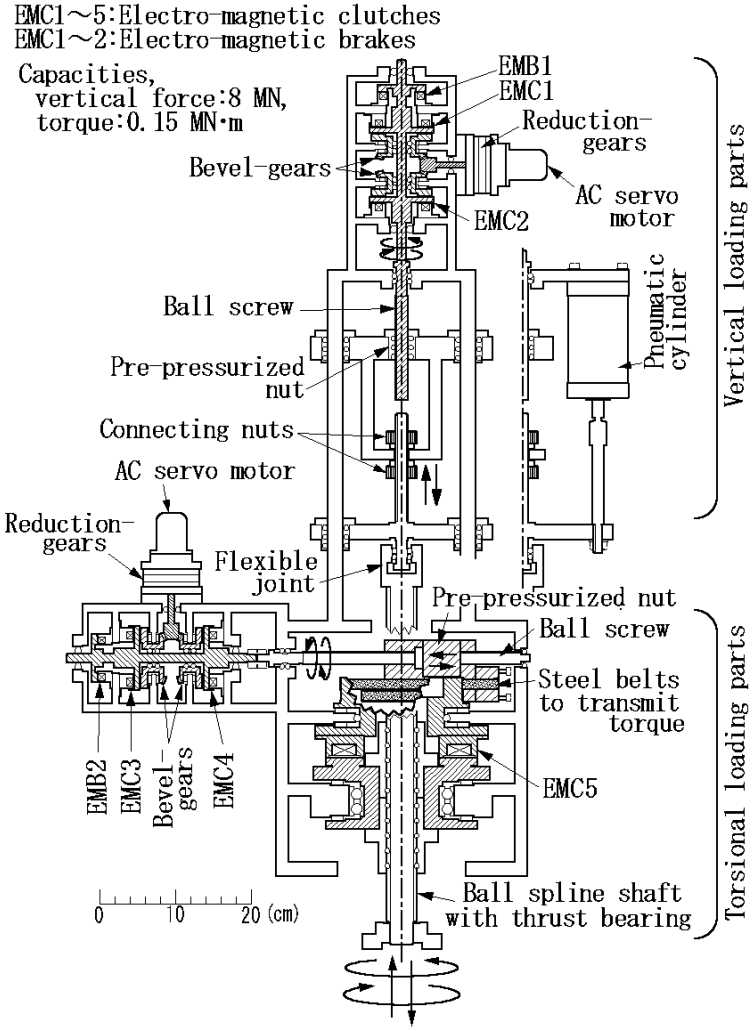

Fig. 3.32 Axial and torsional loading system in hollow cylinder torsional shear apparatus

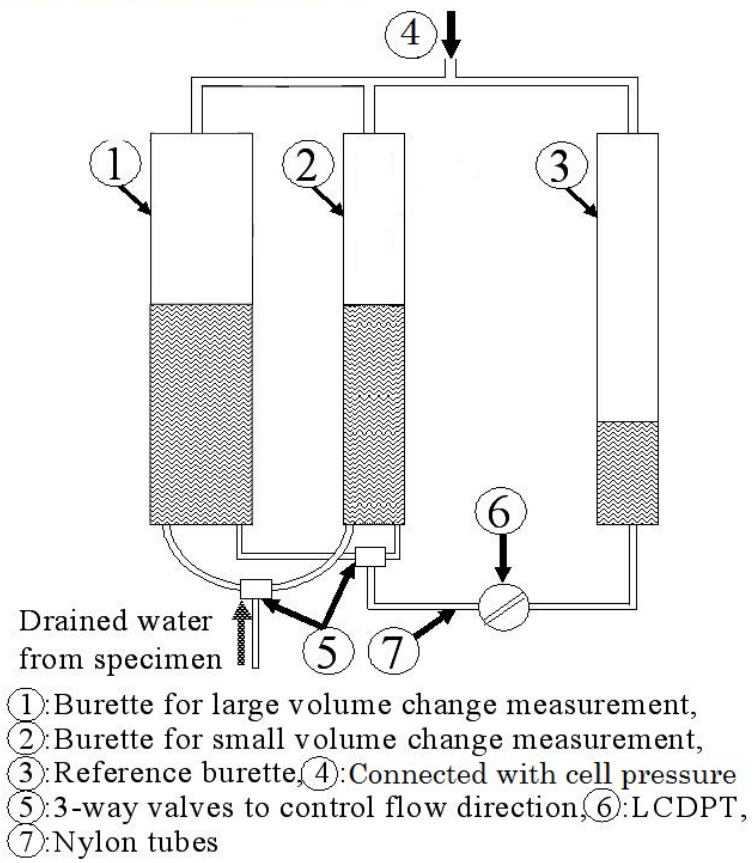

Fig. 3.33Inner hollow volume change measurement system by using LCDPT

Fig. 3.34 Tow-component load cell and the specimen

Fig. 3.35 Low Capacity Differential Pressure Transducer

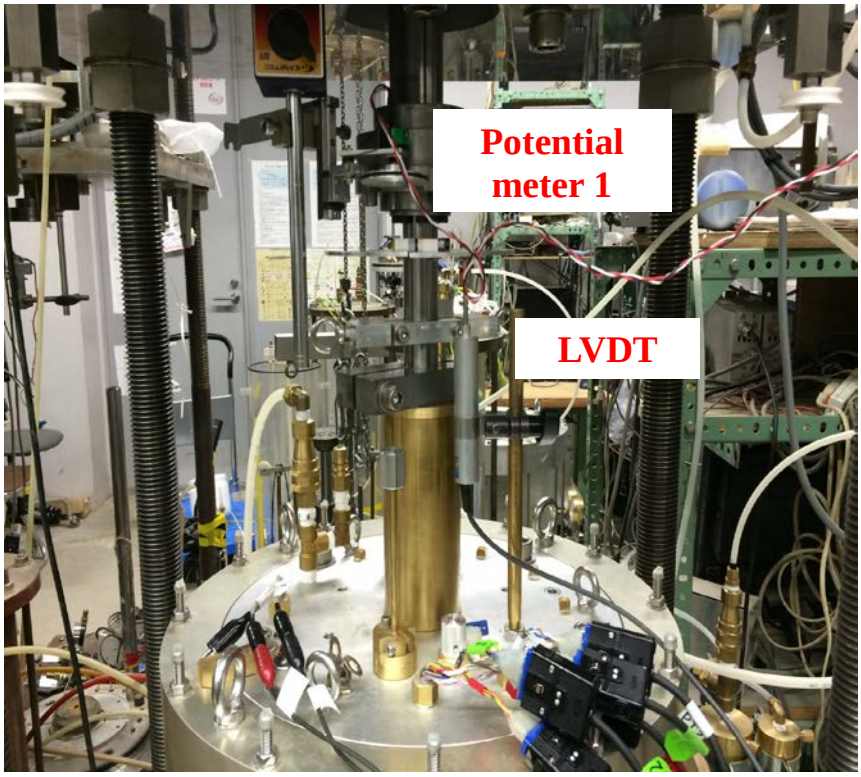

Fig. 3.36 Potential meter

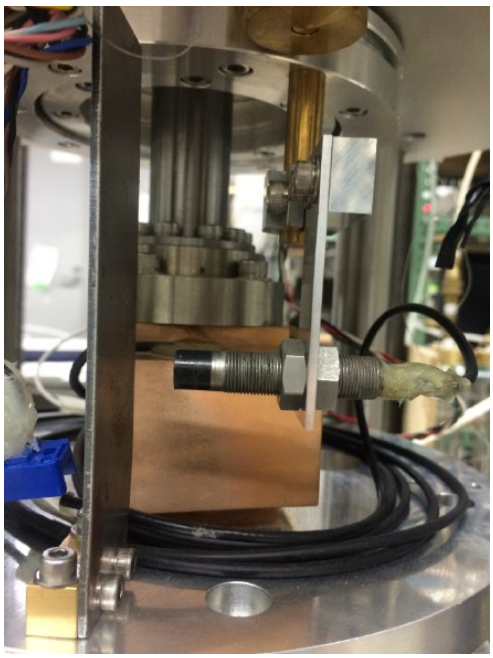

Fig. 3.37 Gap sensor

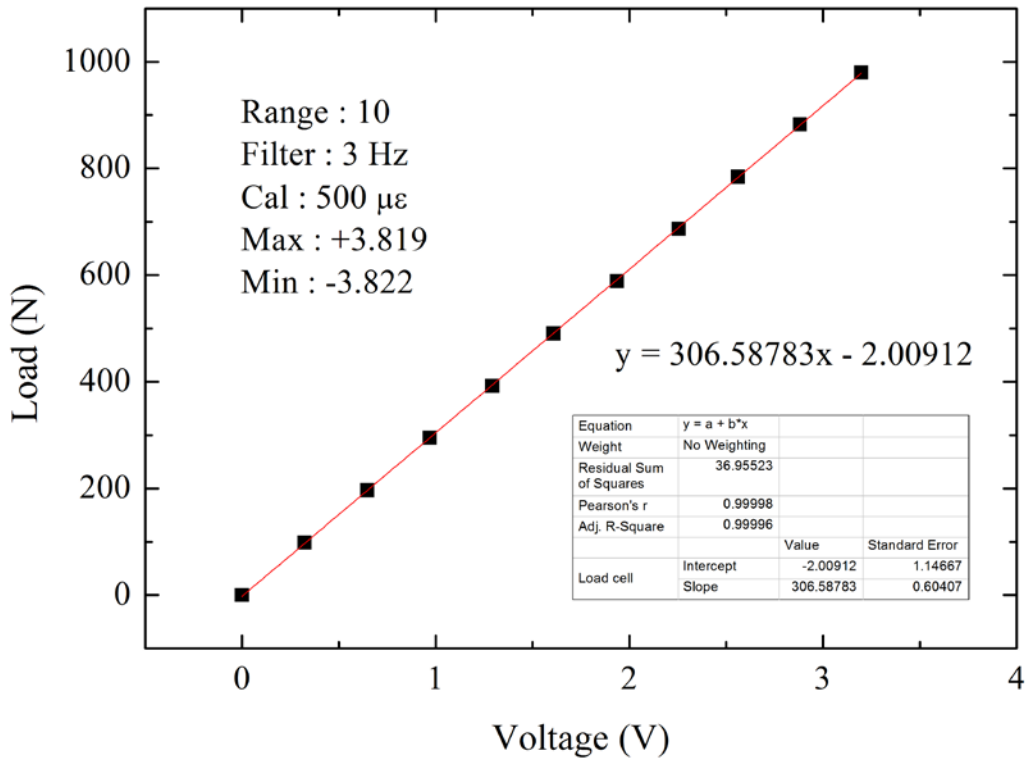

Fig. 3.38 Axial load calibration

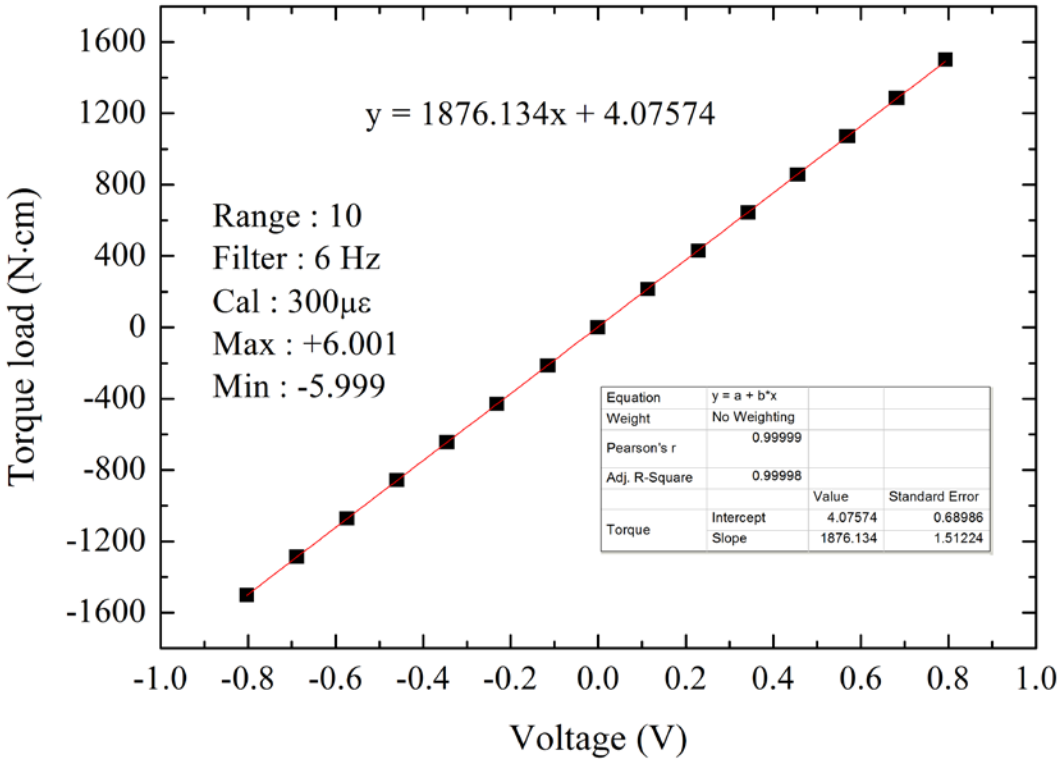

Fig. 3.39 Torque calibration

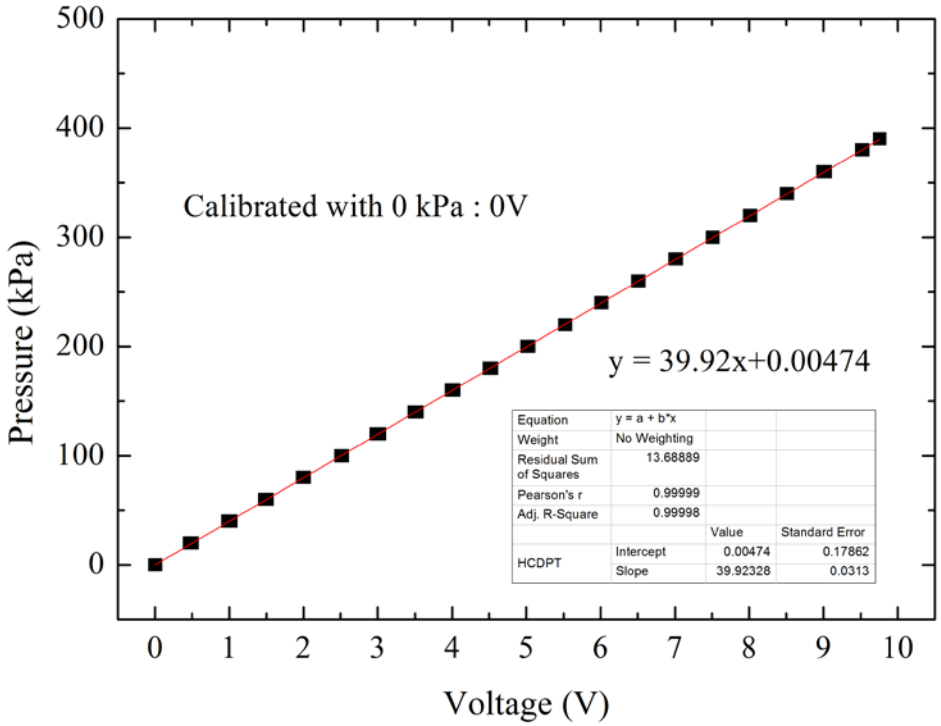

Fig. 3.40 Calibration of HCDPT

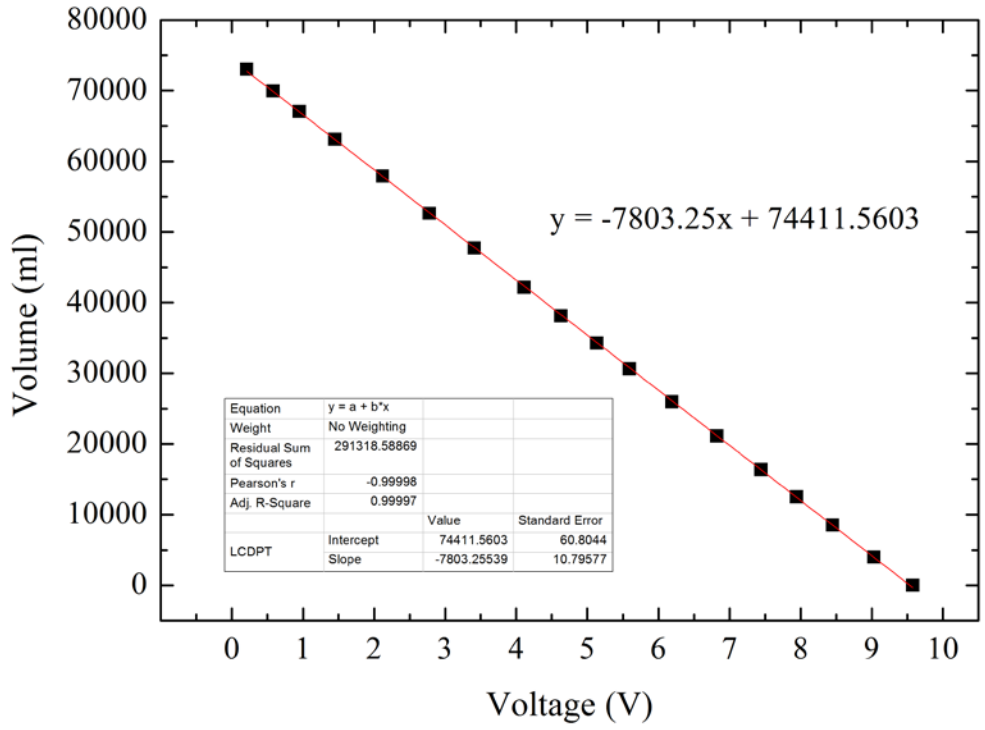

Fig. 3.41 Calibration of LCDPT

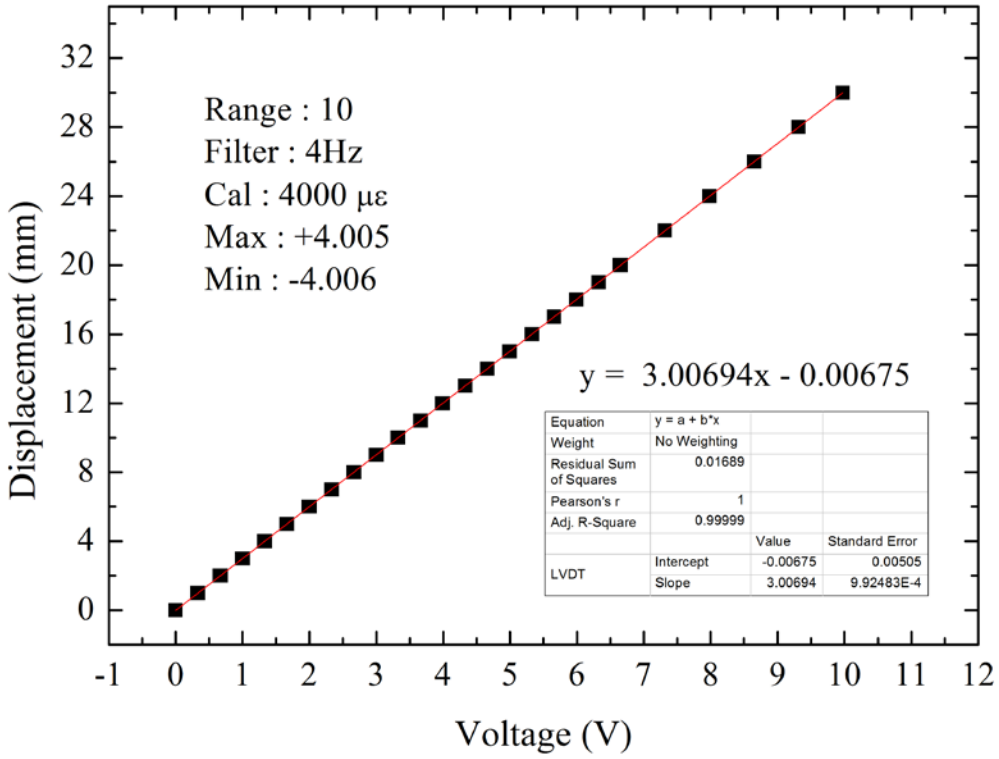

Fig. 3.42 Calibration of LVDT

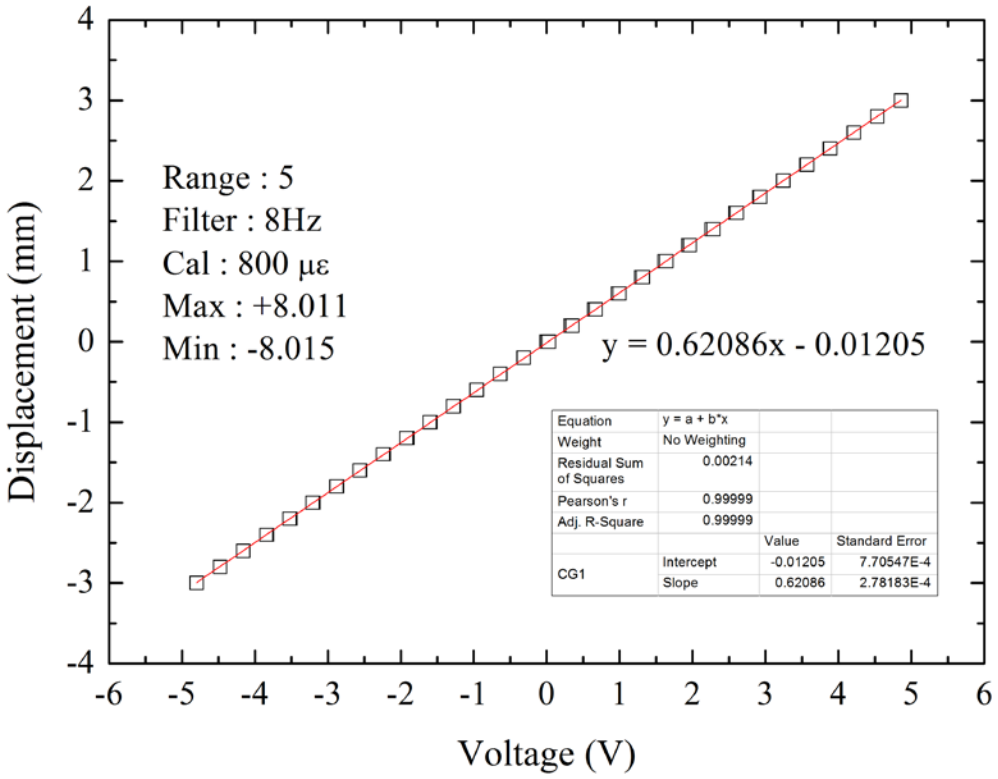

Fig. 3.43 Calibration of CG1

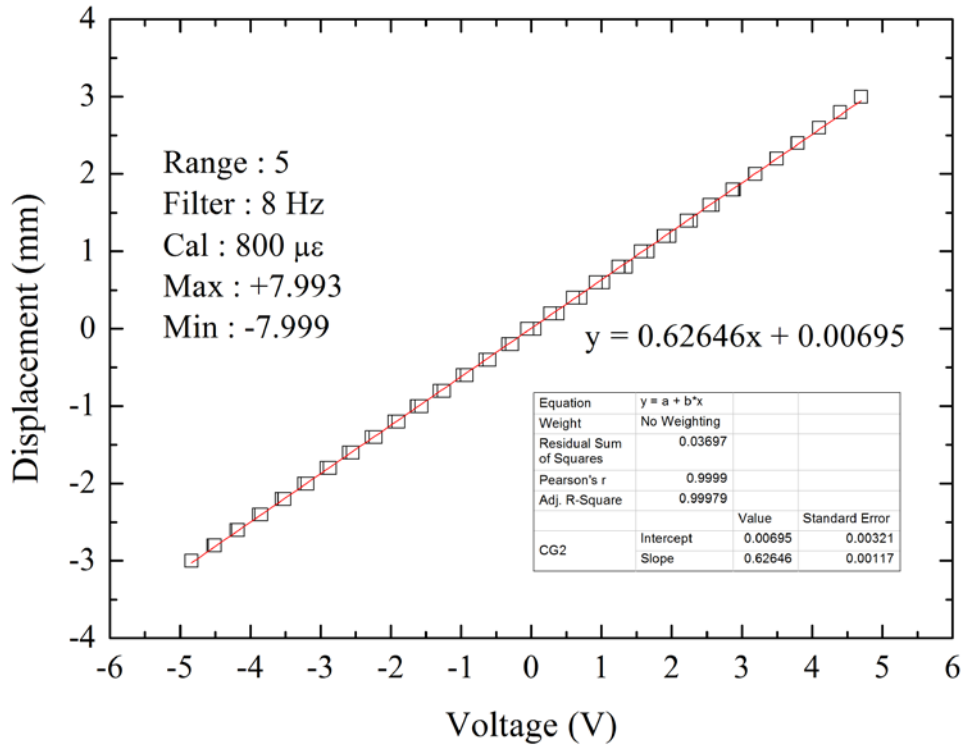

Fig. 3.44 Calibration of CG2

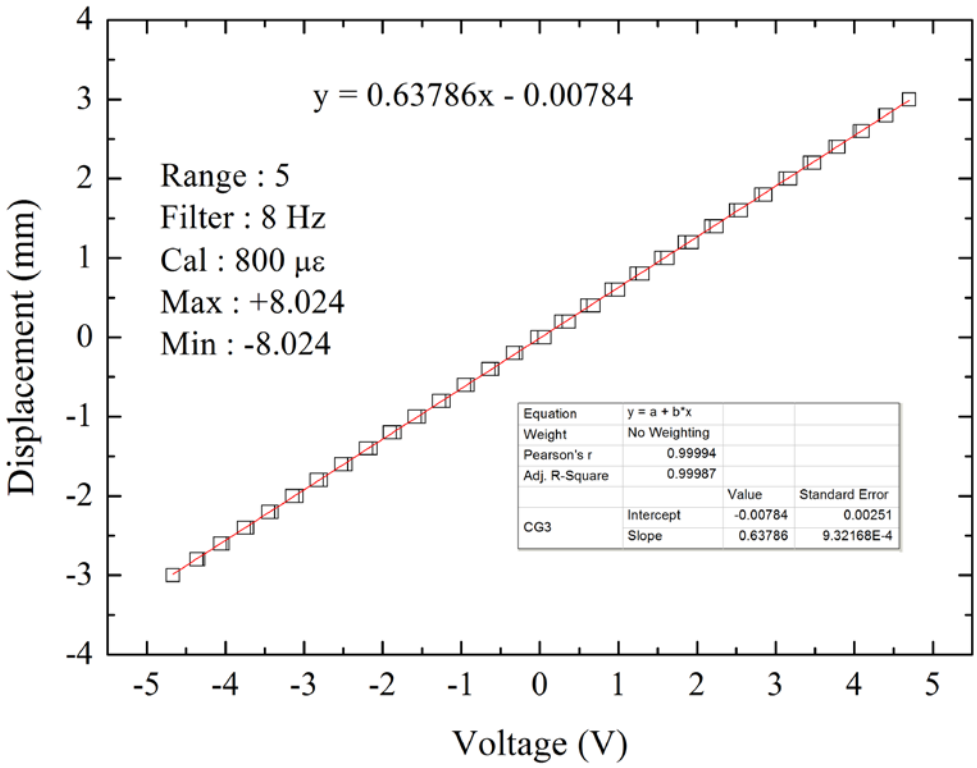

Fig. 3.45 Calibration of CG3

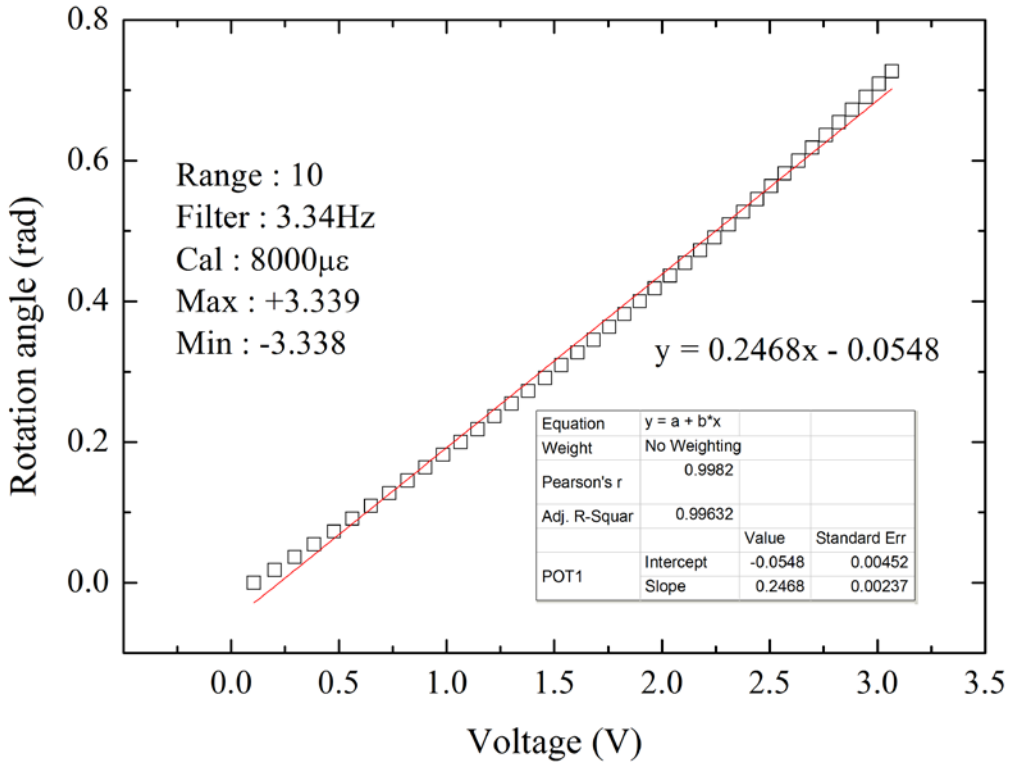

Fig. 3.46 Calibration of POT1 (Big)

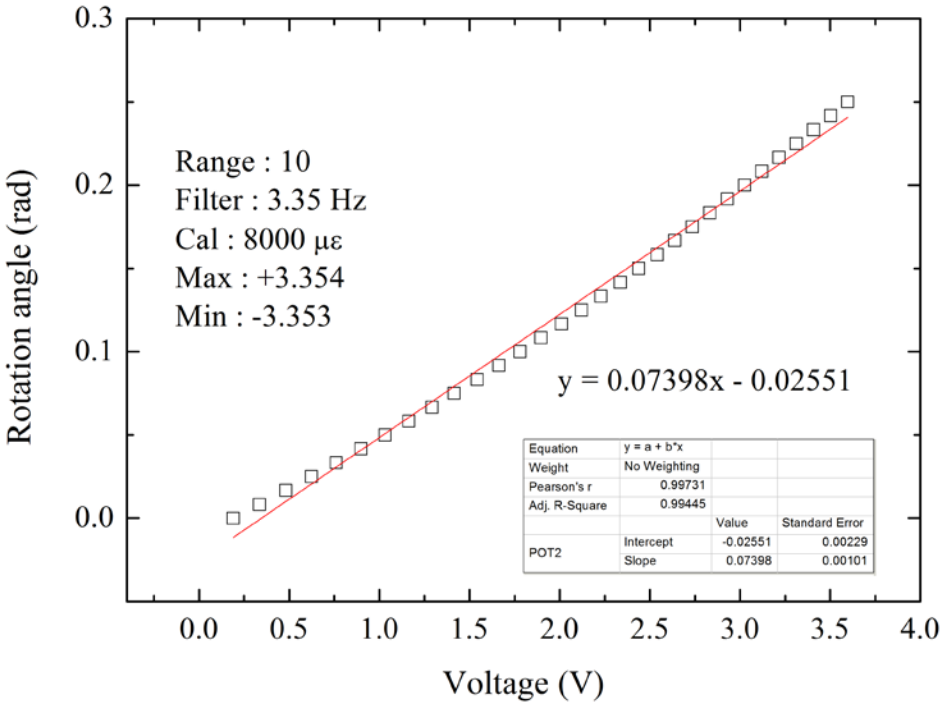

Fig. 3.47 Calibration of POT2 (Small)

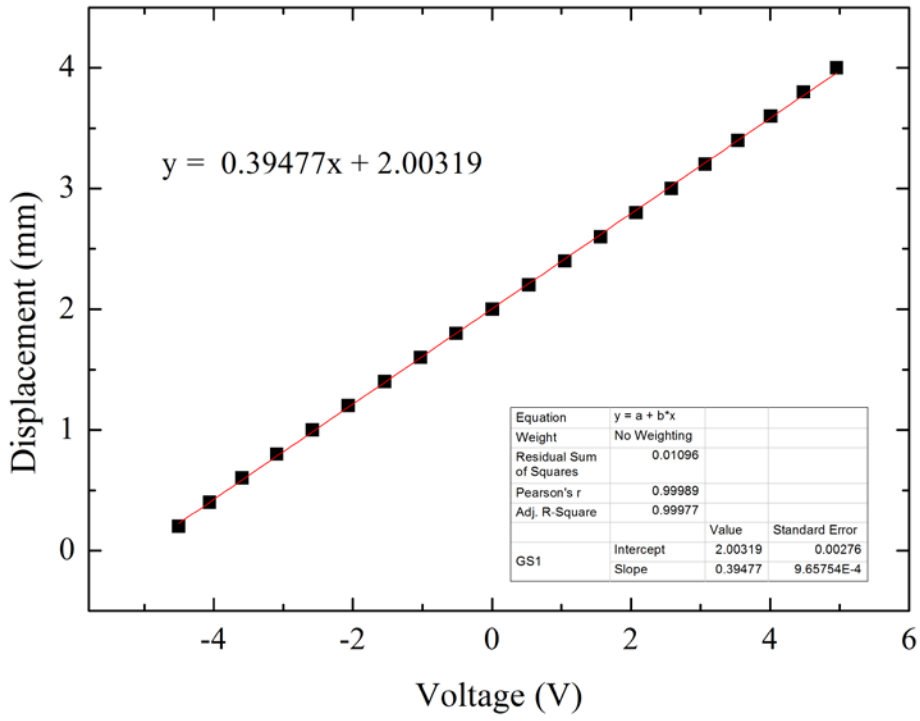

Fig. 3.48 Calibration of Gap sensor 1

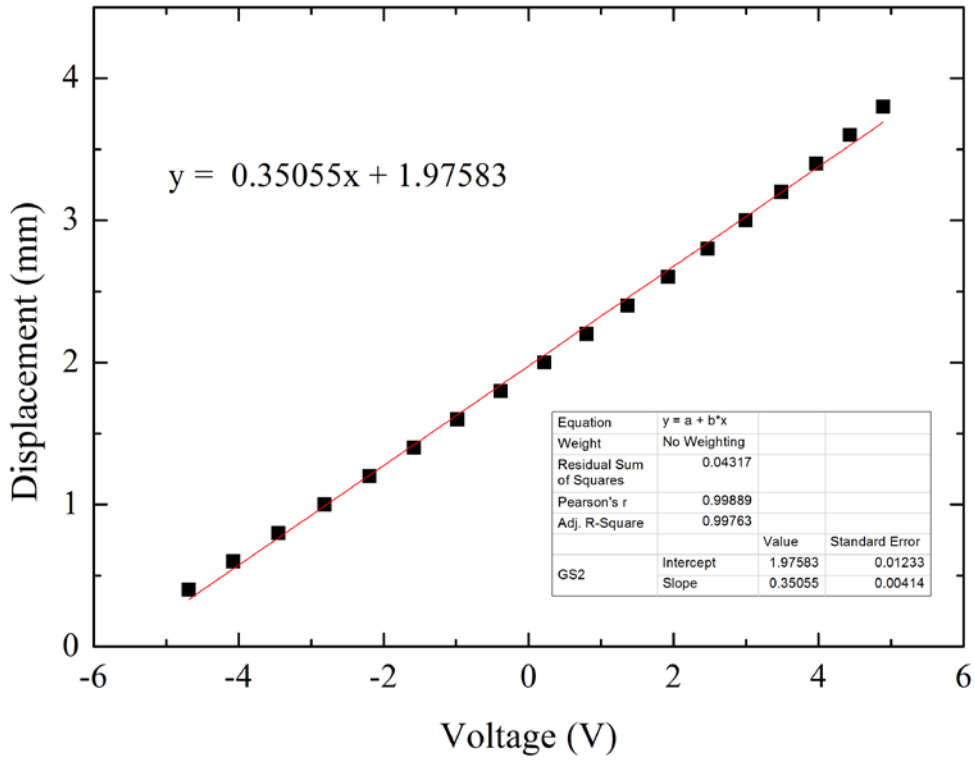

Fig. 3.49 Calibration of Gap sensor 2

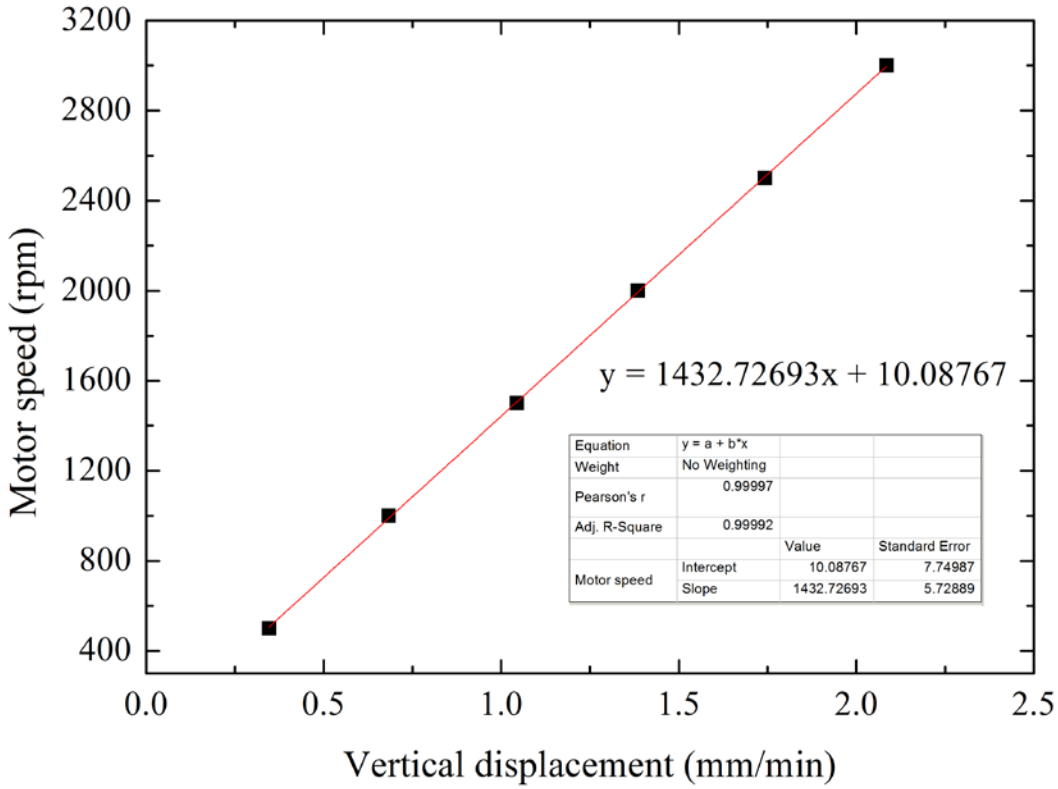

Fig. 3.50 Calibration of motor speed – vertical load

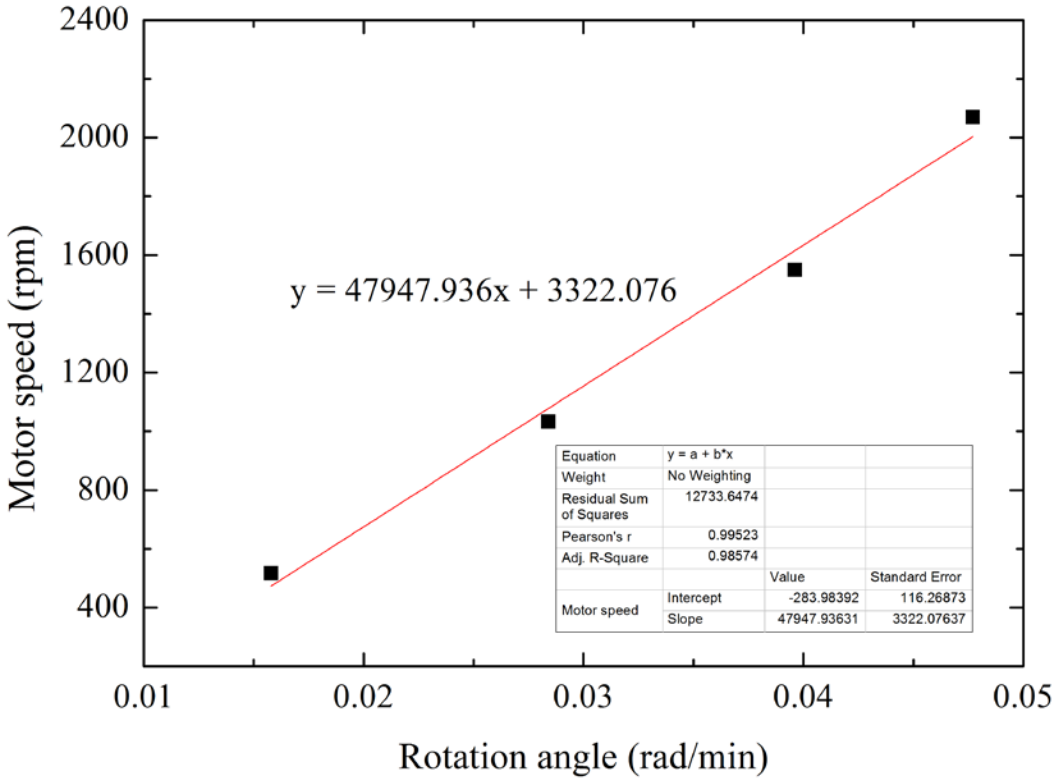

Fig. 3.51 Calibration of motor speed – torsional load

3.5.4 Specimen preparation and test procedure

3.5.4.1 Specimen preparation

- The inner membrane of 0.3 mm thickness was cut into proper length and attached on the inner metal ring, which has a rubber O-ring on the top. Then, the inner metal ring together with the membrane was inserted to the outer metal pedestal, on which small amount of white grease was applied in advance. Following this the inner membrane was taken out from the hole of the pedestal carefully. The pedestal was then set to the base by tightening firmly with 4 bolts.
- The outer membrane (Fig. 3.52a) was attached on metal pedestal, in which a porous stone with blades was inserted so as to apply necessary friction to the sand during torsional shear. Then two rubber bands as well as a rubber O-ring were placed over the membrane to seal the gap between the pedestal and the out membrane.

- The next step was placing the inner mould, which consists of four metal parts to maintain a perfect cylinder. A steel rod was screwed at the end to the base in order to fix the mould, while a steel ring was used to keep the four parts together, as shown in Fig. 3.52b.
- Then the outer mould was fixed, and the outer membrane was attached firmly to the outer mould by applying the external vacuum about -40 kPa.
- Before pouring the sand into the mould, a collector made of carton was attached to the outer mould and four steel poles coming from the base of the apparatus to prevent sand particles that might drop un-intentionally during pluviation. For specimen with internal glucose pipes, vertical plastic straws were inserted at the pre-decided place with the top fixed to the steel poles of apparatus with the help of clamps (Fig. 3.52c). For specimen with horizontal pipes, glucose block with 1 mm in length and 4.5 mm in diameter was placed at the middle height of the specimen in a circle (Fig. 3.52d).
- Same with triaxial test, specimen was prepared by air pluviation. As suggested by De Silva (2008), the pluviation process was started with moving the nozzle towards inner and outer perimeter of mould in the radial direction while at the same time gradually moving in clockwise direction. After 360 degrees of cycle, then the nozzle direction was alternate in counter clockwise direction. Also, falling height should to be kept constant during the whole process to maintain the uniformity of vertical layering.
- After completing the sand pluviation, the top surface of the specimen was leveled horizontally, and the waste material was weight.
- Subsequently, the top cap was placed over the specimen by employing a top cap guider (Fig. 3.52e). The guider consists of a cantilever hand that is attached on one of the steel pole and four branches wire rope with bolts in one end, and the counter balance at the other end. First, the guider was fixed to one of the four steel poles. Then the steel cable was attached over the pulleys of the guider with one end connected to the top cap through four bolts and the other end with counter weight. By adjusting the four bolts, the top cap surface was maintained horizontally until it touched the top surface of the specimen.
- Two clamps were fixed symmetrically to the two steel poles, and the top cap was then fixed to the clamps through the bolts. The counter balance was removed for a while, and the outer membrane was placed over the top cap ring gently. Then the inner membrane was pulled over the top cap inner ring and perfectly sealed by using a rubber band.
- Before applying the vacuum to the specimen, the counter balance was set again and the clamps were removed.

- After a vacuum of 30 kPa was applied to the specimen, the outer mould was remover carefully. Then the top cap was clamped again and the inner mould was removed.
- Then the inner hollow was sealed with a small cap, which has a hole at the bottom and an exit pipe on the top (Fig. 3.52f).
- The load cell cap was place to the apparatus carefully and connected with the top cap by six bolts. Before fixing, the voltage reading of the load cell was set as zero.
- Then the diameter and height of the specimen were measured. And local transducers including CGs and POT1 were attached to the specimen properly, as shown in Fig. 3.52g.
- After checking the condition of all the connections and transducers, the cell was placed (Fig. 3.52h). Then the inner hollow was filled with de-aired water from the pedestal by applying around 5 kPa positive pressure to the water tank.
- After the inner hollow was fully filled with de-aired water, the cell pressure was increased gradually up to 30 kPa through a regulator, while reducing the vacuum in the specimen down to the atmospheric pressure. During this process, same effective stress was maintained.
- The regulator was then replaced by the source with exactly the same pressure. After connecting the LVDT and POT2, the counter balance was removed and the connection to the loading system was made.

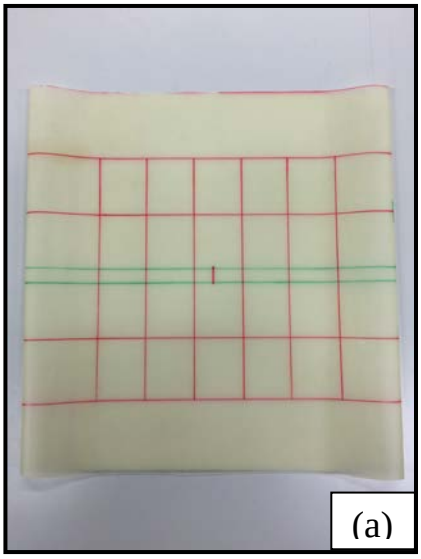
(a)

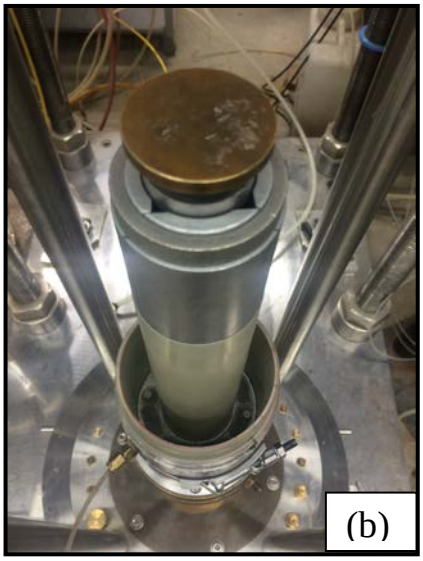
(b)

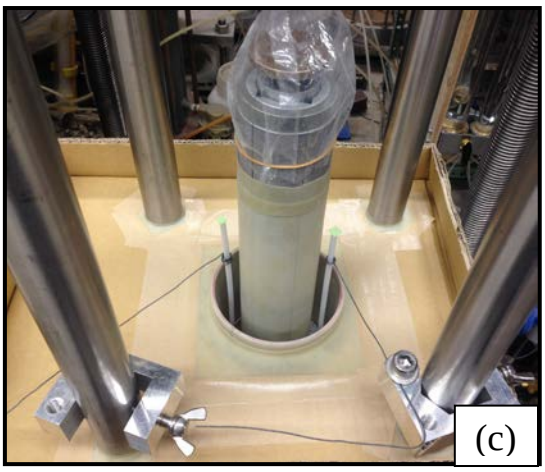
(c)

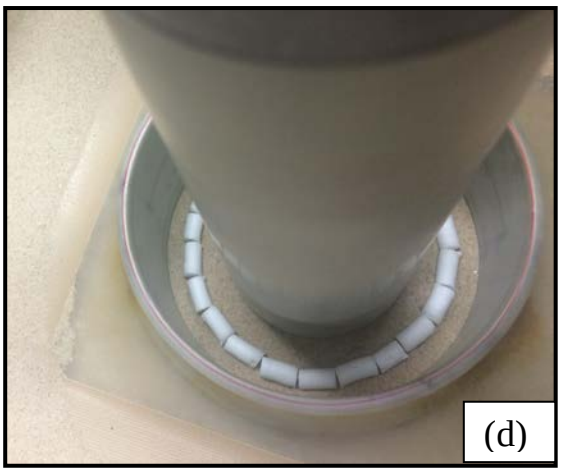
(d)

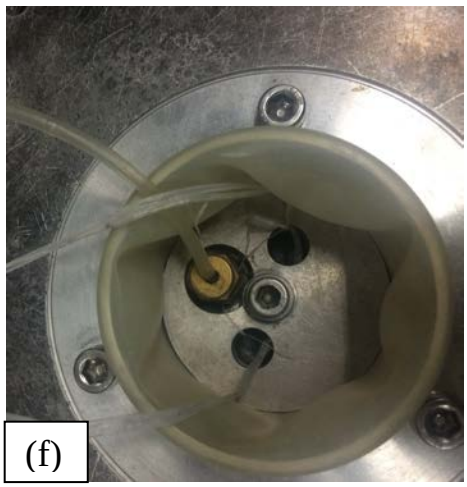

Fig. 3.52 Preparation of specimen in hollow cylindrical torsional shear apparatus

3.5.4.2 Test procedure

All the test were performed on Toyoura sand with relative density around 75~80 % and 45~50 %. After the set up process, effective confining pressure was increased to a prescribed value. Water infiltration was applied after around 12 hours of the isotropic consolidation to completely dissolve the glucose inside the specimen. Then, the specimens were subjected to the following loading steps which were decided into four series for different objectives of the experiment.

Ⅰ) Tests on behavior of sand with constant *α* before shear

As summarized in Table 3.3, in total six cases of test were conducted for the study of sand behavior under constant major principal stress direction. All tests (TC, TE and TS) were conducted on dense sand with the relative density around 75% to 80%.

As shown in the red dotted line in Fig. 3.53, all the specimens mentioned above were isotropically consolidated from 30 kPa to 60 kPa. After the formation of vertical piping inside the specimen, shear modulus were obtained during tiraxial compression, triaxial extension and torsional shear at certain deviator stress or shear stress. Finally, specimens were sheared at a shear strain rate of 0.1%/min under drained condition by applying monotonic torsional shear loadings. During the shearing process the effective mean principal stress (*p'*) was maintained to be kept constant at 60 kPa.

Ⅱ) Tests on behavior of sand with *α* changing from 0 to 30 degree

For the investigation on changing *α*, small cyclic loadings were conducted under certain shear stress during the shearing process. As summarized in Tables 3.4 and 3.5, twelve tests were conducted in this series.

The first eight cases consist of normal stress under (60, 45, 45), (60, 30, 30), (80, 50, 50) were conducted with the relative densities around 75%~80%. Initial piping direction was kept vertical. After piping formation, vertical stress σ_z was increased to the prescribed value, then shear modulus was obtained under different shear stress τ, corresponding to different α.

Second, another two tests, (60, 30, 30) and (80, 50, 50), were conducted with horizontal pipes in the middle height of specimen. The stress path was same with the previous tests where pipes were kept vertical. These tests were aimed to investigate the influence of piping direction to the soil behavior.

Third, two tests were conducted with relative density around 45% under normal stress of (80, 50, 50), with one as controlled specimen, the other with 2 vertical pipe inside.

After α reached 30°, all the specimens were sheared at the shear strain rate of 0.1%/min until 25% shear strain deformation. During the shearing process, the normal stresses were kept constant, which meant the effective mean principal stress (*p'*) was also kept constant. The stress path for each case is illustrated in Fig. 3.53 in the black line.

Ⅲ) Tests on shear modulus variation where *α* changes from 0 to 180 degree

As summarized in Table 3.6, four tests were conducted in this study in order to investigate the relationship between α and shear modulus *G*. Tests were all conducted in dense sand where α varied with increments of 10° from 0° to 180° and internal friction angle φ was kept constant. Both the vertical and horizontal pipe was studied to clarify the anisotropy in sandy soil caused by piping effect.

The specimens were first consolidated by applying confining pressure of 80 kPa isotropically. Then various stress conditions were achieved by varying the cell pressures relative to the shear stress and the vertical deviator stress according to a pre-calculated pattern, as is shown in Fig. 3.54.

Ⅳ) Tests on shear strength variation under constant *α*

Moreover, a series of tests were performed in order to study the failure behavior of sand with internal pipes when sheared under different α.Shear band orientation was also observed at each α (0°, 30°, 45°, 60° and 90°). Stress path was determined by considering the combination of constant effective mean principal stress (*p'*) and constant major principal stress direction (α). The stress path was shown in Fig. 3.55.

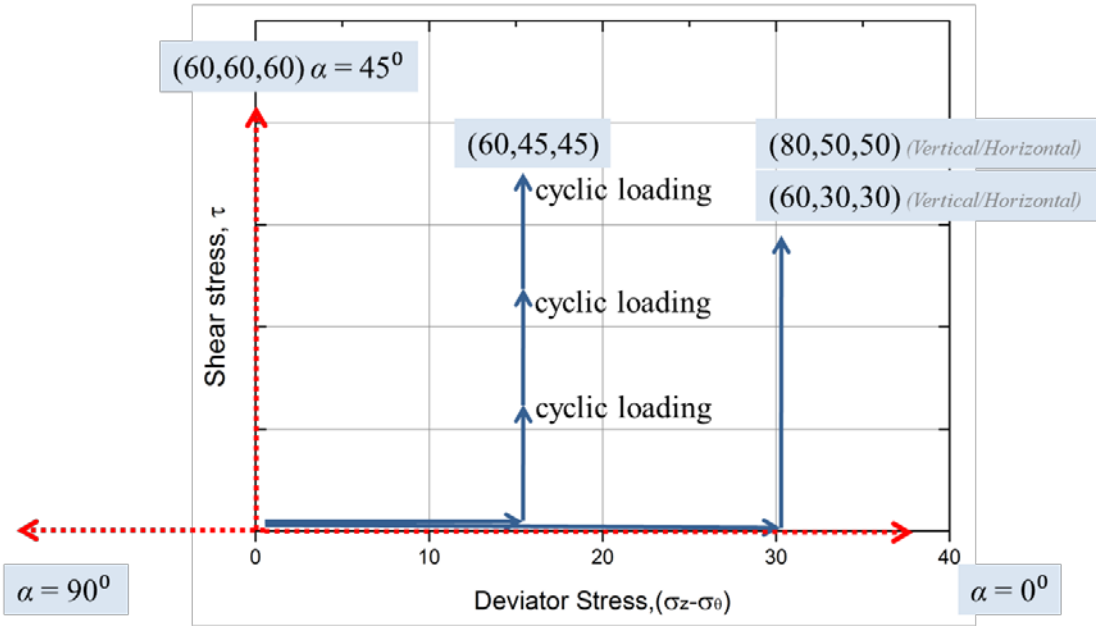

Fig. 3.53 Stress path for test series Ⅰ and Ⅱ

Table 3.3 Test conditions on constant α

Test cases	Initial density (%)	Void ratio (e)	Pipe No.	σ_z (kPa)	σ_z' (kPa)	τ (kPa)	α
TS-NP	82.9	0.676	0	60(keep constant)		Increase from 0	45^0
TS-2P	79.5	0.689	2	60(keep constant)		Increase from 0	45^0
TC-NP	74.0	0.709	0	60	100	0	0^0
TC-2P	76.8	0.699	2	60	100	0	0^0
TE-NP	74.4	0.708	0	60	30	0	90^0
TE-2P	70.0	0.725	2	60	30	0	90^0

Table 3.4 Test conditions on α varies from 0 to 30 degree (dense/vertical pipe)

Test cases	Initial density (%)	Void ratio (e)	Pipe No.	σ_z (kPa)	σ_z' (kPa)	τ (kPa)	α
1	82.0	0.676	0	45	60	Increase from 0	0^0~30^0
2	79.5	0.689	2	45	60	Increase from 0	0^0~30^0
3	71.2	0.720	0	30	60	Increase from 0	0^0~30^0
4	74.5	0.707	2	30	60	Increase from 0	0^0~30^0
5	75.6	0.703	4	30	60	Increase from 0	0^0~30^0
6	76.5	0.700	0	50	80	Increase from 0	0^0~30^0
7	80.2	0.686	2	50	80	Increase from 0	0^0~30^0
8	77.0	0.698	4	50	80	Increase from 0	0^0~30^0

Table 3.5 Test conditions on α varies from 0 to 30 degree (loose and horizontal pipe)

Test cases	Initial density (%)	Void ratio (e)	Pipe No.	σ_z (kPa)	σ_z' (kPa)	τ (kPa)	α
9	57	0.774	0	50	80	Increase from 0	0^0~30^0
10	58	0.768	2	50	80	Increase from 0	0^0~30^0
11	78	0.695	1 (horizontal)	30	60	Increase from 0	0^0~30^0
12	74	0.709	1 (horizontal)	50	80	Increase from 0	0^0~30^0

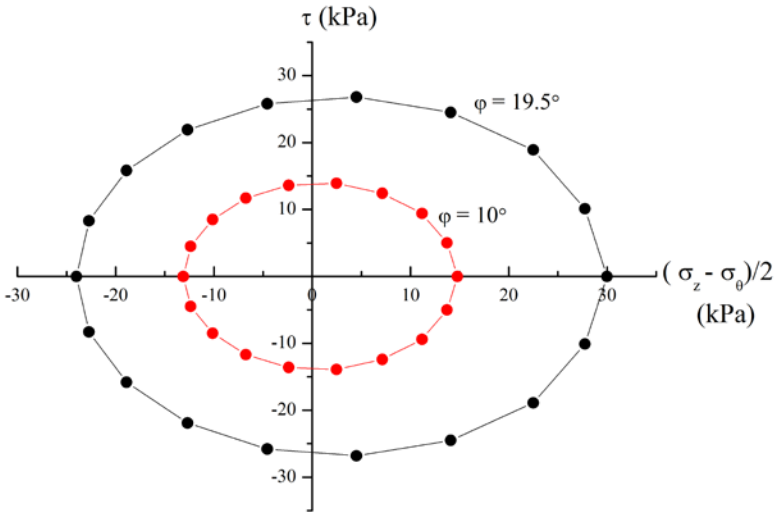

Fig. 3.54 Stress path for test series Ⅲ

Table 3.6 Test conditions on α varies from 0 to 180 degree

Test cases	Initial density (%)	Void ratio (e)	Pipe No.	Pipe direction	p' (kPa)	φ (°)	α
1	73	0.713	0	-	80	15	0^0~180^0
2	71	0.720	1	horizontal	80	15	0^0~180^0
3	78	0.694	4	vertical	80	15	0^0~180^0
4	79	0.691	1	horizontal	80	10	0^0~180^0
5	75	0.747	4	vertical	80	10	0^0~180^0

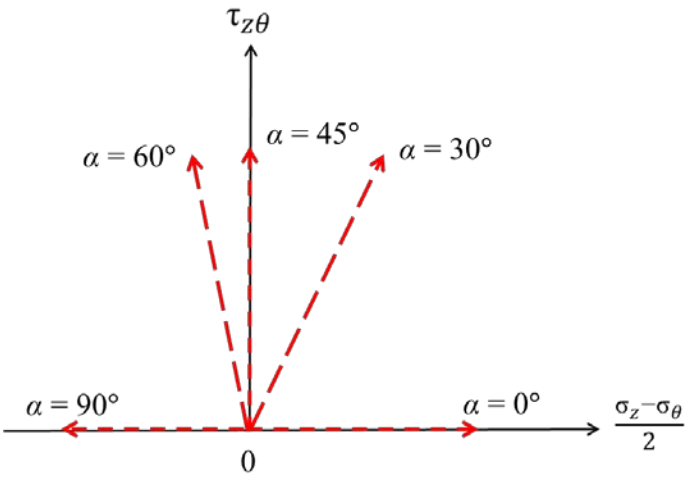

Fig. 3.55 Stress path for test series Ⅳ

3.6 Reference

1. Renuka. S., (2012). Evaluation of ground loosening behavior and mechanical properties of loosend sand associated with underground cavities. Master of Engineering thesis, the University of Tokyo.

2. Renuka, S., Kuwano, R. (2011). Formation and evaluation of loosened ground above a cavity by laboratory model tests with uniform sand, Proc. 13th International summer symp. 211-214.

3. De Silva, L.I.N., Koseki, J., Sato, T. (2006). Effect of different pluviation techniques on deformation property of hollow cylinder sand specimens. Proc. of International Symposium on Geomechanics and Geotechnics of Partical Media, Ube, Yamaguchi, Janpan, 29-33.

Chapter 4 Formulation of Stresses and Strains

Conventional triaxial testing on solid cylindrical specimens is a commonly used approach to study the effect of varying magnitude of the principal stresses on the behavior of soil in the laboratory, using a soil element that is subjected to an axisymmetric stress state. With controlled boundary conditions of stress in both horizontal and vertical directions, triaxial test might be a good start to verify the piping effect in sandy soil.

On the other hand, soil anisotropy caused by piping in different orientations is another focus in this study. It is well understood that the magnitude and orientation of the principal stresses acting on soil constantly change for a variety of field loading conditions. In the previous research related with intermediate principal stress, true triaxial tests with independent control of the three principal stresses on cubical soil specimens have been employed by plenty of researchers (e.g., Wood 1975; Lade and Musante 1978; Kirkgard and Lade1993). However, both in a conventional triaxial test and a true triaxial test, the orientation of principal stresses cannot be rotated.

In order to better understand the fundamental behavior of soil subjected to piping effect, the influence of change in magnitude and orientation of principal stresses should be investigated. As a good tool that can be used to investigate quasi-elastic properties of geomaterials (Connoly and Kuwano, 1999; Hong Nam and Koseki, 2005; De Silva et al., 2005) as well as liquefaction (Yoshimine et al., 1998; Koseki and Ohta, 2001; Oke et al., 1992 and 1999; Kiyota, 2007 and 2008), torsional shear tests show advantage in reproducing actual stress conditions of the ground by controlling four stress components independently.

Experimental research on identifying anisotropy has been commonly pursued using hollow cylinder torsional shear apparatus (Height et al., 1983; Miura et al., 1986), which enables the simulation of principal stress direction changes during shearing process. As an effective tool for studying soil constitutive behavior under generalized stress conditions, the hollow cylinder apparatus allows independent control of the magnitudes of the principal stresses and rotation of the major-minor principal stress axes, thus facilitating more generalized stress path testing than conventional test apparatus.

In spite of the many advantages and the wide range of applications, torsional shear tests on hollow cylindrical specimens have several limitations. Formulations of average stresses and strains on hollow cylindrical specimen are complicated and based on many assumptions on which there is no concrete agreement among the researchers. Most researchers assume linear elasticity of the material when calculating radial and circumferential stresses (σ_r and σ_θ) and perfect plasticity when calculating shear stresses (Hight et al, 1983; Saada, 1988). On the other hand, specimen non-uniformity, end restraint effect and system compliance make the stress distribution over the specimen highly complicated.

In this chapter, index properties of coarse granular soils, evaluation of stresses and strains in both triaxial test and torsional shear tests are described in detail.

4.1 General soil mechanics

Soils are three-phase materials with solid, liquid and air constituents. In between the solid particles there are voids, which are mostly occupied by water or air. In soil mechanics, the proportions of the solid, liquid and air constituents are characterized by five dimensionless quantities: e, n, w, S_r and D_r.

Fig. 4.1 shows a soil sample of weight W and total volume V.

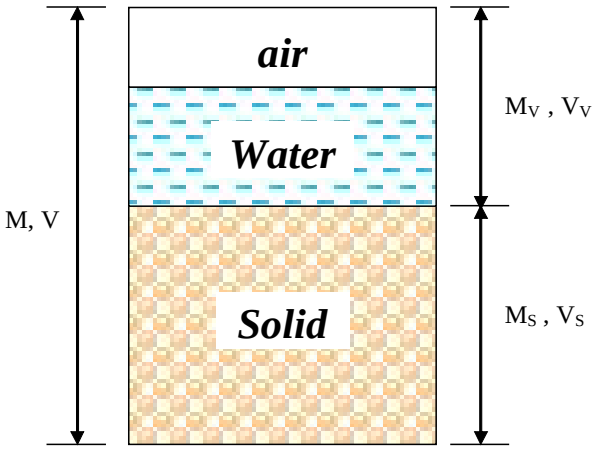

Fig. 4.1 Phase diagram of soil

Relation between volume of soil and void are described by void ratio e and porosity n.

Void ratio is defined as,

$$e = \frac{V_V}{V_S} = \frac{V - V_S}{V_S} \tag{4-1}$$

where, V_V is the volume of voids, V_S is the volume of solids and V is the total volume of the specimen.

$$\Rightarrow \frac{V}{V_S} = 1 + e \tag{4-2}$$

Porosity is the ratio of the volume of voids to the total volume,

$$n = \frac{V_v}{V} \tag{4-3}$$

In case of dry soil where there is no water,

$M = M_S$ (assuming weight of air is negligible)

where M is the total mass of soil and M_S is the weight of solids

Eq. (4-2) gives,

$$\Rightarrow \frac{V}{V_S} = 1 + e \tag{4-4}$$

$$\Rightarrow \frac{M}{V_S} \times \frac{V}{M} = 1 + e \tag{4-5}$$

$$\Rightarrow \frac{M_S}{V_S} \times \frac{V}{M} = 1 + e \ \ (M_S = M \text{ for dry soil})$$

By definition,

$$\frac{M_S}{V_S} = G_S \text{ (Specific gravity of soil)} \quad \text{and} \quad \frac{M}{V} = \rho \text{ (Dry density of soil)}$$

$$\Rightarrow \frac{G_S}{\rho} = 1 + e \quad \Rightarrow \quad e = \frac{G_S}{\rho} - 1 \tag{4-6}$$

The water content w is the ratio of the weight of water W_w to the total volume (V):

$$w = \frac{W_w}{W_s}$$

Relative density (D_r) of soil is defined as,

$$D_r = \frac{(e_{\max} - e)}{(e_{\max} - e_{\min})} \times 100(\%) \tag{4-7}$$

Where e_{max} is the maximum void ratio and e_{min} is the minimum void ratio. e_{max} corresponds to the loosest state of the soil material in a unit volume, while e_{min} corresponds to the densest state.

In conducting the test, all the specimens should be prepared with a certain initial relative density, which requires the determination of e_{max} and e_{min} in laboratory adopting specified procedures beforehand.

4.2 Triaxial tests

4.2.1 Stress analysis

The following are the equations used in the computation of stresses and strains in triaixal test. Deviator stress measured through a load cell,

$$q = \sigma_v - \sigma_r = \sigma_v' - \sigma_r' \tag{4-8}$$

Effective vertical stress, σ_v'

$$\sigma_v' = \frac{P}{A} + \sigma_c' \tag{4-9}$$

Effective radial stress, σ_r':

$$\sigma_r' = \sigma_c' \tag{4-10}$$

Mean effective pressure, p':

$$p' = \frac{\sigma_v' + 2\sigma_c'}{3} \tag{4-11}$$

where P: axial force measured with the load cell

A: cross-sectional area of the specimen

σ_c': confining pressure measured with HCDPT

Fig. 4.2 is the sketch showing the principal stresses in triaxial experiments.

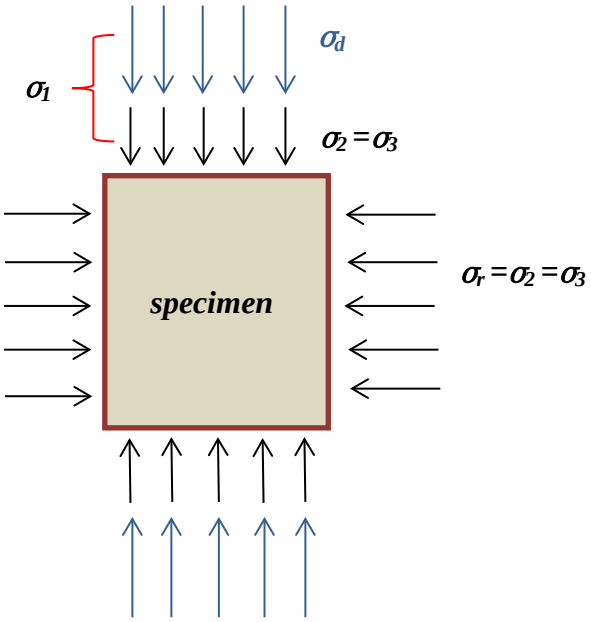

Fig. 4.2 Stress components in triaxial test

4.2.2 Strain analysis

Strain is a normalized measure of deformation representing the displacement between particles in the body relative to a reference length.

For the general case,

$$\varepsilon_{1\to x} = -\int_{H_1}^{H_x} \frac{\Delta H}{H} \tag{4-12}$$

$$\varepsilon_{1\to x} = -lnH_x - lnH_1 \tag{4-13}$$

$$\varepsilon_{1\to x} = -(ln\frac{H_x}{H_1}) \tag{4-14}$$

Axial strain, ε_v (positive for compression):

$$\varepsilon_{axial} = -(ln\frac{H_{current}}{H_{initial}}) * 100 \tag{4-15}$$

Radial strain, ε_r (positive for compression):

$$\varepsilon_{axial} = -(ln\frac{\emptyset_{current}}{\emptyset_{initial}}) * 100 \quad (4\text{-}16)$$

Volumetric strain, ε_{vol} (positive for compression):

$$\varepsilon_{vol} = \varepsilon_v + 2\varepsilon_r \quad (4\text{-}17)$$

where H: the height of the specimen measured by EDT.

H_{initial}: height of the specimen at the start of consolidation stage.

H_{current}: height of the specimen during the test measured by EDT.

φ_{initial}: initial diameter measured at three different heights same as where clip gauges are fixed.

φ_{current}: mean change in the diameter of specimen as monitored by the clip gauges.

4.2.3 Young's modulus and Poisson's ratio

Young's modulus was calculated by evaluating the tangent of stress-strain curve obtained during small cyclic loading. In this study, cyclic loading consisting of 11 cycles from -0.001% to 0.001% strain amplitude was applied three times for each test, i.e. before water infiltration, after the first water infiltration and after the second water infiltration. Accordingly, three Young's modulus denoted by E_0, E_1, E_2 would be obtained. The stress-strain curve during the 10^{th} cycle was selected and E was calculated by Equation 4-18.

$$\mathrm{E} = \frac{\Delta\sigma_1}{\Delta\varepsilon_{\text{axial}}} \quad (4\text{-}18)$$

where

$\Delta\sigma_1$ is the range of axial stress, and $\Delta\varepsilon_{\text{axial}}$ is the range of axial strain.

Poisson's ratio is the ratio of transverse contraction strain to longitudinal extension strain in the direction of stretching force. With the relevant data collected by LDTs and CGs, Poisson's ratio was computed for lower part and upper part of the specimen separately through Equation 4-19.

$$\nu = -\frac{\Delta\varepsilon_{radial}}{\Delta\varepsilon_{\text{axial}}} \quad (4\text{-}19)$$

To eliminate the effect of different void ratios among different specimens, the E and ν values measured in all tests are normalized by the void function shown in Eq. 4-20 (Hardin and Richart, 1963).

$$f(\mathrm{e}) = -\frac{(2.17-e)^2}{(1+e)} \tag{4-20}$$

Small strain modulus G_s was calculated with the measured Young's modulus and Poisson's ratio by Eq. 4-21.

$$G_s = -\frac{E}{2*(1+\nu)} \tag{4-21}$$

4.3 Hollow cylindrical torsional shear test

4.3.1 Stress analysis

As shown in Fig. 4.3, external loads acting on the hollow cylindrical specimen in torsional shear apparatus are axial load (F_z), torque (T), inner cell pressure (P_i) and outer cell pressure (P_o). Therefore hollow cylinder specimen in torsional shear apparatus has four degrees of freedom from the point of view of loads. The four surface tractions induce four stress components in a soil element and therefore four corresponding strain components appear. The four stresses are radial stress σ_r, circumferential stress σ_θ, axial stress σ_z and shear stress $\tau_{z\theta}$ correspond with radial strain ε_r, circumferential strain ε_θ, vertical strain ε_z, shear strain $\gamma_{z\theta}$, respectively. However, since the movement in radial direction is constrained by fixed ring in the case multiple-ring shear specimen, both inner cell pressure and outer cell pressure appear due to indirect effects of vertical load induces lateral pressure. Therefore, the equation of radial stress σ_r and circumferential stress σ_θ were made based on simplified assumption of lateral earth pressure.

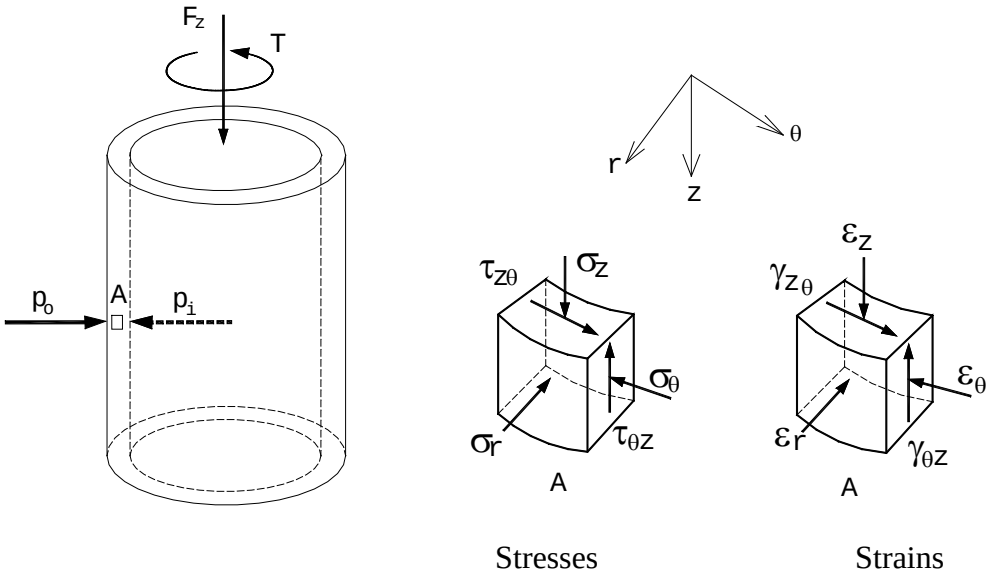

Fig. 4.3 Stresses and strains in soil element A

4.3.1.1 Vertical stress σ_z

Average vertical stress at the middle height of the specimen can be computed as follows:

$$\overline{\sigma_z} = \frac{LC}{A} + \sigma_h + \sigma_g + \sigma_{mem} \tag{4-22}$$

where,

LC : Axial load detected by the inner load cell;

A: Cross-sectional area of the specimen, $A = \pi(R_o^2 - R_i^2)$;

σ_h : Horizontal stress , which is equal to σ_r and σ_θ in this study;

σ_g : Overburden stress of the specimen due to its self-weight at its middle height, $\sigma_g = \gamma' H/2$;

γ' : Unit weight of soil in water (N/cm^3), $\gamma' = (G_S-1)/(1+e) \times \rho_w \times g$

in which,

G_S : Specific gravity,

e : void ratio,

g : gravitational acceleration (9.80665 m/s^2)

ρ_w : density of water (1 g/cm^3)

H : Height of the specimen,

σ_{mem} : Correction for membrane stress (Tatsuoka et al., 1986),

If $\varepsilon_z > 0$, $\sigma_{mem} = 0$

If $\varepsilon_z < 0$, $\sigma_{mem} = -\frac{3}{8} \times \varepsilon_z \times t_{mem} \times \frac{E_{mem}}{(R_o - R_i)}$

where,

ε_z = Axial strain

t_{mem} = Thickness of membrane (0.03 cm in this study)

E_{mem} = Young's modulus of membrane

Note that the output from the inner load cell is initialized at the isotropic stress state ($\sigma_z = \sigma_\theta = \sigma_r$).

4.3.1.2 Radial stress σ_r and circumferential stresses σ_θ

Timoshenko and Goodier (1970) proposed a solution for hollow cylinder as a uniform material subjected to uniform inner pressure (p_i) and outer pressure (p_o). Stress distribution is assumed to be symmetrical with respect to the vertical axis (z) of the hollow cylinder and the stress components do not depend on radial angle (θ) and are a function of radius (r) only. As a result, shear stress ($\tau_{r\theta}$) is equal to 0. The equation of equilibrium in the radial direction yields,

$$\frac{\partial \sigma_r}{\partial r} + \frac{\sigma_r - \sigma_\theta}{r} + \omega = 0 \qquad (4\text{-}23)$$

in which ω is body force. When ω equals to 0, eq. (4-23) is satisfied by the following,

$$\sigma_r = \frac{B}{r^2} + 2C \tag{4-24}$$

$$\sigma_\theta = -\frac{B}{r^2} + 2C \tag{4-25}$$

where *B* and *C* are constants, which can be obtained from the following boundary conditions.

$$\sigma_r \big|_{r=R_i} = p_i \tag{4-26}$$

$$\sigma_r \big|_{r=R_o} = p_o \tag{4-27}$$

where R_o and R_i denote current outer and inner radii of the specimen, respectively.

By substituting eq. (3-11) and eq. (3-12) into eq. (3-9) and eq. (3-8), we get,

$$\sigma_r = \frac{p_o R_o^{\,2} - p_i R_i^{\,2}}{R_o^{\,2} - R_i^{\,2}} - \frac{R_i^{\,2} R_o^{\,2} (p_o - p_i)}{R_o^{\,2} - R_i^{\,2}} \frac{1}{r^2} \tag{4-28}$$

$$\sigma_\theta = \frac{p_o R_o^{\,2} - p_i R_i^{\,2}}{R_o^{\,2} - R_i^{\,2}} + \frac{R_i^{\,2} R_o^{\,2} (p_o - p_i)}{R_o^{\,2} - R_i^{\,2}} \frac{1}{r^2} \tag{4-29}$$

Average stress components are computed with weighting and without weighting (Ampadu, 1991) as follows.

Averaging without weighting

$$\overline{\sigma}_r = \frac{\int_{R_i}^{R_o} \sigma_r dr}{\int_{R_i}^{R_o} dr} \tag{4-30}$$

$$\overline{\sigma}_\theta = \frac{\int_{R_i}^{R_o} \sigma_\theta dr}{\int_{R_i}^{R_o} dr} \tag{4-31}$$

By substituting eq. (3-13) into eq. (3-15) and eq. (3-14) into eq. (3-16), we get,

$$\overline{\sigma}_r = \frac{p_o R_o + p_i R_i}{R_o + R_i} \tag{4-32}$$

$$\overline{\sigma}_\theta = \frac{p_o R_o - p_i R_i}{R_o - R_i} \tag{4-33}$$

These equations were commonly used by a number of researchers such as Hight et al. (1983) and Saada (1988).

Averaging with weighting

$$\int_{R_i}^{R_o} \sigma_r \, r \, dr = \int_{R_i}^{R_o} \overline{\sigma}_r \, r \, dr \qquad (3\text{-}19) \qquad\qquad \int_{R_i}^{R_o} \sigma_\theta \, r \, dr = \int_{R_i}^{R_o} \overline{\sigma}_\theta \, r \, dr \tag{4-34}$$

$$\overline{\sigma}_r = \frac{\int_{R_i}^{R_o} \sigma_r \, r \, dr}{\int_{R_i}^{R_o} r \, dr} \tag{4-35}$$

$$\overline{\sigma}_\theta = \frac{\int_{R_i}^{R_o} \sigma_\theta \, r \, dr}{\int_{R_i}^{R_o} r \, dr} \tag{4-36}$$

By substituting eq. (3-13) into eq. (3-21) and eq. (3-14) into eq. (3-22), we get

$$\overline{\sigma}_r = \frac{p_o R^2{}_o - p_i R^2{}_i}{R^2{}_o - R^2{}_i} - \frac{2R^2{}_i R^2{}_o (p_o - p_i)}{(R^2{}_o - R^2{}_i)^2} \ln\left(\frac{R_o}{R_i}\right) \tag{4-37}$$

$$\overline{\sigma}_\theta = \frac{p_o R^2{}_o - p_i R^2{}_i}{R^2{}_o - R^2{}_i} + \frac{2R^2{}_i R^2{}_o (p_o - p_i)}{(R^2{}_o - R^2{}_i)^2} \ln\left(\frac{R_o}{R_i}\right) \tag{4-38}$$

In this study, the outer and inner cell pressures are kept equal to each other ($p_i = p_o$), therefore, eqs. (3-17) and (3-18) yield $\overline{\sigma}_r = \overline{\sigma}_\theta = p_o$, which can be also derived from eqs. (3-23) and eqs. (3-24).

4.3.1.3 Shear stress $\tau_{z\theta}$

Shear stress $\tau_{z\theta}$ acting on a soil element with the area $dA = r \, d\theta \, dr$ can be computed as follows.

$$dT = \tau_{z\theta} r^2 d\theta dr \tag{4-39}$$

$$T = \int_{R_i}^{R_o} \int_{0}^{2\pi} \tau_{z\theta} r^2 d\theta dr \tag{4-40}$$

$$T = 2\pi \int_{R_i}^{R_o} \tau_{z\theta} r^2 dr \tag{4-41}$$

If the material is perfectly plastic, we get

$$T = 2\pi \tau_{z\theta} \int_{R_i}^{R_o} r^2 dr \tag{4-42}$$

$$T = \frac{2}{3} \pi \tau_{z\theta} \left(R_o^{\ 3} - R_i^{\ 3} \right) \tag{4-43}$$

$$\tau_{z\theta} = \frac{3T}{2\pi \left(R_o^{\ 3} - R_i^{\ 3} \right)} \tag{4-44}$$

If the material is linear elastic, then the distribution of shear stress is linear along the radial direction. In this case, by defining τ_{max} as the shear stress at $r = R_o$, the shear stress at any distance can be computed by the following equation.

$$\tau_{z\theta} = \left(\frac{\tau_{\max}}{R_o} \right) r \tag{4-45}$$

The average shear stress $\bar{\tau}^*_{z\theta}$ can be computed by the following equation.

$$\overline{\tau^*}_{z\theta}\int_{R_i}^{R_o} r^2 dr = \int_{R_i}^{R_o} \frac{\tau_{\max}}{R_o} r^3 dr \tag{4-46}$$

$$\overline{\tau^*}_{z\theta} = \frac{3}{4}\frac{\tau_{\max}}{R_o}\left(\frac{R_o^{\,4} - R_i^{\,4}}{R_o^{\,3} - R_i^{\,3}}\right) \tag{4-47}$$

On the other hand, if the equivalent shear stress that gives the same shears force as the linearly distributed shear stress is considered, then the average shear stress $\bar{\tau}^{**}_{z\theta}$ can be computed as follows.

$$\bar{\tau}^{**}_{z\theta} = \frac{1}{2}\frac{\tau_{\max}}{R_o}\left(R_o + R_i\right) \tag{4-48}$$

By equating the eq. (3-33) and (3-36) to get τ_{max} and substituting it into the eq. (3-37), we get

$$\bar{\tau}^{**}_{z\theta} = \frac{T}{\pi\left(R_o - R_i\right)\left(R_o^{\,2} + R_i^{\,2}\right)} \tag{4-49}$$

In this study, shear stress is averaged from eq. (3-38) and (3-33) as shown below.

$$\bar{\tau}_{z\theta} = \frac{1}{2}\left[\frac{3T}{2\pi\left(R_o^{\,3} - R_i^{\,3}\right)} + \frac{T}{\pi\left(R_o - R_i\right)\left(R_o^{\,2} + R_i^{\,2}\right)}\right] \tag{4-50}$$

where,

$T = T_{LC} + T_{mem}$

T_{LC} = Torque detected by the inner load cell

$$T_{mem} = -2 \times \frac{\pi}{3} \times t_{mem} \times \frac{E_{mem}}{H} \times angle \cdot of \cdot rotation \times \left(R_o^{\,3} + R_i^{\,3} \right)$$

Angle of rotation is detected from the potentiometer.

4.3.1.4 Principal stresses

Principal stresses can be computed from the four stress components.

$$\sigma_1 = \frac{\sigma_Z + \sigma_\theta}{2} + \sqrt{\frac{(\sigma_Z - \sigma_\theta)^2}{2} + (\tau_{z\theta})^2} \tag{4-51}$$

$$\sigma_2 = \sigma_r \tag{4-52}$$

$$\sigma_3 = \frac{\sigma_Z + \sigma_\theta}{2} - \sqrt{\frac{(\sigma_Z - \sigma_\theta)^2}{2} + (\tau_{z\theta})^2} \tag{4-53}$$

The angle α between the directions of the major principal stress σ_1 with the vertical direction is calculated by

$$\alpha = \frac{1}{2} \arctan \frac{2\tau_{z\theta}}{\sigma_z - \sigma_\theta} \tag{4-54}$$

Stress – non-uniformity coefficients

As for the stress-strain non-uniformity along the radial and vertical directions of the specimen, various proposals could be found in literature (Hight et al., 1983; Vaid et al., 1990;

Yoshimine et al., 1998). The stress-strain non-uniformity depends on a number of factors such as stress state, specimen size and dimension, and material constitutive law. This is unavoidable as the specimen has an inherent curvature and end restraint (Hight et al., 1983). Although it is preferable to reduce the wall thickness of the specimen to minimize such non-uniformity, effects of other factors such as membrane effects, boundary conditions and anisotropy of the horizontal bedding plane can become significant in such cases. Therefore, selection of an appropriate specimen geometry and range of cell pressures is important to obtain reliable test data.

Several coefficients have been proposed as follows.

Hight et al. (1983) proposed the following criteria on normalized parameter β_1 and nonuniformity stress parameter β_3.

$$\beta_1 = \frac{|\overline{\sigma^*} - \overline{\sigma}|}{\sigma_L} < 0.11 \tag{4-55}$$

$$\beta_3 = \frac{\int_{R_i}^{R_o} \left|\sigma(r) - \overline{\sigma^*}\right| dr}{(R_o - R_i)\sigma_L} < 0.11 \tag{4-56}$$

where,

$\overline{\sigma^*}$: Real average

$\overline{\sigma}$: Calculated average

σ_L : Stress level

However, Vaid et al. (1990) proposed another criterion using the parameter β_R in terms of nonuniformity in principal stress ratio

$$\beta_R = \left[(\sigma'_1/\sigma'_3)_{\max} - (\sigma'_1/\sigma'_3)_{\min}\right]/(\sigma'_1/\sigma'_3)_{av} < 0.2 \tag{4-57}$$

Yoshimine et al. (1998) also suggested the following parameter relating to the non-uniformity of radial stress σ_r.

$$\frac{p_o - p_i}{\sigma_r} = \frac{-(b - \sin^2\delta)}{\sin 2\delta}\left(\frac{R_o}{R_i} - \frac{R_i}{R_o}\right)\frac{\tau_{z\theta}}{\sigma_r} \tag{4-58}$$

Eq. (3-47) can be rewritten in the following form.

$$\frac{p_o - p_i}{\sigma_r} = -(b - \sin^2\delta)\left(\frac{R_o}{R_i} - \frac{R_i}{R_o}\right)\frac{\sin\phi_{mob}}{1 + (2b-1)\sin\phi_{mob}} \tag{4-59}$$

where ϕ_{mob} is the mobilized angle of friction, and b is the intermediate principal stress coefficient defined as $b = (\sigma_2 - \sigma_3)/(\sigma_1 - \sigma_3)$.

In the present study, the outer and inner cell pressures were kept equal to each other ($p_o = p_i$). Therefore, stress non-uniformity parameters β_1, β_3 and $(p_o - p_i)/\sigma_r$ are equal to zero.

4.3.2 Strain analysis

Axial strain ε_z, radial strain ε_r, circumferential strain ε_θ, and shear strain $\gamma_{z\theta}$ are the four strain components of the soil element to be determined. As shown in Fig. 3.3, ε_r and ε_θ of a soil element can be calculated from,

$$\varepsilon_r = -\frac{u + (\delta u/\delta r)dr - u}{dr} = -\frac{du}{dr} \tag{4-60}$$

$$\varepsilon_\theta = -\frac{(u+r)d\theta - rd\theta}{rd\theta} = -\frac{u}{r} \tag{4-61}$$

where,

u = Deformation of a soil element in radial direction

r = Distance to the center of soil element from the center of specimen

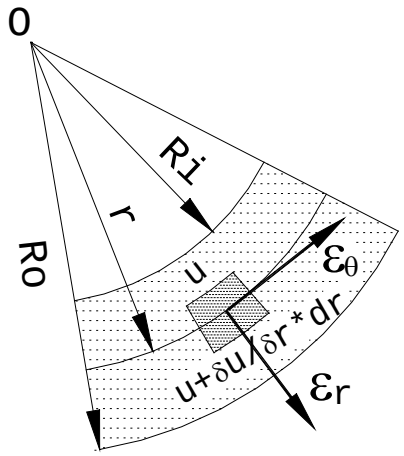

Fig. 3.3 Radial and circumferential strains of a soil element

Combining eqs. (3-49) and (3-50) yields

$$\frac{d\varepsilon_\theta}{dr} + \frac{1}{r}\left(\varepsilon_\theta - \varepsilon_r\right) = 0 \tag{4-62}$$

If it is assumed that distribution of u is linear in the radial direction,

$$u = \frac{u_o - u_i}{R_o - R_i}\, r + \frac{u_i R_o - u_o R_i}{R_o - R_i} \tag{4-63}$$

then ε_r is given by,

$$\bar{\varepsilon}_r = -\frac{u_o - u_i}{R_o - R_i} \tag{4-64}$$

and $\bar{\varepsilon}_\theta$ can be calculated by

$$\bar{\varepsilon}_\theta \int_{R_i}^{R_o} r dr = \int_{R_i}^{R_o} \varepsilon_\theta \, r dr = -\int_{R_i}^{R_o} \frac{u}{r} r dr \tag{4-65}$$

$$\bar{\varepsilon}_\theta = -\frac{u_o + u_i}{R_o + R_i} \tag{4-66}$$

In the case of multiple-ring shear specimen $\bar{\varepsilon}_r = \bar{\varepsilon}_\theta = 0$, since no radial movements are allowed.

ε_z and $\gamma_{z\theta}$ can be calculated by

$$\varepsilon_z = - dw / dz \tag{4-67}$$

$$\bar{\varepsilon}_z = -\frac{\Delta H}{H} \tag{4-68}$$

$$\gamma_{z\theta} = r \, d\theta / dz \tag{4-69}$$

$$\bar{\gamma}_{z\theta} = \frac{(R_o + R_i)}{2}\frac{\Delta\theta}{H} \tag{4-70}$$

where,

$\bar{\varepsilon}_z$, $\bar{\varepsilon}_r$, $\bar{\varepsilon}_\theta$, $\bar{\gamma}_{z\theta}$: Average axial, radial, circumferential, and shear strains of the specimen, respectively

u_o, u_i, w : Displacements in the radial direction at outer and inner radii, and vertical directions of the specimen, respectively

H: Height of the specimen

R_o, R_i: Outer and inner radii of the specimen

$\Delta\theta$: Rotation angle.

As external measurements, displacement in the vertical direction is obtained by an external LVDT. Angle of rotation is measured by using a potentiometers attached at the loading shaft. Low capacity differential pressure transducer (LCDPT) is used to measure the volume change of the inner cylinder, and R_i could be calculated under the assumption that inner hollow is kept as right cylinder during the test. The outer diameter change is measured by CGs and R_o is computed by the average result of the three CGs.

4.4 Reference

1. Connolly, T. M. and Kuwano, R. (1999). The measurement of Gmax in a resonant column, bender element, torsional shear apparatus, Pre-failure Deformation Characteristics of Geomaterials, Jamiolkowski, Lancellotta and Lo Presti (Eds.), Balkema, Rotterdam, Vol.1, 73-80.
2. De Silva, L.I.N., Koseki, J., Sato, T. and Wang, L. (2005). High capacity hollow cylinder apparatus with local strain measurement, Proc. 2nd Japan-U.S. Workshop on Testing, Modeling and Simulation, Geotechnical Special Publication, ASCE, Vol. 156, 16-28.

3. Hight, D. W., Gens, A. and Symes, M. J. (1983). The development of a new hollow cylinder apparatus for investigating the effects of principal stress rotation in soils, Geotechnique, 33 (4), 355-383.
4. Hong Nam, N. and Koseki, J. (2005). Quasi-elastic deformation properties of Toyoura sand in cyclic triaxial and torsional loadings and their modeling", Soils and Foundations, 45 (5), 19-38.
5. Kirkgard, M. M., Lade, P.V. 1993. Anisotropic three-dimensional behavior of a normally consolidate clay. Can. Geotech. J., 30(5), 848-858.
6. Kiyota, T. (2007). Liquefaction strength and small strain properties of in-situ frozen and reconstituted sandy soils. PhD thesis, Dep. of Civil Engineering, University of Tokyo, Japan.
7. Kiyota, T., Sato, T., Koseki, J., and Mohammad, A.M. (2008). Behavior of liquefied sands under extremely large strain levels in cyclic torsional shear tests. Soils and Foundations, 48 (5), 727-739.
8. Koseki, J. and Ohta, A. (2001). Effects of different consolidation conditions on liquefaction resistance and small strain quasi-elastic deformation properties of sands containing fines. Soils and Foundations, 41 (6), 53-62.
9. Lade, P. V., Musante, H. M. 1978. Three-dimensional behavior of remolded clay. J. Geotech. Eng. Div., Am. Soc. Civ. Eng., 104(2), 193-209.
10. Miura, K., Miura, S. and Toki, S. (1986). Deformation behaviour of anisotropic dense sand under principal stress axes rotation, Soils and Foundations, Vol. 26, No-1, 36-52.
11. Oka, F., Yashima, A., Tateishi, Y., Taguchi, Y. and Yamashita, S. (1999). A cyclic elasto-plastic constitutive model for sand considering a plastic-strain dependence of the shear modulus. Geotechnique, 49 (5), 661-680.
12. Saada, A. S. (1988). Hollow cylindrical torsional devices: their advantages and limitations, Advanced Triaxial Testing of Soil and Rock, ASTM STP 977, Donaghe R. T., Chaney, R. C. and Silver, M. L. (Eds.), Philadelphia, 766-795.
13. Wood, D. 1975. Explorations of principal stress with Kaolin in a true triaxial apparatus. Geotechnique, 25(4), 783-797.
14. Yoshimine, M., Ishihara, K. and Vargas, W. (1998). Effects of principal stress direction and intermediate principal stress on undrained shear behavior of sand. Soils and Foundations, 38 (3), 179-188.

Chapter 5 Evaluation of piping effect in Toyoura sand and Edosaki sand by triaxial test

5.1 Introduction

In this chapter, the property of soil subjected to piping effect is studied by conducting a series of triaxial tests. As explained in Chapter 3, 13 experiments were carried out under different densities, pipe number and confining pressure. Piping propagation was observed according to the axial strain, radial strain and volumetric strain measured by local transducers. Furthermore, Young's modulus and Poisson's ratio of sand with internal pipes were also evaluated under cyclic loading before and after water infiltration.

The test conditions are described in detail as follows.

For the specimens with no pipe or 1 pipe in the center, the arrangement of sensors was seen in Fig. 5.1, where both the top view and front view are shown. Axial strain of the upper half of the specimen could be obtained by averaging the results from LDT1 and LDT3, while LDT2 and LDT4 for the lower half. For specimens with 2 pipes, LDT3 and LDT4 were positioned near the glucose side, while LDT1 and LDT2 were attached at the other side (Fig. 5.2). Thus, the local deformation caused by the glucose dissolving could be caught successfully.For radial strain, the results recorded by two relevant Clip Gauges were averaged separately for upper and lower part.

Table 5.1 and Table 5.2 listed all the test cases for Toyoura sand and Edosaki sand, respectively.

Some typical notifications used in Table 5.1 and Table 5.2:

- NP : No-pipe-specimen (controlled specimen)
- 1P_L : Loose specimen with 1 pipe in the center
- 2P_D : Dense specimen with 2 pipes inside
- NP_100 : No-pipe-specimen under confining pressure of 100 kPa
- 1P_9mm : specimen with larger diameter pipe (9mm)

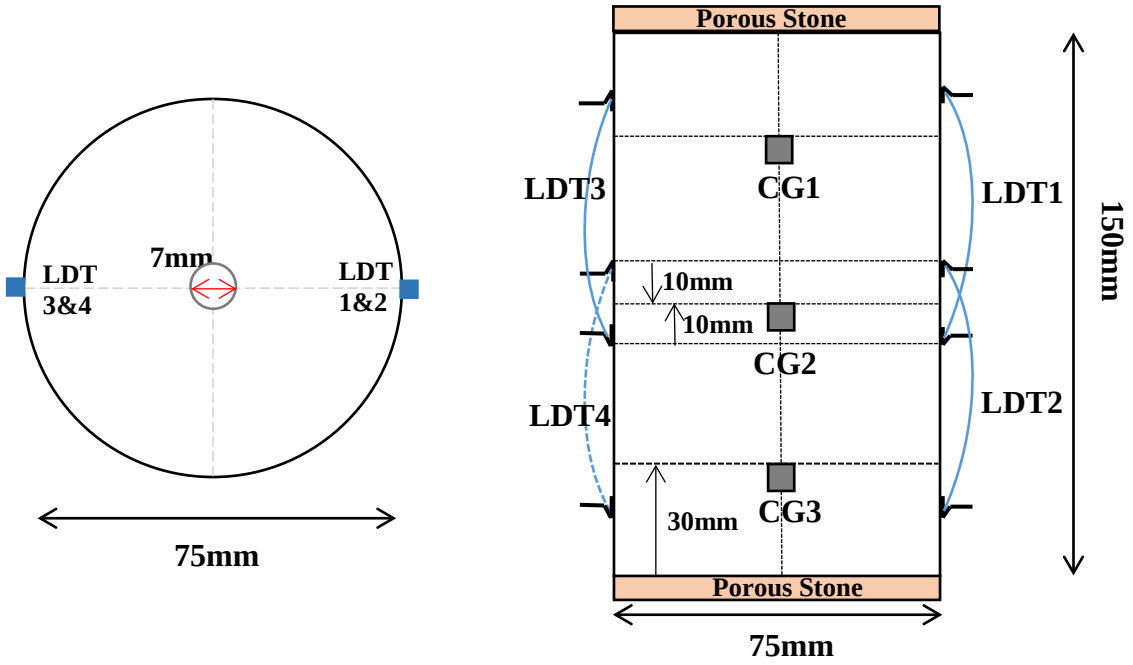

Fig. 5.1 Arrangement of sensors for 1-pipe-specime

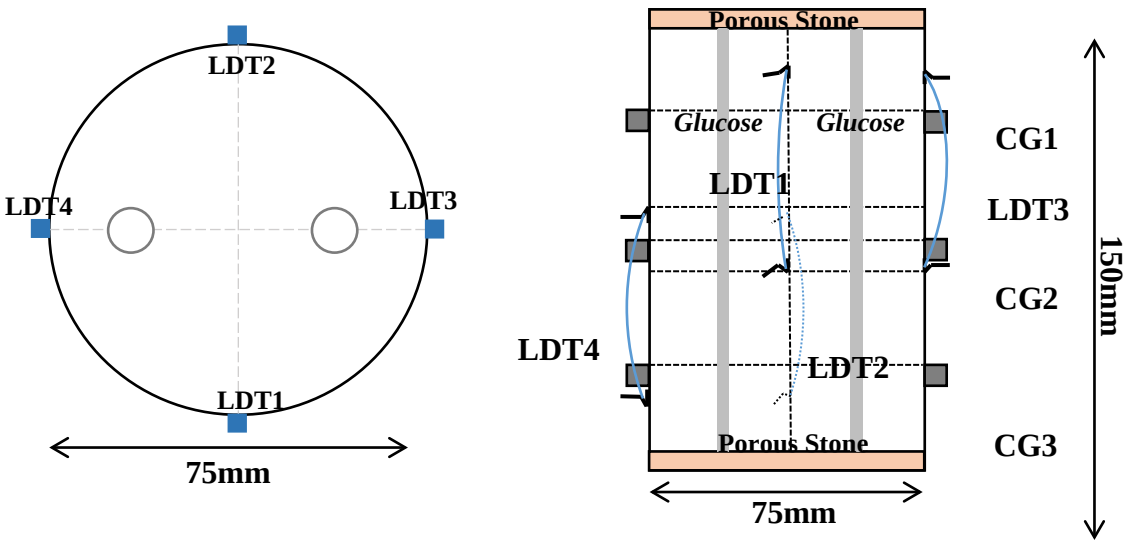

Fig. 5.2 Arrangement of sensors for 2-pipe-specime

Table 5.1 Schedule of triaxial experiments for Toyoura sand

Test cases	Void ratio e	Initial relative densityDr (%)	Confining pressure σ_r' (kPa)	Pipe Number
NP-L	0.846	46.5	50	0
1P-L	0.855	42.8	50	1
2P-L	0.843	46.6	50	2
NP-D	0.757	72.9	50	0
1P-D	0.761	72.0	50	1
2P-D	0.776	67.4	50	2
NP-100	0.854	43.7	100	0
1P-100	0.850	46.4	100	1
1P-9mm	0.855	47.3	50	1

Table 5.2 Schedule of triaxial experiments for Edosaki sand

Test cases	Void ratio e	Initial relative density Dr (%)	Confining pressure σ_r' (kPa)	Pipe Number
NP-50	1.042	66.2	50	0
1P-50	1.021	70.3	50	1
1P-100	1.018	71.5	100	0
NP-100	1.036	68.3	100	1

5.2 Test results of Toyoura sand

By analyzing the results obtained from the above tests, effect of density, pipe number, confining pressure on soil loosening accompanied with piping could be clarified. The following interpretations will focus on three aspects: strain variation during piping formation; shear strength reduction caused by piping effect and small strain stiffness properties.

5.2.1 Strain variation during piping formation

Axial strain and radial strain are shown in Fig. 5.3 ~ Fig.5.6 for loose and dense specimen respectively. Similar strain increment during isotropic stress increment from 25 kPa to 50 kPa was observed for all the cases, although some difference could be found in axial strain due to the creep effect. After around 16 hours of creep, water infiltration started and piping was generated long the specimen. During this process, obviousstrain increment appeared in specimen with internal glucose pipe compared with no-pipe- specimens. In addition, larger deformation was found in loose specimensthan dense specimens.

It should be noted that for no-pipe-specimen and 1-pipe-specimen, both axial strain and radial strain were relative uniform along the specimen, and the average of four LDTs and three clip gauges could represent the overall deformation of the sand. However, for 2-pipe-specimen, actual radial strain could not be obtained because all the clip gauges were attached near the glucose side due to the existence of LDTS. Such layout of sensors would lead to an overestimate of radial strain for 2-pipe-specimen. Still, axial strain was reliable with one pair fixed near the glucose and the other far from the glucose.

Another issue was the water inflow direction. For comparison, test with water coming in from the top cap was also conducted. It was found that water tended to concentrated at the bottom part of the specimen even if the inflow rate was less than 10ml/min, while air was trapped in the upper part of the specimen. After all the 1500ml water was filled in, an obvious difference between the upper and lower part was observed, indicating a non-uniform distribution of the water. Therefore, for all the tests, water was infiltrated from bottom to top cap in order to achieve a more uniform and complete penetration.

When analyzing the strain variation of each local sensor, non-uniform deformation was obviously observed between the lower and upper part of the specimen, shown in Fig. 5.7 ~ Fig. 5.10 for axial strain and Fig. 5.11 ~ Fig. 5.14 for radial strain. A sudden drop of axial strain value can be seen in all the upper transducers at the time when the first water cycle

started for specimen with internal pipe. This could be explained by the fact that the specimen sustained small tension force caused by slight height reduction immediately after the water infiltration. Due to this effect LDTs at upper part showed a small rebound while the LDTs at the lower part began to deform as glucose dissolving.

Variation of the behavior of LDTs and clip gauges depicted that larger axial compression occurred at the lower part of the specimen, where LDT2&LDT4 and CG3 were attached to. One possible reason may lie in the direction of water inflow as explained above. The lower part of the specimen deformed firstly when water infiltration started. Such deformation would continue and expand to the region near initial pipes throughout the whole period of water cycle. Also, hydraulic gradient, controlled by the height of upper water tank, was higher at the bottom part of sand. Although water went quicker in glucose, it took some time for completely dissolve the glucose. During this process, wet sand in upper part was already formed a relative stable structure to resist extra deformation of the sand near the pipe.

In the last of this Chapter (Fig. 5.46), photo of specimens was taken after shear. It could be found that the pipe size became smaller and smaller from the top to the bottom, indicating a more violent disturbance happened at the lower part of specimen.

The volumetric strains shown in Fig. 5.17 were calculated by using the average of radial strains from 3 Clip Gauges and average axial strains from 4 LDTs. Note that the dotted lines represent loose specimen with the density around 45%.

The first strain growth was caused by the change of confining pressure. The increment for the two cases with cell pressure of 100kPa was around 0.40%, and for the other cases it was about 0.14%. The more obvious increments due to the first water infiltration were observed in all the specimens with pipes, especially for the loose specimen with 2 pipes inside. For the controlled specimen, 1-pipe-specimen and 2-pipe-specimen, $\Delta\varepsilon_{vol}$ of the loose sand group were 0.058%, 0.69% and 3.10% respectively, and the results were 0.051%, 0.46% and 2.26% for the dense cases. The results of the cases with 100kPa cell pressure were 0.069% and 0.58% for no pipe and 1 pipe specimen respectively.

For 1-pipe-specimen, larger volumetric strain was caused at the beginning for specimens under 100 kPa confining pressure, however the strain variation due to the first water cycle was smaller when compared with specimen under 50kPa cell pressure.

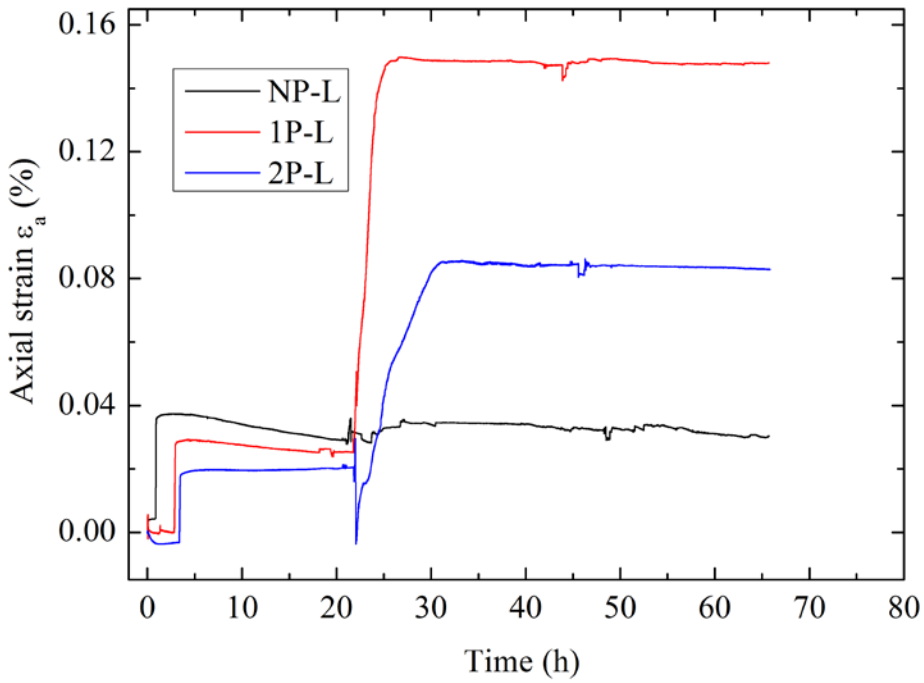

Fig. 5.3 Axial strain before shearing (Loose)

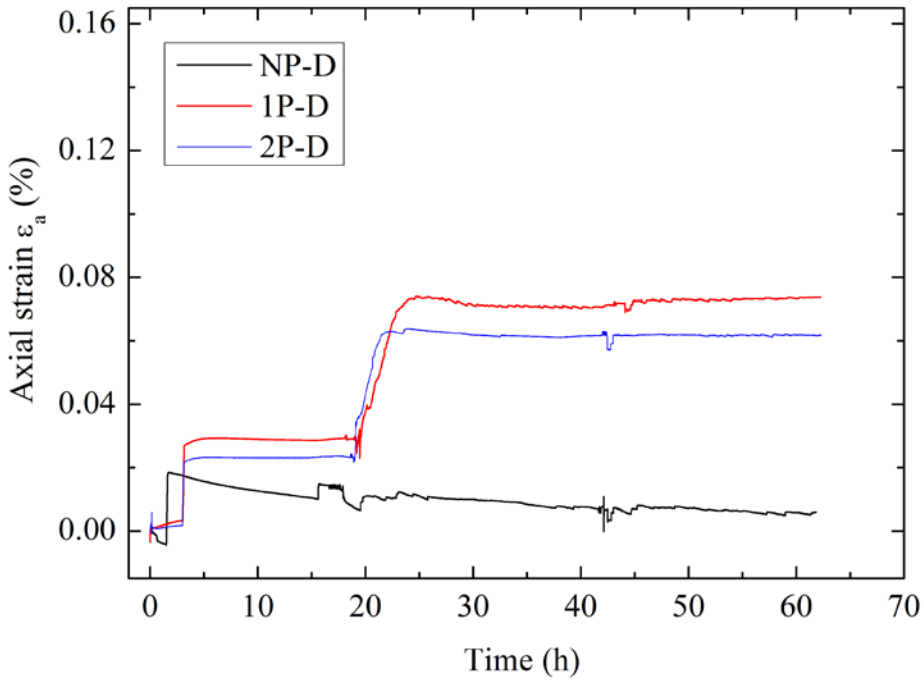

Fig. 5.4 Axial strain before shearing (Dense)

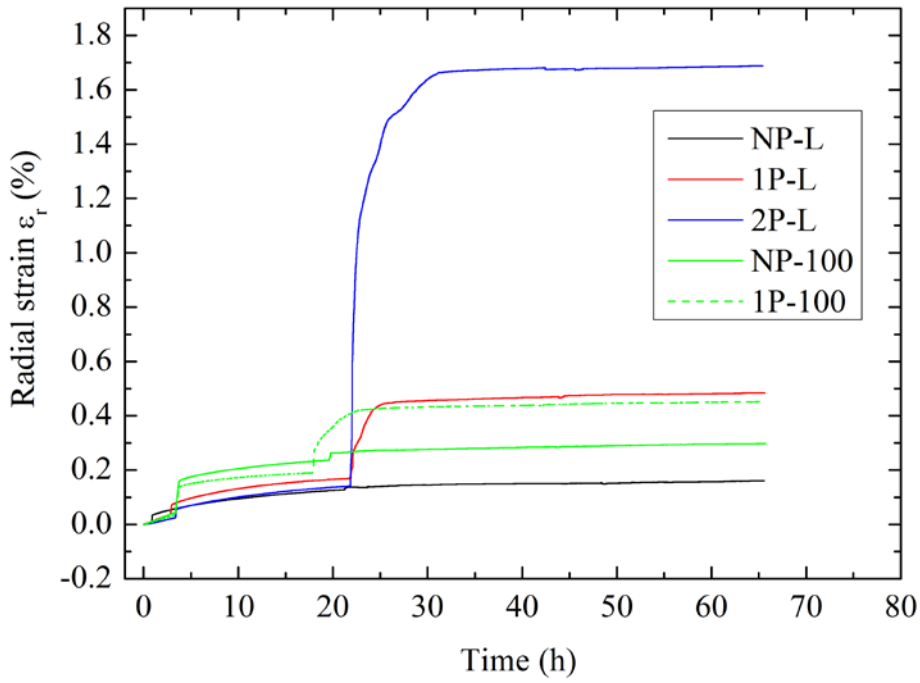

Fig. 5.5 Radial strain before shearing (Loose)

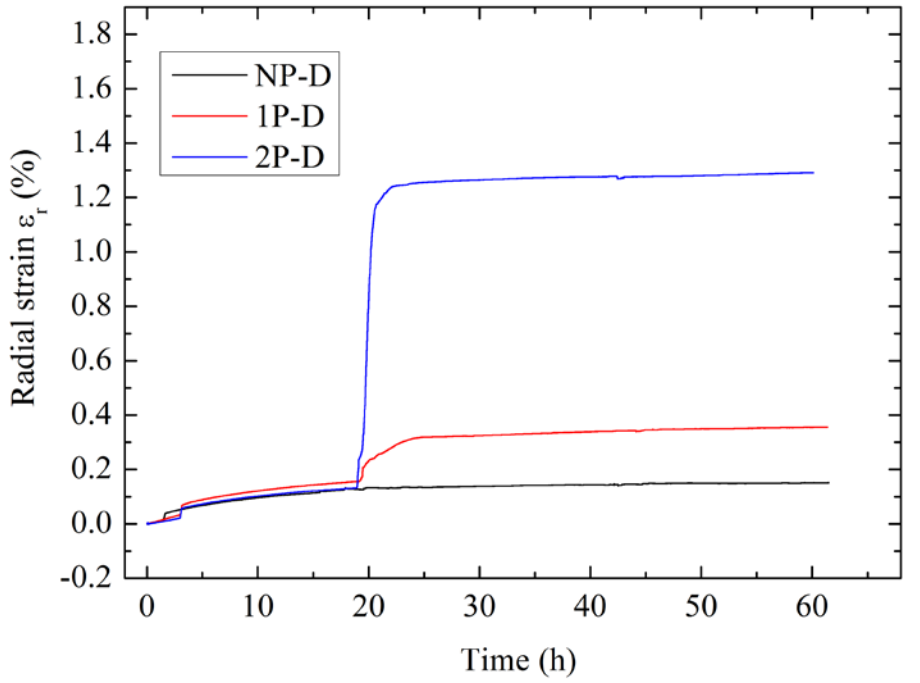

Fig. 5.6 Radial strain before shearing (Dense)

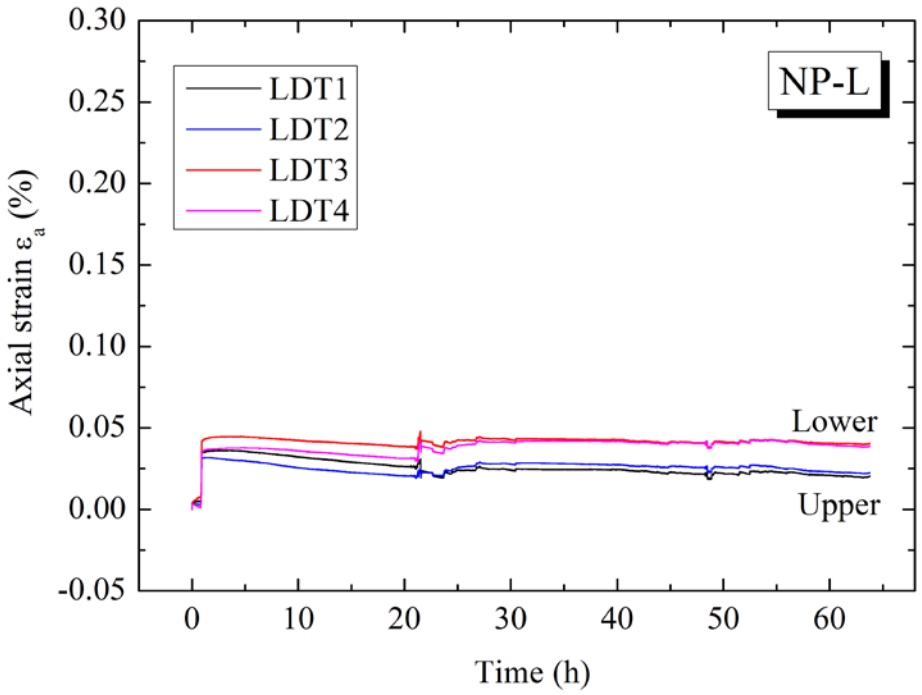

Fig. 5.7 Variation of LDTs of no-pipe-specimen (loose)

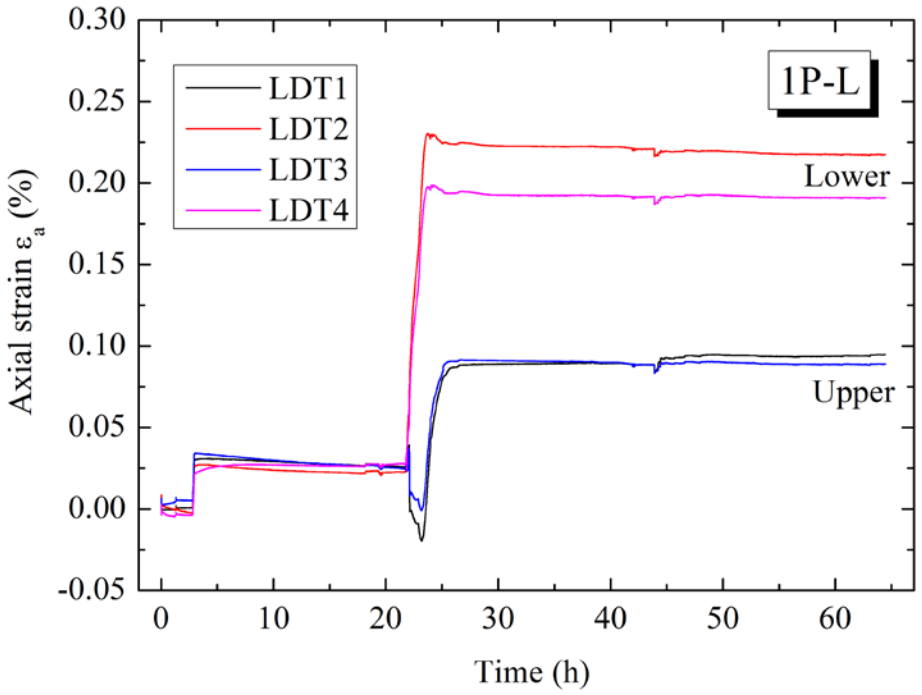

Fig. 5.8 Variation of LDTs of 1-pipe-specimen (loose)

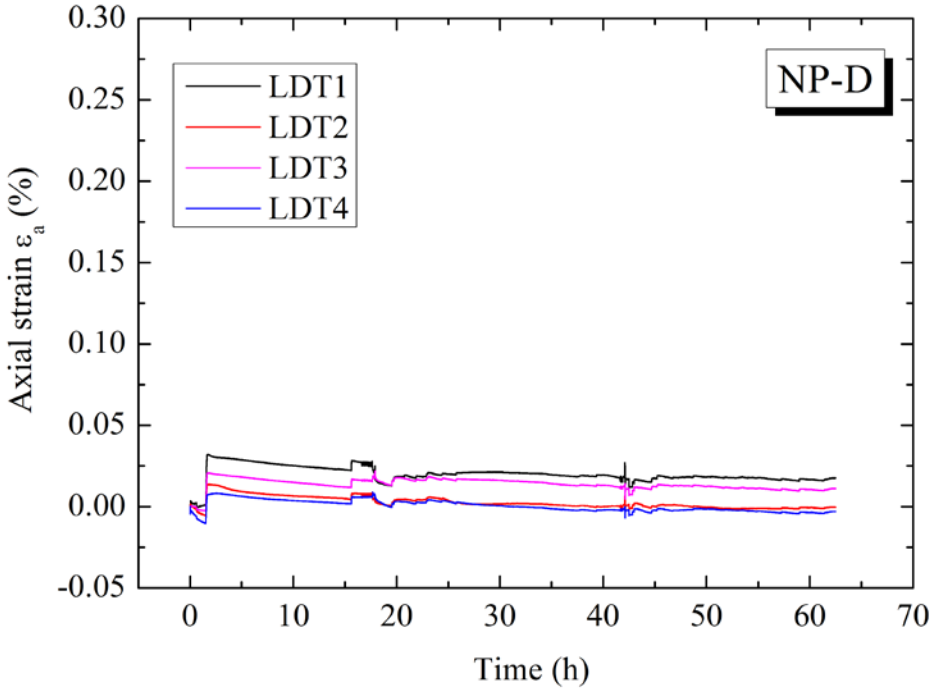

Fig. 5.9 Variation of LDTs of no-pipe-specimen (Dense)

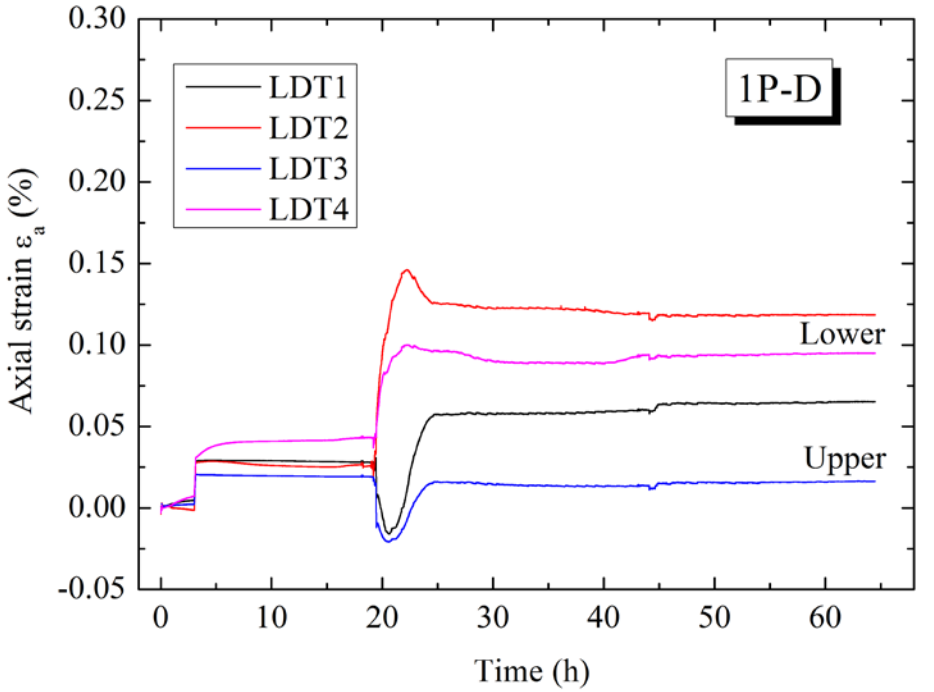

Fig. 5.10 Variation of LDTs of 1-pipe-specimen (Dense)

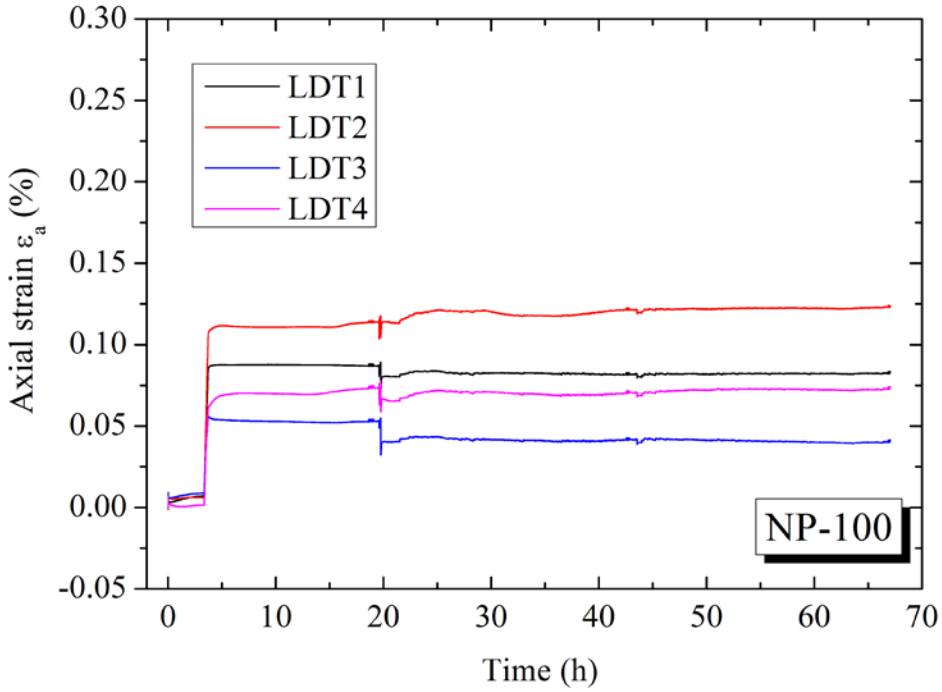

Fig. 5.11 Variation of LDTs of no-pipe-specimen (100 kPa)

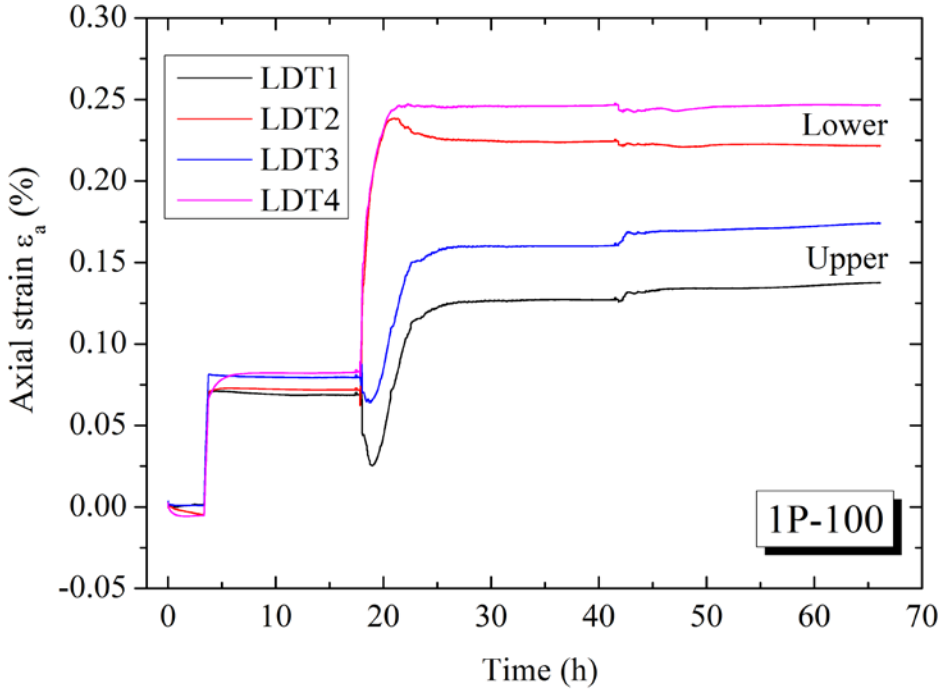

Fig. 5.12 Variation of LDTs of 1-pipe-specimen (100 kPa)

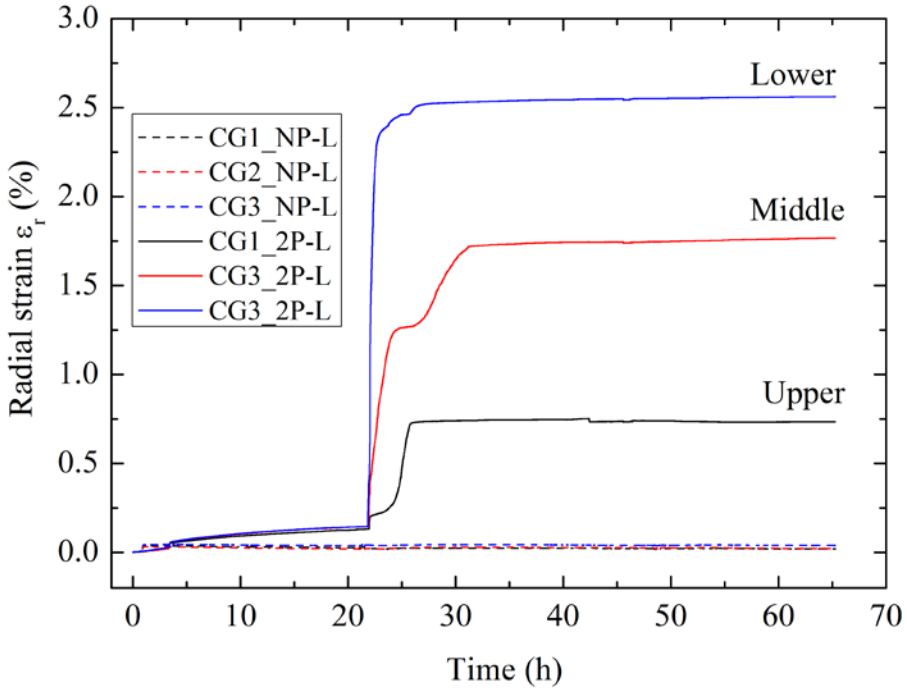

Fig. 5.13 Variation of CGs of no-pipe-specimen and 2-pipe-specimen (Loose)

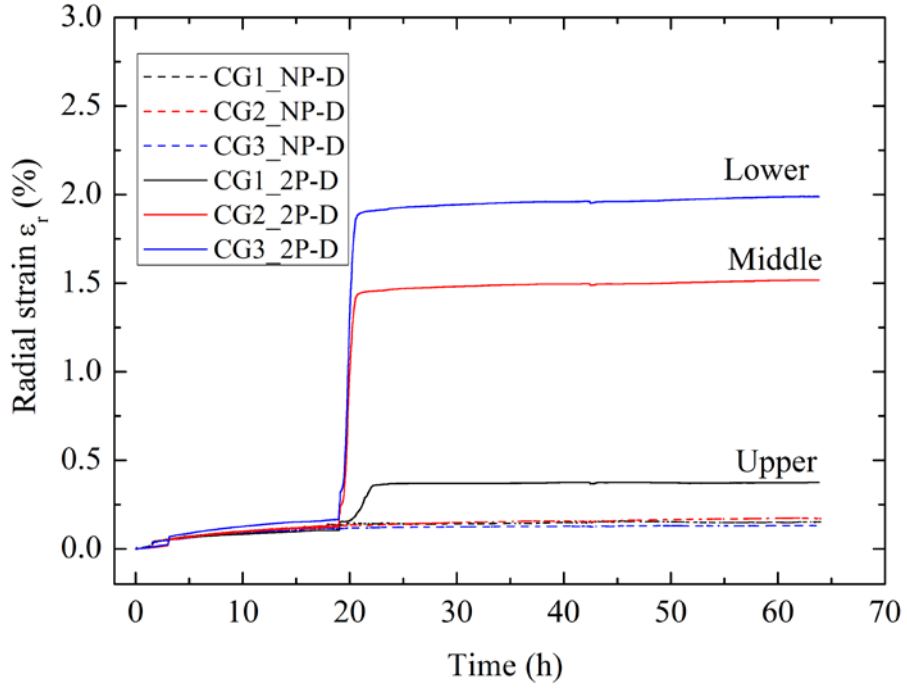

Fig. 5.14 Variation of CGs of no-pipe-specimen and 2-pipe-specimen (Dense)

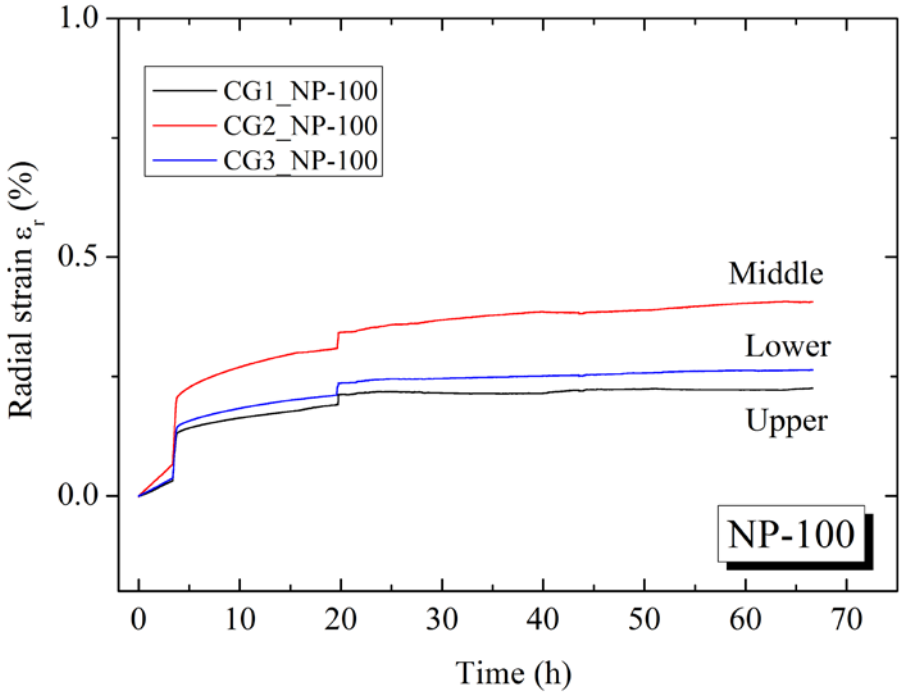

Fig. 5.15 Variation of CGs of no-pipe-specimen (100 kPa)

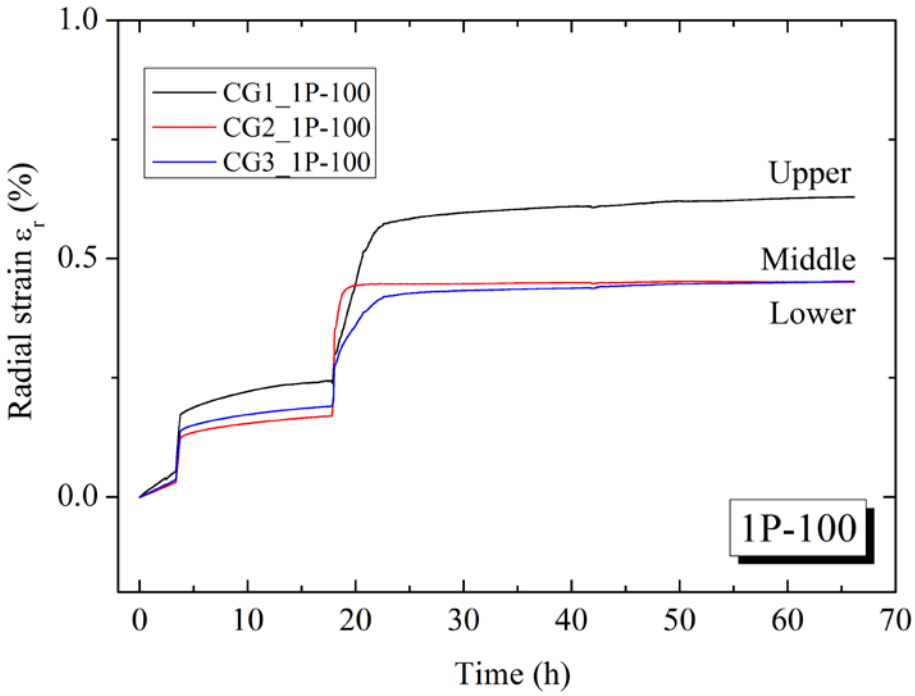

Fig. 5.16 Variation of CGs of 1-pipe-specimen (100 kPa)

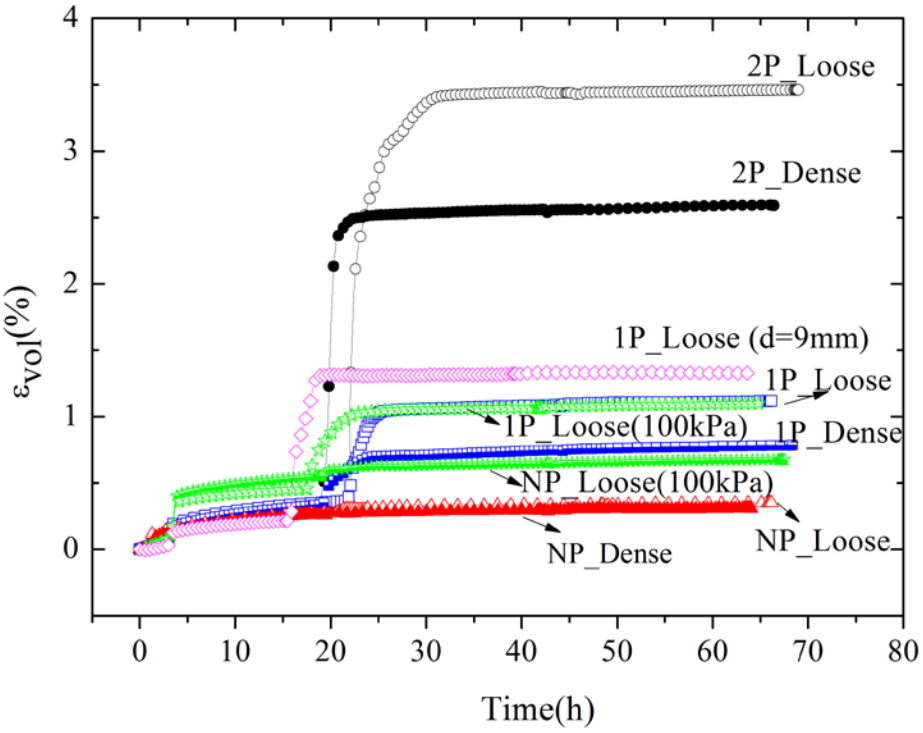

Fig. 5.17 Volumetric strain before shear

Table 5.3 Volumetric strain variation in tiraxial tests of Toyoura sand

Test Cases		$\Delta\varepsilon_{vol}$ (%)	
		Confining pressure	1st Water Cycle
No pipe	Loose	0.12	0.31
	Dense	0.10	0.28
1pipe	Loose	0.18	1.05
	Dense	0.16	0.70
1pipe (d=9mm)	Loose	0.14	1.31
2pipe	Loose	0.14	3.41
	Dense	0.13	2.49
No pipe (100kPa)	Loose	0.40	0.62
1 pipe (100kPa)	Loose	0.35	1.03

5.2.2 Variation of Young's modulus

Mechanical properties of sand at small strains are another focus issue in the current study, as the stress-strain behavior of sand at small strain is of great importance in geotechnical engineering. A stiffness degradation curve is normally used to explain the shear stiffness for a wide range of shear strain. Atkinson and Sallfors (1991) divided the strain levels into three groups: the very small strain level, where the stiffness modulus is constant in the elastic range; the small strain level, where the stiffness modulus varies non-linearly with the strain; and the large strain level, where the soil is close to failure and the soil stiffness is relatively small.

Most strain levels for deformation of the ground of hard soils and soft rocks are generally small; say, less than 0.1 % (Tatsuoka and Kohata 1995). In plenty of construction activities, such as deep excavations and tunnels, it is a prerequisite to accurately define the stress-strain relationships in the range of 0.01~0.1% to predict ground movements (Burland, 1989). In earthquake geotechnical engineering, knowledge of stiffness of soils at strains in the range of 0.0001~0.001% is required (Ishihara, 1996).

In recent years, using local strain measurements such as LDT and CG, quasi-elastic deformation properties of soil at very small strain levels could be investigated (Tatsuoka et al. 1997). Related research about obtaining the quasi-elastic properties such as Young's modulus, shear modulus, and Poisson's ratios by applying unload/reload cycle(s) at very small strain amplitudes could be found in plenty of studies (Koseki et al. 2000; HongNam and Koseki 2003; HongNam 2004; Chaudhary et al. 2004).

In the current study, Young's modulus was evaluated by the vertical stress and related axial strains measured by LDTs at small cyclic loadings. Here, E_0, E_1 and E_2 stand for Young's modulus before the first water cycle (dry state), after the first water cycle and after the second water cycle respectively. Poisson's ratio was computed by measuring the small radial and axial deformations during cyclic loadings. Fig. 5.18 and Fig.5.19 shows the examples of the computation of E and ν, with the average results of LDTs and CGs.

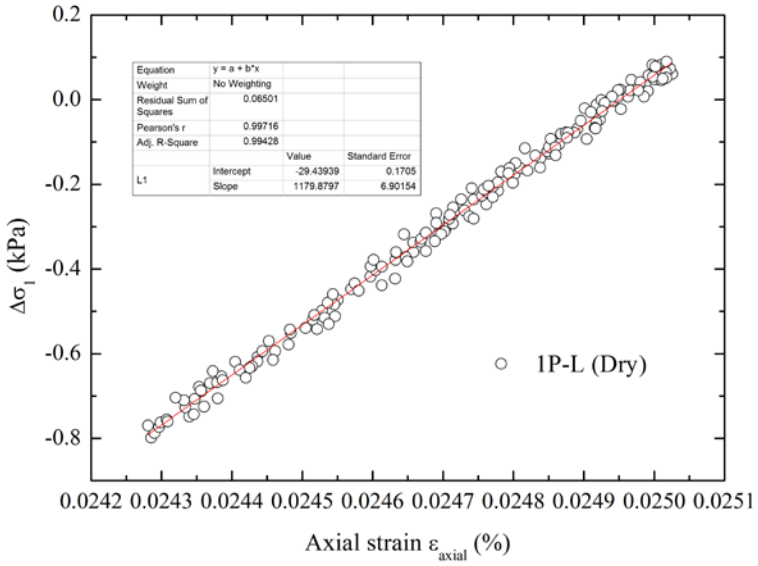

Fig. 5.18 Calculation of Young's modulus E

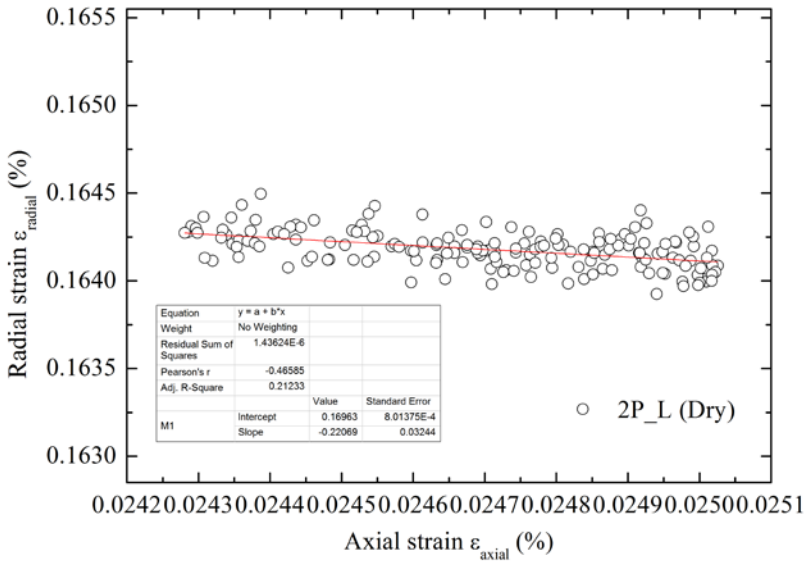

Fig. 5.19 Calculation of Poisson's ratio ν

Fig. 5.20 was the E values obtained from the average axial strain and radial strain for no-pipe-specimen and 1-pipe-specimen. It could be clearly observed that dense specimen and specimen under higher confining pressure showed larger E values compared with loose one. In addition, piping effect could be found from the tendency that specimens with internal pipe(s) exhibited smaller E than controlled ones.

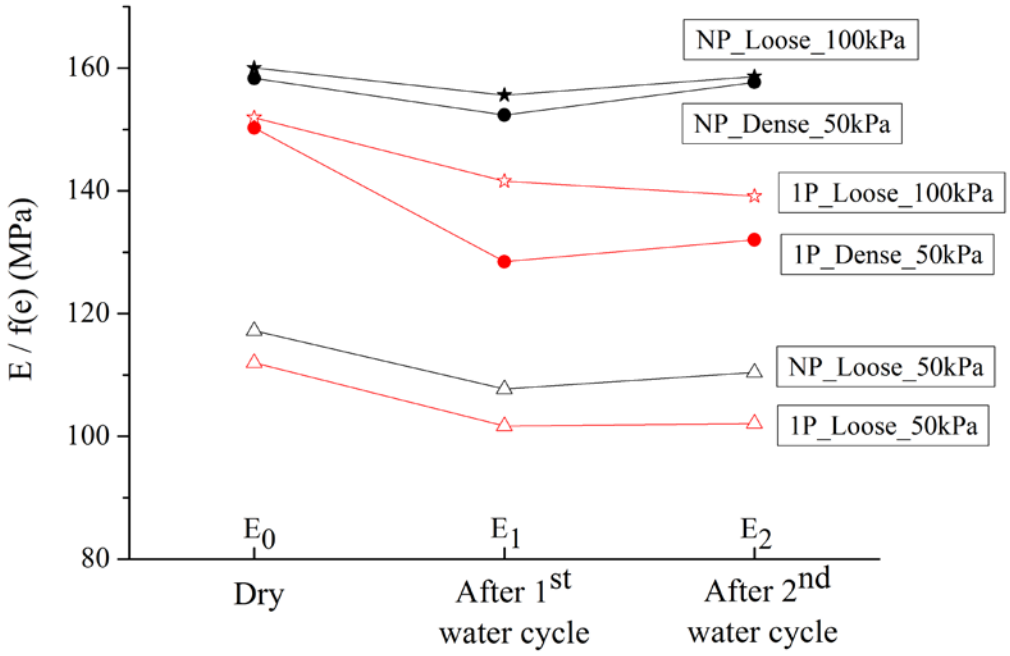

Fig. 5.20 Young's modulus variation

Considering the uniform development of piping along the specimen, E was calculated separately for the upper and lower halves of specimen by averaging the results from two pair of LDTs. Fig. 5.21 showed the results obtained in NP-L case for each LDT.

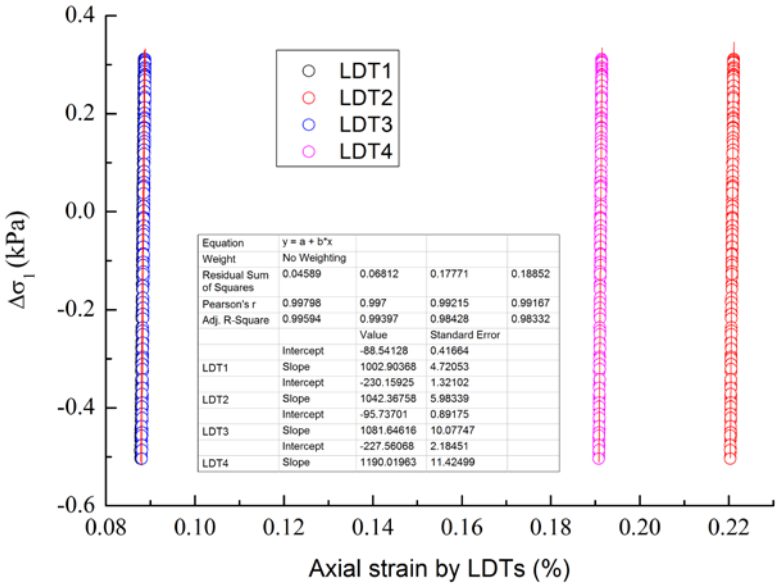

Fig. 5.21 Calculation of E for each local transducer

Young's modulus reduction was plotted by the proportion between different E values in Fig. 5.22 to Fig.24. It could be observed that in controlled tests, shown as dotted lines, reduction of Young's modulus caused by water infiltration was not so significant as specimens with internal pipes, although some inconsistent behavior could be found due to non-uniform particle arrangement (Fig. 5.22). In addition, larger reduction of E was found at the upper part of the specimen due possibly to the fact that more voids were left there compared with the lower part. While in the lower part, sand was loosened in a more uniform way.

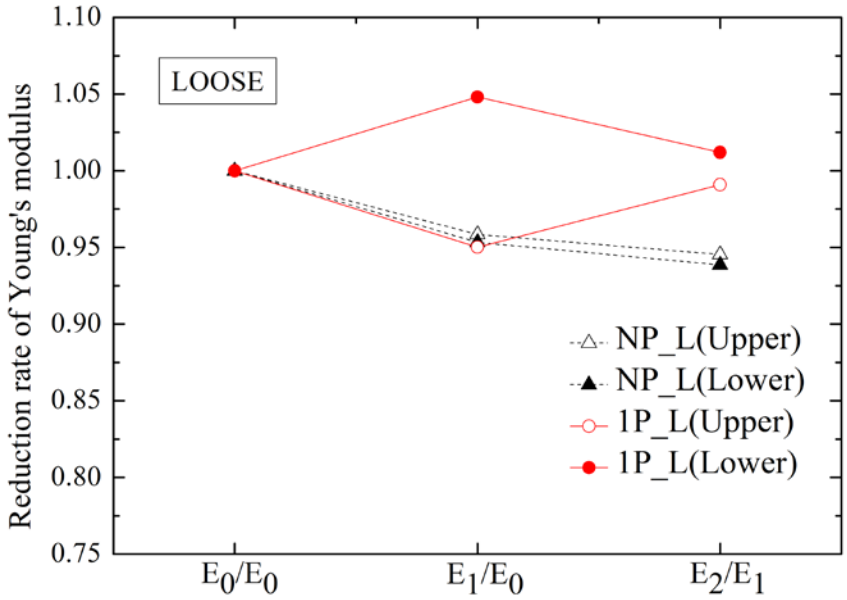

Fig. 5.22 Reduction rate of E due to piping effect (Loose)

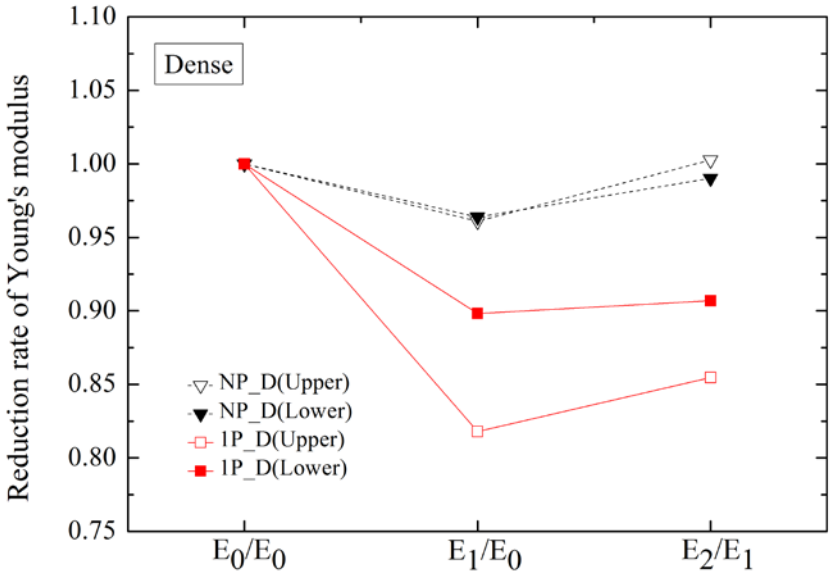

Fig. 5.23 Reduction rate of E due to piping effect (Dense)

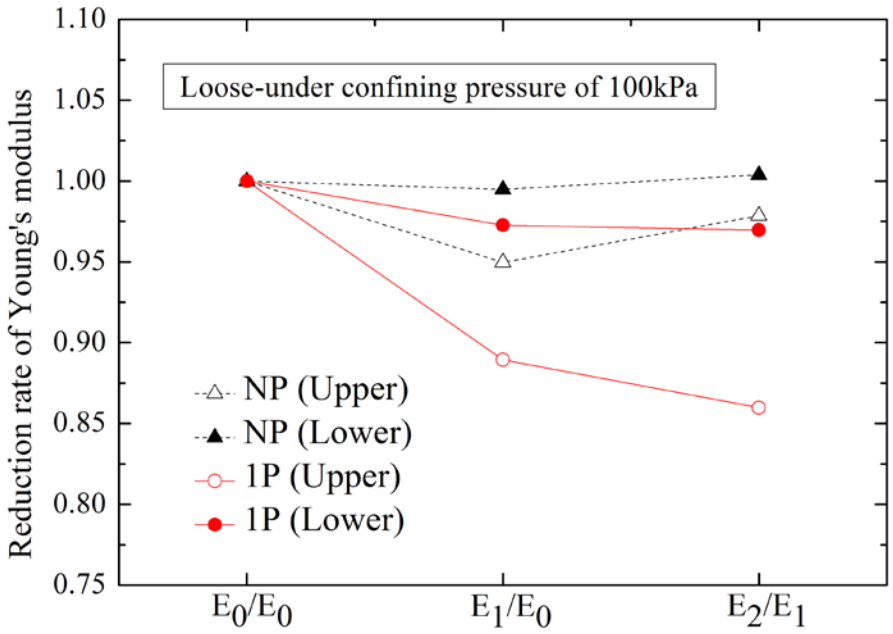

Fig. 5.24 Reduction rate of E due to piping effect (100 kPa)

For 2-pipe-specimen, the results of E were shown for each LDT, seen in Fig. 5.25 and Fig. 5.26. Due to the non-uniform behavior of sand subjected to piping effect, it is difficult to identify a clear tendency of variation of E between the soil side and glucose side. Still, the tendency of smaller Young's modulus was mostly observed after water infiltration.

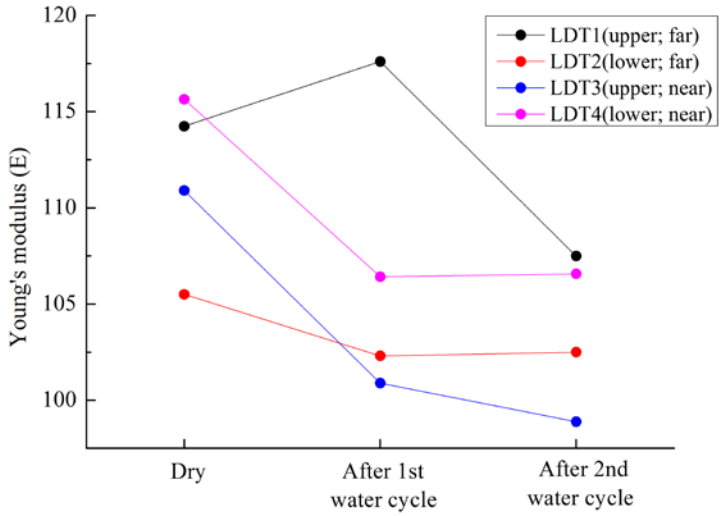

Fig. 5.25 Young's modulus computed according to each LDT (2P-L)

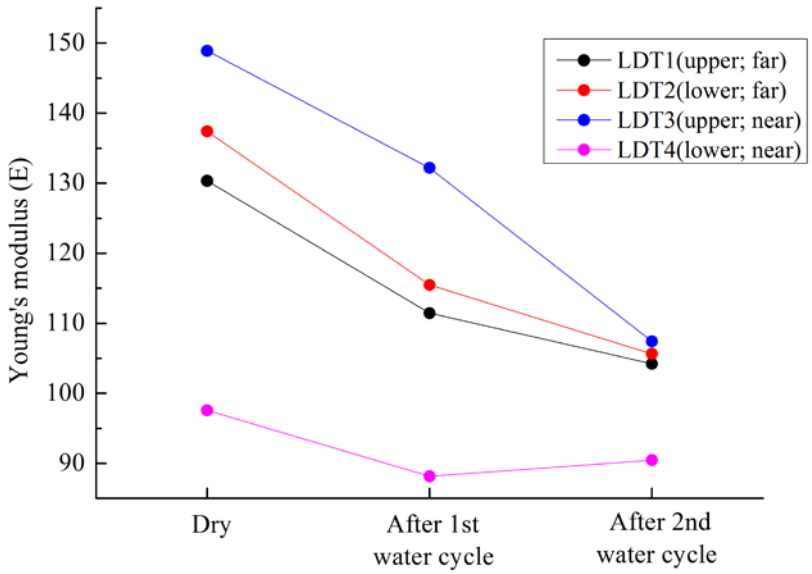

Fig. 5.26 Young's modulus computed according to each LDT (2P-D)

5.2.3 Variation of Poisson's ratio

With the small radial and axial deformations measured during cyclic loading, Poisson's ratio was computed and the results are shown in Fig. 5.27 ~ Fig. 5.29. For specimens with 2 pipes inside, axial strain was obtained by the pair of LDTs attached near glucose pipe (LDT3&LDT4), as the corresponding radial strain measured by Clip Gauges was also at the same place.

Same with Young's modulus, Poisson's ratio was plotted separately at three stages. It could be seen that generally ν became larger with initial density increasing. Furthermore, loosened specimen tended to show a larger Poisson's ratio than controlled one. However a clear tendency of its variation related to piping effect was very difficult to identify.

When comparing Fig. 5.30 and Fig. 5.31, it could be noticed that for dense cases, piping effect was more obvious for the larger increase of ν after the first water cycle. This phenomenon could be explained by different voids arrangement between loose and dense specimens. Various voids with different size were supposed to be generated as glucose pipe dissolving. For the loose soil, these voids would be refilled or partly refilled easily during the water infiltration period, while these voids with different combinations may be left inside the

denser specimen. With more voids inside, the complex behavior of Poisson's ratio could be expected. In addition, it was mostly observed that Poisson's ratio increased after the first water cycle for the 2-pipe-secimen.

Still, these results could not strongly indicate that Poisson's ratio of loosened soil is always larger than uniform soil. Such a complex soil behavior lies in the fact that the initial soil structure was reformed into a new pattern after the glucose dissolving. This non-uniform change would bring an unpredictable deformation of soil.

Results for shear modulus G was shown in Fig. 5.32, in which larger reduction of G was observed in dense specimens with internal pipes, while significant variation of G was not found in the controlled specimen. Specially, 1-pipe-specimen showed further reduction of G by nearly 8% during the second infiltration while some rebound of stiffness was found in 2-pipe-specimen.

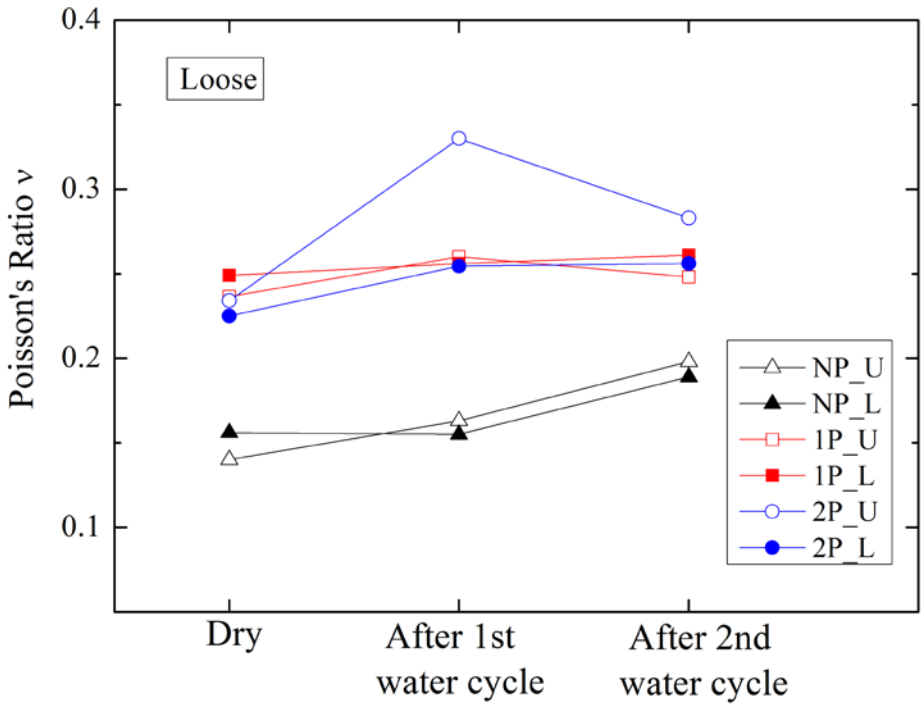

Fig. 5.27 Variation of local Poisson's ratio (Loose)

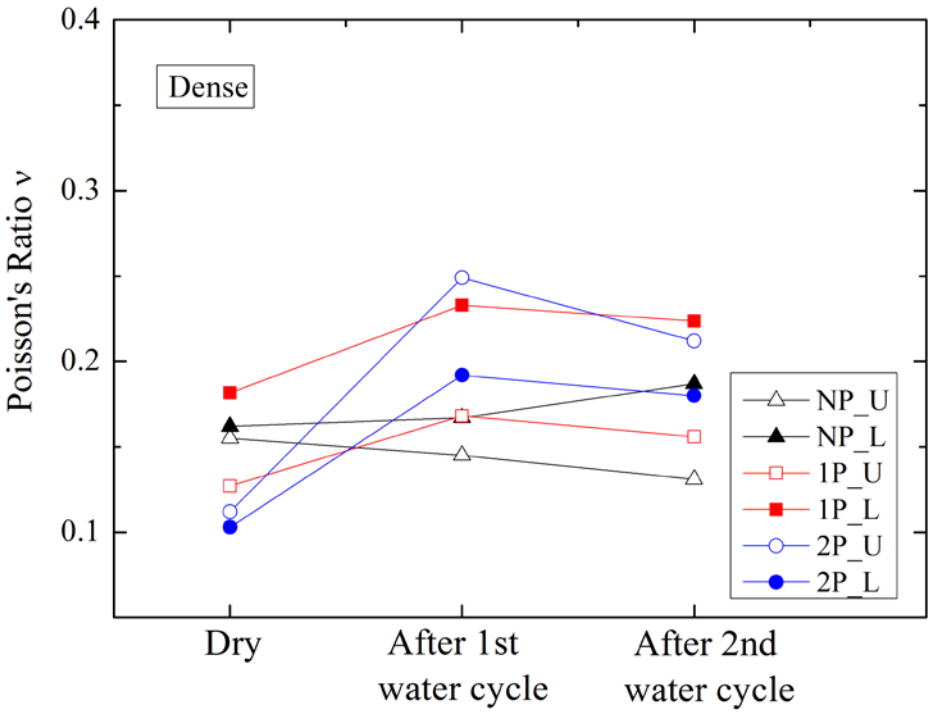

Fig. 5.28 Variation of local Poisson's ratio (Dense)

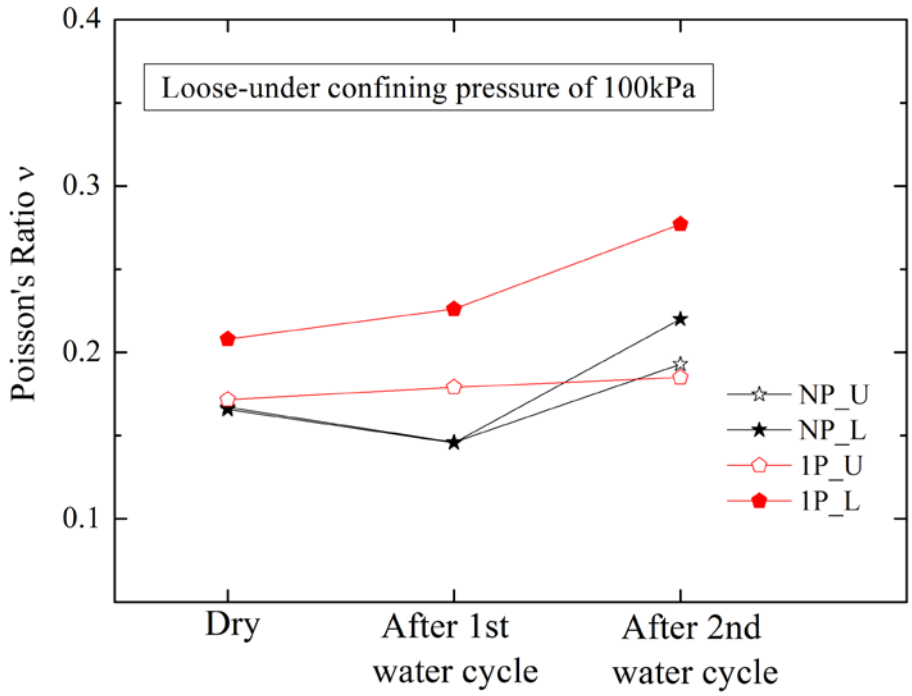

Fig. 5.29 Variation of local Poisson's ratio (100 kPa)

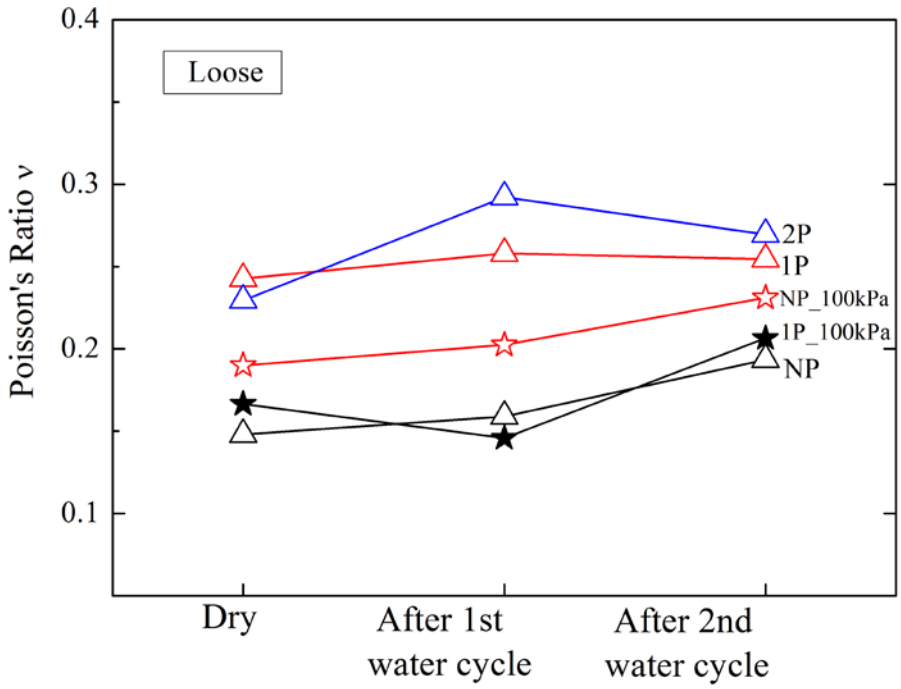

Fig. 5.30 Poisson's ratio variation (Loose)

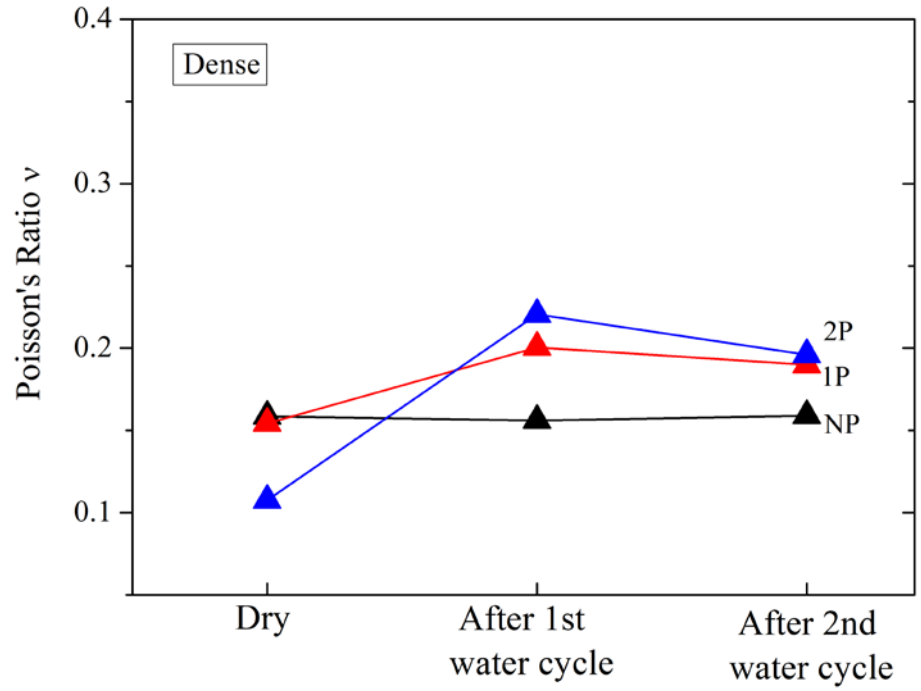

Fig. 5.31 Poisson's ratio variation (Dense)

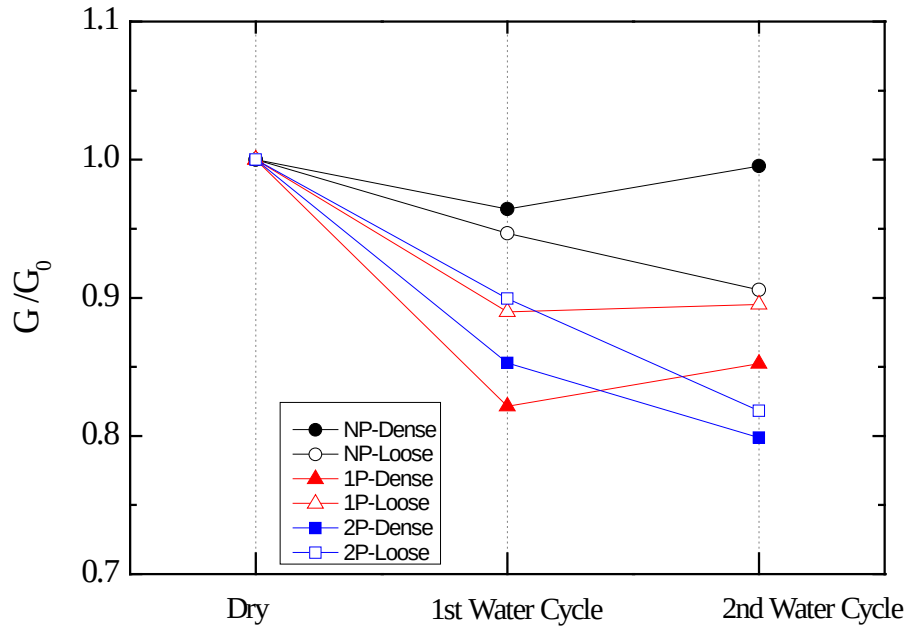

Fig. 5.32 Shear modulus variation for Toyoura sand

5.2.4 Shear strength of Toyoura sand subjected to piping effect

The deformation-strength characteristics of sands have been kept under the investigation by many researchers. It is well recognized that the shear behavior of sands depends on their grading, density, fabric and so on. Given the abundant research on the intact soil, this study focus on the sand with inherent disturbed plane due to piping effect, which could be a good complement to better understand the anisotropy of soil.

Relationship between deviator stress and axial strain during triaxial shearing of all eight experiments are shown in Fig. 5.33 to Fig. 5.35.

It is obvious that the peak shear strength was larger in dense specimen than loose one, while for each density the differences were not so significant for the specimen with and without pipe. Refer to the maximum shear strength of controlled specimen, strength reduction of 2-pipe-specimens was 3.1% for the loose specimen and 5.9% for the dense one. Specimen under 100 kPa confining pressure showed larger shear strength and the reduction caused by piping effect was 2.3%.

The glucose pipe volume was 0.64% for 1-pipe-specimen and 1.28% for 2-pipe-speicmen respectively. After 1500 ml water was filled in, it could be inferred that loosening would be generated along the whole height of specimen with discontinuous small voids. These voids might be refilled with sand during two water cycles, especially for the loose specimens. As a result, larger differences of peak shear strength between controlled specimen and loosened specimen were observed in sand with the density around 70% for the reason that more voids were left inside the specimen. In a series of triaxial tests simulating ground cavity by glucose block (Renuka, S., 2012), similar and more evident failure mechanism was found. Sudden collapse was perceived in dense sand during shearing and nearly 26% strength reduction was observed, which indicated loosening was much localized and cavities existed in the specimen. In this study, although localized density near glucose was slightly changed due to soil piping effect, the overall strength was not significantly influenced. Probably because loosening was generated in a relatively uniform way, sudden collapse was not observed.

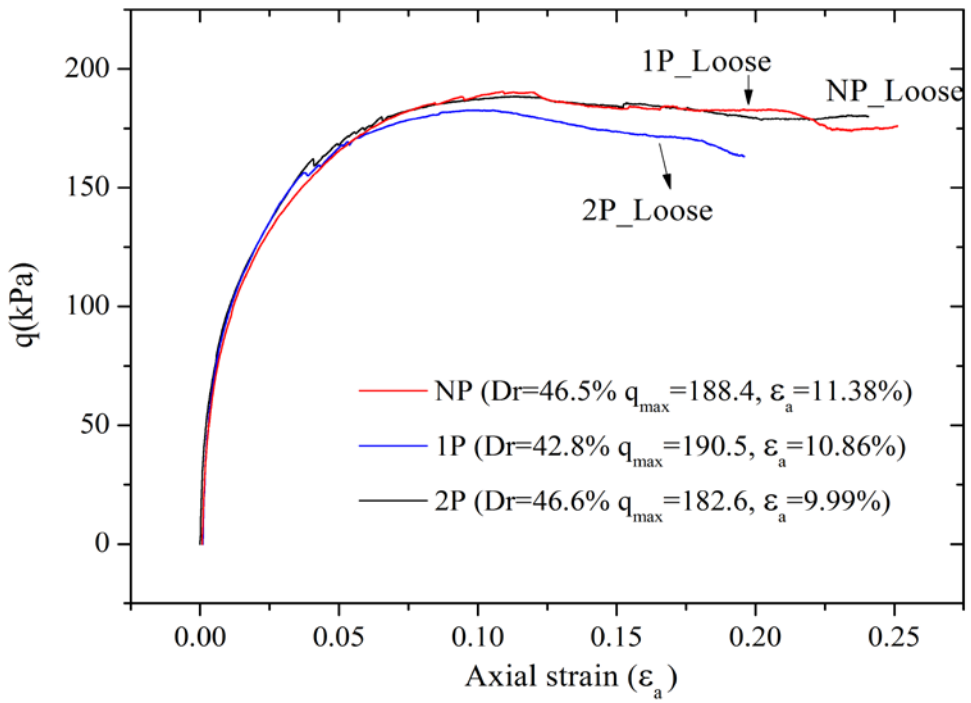

Fig. 5.33 Deviator stress vs. axial stain (Loose)

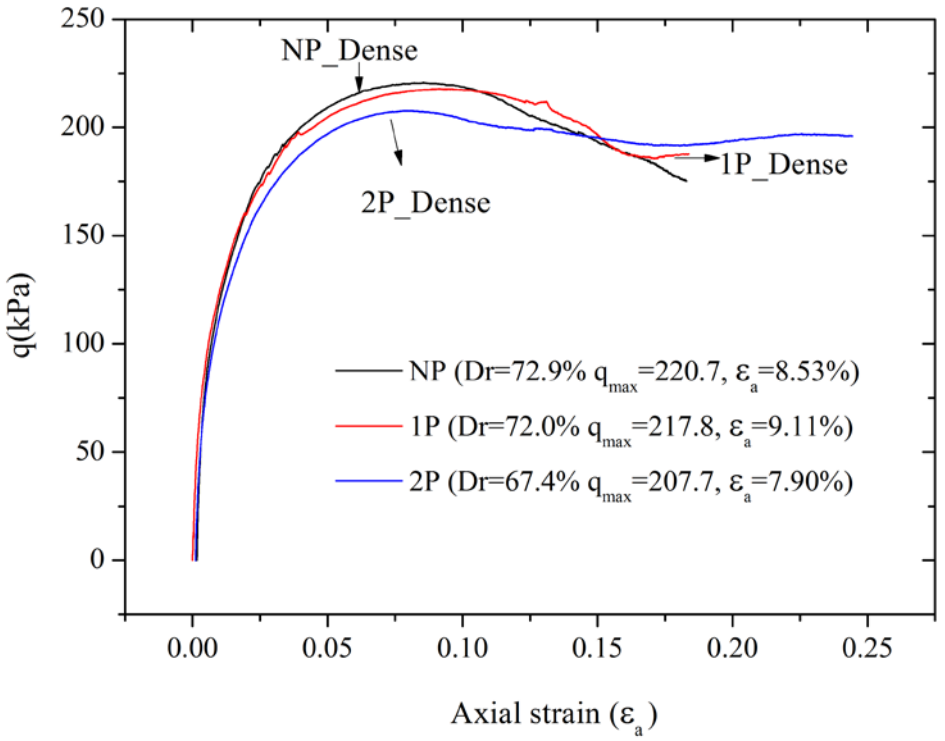

Fig. 5.34 Deviator stress vs. axial stain (Dense)

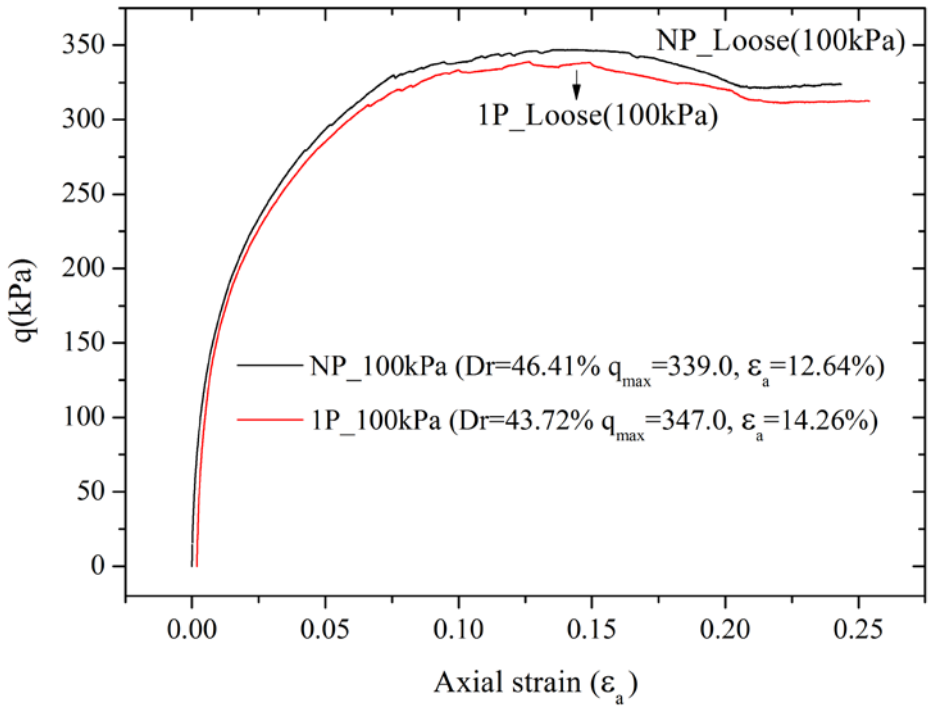

Fig. 5.35 Deviator stress vs. axial stain (Confining pressure of 100 kPa)

Table 5.4 Shear strength in Triaxial compression test for Toyoura sand

Test cases	Void ratio e	q_{max} (kPa)	ε_a at q_{max} (%)
NP-50	0.846	188	11.4
1P-50	0.855	191	10.9
2P-50	0.843	183	10.0
NP-50	0.757	221	8.5
1P-50	0.761	218	9.1
2P-50	0.776	208	7.9
NP-100	0.854	347	14.3
1P-100	0.850	339	12.6

5.3 Test results of Edosaki sand

5.3.1 Strain variation during piping formation

Different from Toyoura sand, fine contents in Edosaki sand presents a more realistic erosion condition in this research. As the seepage-induced erosion mostly results from soil particle migration, i.e. fine particles are eroded through the voids between the larger particles by the seepage flow, leaving behind the coarse skeleton. As a result of the deficiency in particle size, gap-graded soil is especially vulnerable to internal erosion.

As shown in Fig. 5.36, due to the existence of fine particles, more severe migration of soil particles would occur along the piping path offered by the glucose in Edosaki sand. Compared with the “loosening effect” around the initial glucose pipe in Toyoura sand, the influenced area in Edosaki sand was thought to be larger for the movement of fines would be more prominent, leading the internal erosion to a more complete manner.

It should also be noted that moisture tamping method was used here to prepare the specimen with Edosaki sand. As a result, it became important to find the suitable initial water content which could not affect the glucose before the water infiltration. In this study, specimen was compacted under the water content around 6%.

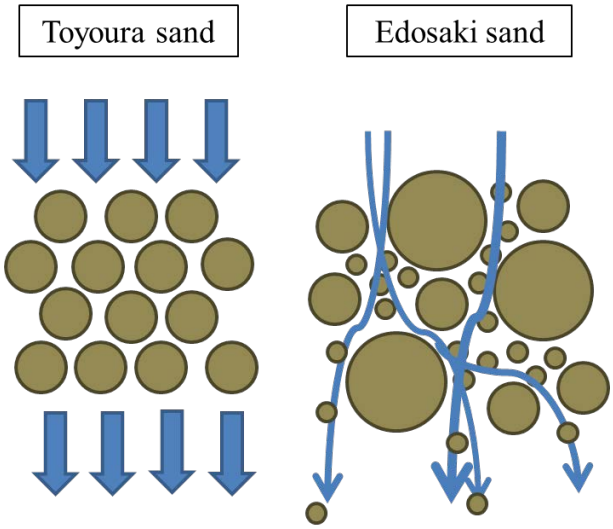

Fig. 5.36 Sketch of water path in Toyoura sand and Edosaki sand (Sato, M. 2014)

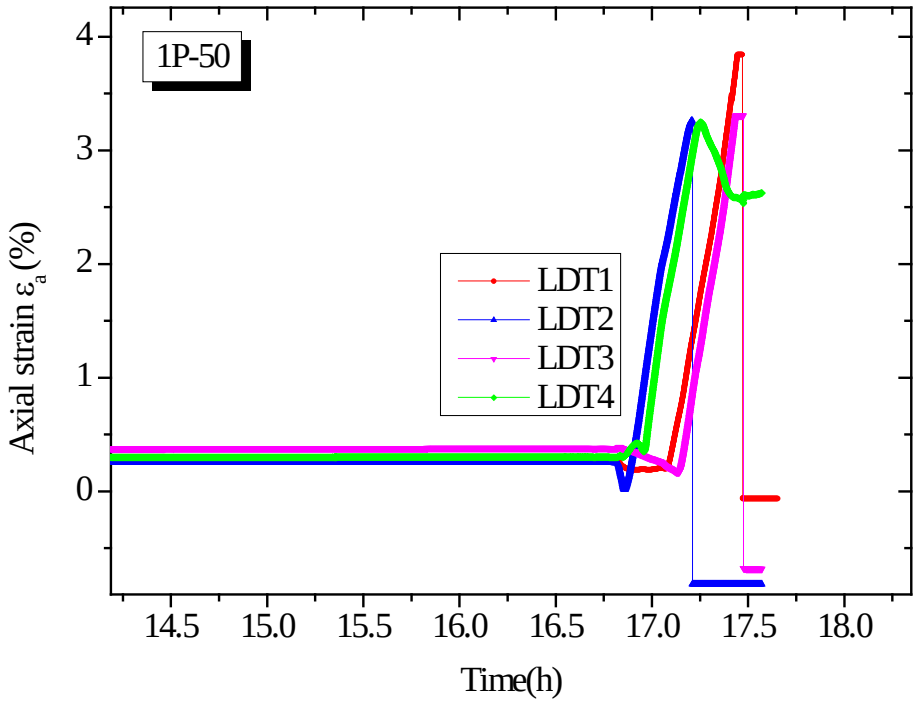

Fig. 5.37 Axial strain during water infiltration for 1P-50

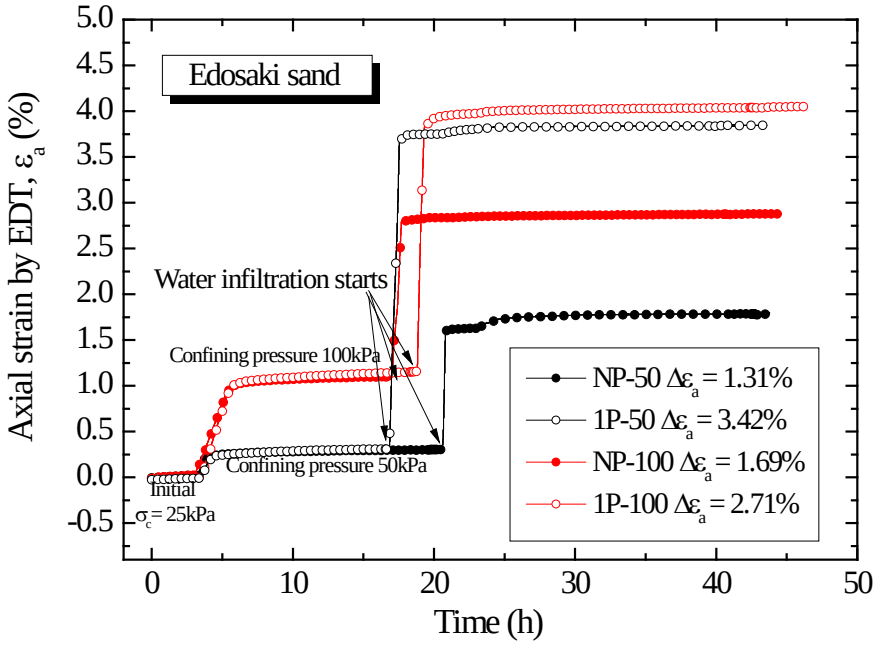

Fig. 5.38 Axial strain variation (from EDT)

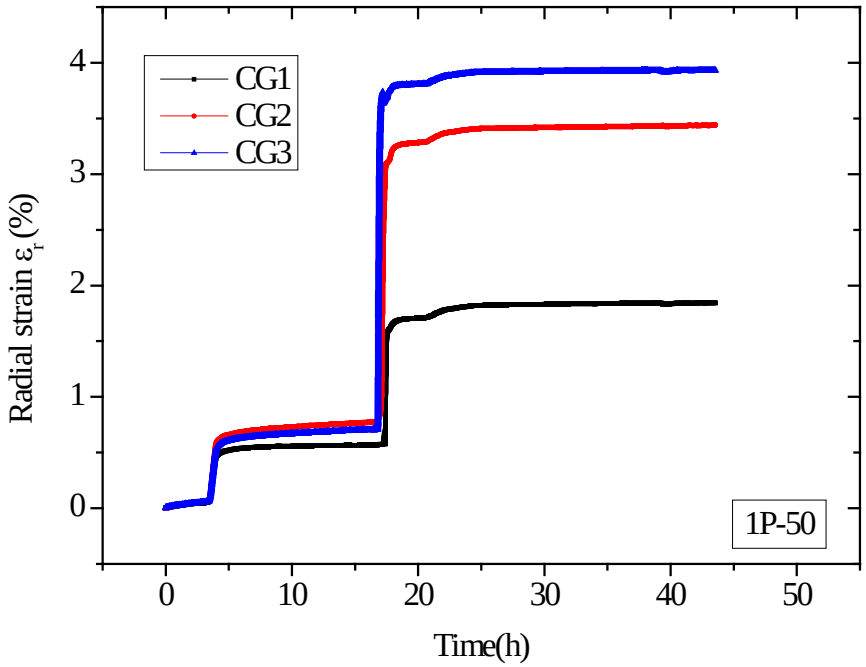

Fig. 5.39 Radial strain during water infiltration for 1P-50

Fig. 5.37 presents the axial strain measured by LDT during water infiltration for the test case of 1P under confining pressure of 50 kPa. Due to the consolidation of the specimen after

water inflow, large deformation occurred even the water was filled into the specimen at very slow rate. As a result, LDT was removed as soon as its range was exceeded. Thus, variation of ε_a was plotted with the data collected from EDT, as shown in Fig. 5.38. It could be found that larger axial strain was caused by the piping effect in specimen under lower confining pressure, same with Toyoura sand. In addition, larger deformation in radial direction was observed at the lower part of the specimen, seen in Fig. 5.39.

5.3.2 Small strain stiffness for Edosaki sand

Due to the removal of local sensors during the water infiltration, results of small strain stiffness only for test cases under confining pressure of 100 kPa were obtained, where a pair of longer LDTs with larger measurement range was used. Fig. 5.40~ Fig. 5.42 showed the results of E, ν and G respectively.

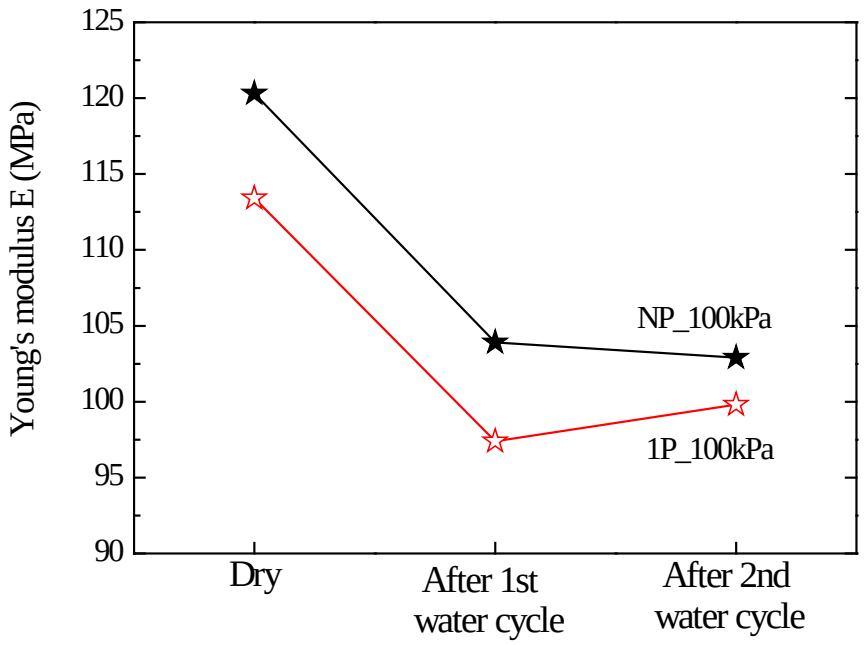

Fig. 5.40 Variation of Young's modulus (100kPa)

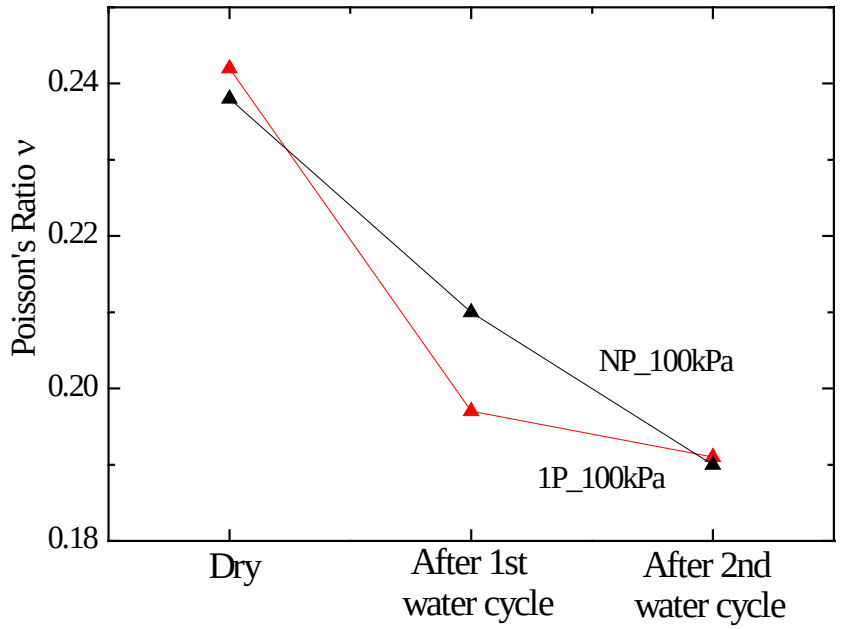

Fig. 5.41 Variation of Poisson's ratio (100kPa)

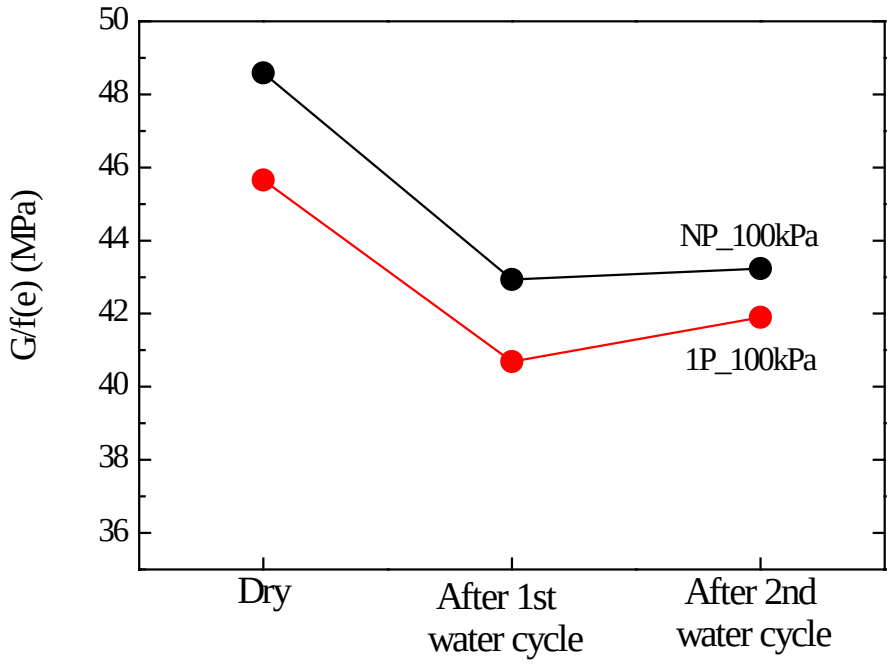

Fig. 5.42 Variation of normalized shear modulus (100kPa)

Different from Toyoura sand, difference of the small strain stiffness reduction in Edosaki sand was found to be small between NP and 1P specimen. Decrease of Young's modulus relative to the initial value was 13.6% and 14.1% respectively, while for Poisson's ratio, a decrease instead of increase was observed. Such "densify effect" is due possibly to the increase of void ratio during water infiltration.

5.3.3 Shear strength variation for Edosaki sand

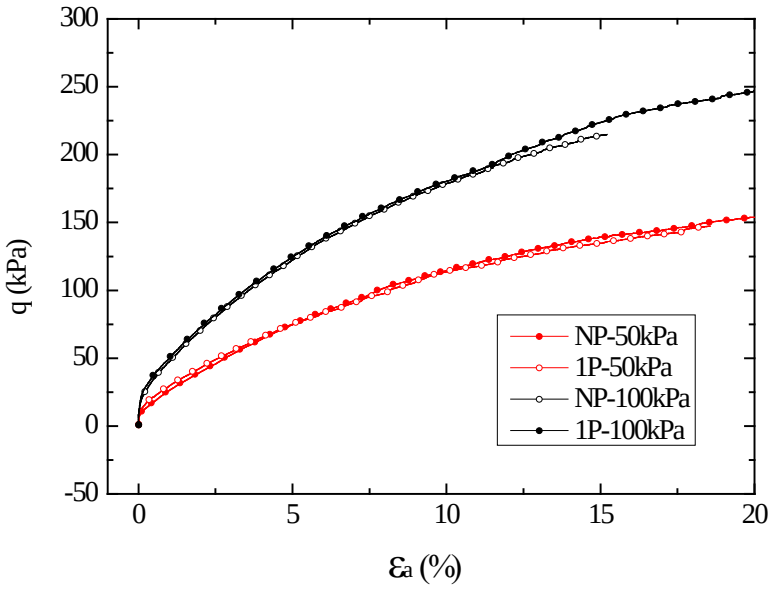

Fig. 5.43 Stress-strain relationship for Edosaki sand

As is shown in Fig. 5.43, stress-strain curve for Edosaki sand develops nearly in the same way for both the specimen with internal pipe and the controlled specimen. A ductile failure manner was observed for all the specimens.

In the previous experimental research, it has also been indicated that changes in the fine content may cause either a decrease or an increase in soil strength. "Inter-granular void ratio" was proposed by Thevanayagam and Mohan (2000) by assuming that the volume of fines is a part of the voids between the coarser particles. And the soil behavior, which depends on the combination of the void ratio and the fine content, is divided into three cases. Case 1 has a relatively smaller void ratio and a smaller fine content. In this case, the inter-granular void ratio of the soil specimen is smaller than the maximum void ratio of the coarse particles. Most of the fines are locked in the inter-granular voids. The soil behavior largely depends on the coarse materials. Case 2 has an intermediate void ratio. The inter-granular void ratio is approximately equal to the maximum void ratio of the coarse particles. The anticipated soil

behavior would depend on whether or not the fines are locked in the inter-granular voids or work as separators between the coarse particles. Case 3 has a relatively larger void ratio. The inter-granular void ratio is larger than the maximum void ratio of the coarse particles. In this case, the coarse particles are separated by the fines, leading to a relatively unstable soil structure.

Vallejo (2001) also suggested that the soil structure is characterized by coarse particles when the coarse particle concentration is greater than 70%, while the fine particles dominate if the coarse particle concentration is less than 40%. In between them, both coarse and fine particles partially characterize the soil structures.

Similarly, shear behavior of Edosaki sand in this research could be explained by the fact that a relative uniform specimen was generated with little voids left inside the specimen due to the limited content of fines influenced by piping effect. In Toyoura sand, piping plane existed as a region where voids with different sizes aligned vertically in general; while for Edosaki sand, these voids were filled with fines during the water infiltration and the piping plane could be taken as an area with concentrated fines (Fig.5.44). Voids in Toyoura sand introduced a new structure with unpredictable properties, especially when checked locally. On the other hand, the rearranged particles in Edosaki sand did not show much piping-induced anisotropy because of the disturbed structure was still uniform in general. Therefore, it could be inferred that localized disturbance and its induced voids were the key issues responsible for the unsuspected behavior of soil. Fig. 5.45 and Fig. 46 was the photo of specimen after shear, and it could be found that nearly all the voids were filled with fine particles.

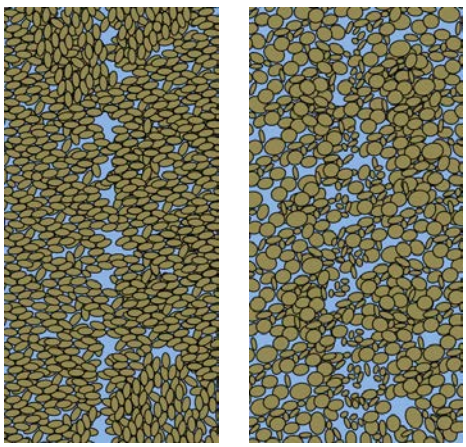

(a) (b)

Fig. 5.44 Sketch of piping generation in Toyoura sand (a) and Edosaki sand (b)

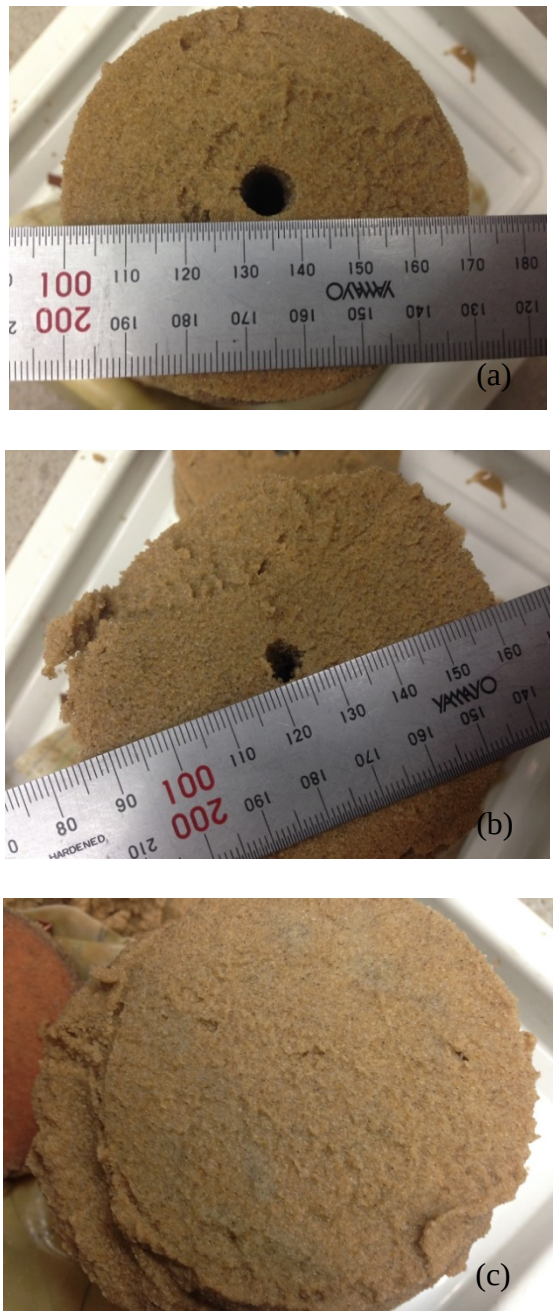

Fig. 5.45 Piping propagation in Toyoura sand (a: top; b: 12mm form the top; c: bottom)

Fig. 5.46 Piping propagation in Edosaki sand

5.4 Chapter conclusions

In this chapter, properties of loosened soil due to piping effect were studied through a series of triaxial tests by dissolving glucose pipes in Toyoura sand. Properties of loosened sand were studied under different densities, pipe number and confining pressure. Piping propagation was observed according to the axial strain, radial strain and volumetric strain measured by local transducers. Furthermore, Young's modulus and Poisson's ratio of sand with internal pipes were also evaluated under cyclic loading before and after loosening. The following conclusions could be drawn based on the results.

(1) It was found that smaller density samples (initial relative density around 45%) were observed with more than 1.5 times larger volumetric strains than samples with initial relative density around 70% during the first water infiltration.

(2) Lower part of the specimen tended to exhibit larger deformation possibly due to the direction of water infiltrations, indicating a non-uniform generation of the piping along the specimen.

(3) For Toyoura sand, Young's modulus tended to decrease and Poisson's ratio showed a tendency of increase in most cases after the first water cycle, while a clear variation trend is still difficult to identify because of the non-uniform distribution of soil and voids.

(4) For Toyoura sand, shear strength in general was not significantly influenced by piping effect compare with controlled specimen, due possible to the end restrain effect of the top cap and the pedestal. While in dense specimen, some reduction still could be observed. Such reduction could be caused by the voids left inside the specimen, and a future verification should be conducted by X-ray or other scanning technic.

(5) For Edosaki sand, larger deformation occurred during water infiltration, leading to a "densification effect" instead of piping effect. Some contradicted results were obtained for the Young's modulus and Poisson's ratio. Similar shear strengths were observed for both the specimen with and without pipe.

(6) Fines play an important role in the piping formation. For uniform sand with little fine particles, voids in different size tend to be generated during water inflow, which bring an unstable soil structure locally. For Edosaki sand, migration of the fine particles to the initial pipe would result in a concentration of fines. Although the effect caused by such migration was not observed in the current study, a different behavior of the sand could be expected when changing the fines content and the initial piping volume.

5.5 Reference

1. Atkinson, J. H., Sallfors, G. (1991). Experimental determination of soil properties. Proceedings of the 10th ECSMFE, vol.3, Florence, 915-956.

2. Burland, J. B. (1989). The Ninth Lauritis Bjerrum Memorial Lecture: 'Small is Beautiful'- the stiffness of soils at small strains. Canadian Geotechnical Journal, Vol. 26, 499-516.

3. Chaudhary, S., K., Kuwano, J., and Hayano, Y. (2004), Measurement of Quasi-Elastic Stiffness Parameters of Dense Toyoura Sand in Hollow Cylinder Apparatus and Triaxial Apparatus With Bender Elements, Geotech. Test. J., Vol. 27, No. 1, 23-35.

4. HongNam, N., Koseki, J. (2003), Modeling Quasi-Elastic Deformation Properties of Sand, Proceedings of the 3rd International Conference on Deformation Characteristics of Geomaterials, Balkema, Rotterdam, Vol. 1, 275-283.

5. HongNam, N. (2004), Locally Measured Deformation Properties of Toyoura Sand in Cyclic Triaxial and Torsional Loadings and Their Modelling, PhD thesis, Department of Civil Engineering, The University of Tokyo, Japan.

6. Ishihara, K. (1996). Soil behavior in Earthquake Geotechnics, Oxford University Press, Inc., NY.

7. Koseki, J., Kawakami, S., Nagayama, H., and Sato, T. (2000), Change of Small Strain Quasi-Elastic Deformation Properties During Undrained Cyclic Torsional Shear and Triaxial Tests of Toyoura Sand, Soils and Foundations, Vol. 40, No. 3, 101-110.

8. L.E. Vallejo. (2001). Interpretation of the limits in shear strength in binary granular mixtures. Canadian Geotechnical Journal, 38, 1097-1104.

9. Thevanayagam, S., Mohan, S. (2000). Intergranular state variables and stress–strain behavior of silty sands. Geotechnique, 50 (1), 1-23.

10. Tatsuoka, F., and Kohata, Y. (1995). Stiffness of Hard Soils and Soft Rocks in Engineering Applications, Prefailure Deformation of Geomaterials, Balkema, Rotterdam, Vol. 2, 947-1063.

11. Tatsuoka, F., Jardine, R. J., Lo Presti, D., Di Benedetto, H., and Kodaka, T. (1997). Characterising the Pre-Failure Deformation Properties of Geomaterials. Theme Lecture for the Plenary Session No. 1,Proceedings of XIV IC on SMFE, Hamburg, Vol. 4, pp. 2129-2164.

Chapter 6 Evaluation of piping effect by torsional shear test

6.1 Introduction

In order to investigate the small strain stiffness and the deformation behavior of sand under more general stress condition involving the rotation of principal stress axes, hollow cyclinder torsional shear apparatus was employed to carry out a series of drained tests on an anisotropic sand subjected to piping effect.

In this chapter, three types of tests including drained torsional shear test with partially rotated σ_1, small cyclic loading test during full rotation of σ_1 and drained torsional shear test under constant σ_1 direction conducted on the hollow cylindrical torsional shear apparatus are described in detail.

The focus in torsional shear test would be the direction of major principal stress σ_1, which is noted with α. As is explained in Chapter 3, calculation of α is shown in Fig. 6.1.

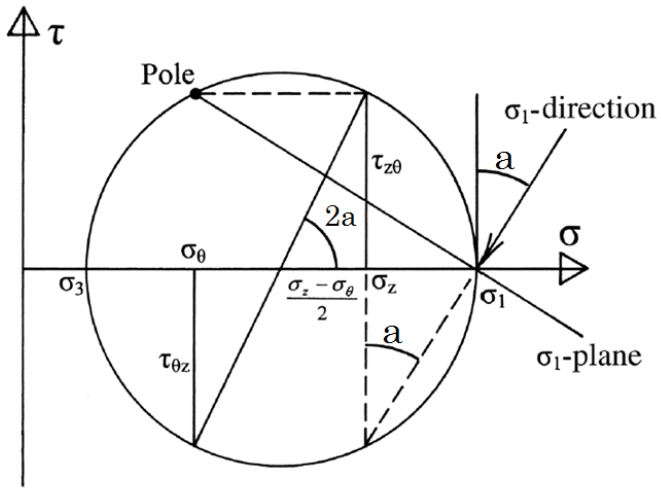

Fig. 6.1 Direction of σ_1 in Mohr Coulomb circle

First, drained torsional shear test with partially rotated σ_1 was conducted to study the role of stress-induced anisotropy combined with the anisotropy caused by piping on the mechanical behavior of sand. For some tests in this series, α changed from 0° (isotropic consolidation) to 45° (sheared to failure), and shear modulus G was examined at certain stages corresponding to

predetermined τ in order to find the influence of σ_1 rotation. For some other cases, α was kept constant (0°, 45° and 90°) during small cyclic loadings and sheared by simply applying τ after the inspection of G variation. These cases were introduced in 6.2.1 firstly.

Small cyclic loading test was conducted to understand the influence of α to shear modulus for sand with or without internal pipes. Here mean effective principal stress *p'* was kept as 80 kPa for all the test cases, so that the value of *p'* was not considered as the influencing factor for the result of G. In addition, internal friction angle φ was kept constant as well. Thus, the normal stress together with the shear stress could be decided according to the equations shown below where φ was determined in advance and varied for different cases.

$$\sigma_z + 2\sigma_\theta = 80 \text{ kPa} \tag{6-1}$$

$$\tan(2\alpha) = \frac{2\tau}{\sigma_z - \sigma_\theta} \tag{6-2}$$

$$\sin\varphi = \frac{\sigma_1 - \sigma_3}{\sigma_1 + \sigma_3} \tag{6-3}$$

Finally, drained torsional shear test under constant α was conducted to obtain the failure behavior of Toyoura sand with internal piping plane in different direction when sheared at certain direction of σ1. A new test program was developed with combined axial-torsional loading control, in which the major principal stress axis was fixed. Typical test results such as effective friction angle, drained shear strength and stress-strain relationship were presented as a function of α.

6.2 Drained torsional shear test with partially rotated σ_1

For all the cases in this series, torsional shear was conducted after the measurement of shear modulus. Before shearing, α was kept constant as 0°, 45° and 90° for some cases, and changed from 0° to 30° for other cases. Therefore, the following interpretation will be divided into two parts.

6.2.1 Constant α during measurement of G before torsional shear

Specimen with relative densities around 75% were tested, and the number of internal pipe was 0 and 2. Specimens were erected at isotropic stress of 30kPa and then the confining pressure was increased to 60kPa. After isotropic consolidation around 12 hours, 1300ml water was infiltrated into specimen, with the aim of completely dissolving the glucose pipe. Small torsional cyclic loading were conducted at the initial dry state, after water infiltration and during TC (triaxial compression), TE (triaxial extension) and TS(torsional shear) under certain stress state while kept p' constant. Monotonic torsional shear test were applied for all the specimens at last.

Table 6.1 Test conditions for fixed principal stress axes

Test ID	D_{rini} (%)	e_{ini}	Pipe number	Pipe direction	σ'_{zini} (kPa)	σ'_{z} (kPa)
TC_NP	82.0	0.676	0	-	30	60
TC_2P	79.5	0.689	2	Vertical	30	60
TE_NP	71.2	0.720	0	-	30	60
TE_2P	74.5	0.707	2	Vertical	30	60
TS_NP	75.6	0.703	0	Vertical	30	60
TS_2P	77.8	0.695	2	Horizontal	30	60

6.2.1.1 Volumetric strain variation before shearing

Fig. 6.2 shows the volumetric strain during the increase of confining pressure and the water infiltration. During isotropic consolidation, similar increment of ε_{vol} was observed. When it came to the water infiltration, specimens with internal pipes showed large growth of ε_{vol} compared with the no-pipe-specimen, which is around 0.328% in average. Considering the

initial glucose volume, it could be inferred that more than 50% of the voids occupied by the initial glucose was filled with loosened sand. Still, some voids were left in the specimen and might be compressed or refilled again during the shearing. The loosened area, together with the remaining voids, would play an important role in the mechanical behavior of the specimen.

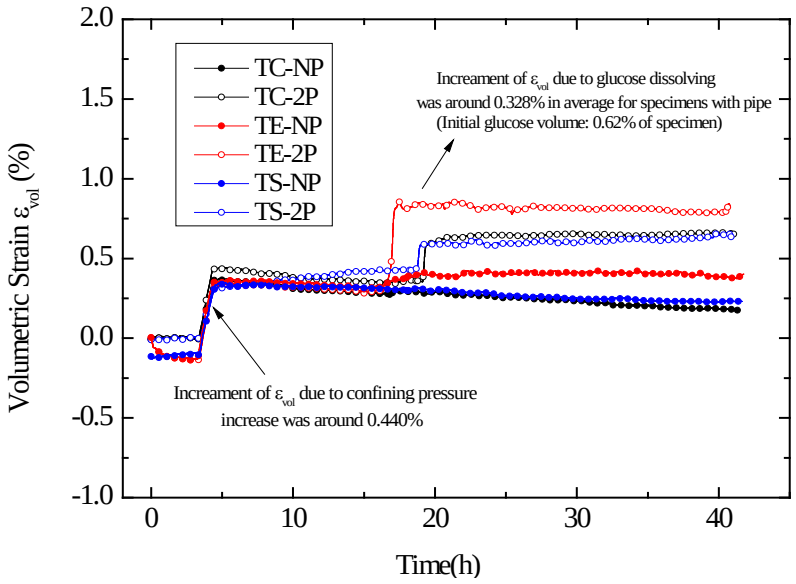

Fig. 6.2 Volumetric strain variation during aisotropic consolidation and water infiltration

6.2.1.2 Shear modulus variation under constant α

Fig.6.3 to Fig. 6.5 presents the results of shear modulus variation during TC, TE and TS.

As suggested by Nguyen and Koseki (2005) in IIS model, *G* could be modelled as a function of the void ratio *f*(*e*), vertical stress and circumferential stress during isotropic consolidation and cyclic triaxial loadings without rotation of principal stress axes from the material axes. In this study, similar result was obtained by plotting normalized shear modulus and $(\sigma_z \cdot \sigma_\theta)^{0.5}$ in logarithm axes. For TC, n was around 0.5 for both of the specimen with and without internal pipe, although larger reduction of shear modulus was found in the 2-pipe-sepcimen, as is seen in Fig. 6.3 where the initial shear modulus was shown by the signal of solid star.

However, in TE n was found to be smaller, especially for the 2-pipe-specimen, as shown in Fig. 6.4. Such results might due to the fact that disturbed specimen caused by piping effect behaved weaker under the extension stress. In addition, with the increase of stress ratio, damage might be caused to the sand fabric. It should be also noticed that the current result

was drawn based on the limited data, while more data with a wider range of stress level should be obtained in order to get a more reliable relationship.

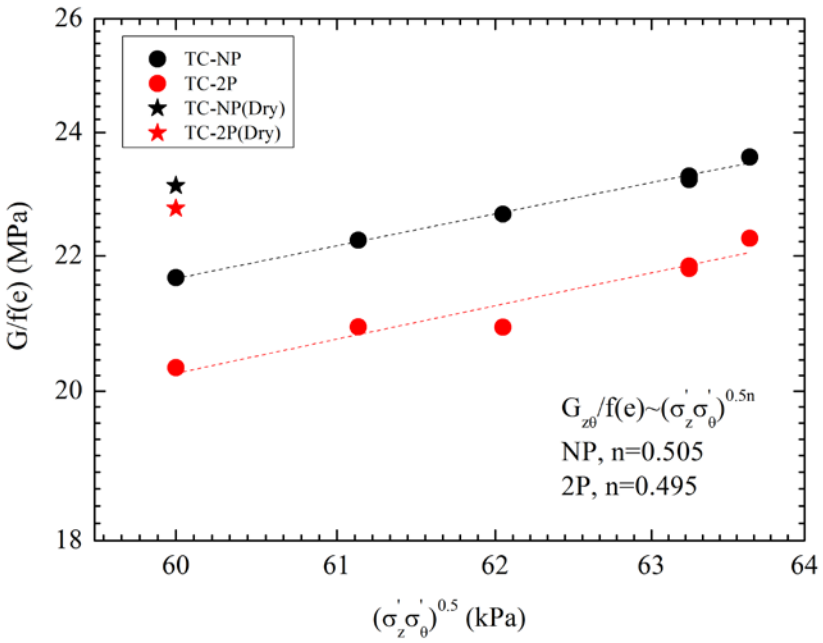

Fig. 6.3 $G/f(e)$ vs. $(\sigma_z.\sigma_\theta)^{0.5}$ for TC

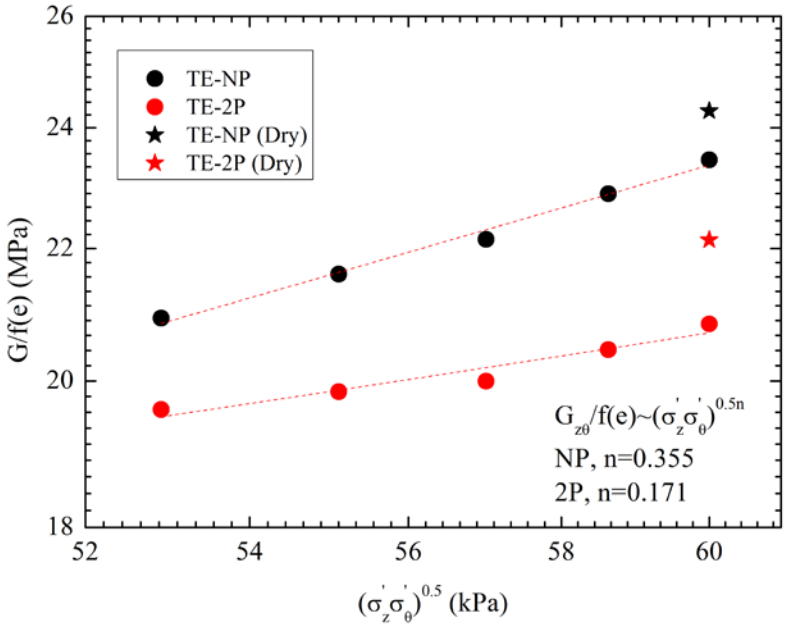

Fig. 6.4 $G/f(e)$ vs. $(\sigma_z.\sigma_\theta)^{0.5}$ for TE

Shear modulus in TS was measured under different shear stress while the normal stresses were kept constant as 60 kPa. For 2-pipe-specimen, larger degradation of G was found after the water infiltration, and during torsional shear, smaller value of G was observed. However, the variation of shear modulus along with the shear stress τ was subtle, seen in Fig. 6.5.

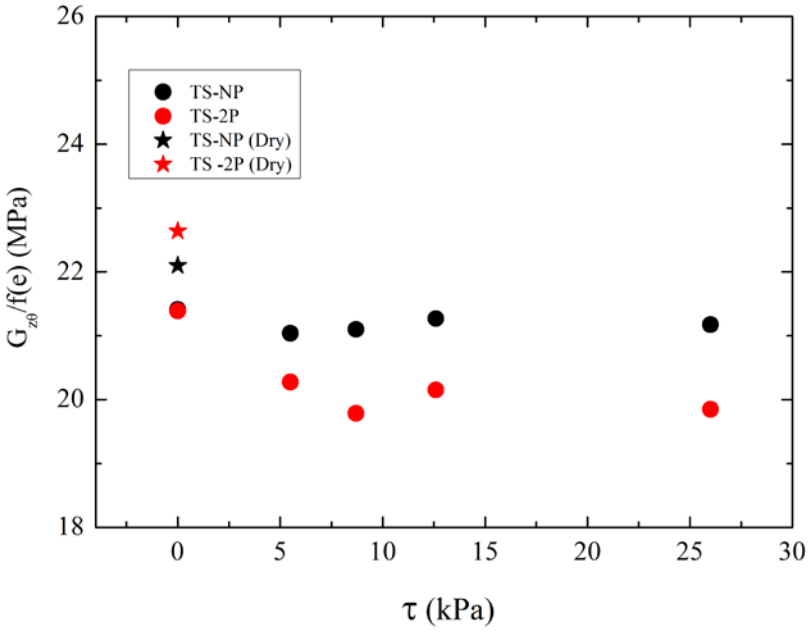

Fig. 6.5 $G/f(e)$ vs. τ for TS

6.2.1.3 Shear strength

Fig. 6.6 shows the stress-strain relationship for all the cases in this series. The normal stresses when the torsional shear started were shown in the figure as well, which was also the stress state for the last small cyclic loading. Direction of the major principal stress rotated from 0^o and 90^o to 45^o for TC and TE respectively. For TS, α was 45^o during the whole test.

Jardine et al. (1997) and Zdravkovic (2001) demonstrated that shear strength anisotropy of granular soils depends strongly on their consolidation history, especially when this involved rotation of the σ_1 axis. In this study, stress induced anisotropy could be found among the three curve of TC, TE and TS for controlled specimen. Smallest peak shear strength was observed for TE, which showed about 33% reduction compared with TC. In TC tests, the post-peak behavior exhibited a marked displacement softening, which was the same with triaxial test. However, such behavior was not observed in other cases. As discussed by Burland (1990), this was due to the non-uniform boundary in hollow cylindrical torsional

shear test. The behavior observed after shear surface formation is a consequence of interactions between the intact soil, the soil within shear bands and the apparatus.

On the other hand, piping effect could be observed between the controlled specimen and the one with internal pipes. For most cases, it could be found that the two peaks between no-pipe-specimen and 2-pipe-specimen were concurrent during the preceding of rupture. And α at the peak shear stress was around 30°~33°. Largest difference of the peak shear strength was found at TS, where 11% strength reduction occurred, while for TE, no obvious decrease in peak shear stress was noticed. This could be explained by the fact that voids caused by the piping effect were not influenced so much during the measurement of *G*, whereas for TC and TE, due to the compression and extension before torsional shear, voids might be refilled or closed. Especially for TE, piping would be blocked easily under large radial stress.

Volumetric strain observed during torsional shear is plotted in Fig. 6.7 against the shear strain. Cases of simple torsional shear were found to deform in a faster manner compared with the other four cases. Such behavior was also considered to be one reason that the residual strength for TS was larger than TC. When comparing the controlled specimen and specimen with pipes, larger volumetric strain was found in the latter.

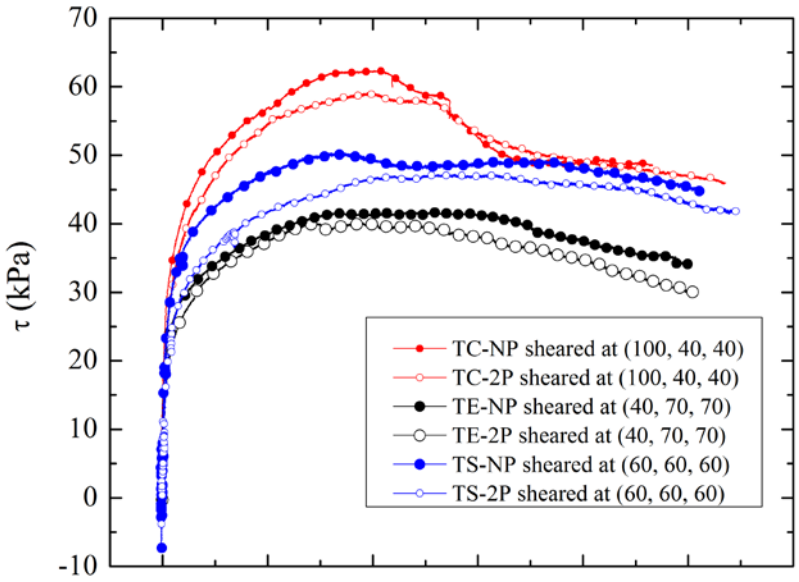

Fig. 6.6 Stress-strain relationship

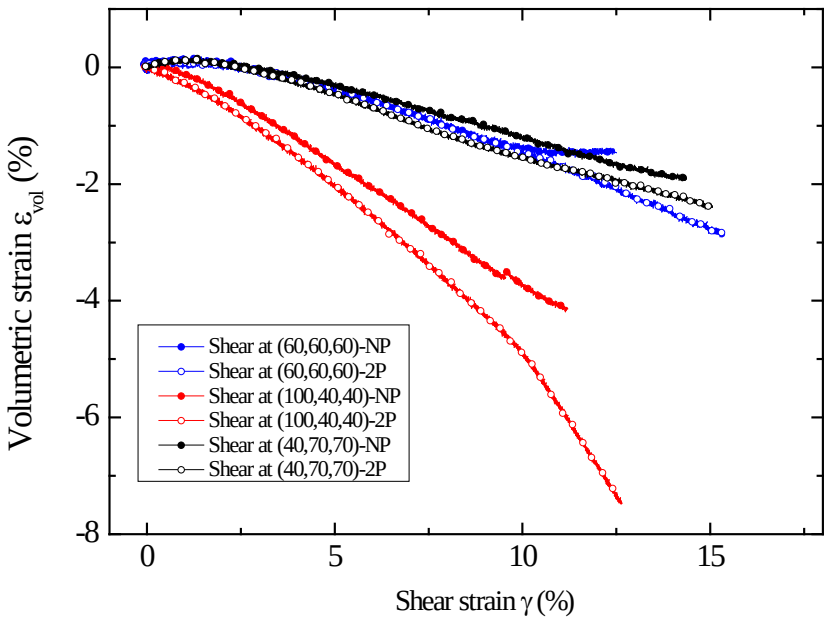

Fig. 6.7 Volumetric strain during torsional shear

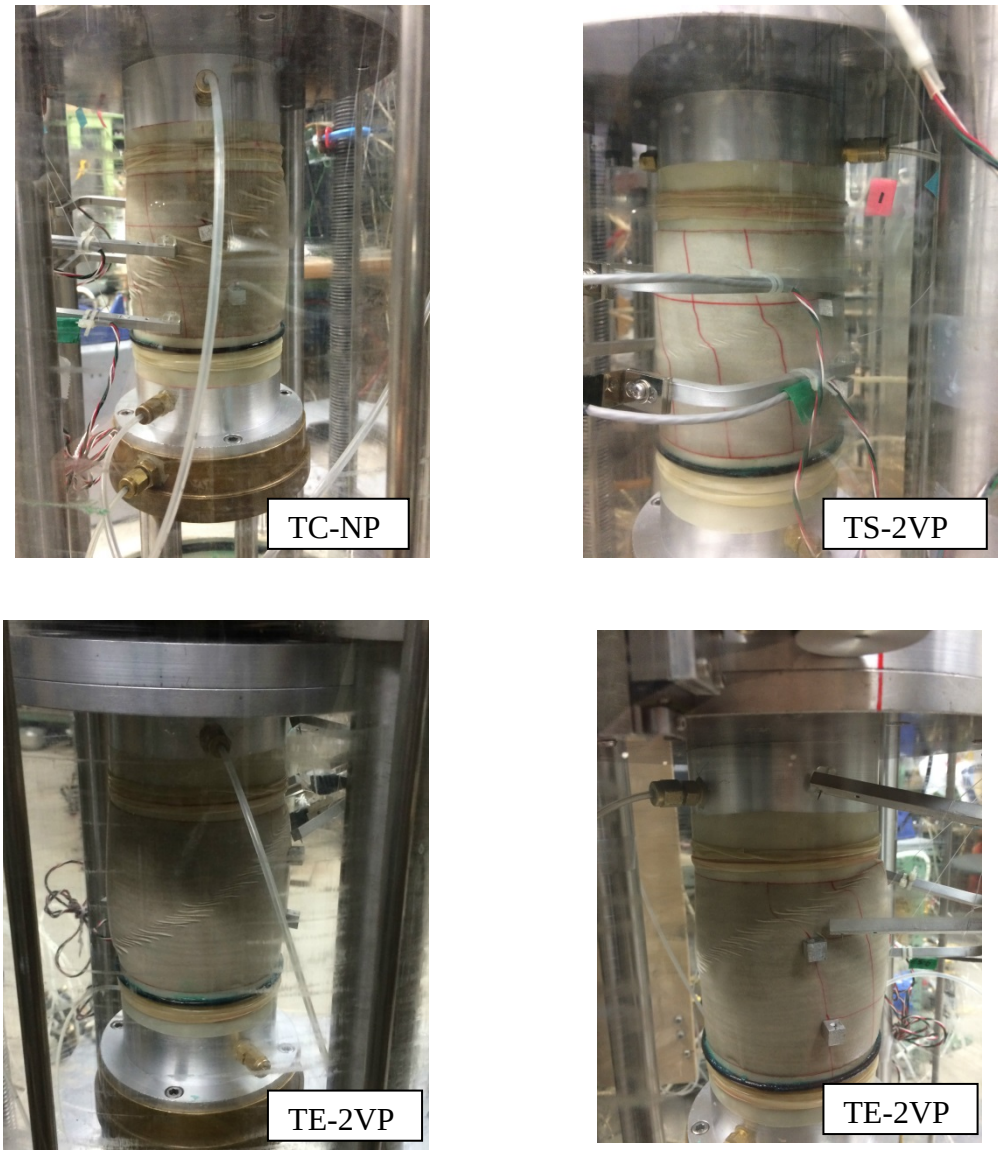

Fig. 6.8 Shear bands

Photos in Fig. 6.8 were taken after the torsional shear, from which clear shear band could be observed along the specimen. Shear strength reduction was found after the formation of shear band for TC and TE, whereas a gradual ductile behavior with the increase in shear strain was observed in TS, and the shear band was gentler. This is because the angle of σ_1 relative to vertical during the pre-peak state was larger for TS (45°) than TC and TE (33°).

Also, in the above tests only the shear band nearest to the horizontal direction was developed. This is because the resistance from the end platens tends to impede development of the steeper shear band. The other reason is that the cross anisotropic sand in this study is weaker

towards the horizontal direction, thus the development of the shear band near this direction is easier to develop. Once development is initiated, it continues in this direction and the shear band in the other direction may not be seen.

6.2.2 Rotated α during measurement of G before torsional shear

Stress path for test cases in this series was shown in Fig. 6.9. Specimen was first subjected to isotropic consolidation. After around 16 hours dissipating the creep effect, small torsional cyclic loading, with peak to peak stress amplitude of 4 kPa, was applied in order to obtain the shear modulus *G* of dry sand. The second small torsional cyclic loading was applied after 15 hours from the water infiltration to examine the variation of *G* of sand subjected to piping effect. Before τ was applied, axial stress σ_z was increased to a certain value. Again at several stable stress of τ, followed by a creep period of about 10 minutes, torsional cyclic loadings were conducted, corresponding to different α. After α reached 30°, all the specimens were monotonically sheared at a strain rate of 0.08%/min under drained conditions. Test conditions for each specimen are summarized in Table.6.2. One example of the actual stresses and strains measured during the test was shown in Fig. 6.10 (HP50).

Table 6.2 Test conditions for partially rotated σ_1.

Test ID	D_{rini} (%)	e_{ini}	Pipe number	Pipe direction	σ'_{zini} (kPa)	σ'_z (kPa)	τ_{peak} (kPa)
NP45	82.0	0.676	0	-	45	60	54.1
2VP45	79.5	0.689	2	Vertical	45	60	50.2
NP30	71.2	0.720	0	-	30	60	53.9
2VP30	74.5	0.707	2	Vertical	30	60	47.7
4VP30	75.6	0.703	4	Vertical	30	60	46.8
HP30	77.8	0.695	1	Horizontal	30	60	45.3
NP50	76.5	0.700	0	-	50	80	66.7
2VP50	80.2	0.686	2	Vertical	50	80	60.8
4VP50	77.0	0.698	4	Vertical	50	80	61.1
HP50	74.1	0.709	1	Horizontal	50	80	63.9
NP50_L	56.8	0.774	0	-	50	80	56.6
2VP50_L	58.2	0.766	2	Vertical	50	80	51.5
HP90	78.0	0.695	1	Horizontal	90	120	88.16

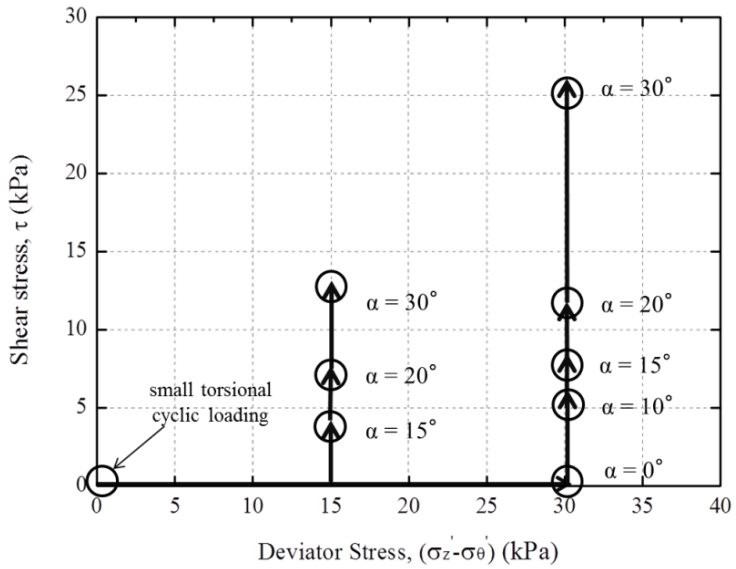

Fig. 6.9 Prescribed stress path for tests of partially rotated σ_1.

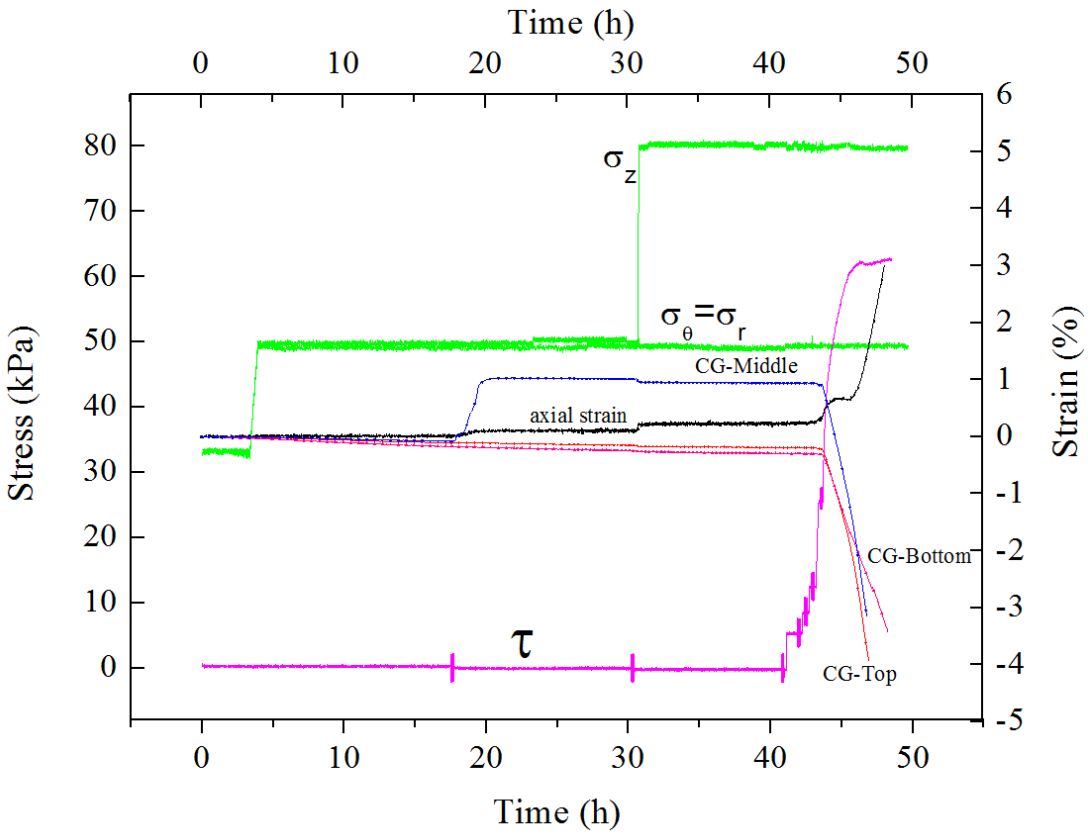

Fig. 6.10 Measured stresses and strains in HP50.

6.2.2.1 Volumetric strain before shearing

For cases NP45, 2VP45, NP30, 2VP30 and 2VP50, only two clip gauges were used due to the availability. Thus, the volumetric strain for the specimen with two vertical pipes was not accurate for the radial strain along the sand side was not recorded.

Fig. 6.11 and Fig. 6.12 show the strain variation during the isotropic consolidation and water infiltration of specimens with two vertical pipes under confining pressure of 30kPa and 50kPa respectively. Axial strain showed little change during the water infiltration for both cases, while the two clip gauges showed similar strain increments during the piping formation, which were around 0.085% for specimen under confining pressure of 30 kPa and 0.216% for the specimen under 50 kPa. It should be also noted that the volumetric strain for inner hollow decreased around 0.113% during the water infiltration for specimen under 30 kPa, indicating an expansion of the hollow, i.e. the compression of the specimen. However, such variation was not observed for specimen under 50 kPa. The reason might lie in the place where the initial glucose pipe was put in. Although the pipes were set with great care, the unexpected disturbance during removing the pipes could not be eliminated completely. Such non-uniform deformation would be caused due to the inclination or deviation of the initial pipe.

Therefore, the following analysis for vertical-pipe-specimen would focus on the cases with four pipes where three glip gauges were used, so that the deformation on both of the glucose side and sand side could be obtained. Here “VP” without indicating the internal piping number stands for 4-vertical pipe-specimen.

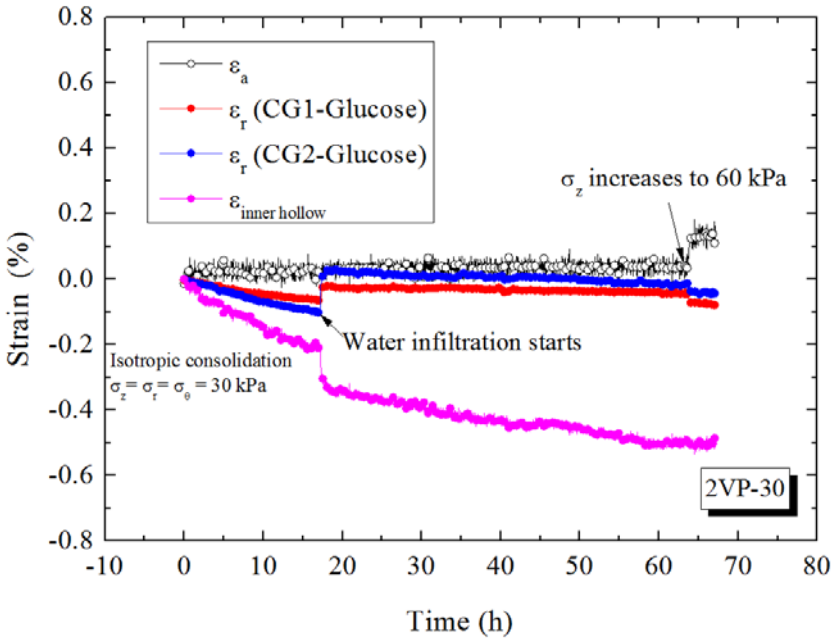

Fig. 6.11 Variation ε_a and ε_r before shearing (2VP-30)

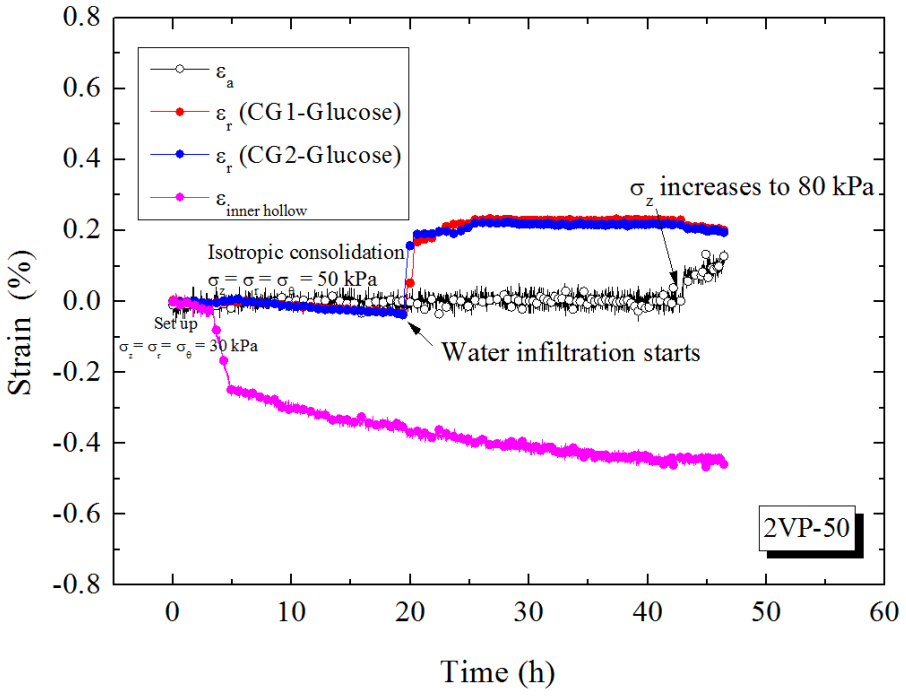

Fig. 6.12 Variation of ε_a and ε_r before shearing (2VP-50)

In order to calculate the average radial strain ε_r and circumferential strain ε_θ, two assumptions were made: i) the specimen remained right cylinder for the inner hollow, and ii) the sand influenced by piping effect is 1/4 of the total volume for 4 vertical-pipe-specimen and 1/5 for horizontal-pipe-specimen. Fig. 6.13 and Fig. 6.14 showed the radial strain variation before shearing for HP50 and VP50. For all of three clip gauges, similar strain increments during isotropic stress increased from 30kPa to 50kPa was observed, which were around 0.254% for vertical-pipe-specimen and 0.279% for horizontal-pipe-specimen. Another obvious increment was found when water started to be filled in. For specimen with 4 vertical pipes, where three clip gauges were attached near the glucose, similar shrinkage along the height of specimen appeared (Fig. 6.13). On the other hand, for specimen with horizontal pipe at the mid-height where clip gauge 3 was fixed on, large non-uniform deformation was observed (Fig. 6.14).

Volumetric strain variation among test cases for confining pressure of 30 kPa and 50 kPa are shown in Fig. 6.15 and Fig. 6.16. It should be noted that the volume proportion of glucose to the total specimen is about 1.27 % for four vertical glucose pipes and 1.17 % for horizontal glucose pipe. During water infiltration, slightly larger volumetric strain increments were observed for specimen under lower confining pressure (30 kPa) in comparison with those under larger confining pressure (50 kPa). When comparing the data with the initial glucose volume, it could be inferred that piping was successfully generated in sand, in other words, voids more than 60% of the original volume of glucose were left in the specimen. Still, it should be noticed that some compression was induced due to the increasing of σ_z before shear stress was applied.

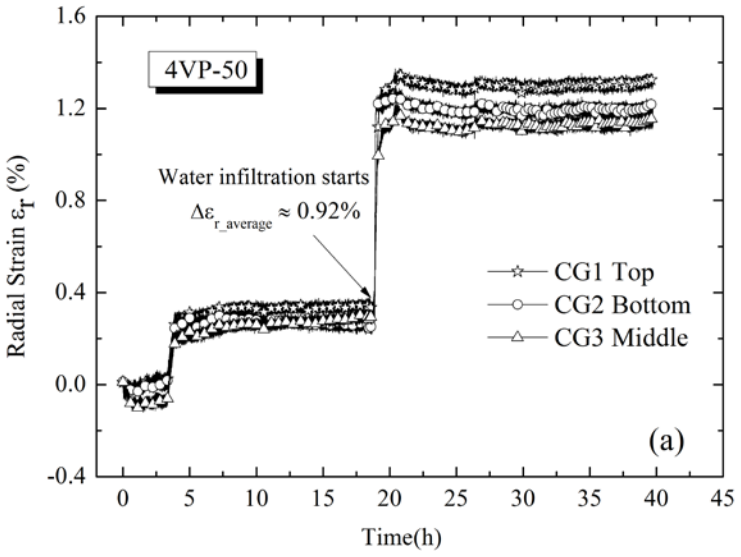

Fig. 6.13 Variation of ε_r by 3 CGs before shearing (4VP-50)

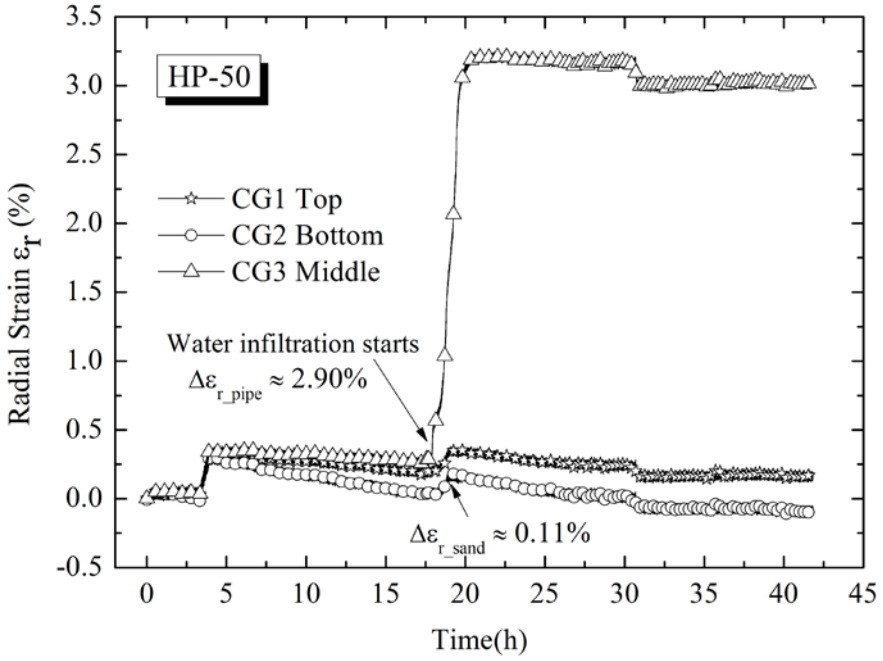

Fig. 6.14 Variation of ε_r by 3 CGs before shearing (HP-50)

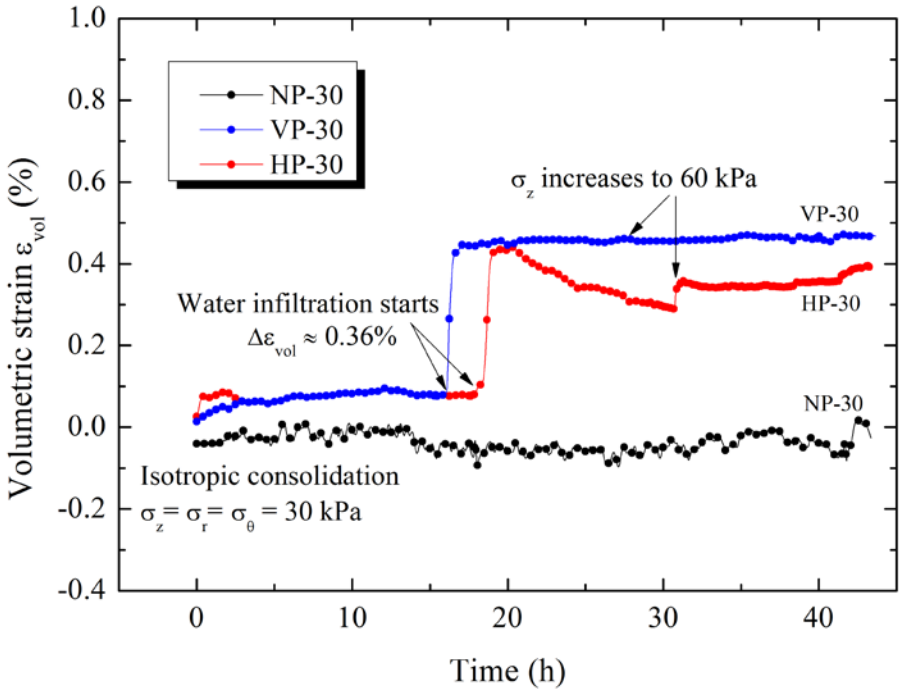

Fig. 6.15 Variation of ε_{vol} before shearing (confining pressure = 30 kPa)

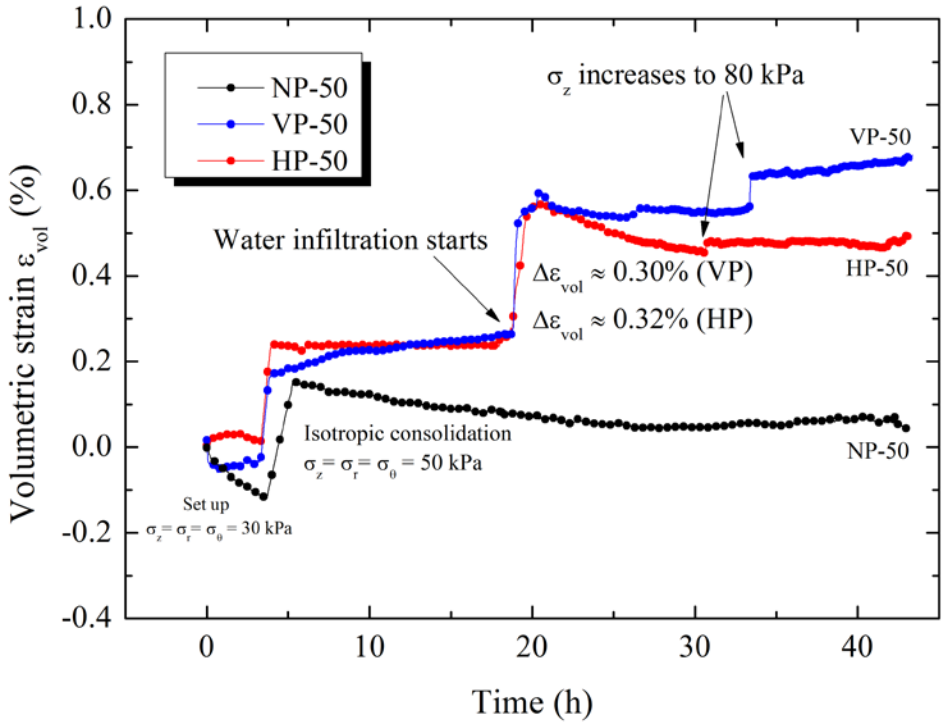

Fig. 6.16 Variation of ε_{vol} before shearing (confining pressure = 50 kPa)

Fig. 6.17 showed the volumetric strain variation of specimens with lower density under the confining pressure of 50 kPa. Increment ε_{vol} during water infiltration was around 0.59% for 2VP_L, which was larger than the case of denser specimen under the same confining pressure.

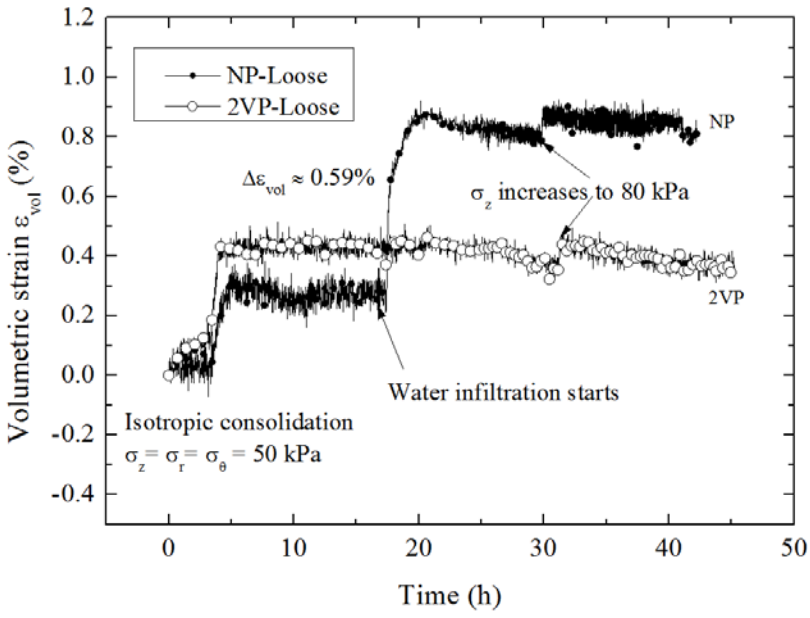

Fig. 6.17 Variation of ε_{vol} before shearing (D_r = 55%)

6.2.2.2 Shear modulus variation under α rotated from 0° to 30°

Shear modulus $G_{z\theta}$ measured by gap sensors were normalized by void ratio function f(e) = $(2.17 - e)^2/(1+e)$. Fig. 6.18 and Fig. 6.19 show the $G/f(e)$ values during the isotropic consolidation, after piping formation, increase of axial stress σ_z, and the rotation of major principal stress σ_1.

It should be noted that the stresses were not uniform across the wall of hollow cylinder specimen. However, such non-uniformity was not considered in this study for the fact that the specimen itself was not homogenous and disturbed due to the existence of piping effect. In addition, the influence of intermediate principal stress parameter *b*, which changes simultaneously with α ($b = \sin^2\alpha$) due to the same inner and outer cell pressure, is not discussed in this paper.

Decrease of *G* was found for all cases after the water infiltration, where larger reduction occurred for specimens subjected to piping effect. Increment of *G* was observed after σ_z increased, from which $(\sigma_z \cdot \sigma_\theta)^{0.5n}$ (Nguyen, H. and Koseki, J., 2005) was considered to be the factor influencing the growth.

Since the test cases in which deviator stress was kept 30 kPa, the same value of α could be achieved under the same value of τ during shearing. Therefore, the effect of principal stress rotation could be clearly identified (Fig. 6.20 and Fig. 6.21). A general degradation of *G* was observed for most the specimens. A Larger reduction appeared when α reached 30°.

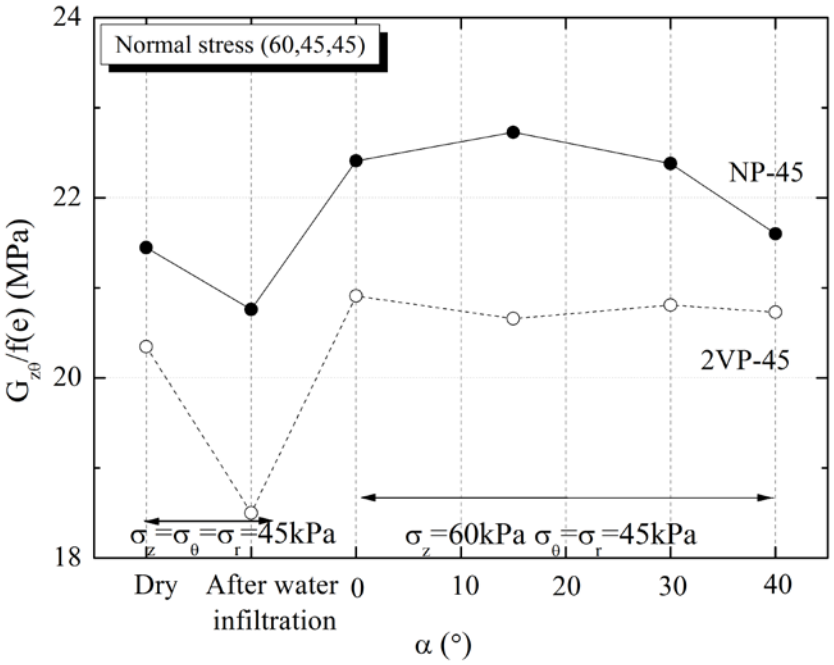

Fig. 6.18 *G* variation for NP-45 and 2VP-45

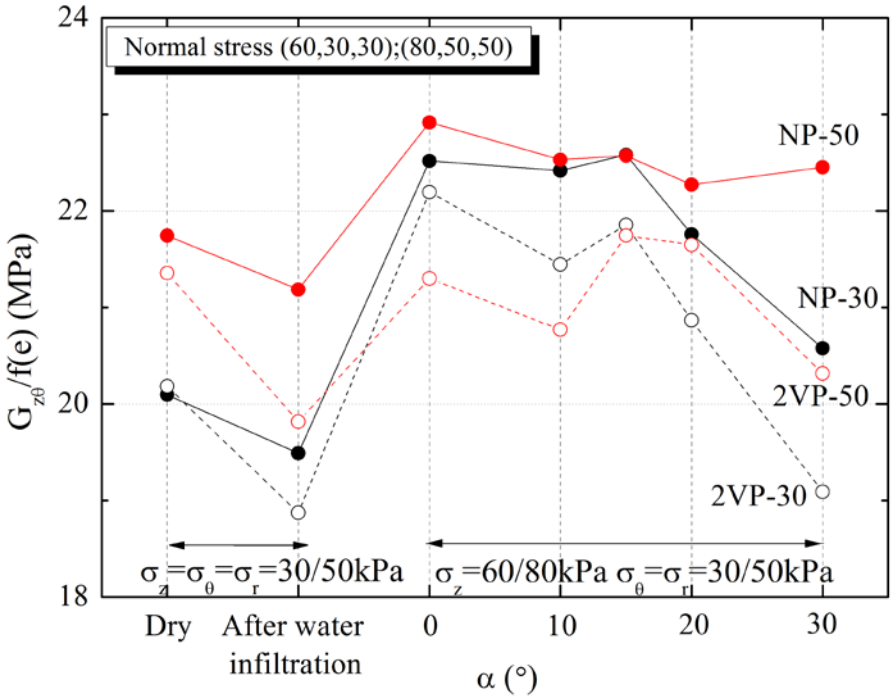

Fig. 6.19 *G* variation for NP and 2VP under different initial confining pressures

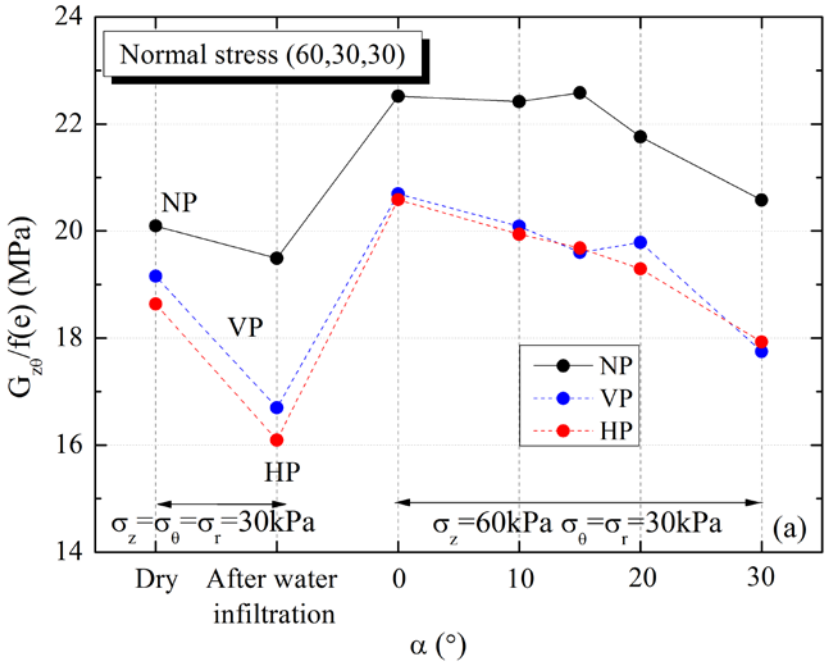

Fig. 6.20 *G* variation for tests under initial confining pressure of 30 kPa

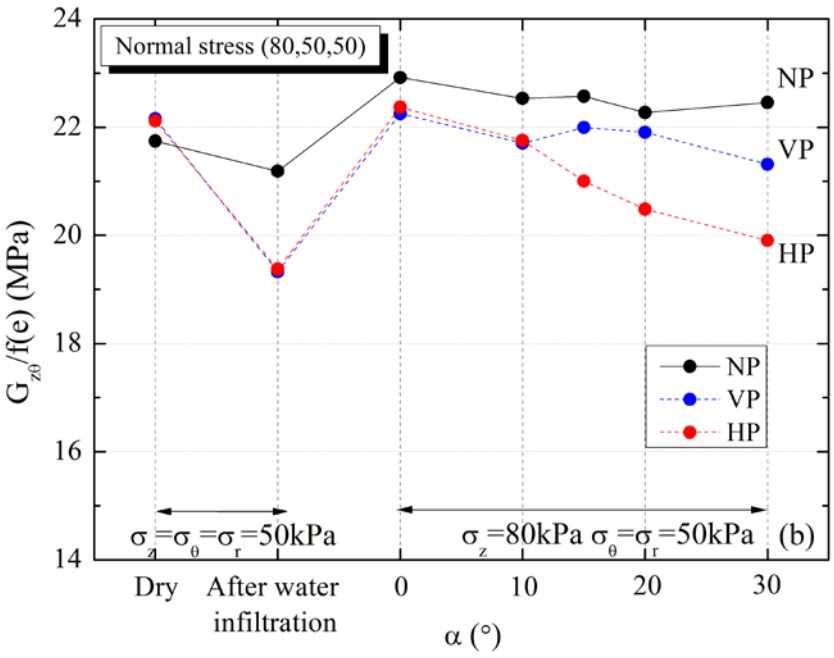

Fig. 6.21 *G* variation for tests under initial confining pressure of 50 kP

When plotting the reduction rate of G_1 relative to the G_0 at initial dry state (Fig. 6.22), rather similar value of reduction ratio was found for specimens with the same glucose volume, indicating that such degradation of *G* might be independent of pipe direction.

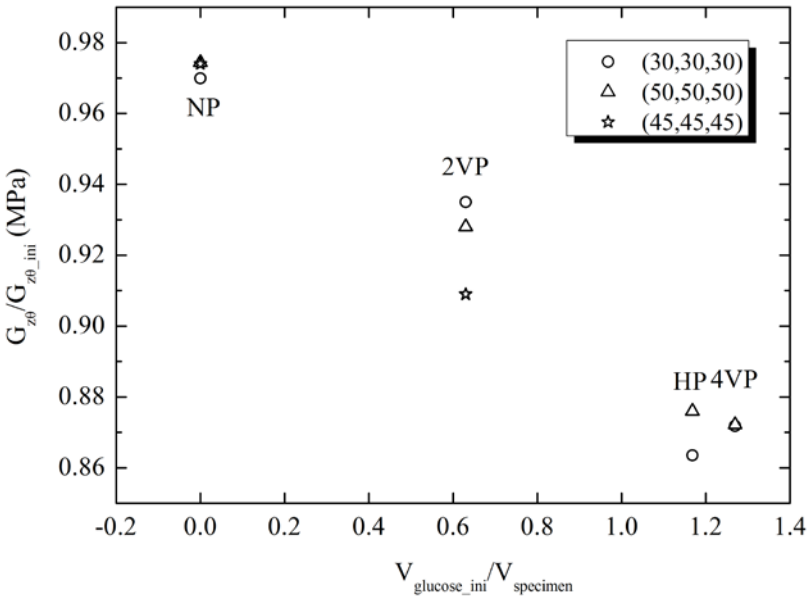

Fig. 6.22 Reduction of shear modulus against initial glucose volume proportion

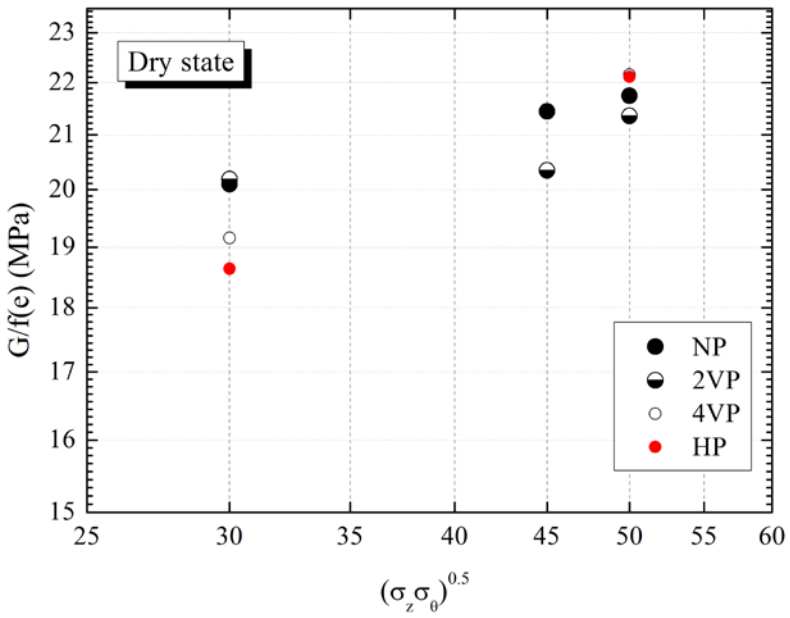

Fig. 6.23 $G/f(e)$ vs. $(\sigma_z \cdot \sigma_\theta)^{0.5}$ at initial dry state

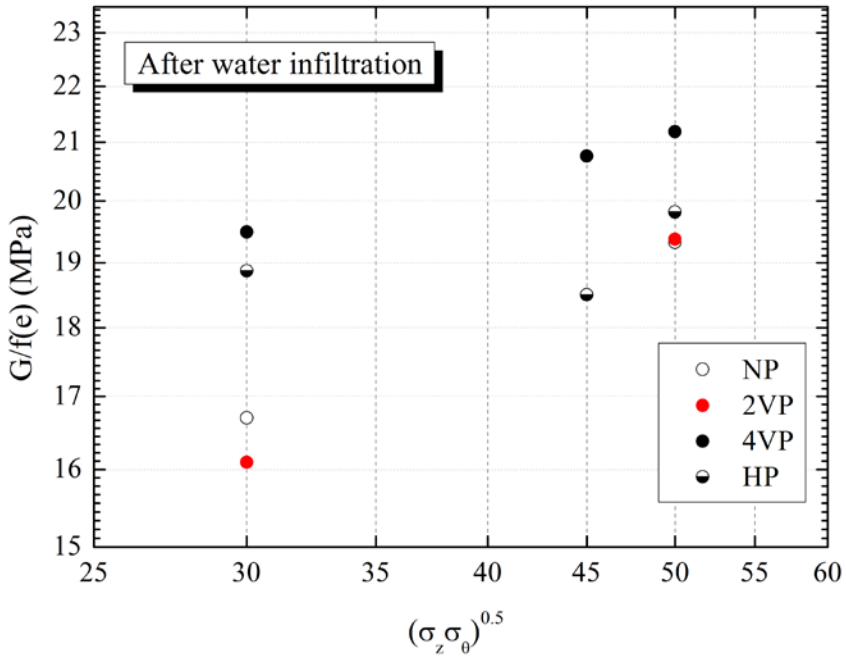

Fig. 6.24 $G/f(e)$ vs. $(\sigma_z \cdot \sigma_\theta)^{0.5}$ after water infiltration

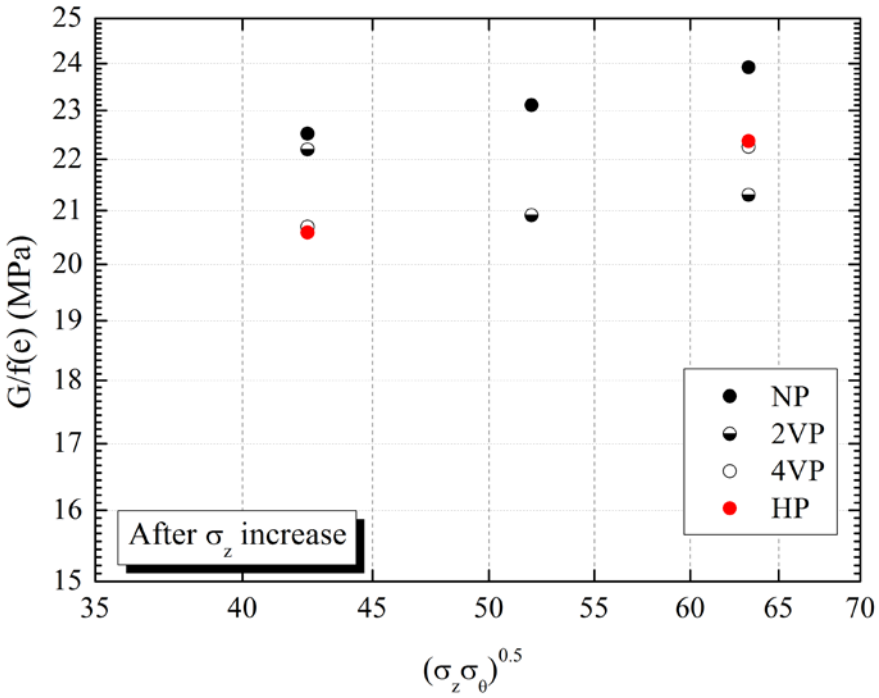

Fig. 6.25 $G/f(e)$ vs. $(\sigma_z \cdot \sigma_\theta)^{0.5}$ after σ_z increase

Fig. 6.23 to Fig. 6.25 show the relationship between the normalized shear modulus and $(\sigma_{z*}\sigma_{\theta})^{0.5}$ before the rotation of σ_1. It is noticed that at the initial state, G was rather close among each case, and the dependency on $(\sigma_{z*}\sigma_{\theta})^{0.5}$ was clear.

After the formation of piping, reduction of G was found in different extent, as piping effect was influenced by the effective confining pressure. In all the three figures, *G* in cases of 4VP and HP were found to be close to each other, indicating that voids left inside the specimen, which related with piping effect, should also be considered as the influencing factor of shear modulus.

Rotation of α stopped at 30° in this series for the measurement of *G*, and thus it is difficult to draw clear conclusion. In the next section, another series of tests in which a fully rotation of σ_1 was conducted to obtain a better understanding of the role of α, which would be introduced.

Another test with horizontal pipe was conducted following the stress path shown in Fig. 6.26. Confining pressure was increased to 90 kPs for this case so as to achieve larger value of α under the reasonable φ value without causing unrecoverable plastic deformation to the specimen.

During the increasing of shear stress under constant of normal stresses, degradation was observed in G (**Error! Reference source not found.**), which showed similar tendency as previous tests. After τ reached 26 kPa, rotation of σ_1 was achieved by decreasing the deviator stress (σ_z-σ_θ). During this process, larger reduction of G. However, such reduction could not be attributed to the larger α only, for the variation in the normal stresses also played an important role.

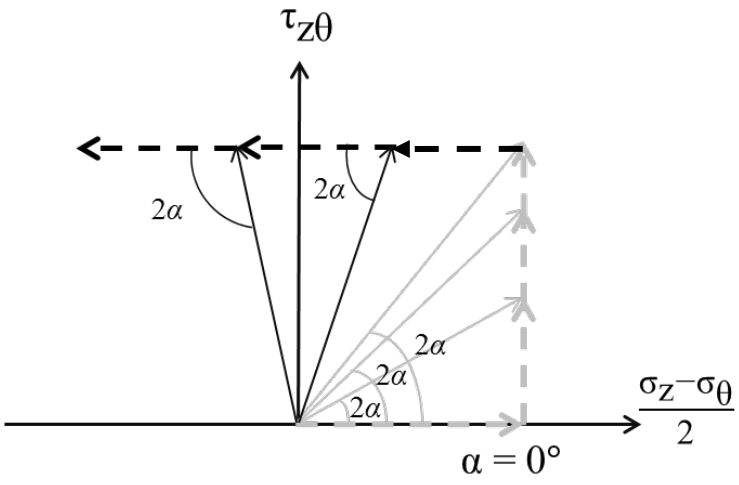

Fig. 6.26 Stress path for HP90

Table 6.3 Test conditions.

Step	σ_z (kPa)	σ_r (kPa)	σ_θ (kPa)	τ (kPa)	α (°)	φ_{mob} (°)
1	90	90	90	0	0	0
2	90	90	90	0	0	0
3	120	90	90	0	0	8.2
4	120	90	90	8.7	15	9.5
5	120	90	90	12.6	20	10.8
6	120	90	90	26	30	16.6
7	106	97	97	26	40	15.1
8	94	103	103	26	50	15.5
9	80	110	110	26	60	18.4

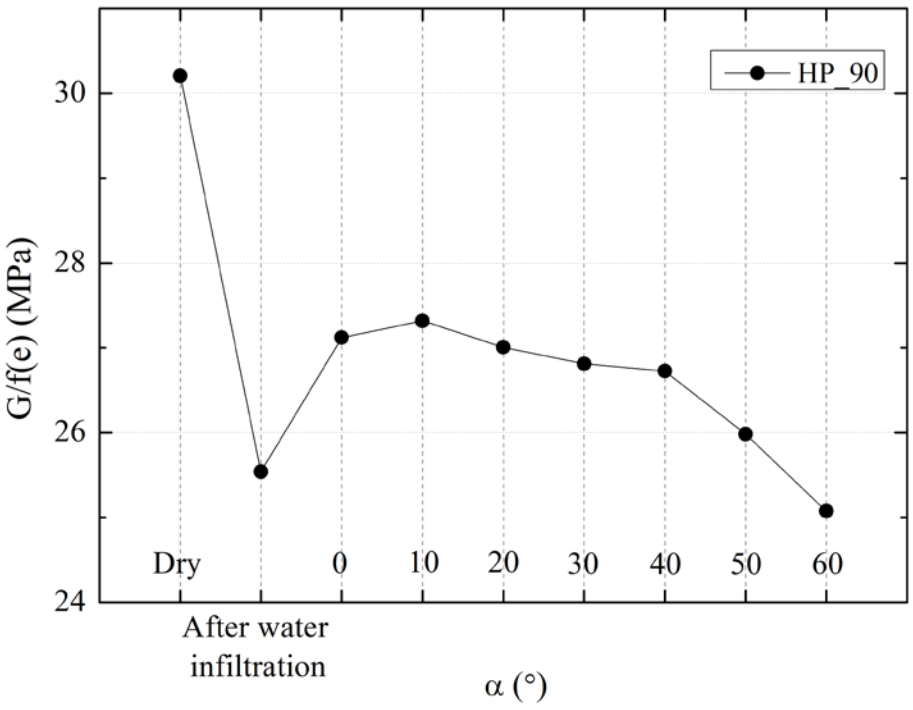

Fig. 6.27 G variation in HP90

6.2.2.3 Shear strength

Followed by the last small torsional cyclic loading, monotonic shear was conducted at a strain rate of 0.08%/min under drained conditions, while the normal stresses were kept constant. Shear strain was obtained from the average results of two potentiometers.

As shown in Fig. 6.28, for the loose specimens, different shear modes were exhibited as compared with the specimens with larger density in Fig. 6.29. Fig. 6.29 and Fig. 6.30 shows the relationship between shear strain and stress as well as major principal stress angle. Reduction of peak shear strength could be found for sand subjected to piping effect. For all the specimens, the major part of principal stress rotation took place at the very early stage of shearing where γ was less than 1%, and residual state was reached at shear strain about 15%. σ_1 direction at the peak state was in the range of 35°~40° from vertical, and this value was slightly smaller for specimen with pipe.

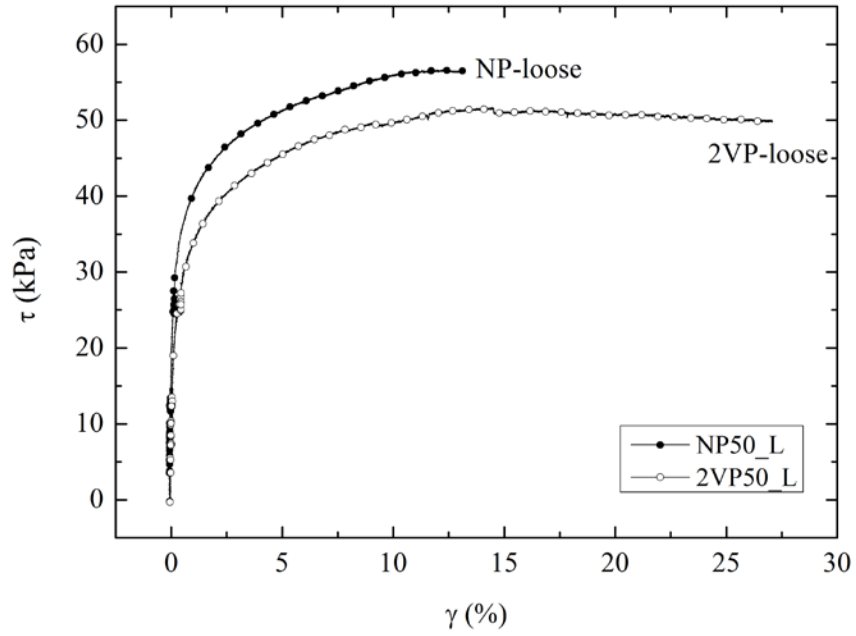

Fig. 6.28 Shear stress-strain relationship for loose cases

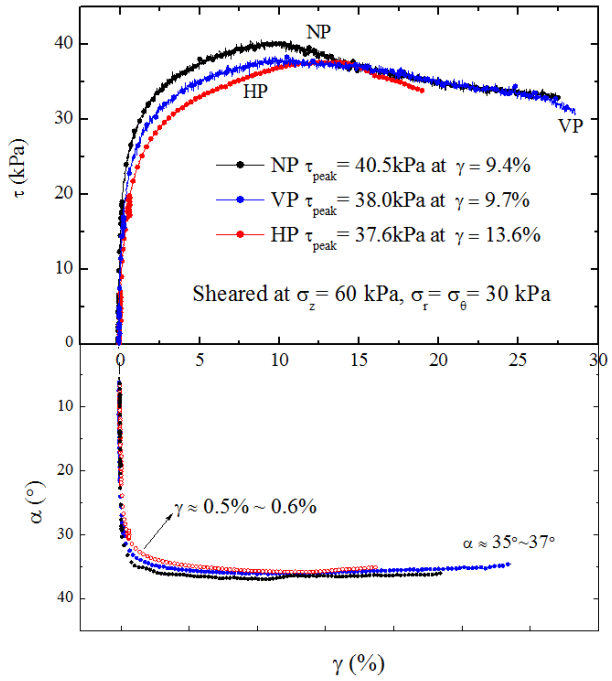

Fig. 6.29 Relationship among τ, γ and α during shearing (60, 30, 30)

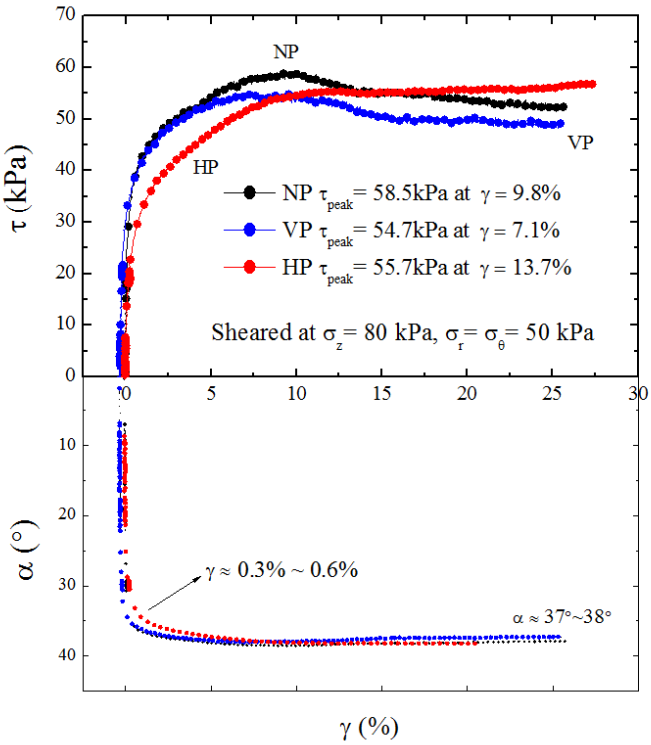

Fig. 6.30 Relationship among τ, γ and α during shearing (80, 50, 50)

Generally, shear bands appear at intermediate directions between zero-extension direction and maximum stress ratio plane. The peak mobilized angle of internal friction φ_{peak} for the Toyoura sand in this research was confirmed to be around 40^{o} from the previous triaxial compression tests conducted under similar density (Yang,Y., Kuwano, R. 2014). Therefore, the direction of shear band θ was expected to be 50°~65° relative to the direction of σ_3 (Fig. 6.31). Due to the restriction of the rigid top and bottom pedestals, only a single shear band was developed freely. However, for horizontal-pipe-specimen, where the bedding plane of air-pluviated Toyoura sand coincided with piping direction, shear band which partially developing along the pipe was observed.

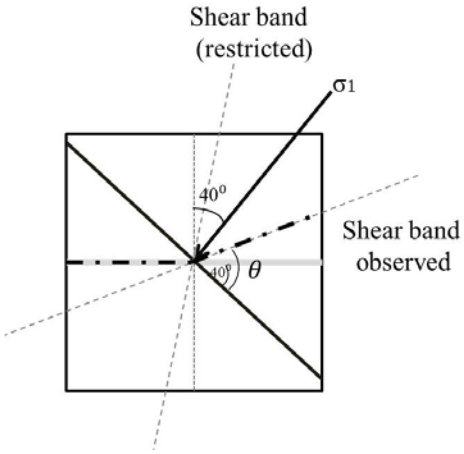

Fig. 6.31 Sketch of shear band.

Fig. 6.32 shows the shear band in specimen with horizontal pipe (50HP) from the backside and front side. The angle between pipe plane (horizontal) and shear band was measured to be around 25°, which coincides with the previous analysis.

Fig. 6.32 Shear band in specimen with horizontal pipe

6.3 Small cyclic loading test during full rotation of σ_1

Tests in this series were designed to investigate the anisotropy in small strain stiffness *G* depending on the major effective principal stress direction α. Specimens with internal pipes both in vertical and horizontal direction were tested. Therefore, piping effect on shear modulus variation could also be obtained.

Specimens were first allowed to creep for around 12 hours to be stabilized under isotropic consolidation of 80 kPa, which was increased from 30 kPa after setting up the specimen. After 11 small cyclic loadings with stress amplitude of 3 kPa with the purpose of measuring the shear modulus *G*, 1300 ml of de-aired water was infiltrated from the bottom pedestal and drainage was allowed from the top cap. Then, the specimen was sent to another creep state under drained condition for 10 hours, followed by the second small cyclic loadings. Before the rotation of α, σ_z was increased and σ_r (equal to σ_θ) was decreased while p' was kept constant as 80 kPa. During this process, several cyclic loadings were conducted to obtain *G*. After that, with the separate control of σ_z, σ_r and τ, direction of major principal stress was changed continuously and halted temporarily for about 15 minutes at certain state for the small torsional cyclic loading.

Two different φ values were tested in this study, and the stress levels corresponding to different α were shown in the dots in Fig. 6.33.

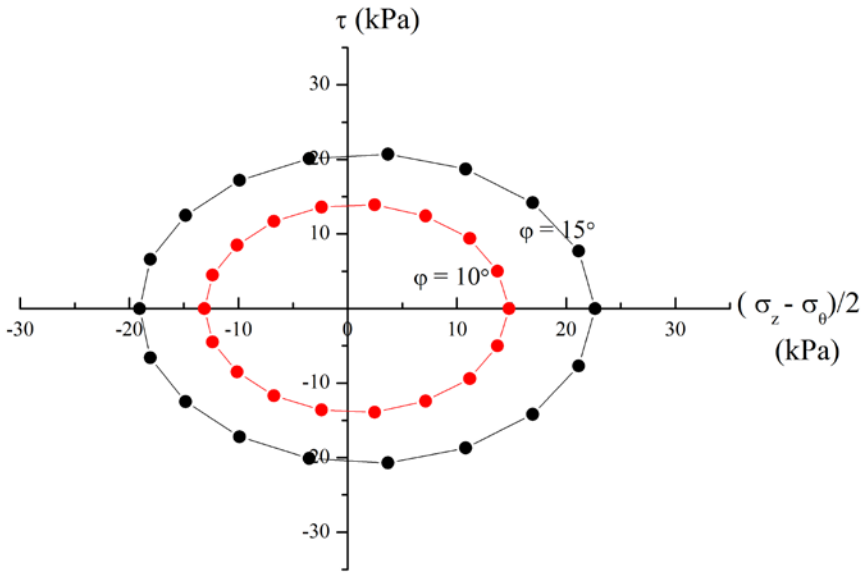

Fig. 6.33 Prescribed stress path for small torsional cyclic loadings.

Fig. 6.34 shows an example of the stress path measured in the test of specimen under $\varphi = 15^{\circ}$ after water infiltration and before shear.

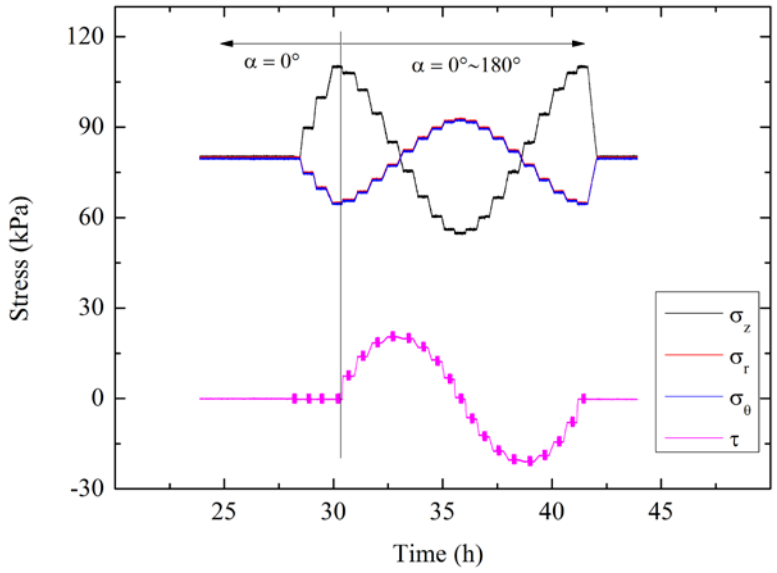

Fig. 6.34 Measured stress path during fully rotation of α

According to the above figure, stress path was plotted in the τ - (σ_z- σ_r)/2 coordinate axis, as is shown in the black line in Fig. 6.35. The red dots represent the predetermined values of normal stresses and shear stress, which coincide with the actual stress in the experiment.

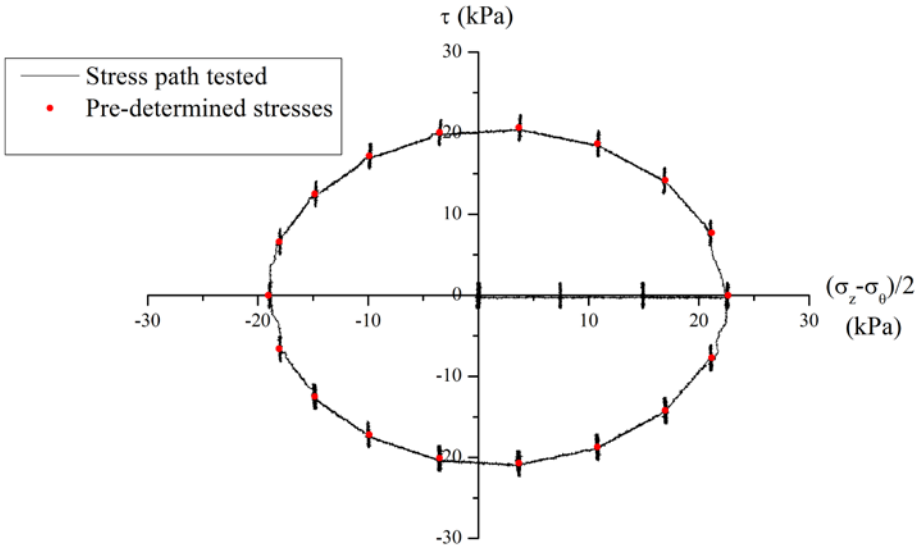

Fig. 6.35 Measured cyclic loadings

Test cases in this series are shown in Table. 6.4.

Table 6.4 Test conditions of fully rotation of σ1

Test cases	Void ratio (e)	Pipe No.	Pipe direction	p' (kPa)	φ (°)	α
NP15	0.713	0	-	80	15	0^o~180^o
HP15	0.707	1	horizontal	80	10	0^o~180^o
VP15	0.691	4	vertical	80	10	0^o~180^o
HP15	0.720	1	horizontal	80	15	0^o~180^o
VP15	0.694	4	vertical	80	15	0^o~180^o

The following discussion will focus on these aspects: 1) volumetric strain variation during water infiltration and rotation of α; 2) shear modulus reduction due to piping generation; 3) shear modulus variation during rotation of α.

6.3.1 Volumetric strain variation during water infiltration and rotation of α

Fig. 6.36 shows the arrangement of clip gauges of local deformation measurement. Fig. 6.37 ~ Fig. 6.41 show the variation of radial strain and axial strain calculated based on the data from CGs and EDT before shearing. The increment of each strain is presented in Table. 6.5.

For specimen with horizontal pipe, the proportion of glucose was around 1.17%. For specimen with vertical pipe, unlike the previous test cases, larger plastic straw with the diameter of 6 cm was used, and the glucose proportion was about 3.20%. The arrangement of CGs was also changed in order to obtain the radial strain in a more accurate way, as is shown in Fig. 6.36. It could be seen that during the creep state under the isotropic consolidation of 30 kPa, larger compression happened in the specimen with vertical pipes due to the existence of four pipes, mainly in the radial direction. Also, more obvious increment of volumetric strain was observed for vertical-pipe-specimen during the growth of p from 30 kPa to 80 kPa.

In the period of water infiltration, there was little change of the axial strain for specimens with vertical pipe, indicating that piping primarily spread in the horizontal direction. While for horizontal-pipe-specimen, loosening spread in both horizontal and vertical direction. The

average volumetric strain variation for the two cases of specimen with horizontal pipe was around 0.46%, and 1.56% for vertical-pipe-specimen (Fig. 6.42). Considering the initial glucose volume, it could be inferred that the less than 50% of the volume occupied by glucose was compressed and loosening effect seemed to be generated in a more complete way in vertical-pipe-specimen.

Compared with triaxial experiments, in which larger compression occurred in the lower part of specimen, torsional shear specimen showed more uniform deformation and the difference between sensors except for those attached near glucose was small.

During the rotation of major principal stress, cyclic variation of strains was also observed, which would be discussed later in the analysis of shear modulus.

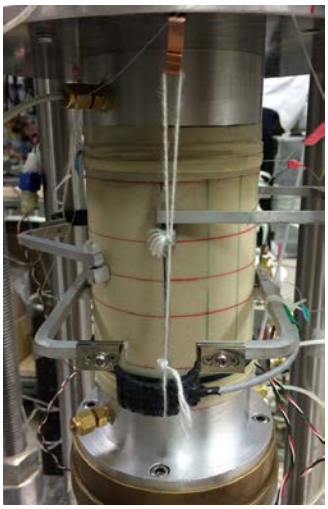

Fig. 6.36 Arrangement of Clip Gauges

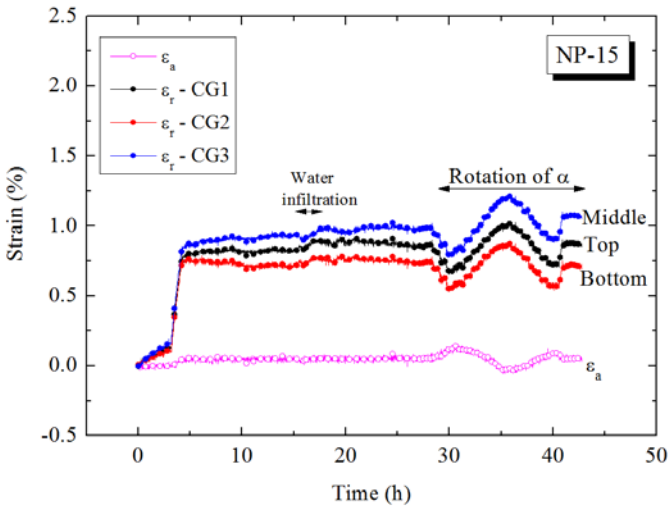

Fig. 6.37 Variation of ε_a and ε_r before shearing (NP-15)

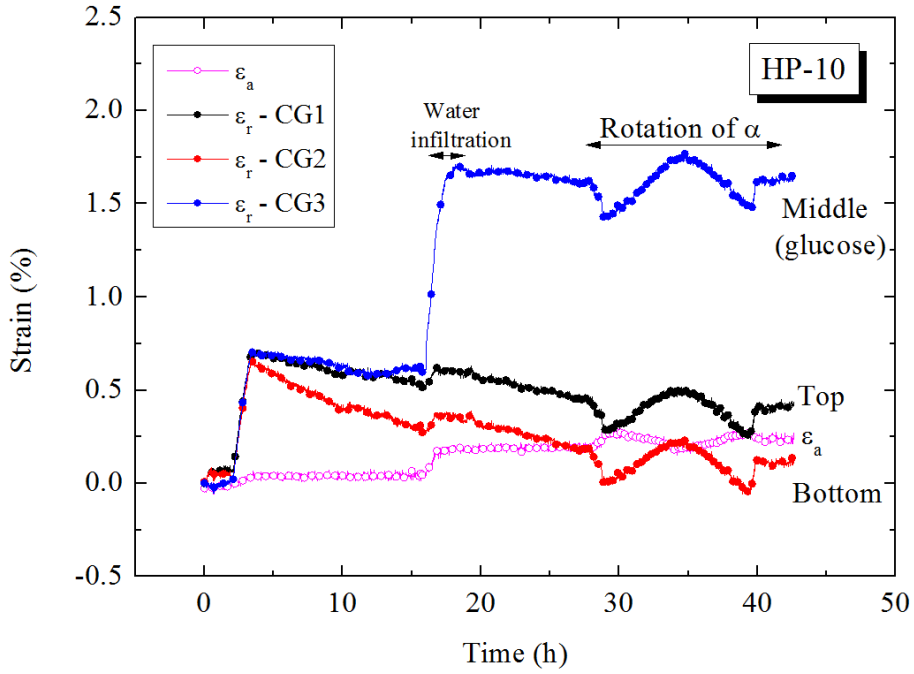

Fig. 6.38 Variation of ε_a and ε_r before shearing (HP-10)

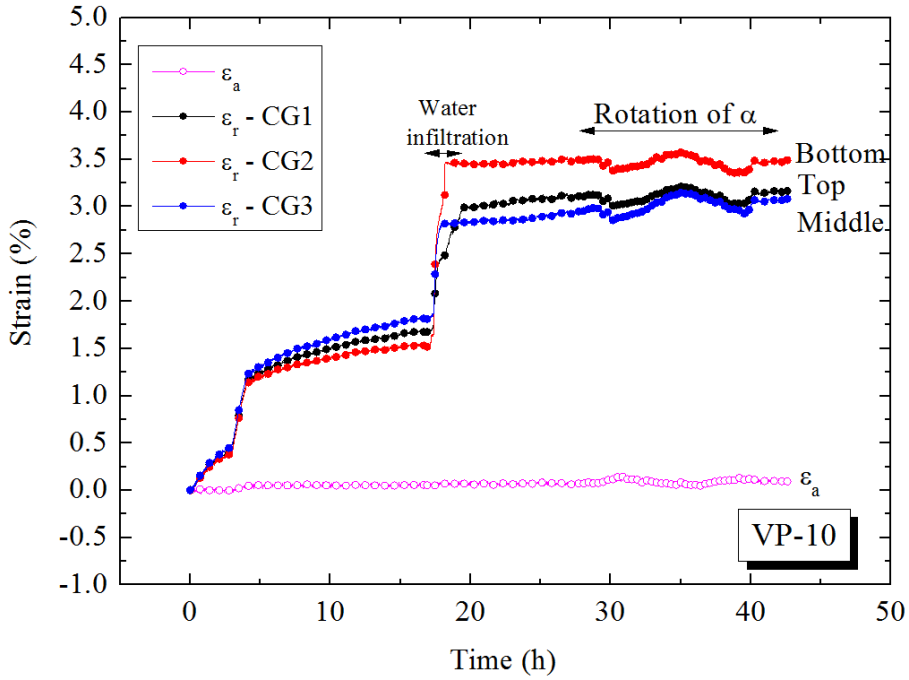

Fig. 6.39 Variation of ε_a and ε_r before shearing (VP-10)

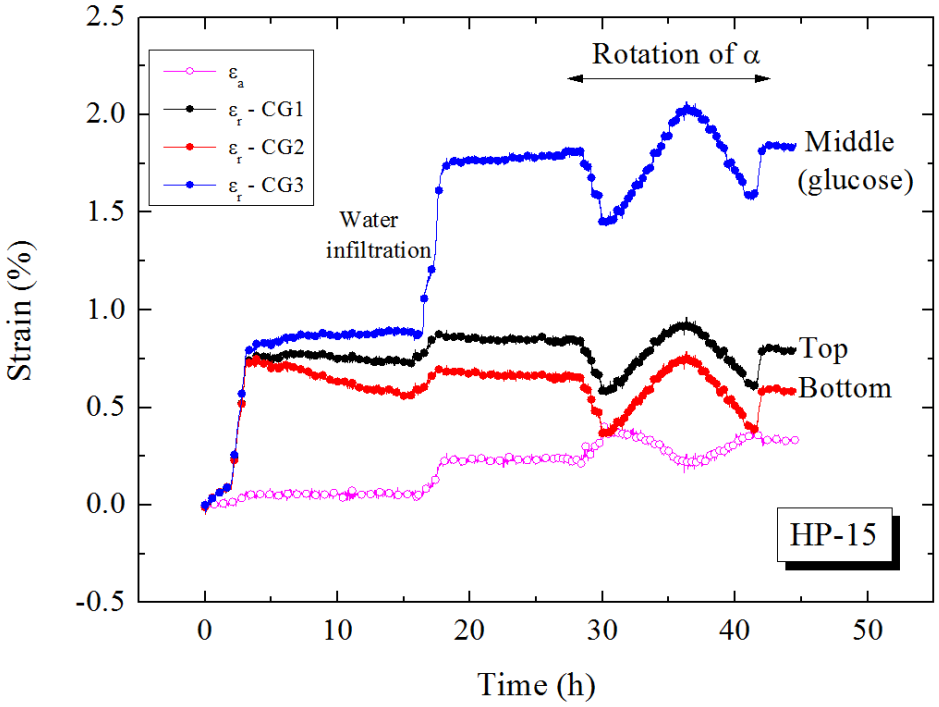

Fig. 6.40 Variation of ε_a and ε_r before shearing (HP-15)

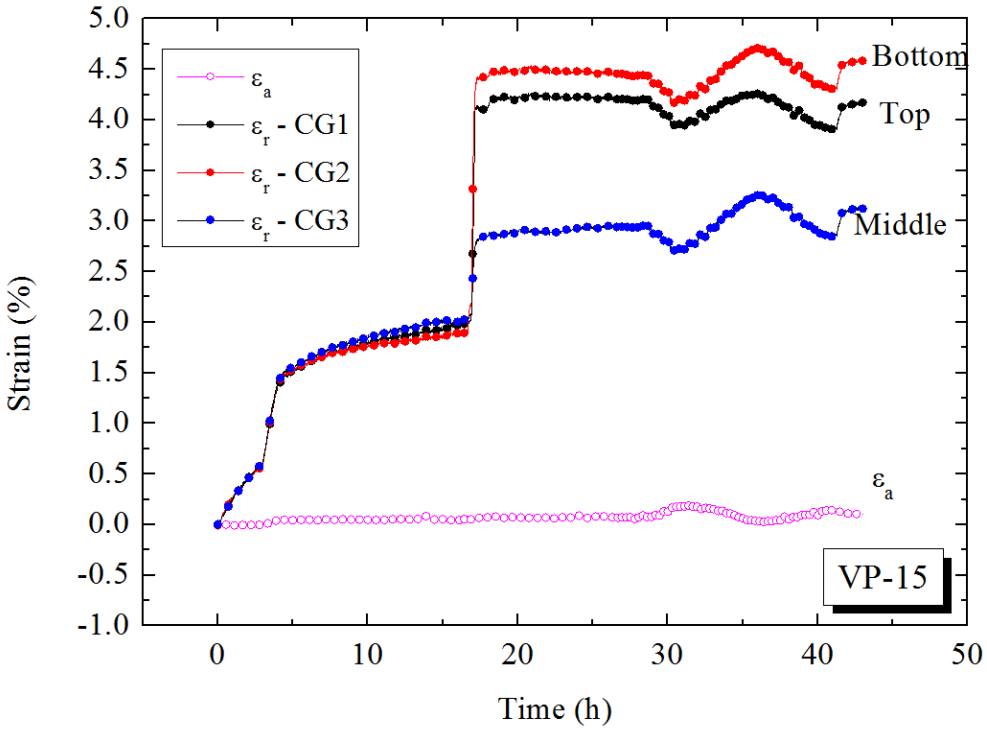

Fig. 6.41 Variation of ε_a and ε_r before shearing (VP-15)

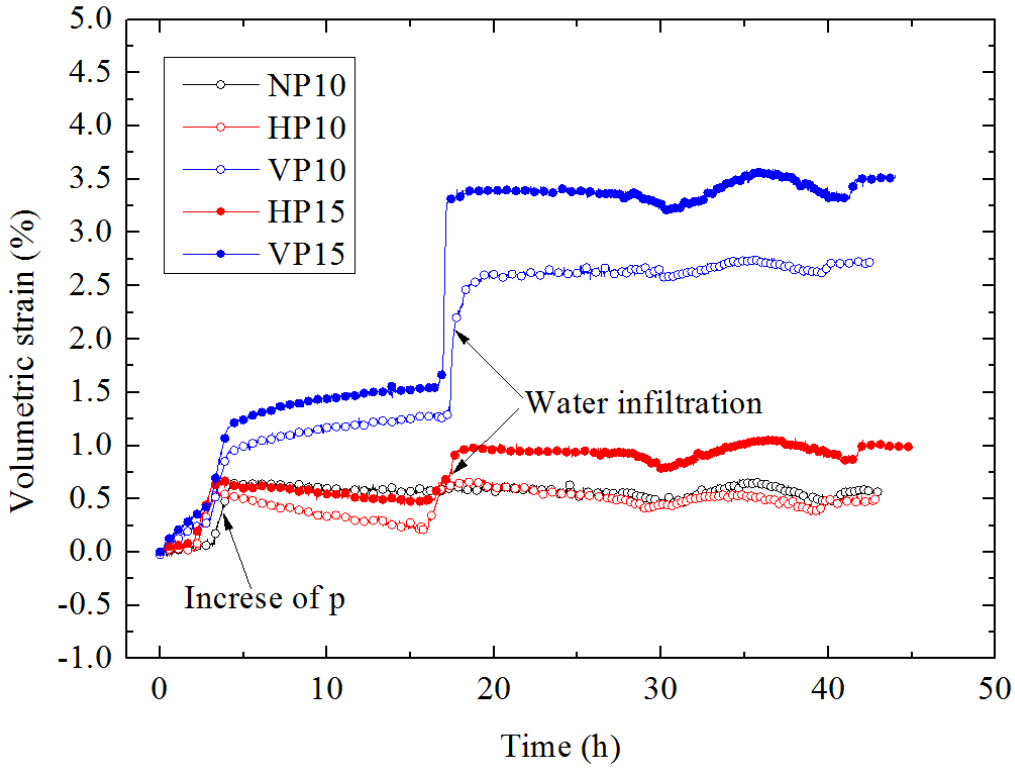

Fig. 6.42 Variation of ε_{vol} before shearing

Table 6.5 Test conditions of isotropic consolidation test

Test cases	ε_{vol} during increase of p (%)	ε_{vol} during water infiltration (%)	Voids proportion (%)
NP15	0.578	0.026	0.578
HP10	0.529	0.440	0.529
VP10	0.656	1.341	0.656
HP15	0.556	0.483	0.556
VP15	0.771	1.779	0.771

6.3.2 Shear modulus reduction due to piping generation

For all the five tests in this series, normal stresses were kept as 80 kPa before and during the piping generation. Shear modulus at the dry state and after the water infiltration could be compared and the reduction ratio due to piping effect could be obtained.

Shear modulus $G_{z\theta}$ measured by gap sensors were normalized by void ratio function $f(e) = (2.17 - e)^2/(1+e)$ (Hardin and Richart, 1963) in order to eliminate the effect of void ratios among different specimens. Fig. 6.43 shows the $G/f(e)$ values during the isotropic consolidation (G_0) and after piping formation (G_1) for each test case.

From Fig. 6.43 it could be found that larger reduction of shear modulus occurred in specimen with glucose pipe compared with controlled specimen. For cases HP10 and HP15, similar reduction of G was observed, while for cases VP10 and VP15, the difference was large. It could be explained by the results of the volumetric strain during the water infiltration in the previous interpretation. Even with same volume of initial glucose under same confining pressure, actual piping generation in different specimens could be different. This might be attributed to the anisotropy cause by the pluviated specimen itself together with the existence of glucose. Such complicated soil structure would lead to an unpredictable soil behavior under the hydraulic action.

When plotting the observed volumetric strain for each test case together with the reduction rate defined by G_1/ G_0, it could be seen that greater reduction rate was found in specimen with larger volumetric strain, indicating a more complete formation of piping effect (Fig. 6.44).

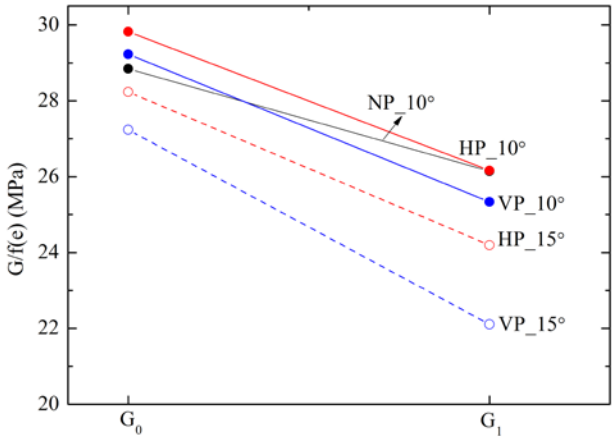

Fig. 6.43 Degradation of normalized shear modulus after water infiltration

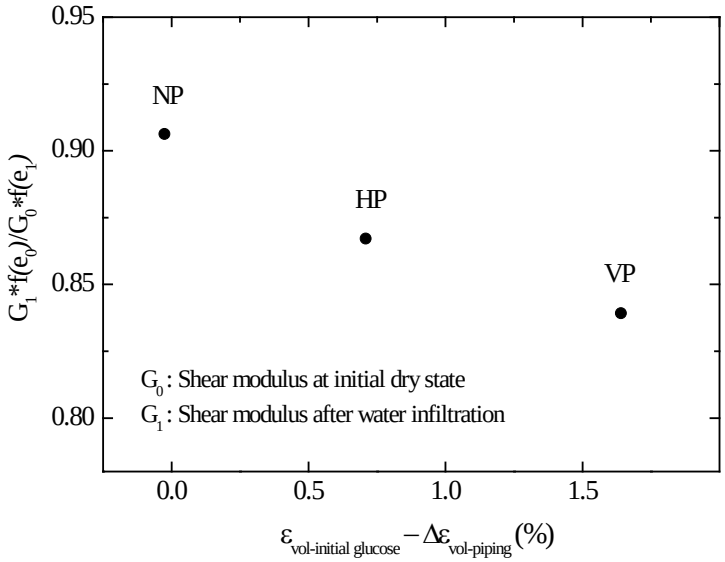

Fig. 6.44 Reduction ratio of *G* against volumetric strain variation during water infiltration

6.3.3 Shear modulus variation during rotation of α

Before the rotation of α, deviator stress (σ_z - σ_r) was increased to the pre-decided value according to different φ for each case. During this process, vertical stress σ_z was gradually increased while radial stress σ_r was decreased under a controlled speed with the aim of keeping the mean effective pressure constant as 80 kPa. Here, direction of σ_1 was 0°.

Small torsional cyclic loadings were applied during this period for every increment of 10 kPa of the vertical stress after a creep around 15 minutes, as is shown in Fig. 6.45.

Fig. 6.46 represents the result of normalized shear modulus with $(\sigma_{z*}\sigma_{\theta})^{0.5}$ in the logarithmic plot. Generally shear modulus became larger with the increase of normal stress level, while for most cases of specimen with internal pipes, some abnormal points could be observed due to piping effect.

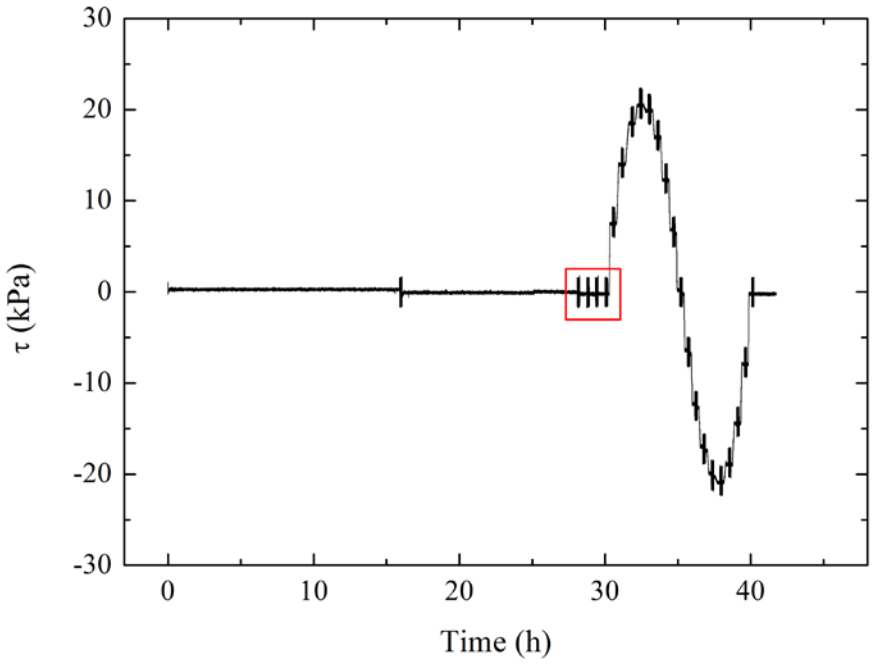

Fig. 6.45 Small torsional cyclic loadings before rotation of σ_1

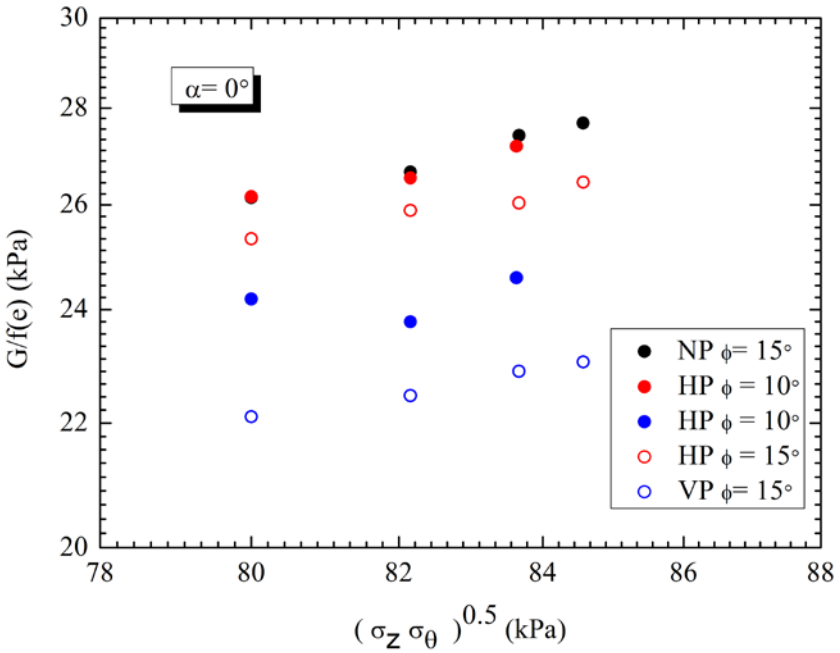

Fig. 6.46 Normalized shear modulus against $(\sigma_{z*}\sigma_{\theta})^{0.5}$ during $\alpha = 0^{\circ}$

During the rotation of σ_1, both radial strain and axial strain of the sand also showed plastic deformation with the variation of normal stresses. Take the case of HP10 for example, where $(\sigma_z - \sigma_r)_{max}$ was around 30 kPa. More obvious of plastic behavior was observed in CG3 (Fig. 6.47), the one attached in the middle height of specimen where horizontal glucose pipe laid in. Axial strain calculated from EDT during the rotation of σ_1 was shown in Fig. 6.48, in which some plastic history could also be observed.

Fig. 6.49 show the shear strain variation collected by gap sensors during the rotation of α. Lager plastic deformation could be found in specimen with horizontal pipes compared with vertical-pipe-specimen, although there was more glucose in the latter. The reason may lies in the direction of piping, which coincided with the direction of shear stress for horizontal-pipe-specimen.

Fig. 6.50 shows the normalized shear modulus variation for each cyclic loading under different shear stress τ. For cases with $\varphi=10^\circ$, shear modulus at $\alpha=0^\circ$ was similar with the one at $\alpha=180^\circ$. However, larger shear modulus was found at $\alpha=180^\circ$ for those with $\varphi=15^\circ$, for the reason that voids caused by piping effect might partially refilled or compressed during larger variation of stresses. Such "densification" effect was also observed in specimen with no pipe.

Relationship between the direction of σ_1 and normalized shear modulus G/f(e) was shown in Fig. 6.51 and Fig. 6.52 for the cases of HP10 and VP10. Larger variations in the values of G were observed in horizontal-pipe-specimen in comparison with vertical-pipe-specimen. The minimum value of G was found at 80° for HP-specimen and 120° for VP-specimen. For the other three cases with $\varphi=15^\circ$, results were presented in Fig. 6.53, in which G_{min} was found at $\alpha=90^\circ$ for the controlled case. However, with larger value of internal friction angle, more unstable behavior occurred in specimen with internal pipes. G_{min} for HP-specimen was observed at $\alpha=100^\circ$, while reductions were also found at 30°, 70° and 160°. For VP-specimen, similar with VP10, G_{min} seemed to be located in the range of 80° ~110° of α, still some abnormal increase occurred.

From the above analysis, both the stress induced anisotropy and the anisotropy due to piping effect were observed by comparing small strain stiffness results. Controlled specimen showed smallest shear modulus at $\alpha=90^\circ$, which matches the bedding plane direction of air pluviated specimen. For specimen with internal pipes, α at which G_{min} was observed varies for different piping direction and different pre-set mobilized angle. More obvious anisotropy was found

for specimen with horizontal piping plane, and this could be explained by the combined effect of the stress induced anisotropy and "inherent anisotropy".

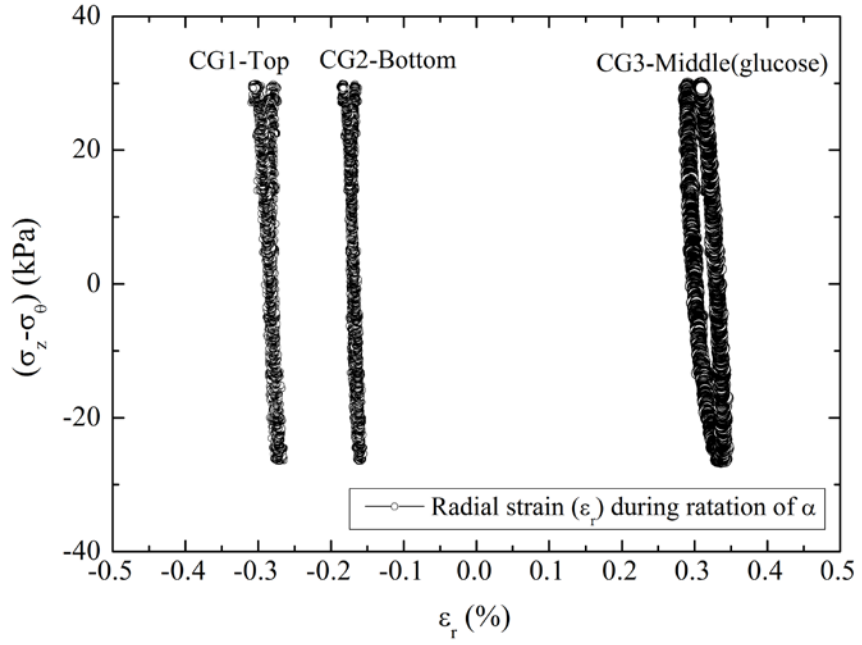

Fig. 6.47 Radial strain variation during rotation of σ_1 (HP10)

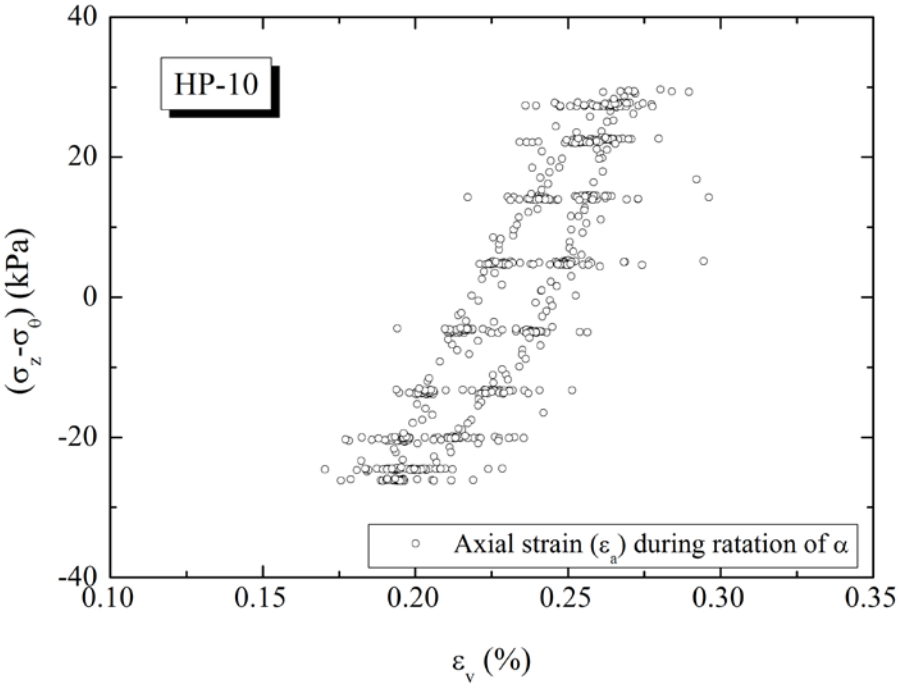

Fig. 6.48 Axial strain variation during rotation of σ_1 (HP10)

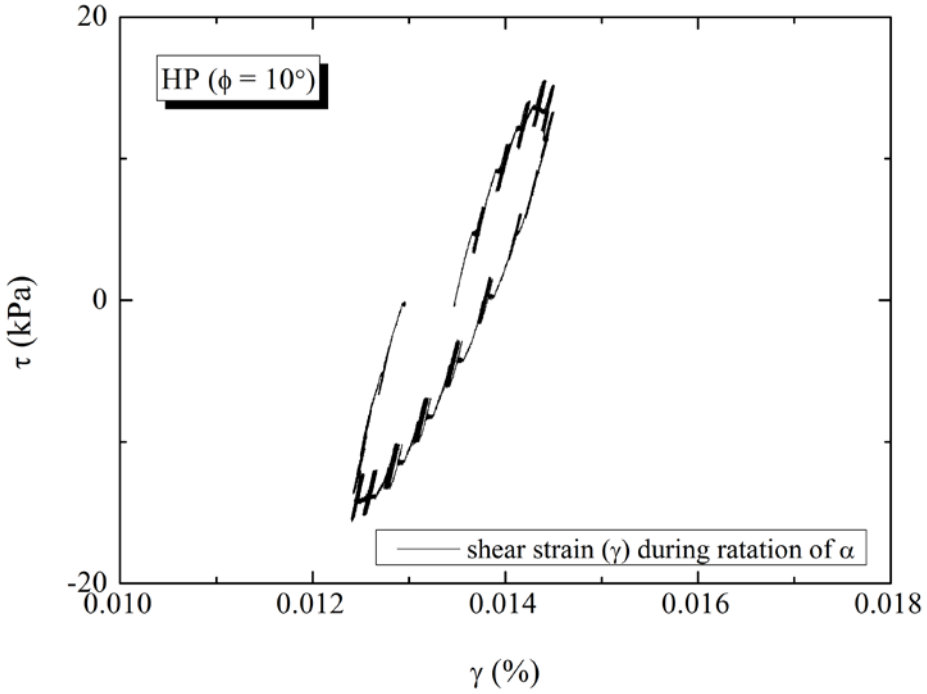
HP (ϕ = 10°)
shear strain (γ) during ratation of α
τ (kPa)
γ (%)
20
0
-20
0.010
0.012
0.014
0.016
0.018

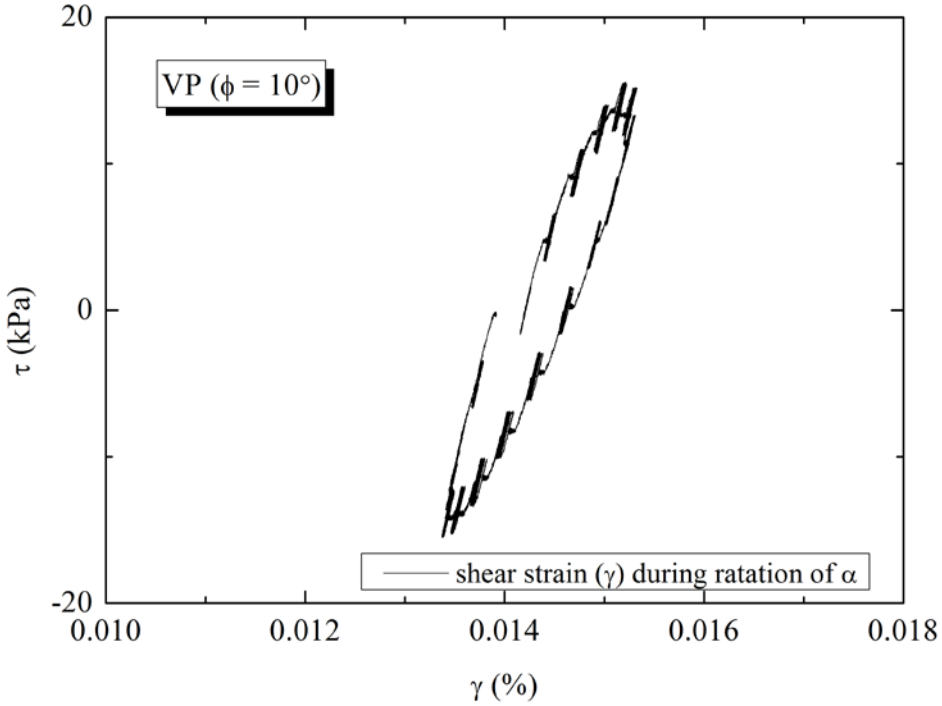
VP (ϕ = 10°)
shear strain (γ) during ratation of α
τ (kPa)
γ (%)
20
0
-20
0.010
0.012
0.014
0.016
0.018

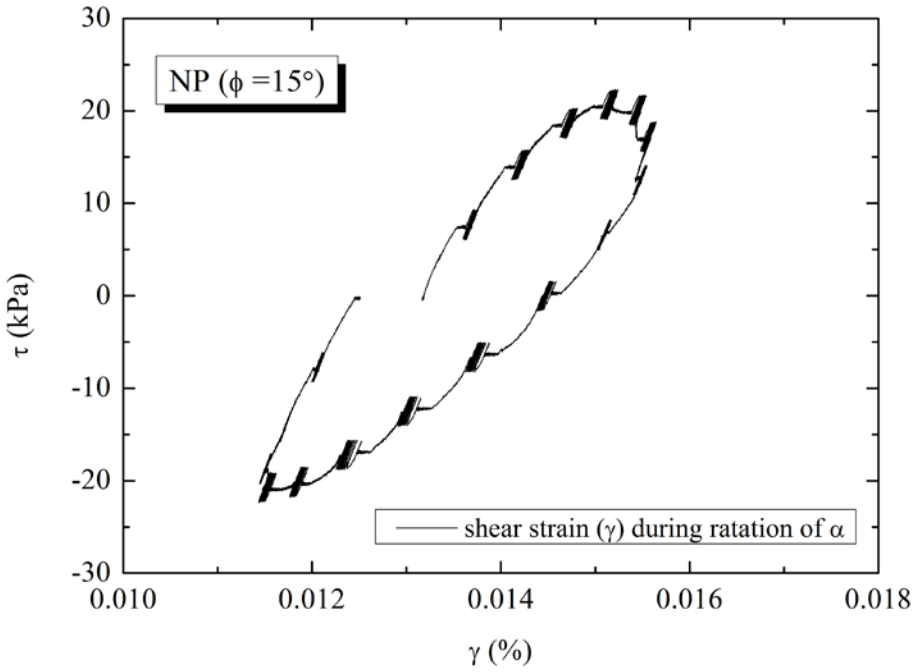
NP (ϕ =15°)
shear strain (γ) during ratation of α
τ (kPa)
γ (%)
30
20
10
0
-10
-20
-30
0.010
0.012
0.014
0.016
0.018

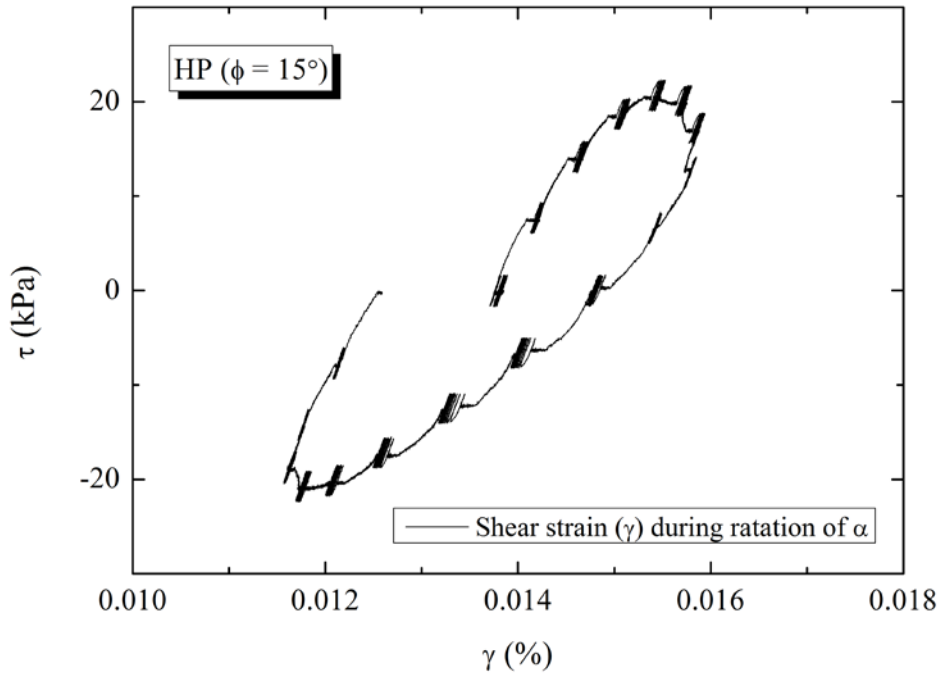
HP (ϕ = 15°)
Shear strain (γ) during ratation of α
τ (kPa)
γ (%)
20
0
-20
0.010
0.012
0.014
0.016
0.018

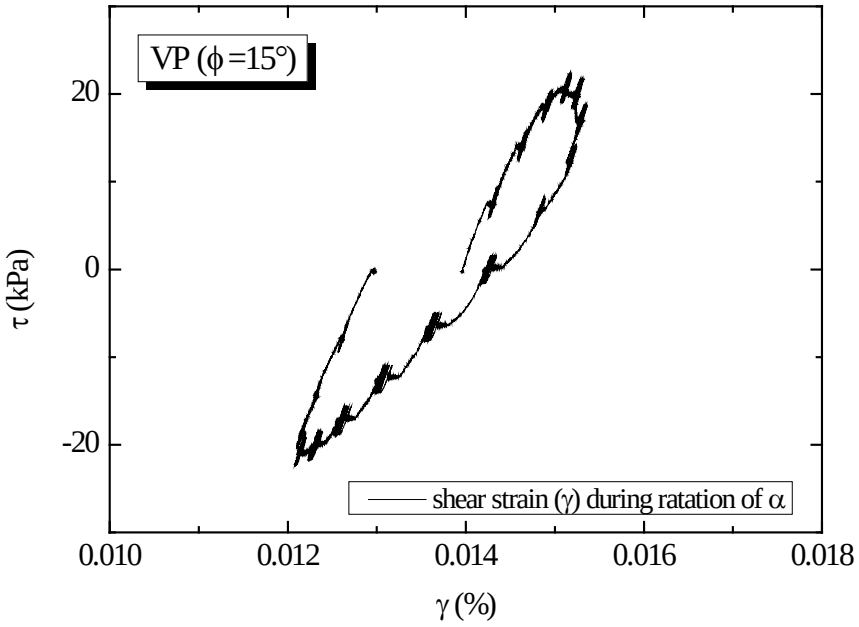

Fig. 6.49 Shear strain variation during rotation of σ_1

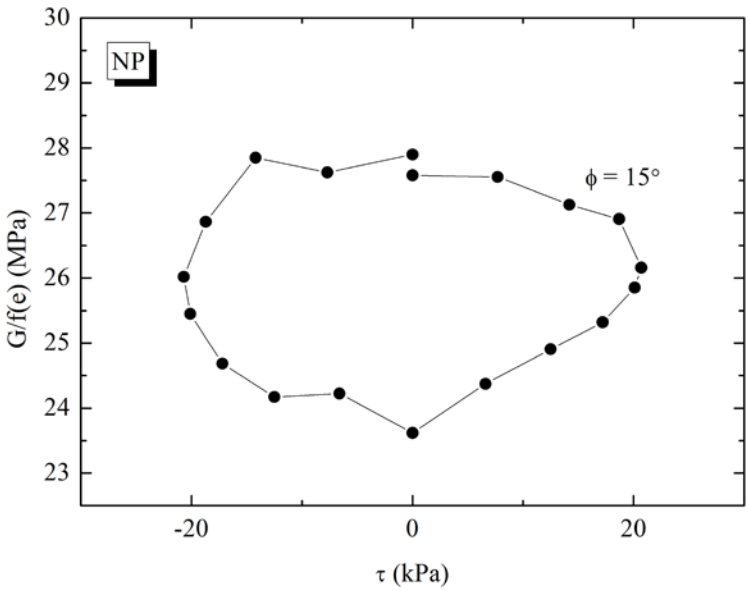

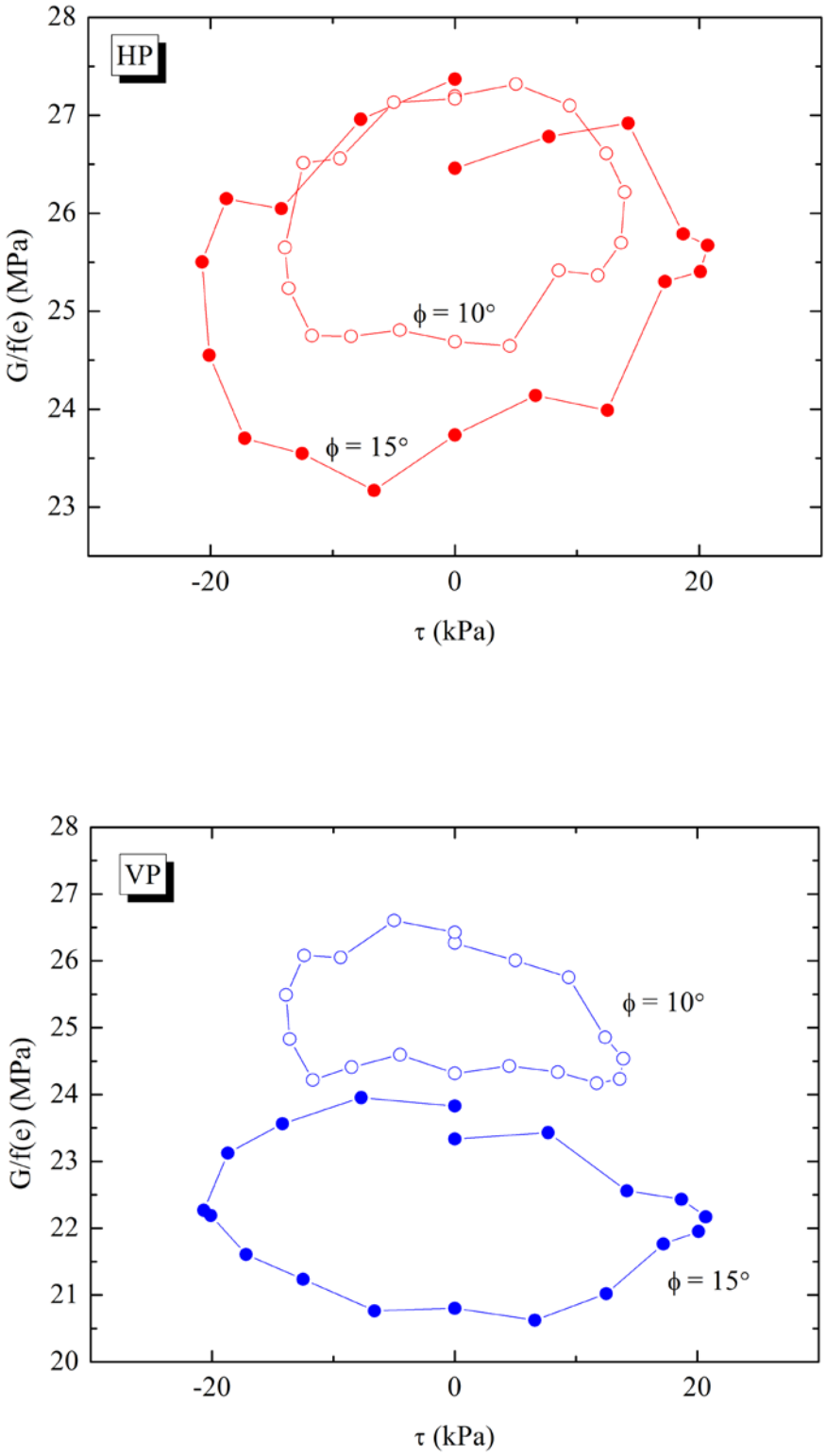

Fig. 6.50 Normalized shear modulus against shear stress under different φ

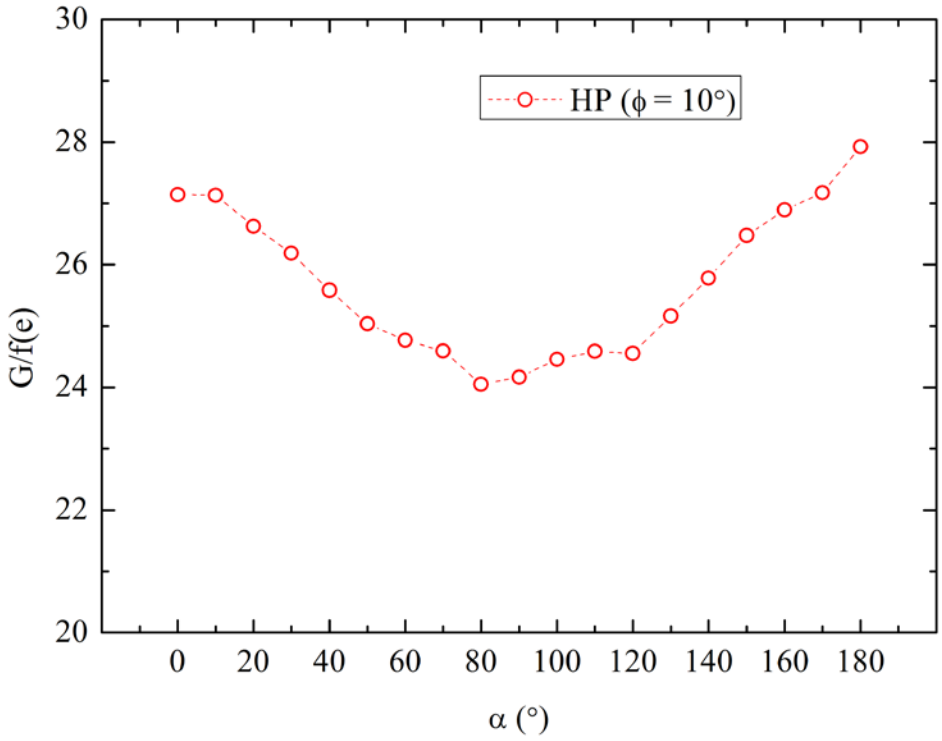

Fig. 6.51 Variation of G during the rotation of σ_1 (HP-10)

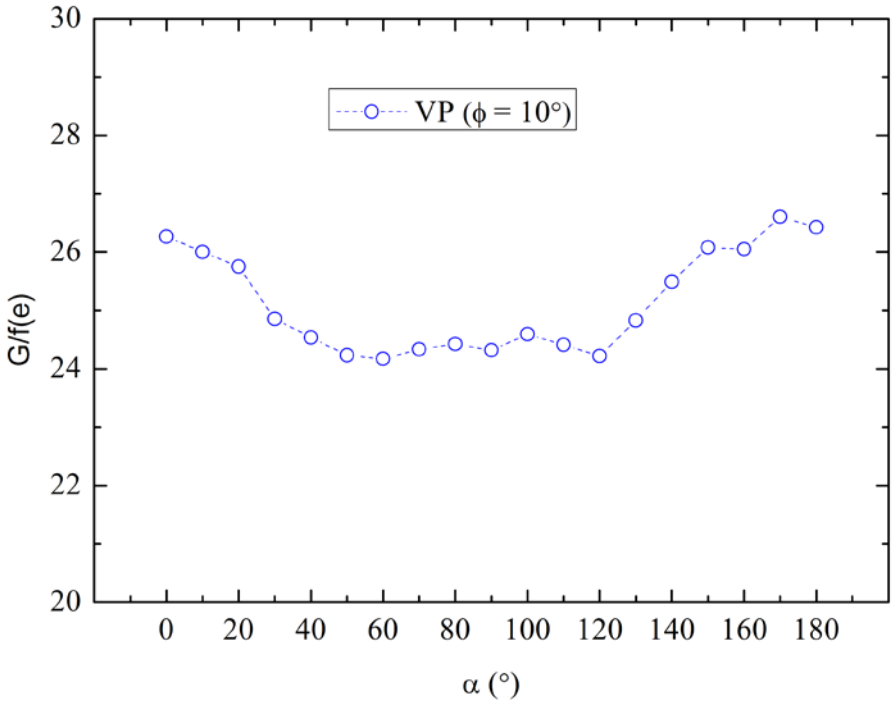

Fig. 6.52 Variation of G during the rotation ofσ_1 (VP-10)

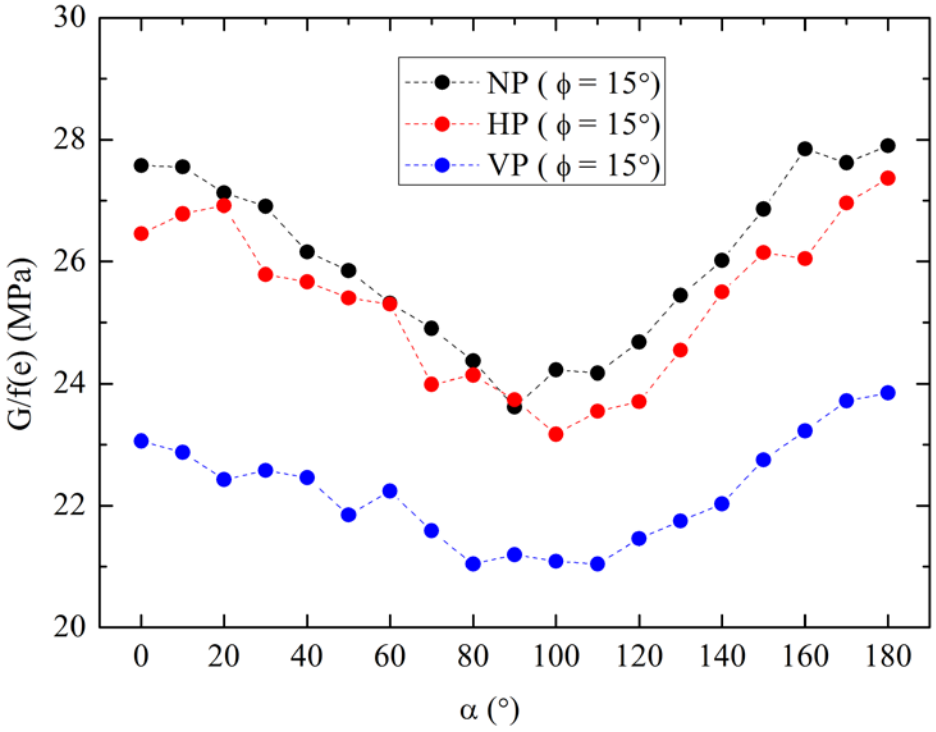

Fig. 6.53 Variation of G during the rotation of σ_1 ($\varphi = 15^{\circ}$)

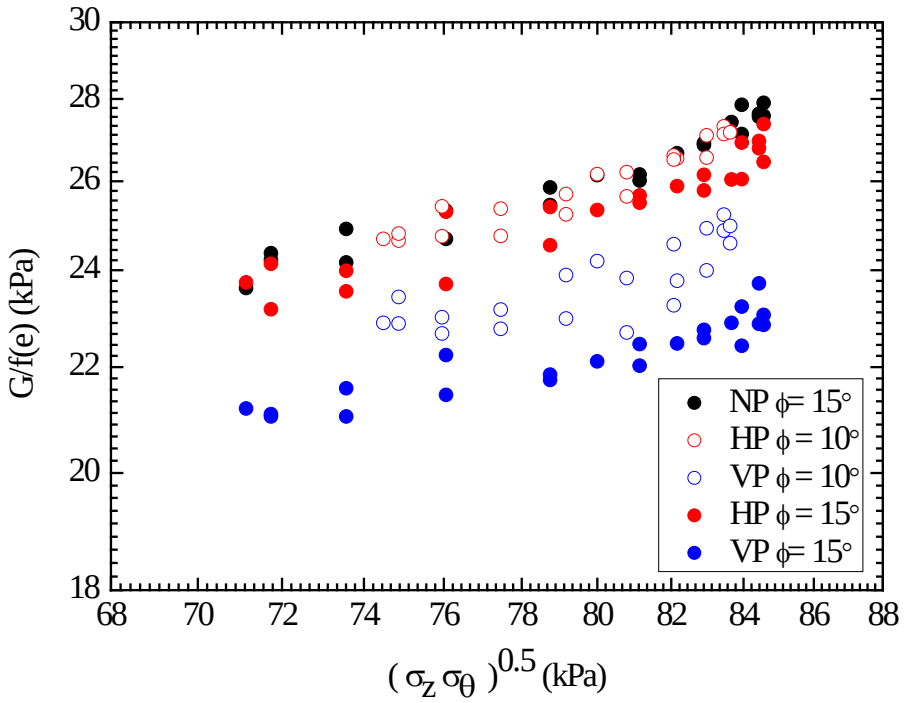

Fig. 6.54 Normalized shear modulus against $(\sigma_{z*}\sigma_{\theta})^{0.5}$ during rotation of σ_1

Similar with the model used in the analysis of cyclic torsional loadings without rotation of principal stress axes, function of $(\sigma_{z*}\sigma_{\theta})^{0.5}$ was employed here as well for the results obtained during rotation of σ_1, as is shown in Fig. 6.54. The dependency of $G/f(e)$ with $(\sigma_{z*}\sigma_{\theta})^{0.5}$ was observed again. And slight reduction in the gradient was seen for specimen subjected to piping effect.

In order to get rid of the influence caused by the variation of normal stresses, IIS model was employed to normalize the shear modulus with the assumption of n = 0.5 for all the case. By this way, piping effect as well as the rotation of σ_1 could be observed in a more clear way.

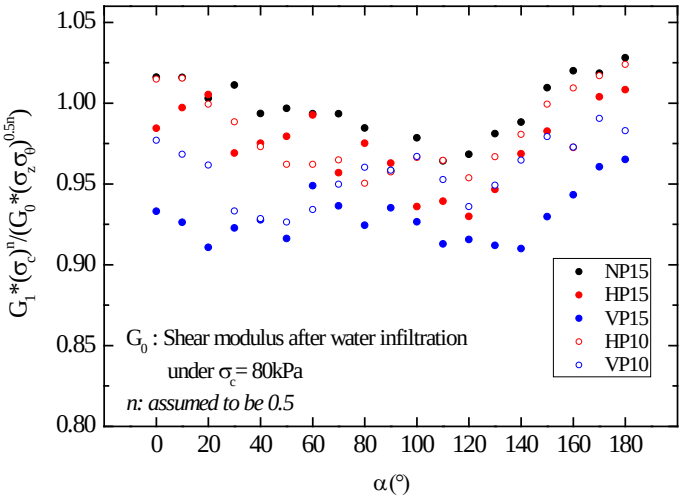

Fig. 6.55 Normalized shear modulus vs. α

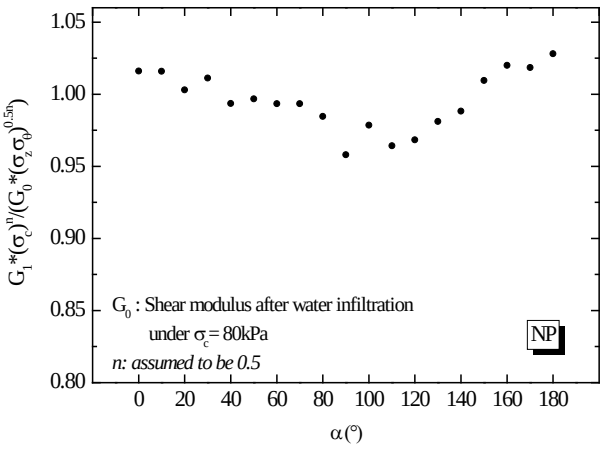

Fig. 6.56 Normalized shear modulus vs. α for NP (φ=15°)

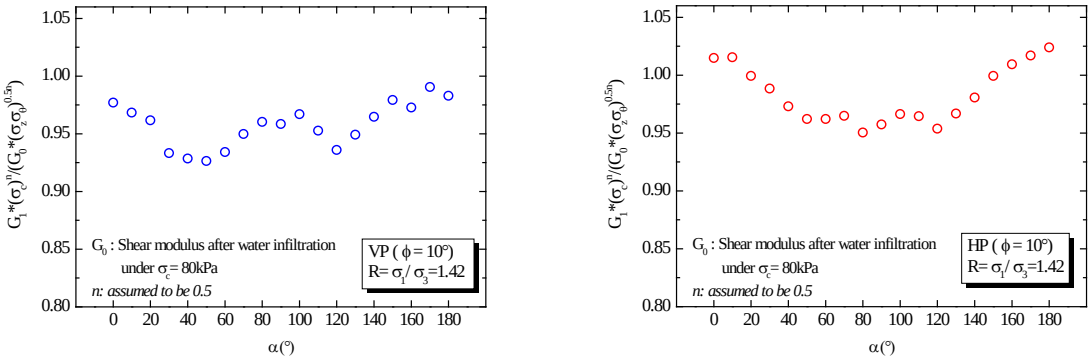

Fig. 6.57 Normalized shear modulus vs. α for HP and VP (φ=10°)

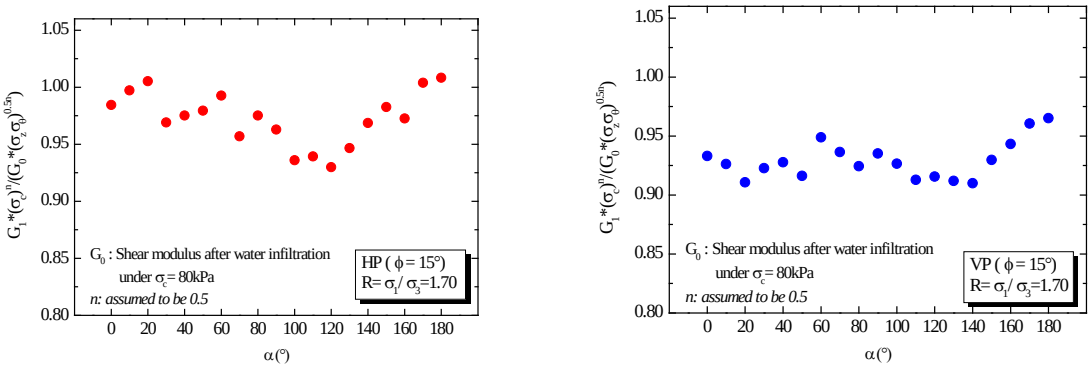

Fig. 6.58 Normalized shear modulus vs. α for HP and VP (φ=15°)

From Fig. 6.55, it could be found that degradation of shear modulus was caused by piping effect by comparing with the data of NP case. Such effect of major principal direction was supposed to be considered in the modelling of shear modulus. Moreover, variation of shear modulus on α was observed from Fig. 6.56-Fig. 6.58 by removing the influence caused by the variation of normal stresses. Especially, value of G was found smaller for α around 120° for piping-influenced specimen. For the cases under φ=15°, variation of G became more obvious due possibly to the increase of stress ratio R. Degradation of G due to R over 3 was observed also by Nguyen, H., Koseki, J. (2005). In the current study, although R was smaller, as a result of piping effect, soil was less stable and fluctuation of shear modulus appeared.

6.4 Drained torsional shear test under constant α

Specimen was first consolidated isotropically by applying the pressure of 80 kPa. After creeping for around 12 hours, water was filled into the specimen to generate piping effect. Then different stress paths with constant angles of principal stress of 0°, 45°, 60° and 90° were

carried out to observe the effect of stress rotation, by adjusting the vertical stress, the circumferential stress and the shear stress so that α was kept constant. Meanwhile, mean effective pressure was kept as 80 kPa all the time. With a same inner and outer pressure in the hollow specimen, combination of axial and torsional load could rotate the principal stress and introduce the coefficient of intermediate principal stress simultaneously, which is expressed as Eq. 6-4.

$$b=sin^2\alpha \tag{6-4}$$

In order to compare the results obtained from the above tests, the principal strains were calculated using the following equations presented in Saada and Townsend (1980):

$$\varepsilon_1 = \frac{\varepsilon_z+\varepsilon_\theta}{2} + \frac{1}{2}\sqrt{(\varepsilon_z+\varepsilon_\theta)^2+\gamma^2} \tag{6-5}$$

$$\varepsilon_3 = \frac{\varepsilon_z+\varepsilon_\theta}{2} - \frac{1}{2}\sqrt{(\varepsilon_z+\varepsilon_\theta)^2+\gamma^2} \tag{6-6}$$

The deviator stress is calculated as Eq. 6-7.

$$q = \sqrt{\frac{(\sigma_1-\sigma_2)^2+(\sigma_2-\sigma_3)^2+(\sigma_3-\sigma_1)^2}{2}} \tag{6-7}$$

For α = 0° and α = 90°, it was similar to triaxial compression and triaxial extension. It was worth noting that restraining of angular deformation would generate some torsional stresses about 3 kPa. In the current experiment, it was neglected.

6.4.1 Stress-strain relationship

Test results from a series of tests with different directions of major principal stress are presented in this section. Fig. 6.59 shows the relationship between the deviator stress and major principal strain for α = 0°.

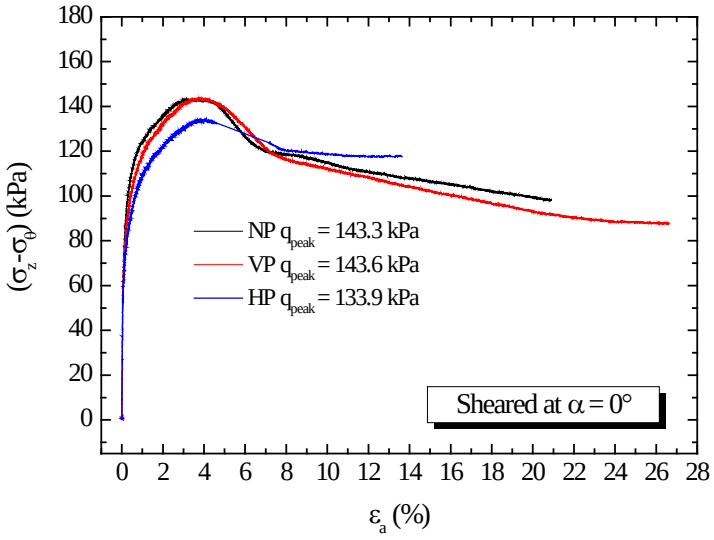

Fig. 6.59 Relationship between deviator stress and axial strain for $\alpha = 0^\circ$

Piping-induced anisotropy could be observed from the results shown in the above figure, where reduction of peak shear strength was observed for specimen subjected to piping effect. Similar with triaxial compression test, specimen with internal vertical pipes seemed not to be strongly influenced by the existence of piping plane compared with horizontal-pipe-specimen, although some increase of strength was found at larger strain due possibly to the compression of the pipe.

In Fig. 6.60, volumetric strain during shearing of the three cases under $\alpha = 0^\circ$ was plotted. It should be pointed out that due to the limited measure range of clip gauges, the accuracy of the outer diameter d_o calculation would be reduced, as is shown in Fig. 6.61. Especially after the development of shear band, the specimen would undergo large non-uniform deformation, and it becomes quite difficult to compute the volumetric strain. Thus, ε_{vol} in the analysis in this section was calculated only during the initial stage of shearing.

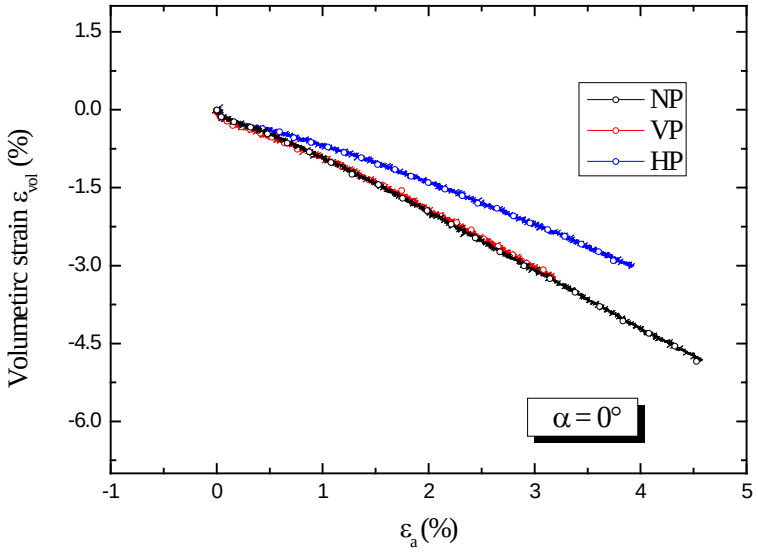

Fig. 6.60 ε_{vol} during shearing for $\alpha = 0^{\circ}$

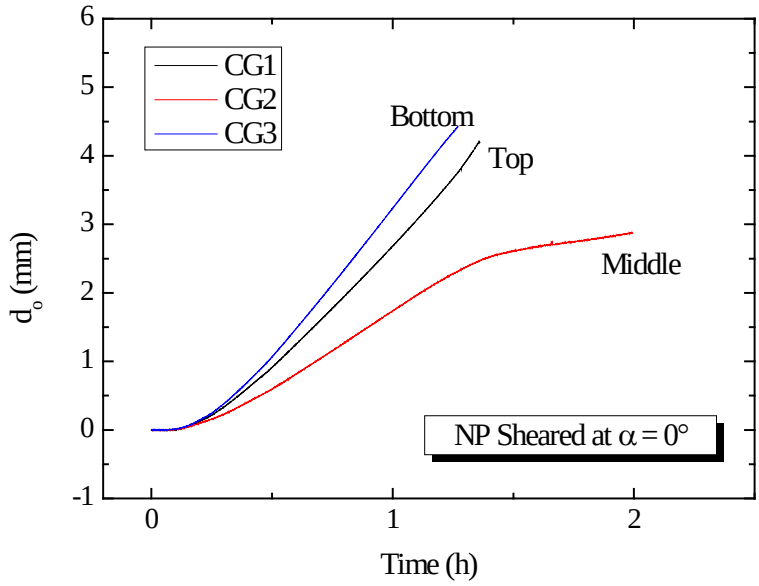

Fig. 6.61 Localized deformation during shearing

In the previous studies on Toyoura sand (Oda, 1981; Lam and Tatsuoka, 1988), smaller peak strength was found when the maximum stress obliquity plane was in parallel with the bedding plane. However, in this study, failure behavior of specimen with vertical pipes were similar

with the specimen without pipe both in triaxial compression test and torsional shear test with $\alpha = 0^{\circ}$. This could be explained by the fact that the combination of the bedding plane (horizontal) and piping plane (vertical) would bring a more complex structure, in which the influence of the piping plane was restrained by the rigid top cap and pedestal. In addition, all the specimens were failed in a brittle manner with small failure strains ranging from 3%~5%. As is shown in Fig. 6.60, similar with the peak deviator stress, larger dilatancy rate was found in the case of NP and VP.

Fig. 6.62 and Fig. 6.63 show the stress-strain relationship and the variation of volumetric strain for $\alpha = 90^{\circ}$. Approximately 12.7% decrease of peak shear strength was found in the case HP compared with vertical-pipe-specimen, which was round 6.7% when sheared at $\alpha = 0^{\circ}$. Such lowest resistance against horizontal compression was predictable for the specimen with horizontal piping plane, which was in parallel with the bedding plane. The peak shear strength appeared with the strains ranging from 4%~6.5%, from where the volumetric strain started to develop in a faster manner, showing a dilatant behavior.

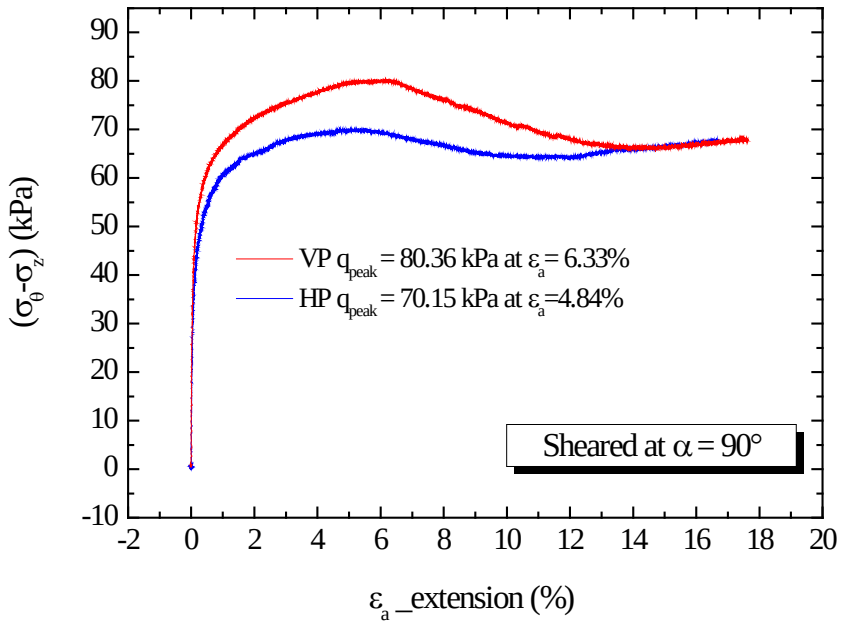

Fig. 6.62 Relationship between deviator stress and axial strain for $\alpha = 90^{\circ}$

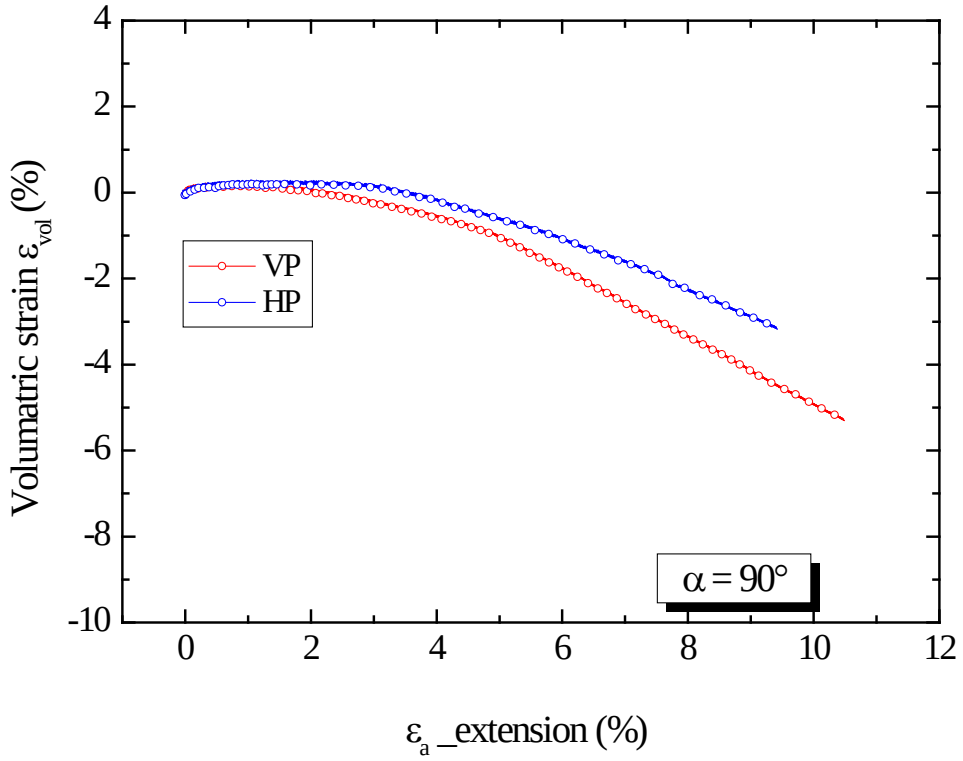

Fig. 6.63 ε_{vol} during shearing for α = 90°

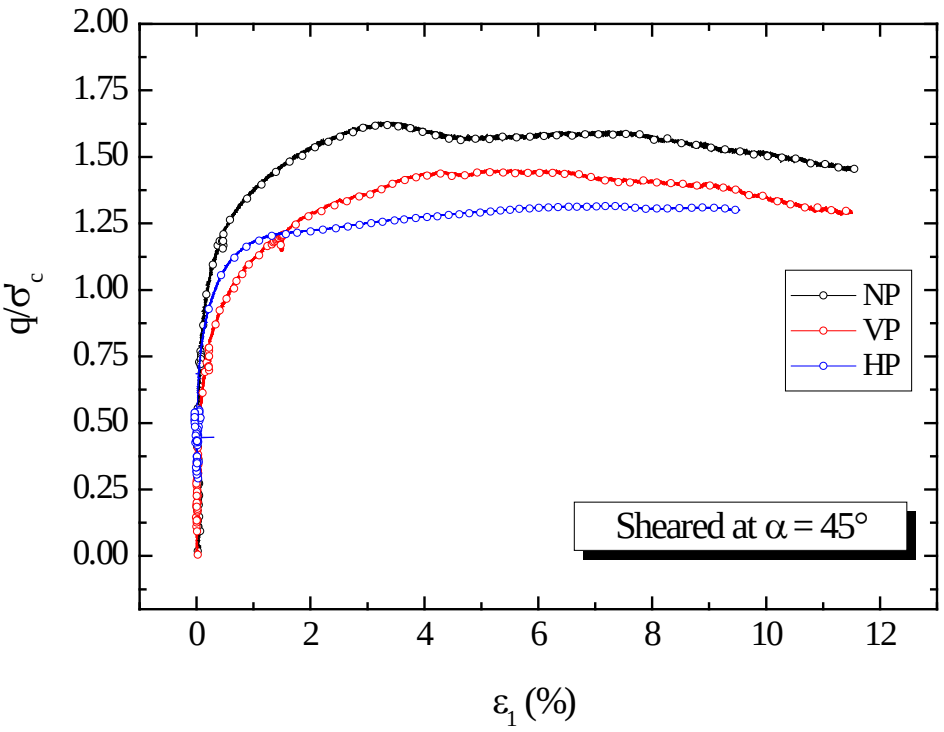

Fig. 6.64 Relationship between deviator stress and axial strain for α = 45°

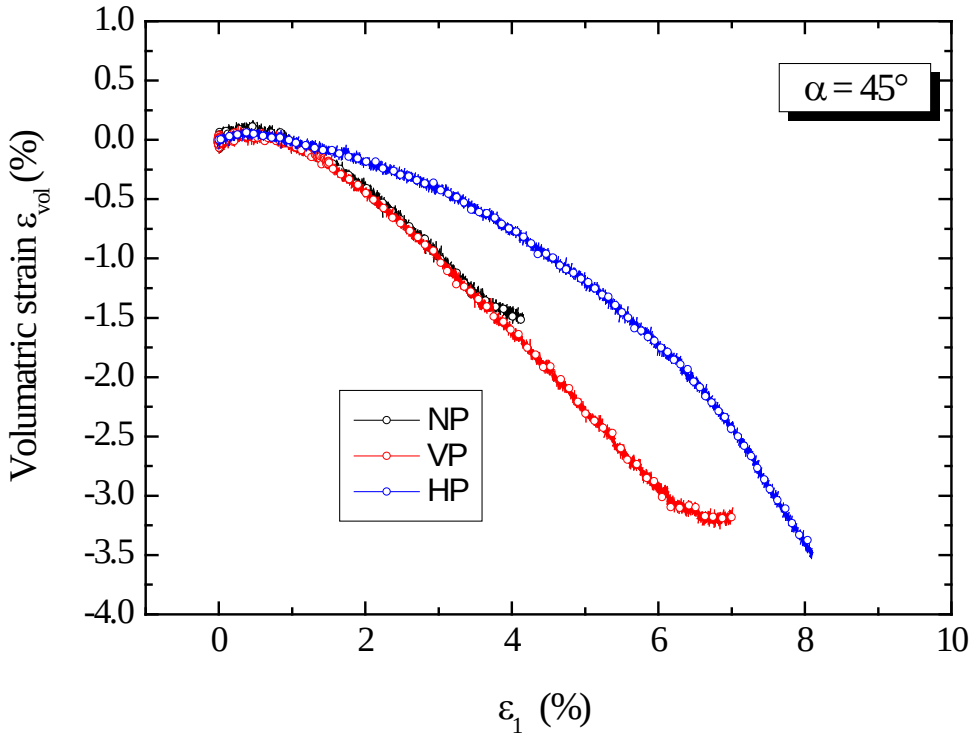

Fig. 6.65 ε_{vol} during shearing for $\alpha = 45^{\circ}$

Fig. 6.64 and Fig. 6.65 show the results for $\alpha = 45^{\circ}$, where larger reduction was found in VP relative to NP compared with $\alpha = 0^{\circ}$. Here the specimens failed in a ductile manner for the specimen with internal pipes with relatively large failure strains over 5%. Smaller dilatancy rate as well as lower peak strength was found in specimen with horizontal pipe. Some volume contraction was observed at the very beginning period of shearing due to the high density of specimens. It is therefore evident that initial anisotropy has obvious influence not only on the shear deformation behavior, but also on the dilatancy behavior.

Fig. 6.66 shows the relationship between stress ratio σ_1/σ_3 and the shear strain (ε_1-ε_3) for all the direction of principal stress of specimen with horizontal pipe. Such stress-induced anisotropy as well as piping-induced anisotropy could be seen by the variation of the peak internal friction angles for all the specimens (seen in Fig. 6.67).

It is worth noted that for $\alpha = 60^{\circ}$, at which the major principal stress is inclined such that the potential shear band directions coincide with the piping planes, a lower strengths is expected. While in this study, $\alpha = 90^{\circ}$ was found to be the weakest. The reason lies in the extreme narrow cross section area in the horizontal direction due to the existence of piping. Hence, the smallest φ appeared when the specimen was sheared under large extension stress.

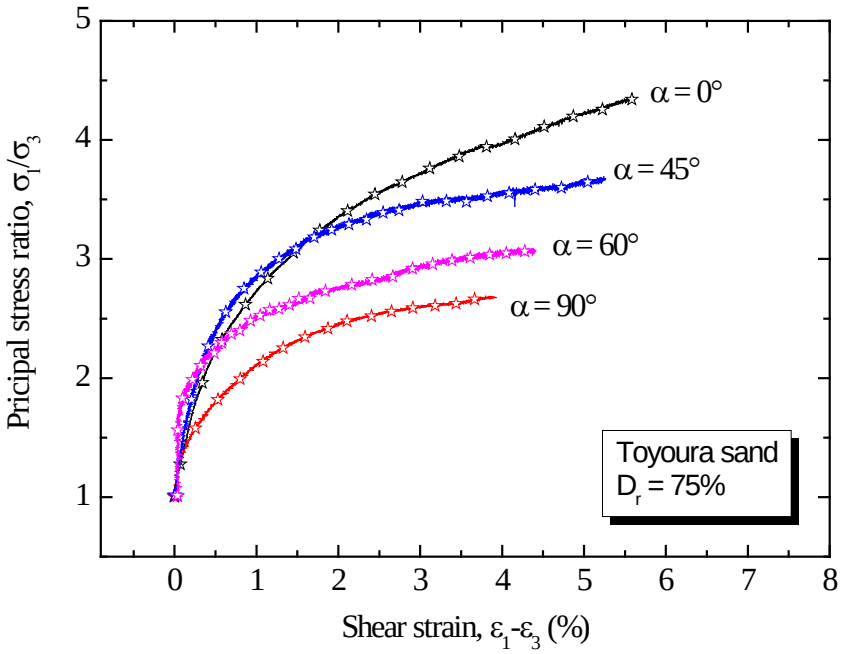

Fig. 6.66 Relationship between deviator stress and axial strain for HP

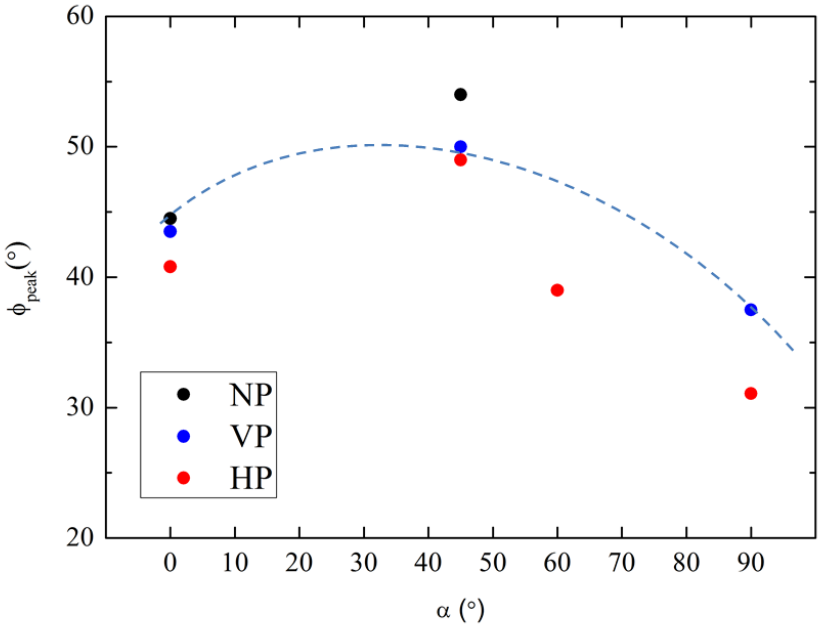

Fig. 6.67 Friction angle vs. major principal stress directions

Fig. 6.67 shows an growth of φ value with the increase of α from 0° to 45°, and a trend of decrease when α was larger 45°. The smallest φ was found at α equals 90°. Since $b=\sin^2\alpha$, the influence of the intermediate principal stress and the direction of major principal stress could not be separated.

In the study by Towhata I. and Ishihara K. (1985), through several series of undrained tests using a triaxial torsional shear apparatus concerning the rotation of principal stress, similar results of the magnitude of intermediate principal stress's influence on friction angle were obtained.

Lade et al. (1994) has also reported similar trend of friction angles with a variation of about 8° during the changing of b. In his recent research about cross-anisotropy in torsion shear apparatus (2014), the effects of major principal stress direction on the variation in strength were investigated. The apparatus allow application of different pressures in the inside and outside cells, thus b was separated from α. The increase of φ was observed for b from 0 to 0.5 for all the cases.

In addition to the intermediate principal stress, the friction angles obtained from are influenced by shear banding (Wang and Lade 2001; Lade and Wang 2001; Lade 2003). It could be found in Fig. 6.63 that a relative higher φ was computed in this study. The reasons could be due to the fact that a shorter specimen was tested in the current study.

Tarek Omar and Abouzar Sadrekarimi (2014) performed several drained and undrained monotonic triaxial compression shear tests on three different specimen sizes of the same sand. It was found that shear banding and specimen boundary conditions brought a great influence on the behavior of the specimen, which are manifested as specimen size effects. The results show that larger shear strengths and effective friction angles are mobilized in the smaller specimens during shearing.

In the torsional shear test conducted by Lade. et al (2008), the effect of specimen height on the soil behavior was investigated with heights of 40 and 25 cm. It was noted that the shorter specimen picked up more load due to the restrained of the end rings when the sliding of one part of the specimen on the other occurred.

Upon formation of a shear band, the sliding of one part of the specimen on the other resulted in these parts being restrained at the rough ends, and the specimen therefore picked up a little more load. This produced a temporary slight increase in the stresses. In a study of the effect

of height-to-diameter ratio of true triaxial specimens (Lade and Wang 2002), higher strengths were consistently found in the tests with H/D = 1.0 than in the tests with H/D = 2.4 in which the shear bands were free to develop without interference from the stiff, lubricated end plates.

Some researchers (e.g., Hight et al. 1983 and Vaid et al. 1990) have proposed different criteria to select the size, based mainly on the analyses of the degree of stress nonuniformity within the specimen. And the recommended dimensions for torsional specimens are: $r_o - r_i = 20$ to 26mm; $0.65 \leq r_i / r_o \leq 0.82$; and $1.8 \leq H/2r_o \leq 2.2$, while for the specimen used in this study $H/2r_o$ equals 1. It could be inferred that nonuniformity in the shear stress would be caused across the specimen wall. Such effect due to the specimen size could be evaluated by conducting new cases with larger specimen in the same apparatus. Since the main focus in this study is piping effect, shorter specimen is preferred in order to generate a more uniform piping in the sand.

6.5 Chapter conclusions

Three types of tests are discussed in this chapter focusing on the drained behavior of Toyoura sand subjected to piping effect and the variation of shear modulus under the rotation of major principal stress, the following conclusions can be inferred:

1) Similarly with triaxial test, larger volumetric strains were observed in specimen with internal pipes under lower confining pressure during piping formation at isotropic stress state.

2) Piping generation in torsional shear test was rather uniform compared with triaxial test since the height of the specimen is smaller.

3) Reduction of shear modulus caused by piping effect showed more dependency on the volume of influenced area compared with the piping direction.

4) IIS model is employed to evaluate the variation of shear modulus under constant α as well as the complete rotation of α. For constant α, piping effect was found to have a more obvious influence under $\alpha = 90^{\circ}$, in which the reduction of shear modulus show smaller dependency on the variation of normal stresses. For complete rotated α, reductions of G was found in specimen with internal pipes, where a smallest G value was found under $\alpha = 120^{\circ}$.

5) Specimen subjected to piping effect showed lower resistance against shear.

6) For vertical-pipe-specimen, piping effect in the shear strength was found to be small, possibly due to the end restraint by the top cap and pedestal during the formation of shear band. For horizontal-pipe-specimen, piping effect was more obvious when sheared at different direction of σ_1. A weakest behavior was found at $\alpha = 90^{\circ}$.

7) For horizontal-pipe-specimen, development of shear band was greatly influenced by the piping plane, due to the non-uniformity of stress.

6.6 Reference

1. Burland, J. B. (1990). On the compressibility and shear strength of natural clays.Ge´otechnique40, No. 3, 329-378.

2. Abelev, A.V., Lade, P.V. (2003). Effects of cross-anisotropy on three-dimensional behavior of sand. Part I: Stress–strain behavior and shear banding. Journal of Engineering Mechanics, 129:160-166.

3. Abelev, A.V., and Lade, P.V. (2004). Characterization of failure in cross-anisotropic soils. Journal of Engineering Mechanics, 130:599-606.

4. Hight, D. W., Gens, A. and Symes, M. J. (1983). The development of a new hollow cylinder apparatus for investigating the effects of principal stress rotation in soils, Geotechnique, Vol. 33, No. 4, 355-383.

5. Jardine, R. J., Zdravkovic, L. & Porovic, E. (1997). Anisotropic consolidation including principal stress axis rotation: experiments, results and practical implications.Proc. 14th Int. Conf. Soil Mech. Found. Engng, Hamburg, 4, 2165-2168.

6. Lade, P.V., and Wang, Q. (2001). Analysis of shear banding in true triaxial tests on sand. Journal of Engineering Mechanics, 127:762-768.

7. Lade, P.V., and Wang, Q. (2002). Effect of slenderness ratio on shear banding in true triaxial tests on sand. In Proceedings of the 8th International Symposium on Numerical Models in Geomechanics – NUMOG VIII, Rome, Italy, 10–12 April 2002. Edited by G. N. Pande and S. Pietruszczak, A.A. Balkema, Lisse, the Netherlands, 149-154.

8. Lam,W-K. and Tatsuoka,F. (1988). Effect of initial anisotropic fabric andM2on strength and deformation characteristics of sand, Soils and Foundations, Vol. 28, No.1, 89-106.

9. Nguyen, H., Koseki, J. (2005). Quasi-elastic deformation properties of Toyoura sand in cyclic triaxial and torsional loadings. Soils and Foundations, 45(5): 19-38.

10. Oda, M., (1981). Anisotropic Strength of Cohesionless Sands, Journal of the Geotechnical Engineering Division, ASCE, Vol. 107(9), 1219- 1231.

11. Poul V. Lade, Jungman Nam, Won Pyo Hong, (2008). Shear banding and cross-anisotropic behavior observed in laboratory sand tests with stress rotation. Canadian Geotechnical Journal, 45(1): 74-84.

12. Tarek. O., Abouzar. S., (2014). Specimen size effects on behavior of loose sand in triaxial compression tests. Canadian Geotechnical Journal, 2015, 52(6): 732-746.

13. Towhata, I., Ishihara, K. (1985). Undrained strength of sand undergoing cyclic rotation of principal stress axes. Soils and foundations, 25(2): 135-147.

14. Vaid, Y. P., Sayao, A., Hou, E. Negussey, D. (1990b). Generalized stress-path-dependent soil behavior with a new hollow cylinder torsional apparatus, Can. Geotech. J., Vol. 27, No. 5, 601-616.

15. Wang, Q., and Lade, P.V. (2001). Shear banding in true triaxial tests and its effect on failure in sand. Journal of Engineering Mechanics, 127: 754-761.

16. Yang,Y., and Kuwano, R., (2014). Evaluation of mechanical properties of sand loosened due to piping, 7th International Conference on Scour and Erosion, 257-266.

17. Zdravkovic, L. & Jardine, R. J. (2001). The effect on anisotropy of rotating the principal stress during consolidation. Geotechnique, 51, No. 1, 69-83.

Chapter 7 Conclusions and Recommendations

7.1 Introduction

Landslides due to piping have occurred frequently in rainy season recently. Piping, known as a complex phenomenon of internal erosion, has not been quantitatively studied in laboratory by element experiment. Acting as a weak plane, piping-induced anisotropy on the behavior of soil has not been studied before, while in reality, severe failure could occur due to the existence of piping.

As an attempt to achieve piping effect, artificial pipes both in vertical and horizontal were created by dissolving glucose in Toyoura sand. Both the triaxial test and the hollow cylindrical torsional shear tests were conducted for specimens with and without pipes. Influencing factors were chosen as relative density, confining pressure, number of piping, and direction of piping. Strains during piping propagation were measured locally by LDTs and CGs. Small strain stiffness of sand was investigated by applying small cyclic loadings. Failure behavior of sand with piping plane was observed. Further insights into anisotropy of sand subjected to piping effect were also realized by rotating the direction of major principal stress in torsional shear apparatus.

7.2 Conclusions

In this chapter, properties of loosened soil due to piping effect were studied through a series of triaxial tests by dissolving glucose pipes in Toyoura sand. Properties of loosened sand were studied under different densities, pipe number and confining pressure. Piping propagation was observed according to the axial strain, radial strain and volumetric strain measured by local transducers. Furthermore, Young's modulus and Poisson's ratio of sand with internal pipes were also evaluated under cyclic loading before and after loosening. The following conclusions could be drawn based on the results.

7.2.1 Piping propagation during water infiltration

Volumetric strains during water infiltration in all the tests were summarized in Table. 7.1.

Toyoura sand:

(1) Smaller density samples (initial relative density around 45%) were observed with larger deformation than samples with initial relative density around 70% during the first water infiltration, while no obvious change in volumetric strain was observed during the second water inflow after piping formation.

(2) An anisotropic development of piping was observed in specimen with the height of 150mm in triaxial test, i.e. lower part of the specimen exhibited larger deformation than the upper part. Such non-uniform in piping dimension was not so significant in torsional shear test, in which the specimen of 100mm height was tested.

(3) In torsional shear tests, increase of volumetric strain during to piping in specimens with the initial relative density around 75% was found to be 30%~40% of the initial glucose volume for most cases.

(4) Influence of confining pressure on the piping formation was less obvious, while a slight larger increase was found in specimen under smaller confining pressure.

(5) With the increase of the initial pipe number, larger deformation was caused during water infiltration.

Edosaki sand:

(1) Compared with Toyoura sand, larger deformation occurred during water infiltration, indicating a severe migration of the particles.

(2) Fines are tended to concentrate into the voids of the initial glucose pipe, resulting in a relative uniform piping in general.

Table 7.1 Volumetric strain variation during water infiltration

σ_c (kPa)	Pipe condition	$\Delta\varepsilon_{vol}$ during water infiltration	$\Delta\varepsilon_{vol}/\varepsilon_{glucose}$ (%)
30	2VP	0.223	0.35
	4VP	0.563	0.44
	HP	0.360	0.31
50	1P (triaxial)	0.360	0.41
	2VP	0.209	0.33
	4VP	0.573	0.45
	HP	0.32	0.27
	1P (Loose_triaxial)	0.670	0.87
	2VP (Loose)	0.479	0.76
60	2P	0.205	0.33
80	4VP*	1.560	0.49
	HP	0.461	0.39
100	1P (Loose_triaxial)	0.580	0.67

7.2.2 Variation of Young's modulus, Poisson's ratio, and shear modulus

(1) According to triaxial test, Young's modulus tended to decrease and Poisson's ratio showed a tendency of increase in most specimens with internal pipes after the first water cycle for Toyoura sand.

(2) For Edosaki sand, both controlled specimen and piping-influenced specimen showed similar variation in Young's modulus and Poisson's ratio, indicating subtle effect was induced by the disturbance in the current study to the soil structure.

(3) In torsional shear test, reduction of shear modulus caused by piping effect showed more dependency on the volume of influenced area compared with the piping direction.

(4) IIS model is employed to evaluate the variation of shear modulus under constant α as well as the complete rotation of α. For constant α, piping effect was found to have a more obvious influence under $\alpha = 90^{\circ}$, in which the reduction of shear modulus show smaller dependency on the variation of normal stresses. For complete rotated α, reductions of G was found in specimen with internal pipes, where a more unstable soil structure was found by the fluctuation of G value against α.

7.2.3 Shear strength variation

(1) In both triaxial test and torsional shear test, specimen subjected to piping effect showed lower resistance against shear in Toyoura sand.

(2) Similar shear strengths were observed for both the specimen with and without pipe in Edosaki sand in the current research.

(3) For vertical-pipe-specimen, piping effect in the shear strength was found to be small, possibly due to the end restraint by the top cap and pedestal during the formation of shear band.

(4) For horizontal-pipe-specimen, in which the piping plane is coincided with the bedding plane, piping effect on shear strength was more obvious.

(5) For horizontal-pipe-specimen, development of shear band was greatly influenced by the piping plane. A partially restricted shear band along the piping plane was observed under the shearing of $\alpha = 45^{\circ}$.

(6) A weakest behavior was found at $\alpha = 90^{\circ}$ in horizontal-pipe-specimen due to the narrow cross sectional area.

7.3 Recommendations for Future Research

As the first attempt of simulating piping effect with dissolving glucose powder, this study offers a new methodology to gain an insight to the piping phenomenon through mechanical experiments. Due to the limitation of the scope of the current study, some important issues are not paid attention in detail. The following suggestions for future research could be identified.

(a) Most of the findings in the current study were limited to Toyoura sand. In order to represent piping effect in a more realistic way, sand with different content of fines should be studied.

(b) Range of the local sensors used in this research is limited, and the volume change of specimen during shear could not be recorded accurately. Sensors with larger range or other method for the measurement of the volume change in unsaturated specimen (double cell) could be developed in piping effect study.

(c) Particle Image Velocimetry (PIV) could be used to record the migration of particles during piping propagation by X-ray CT images. Thus, a better understanding of the development of piping could be obtained.

(d) The size of specimen has an important influence on the piping generation, which also effects sand behavior in the torsional apparatus. Reproducibility could be improved by properly choose the dimension of specimen.

(e) In the current study, the influence of intermediate principal stress could not be separated from the rotation angle of σ_1 due to the same inner and outer cell pressure. Future investigation on the shear behavior could remove this impact by applying different cell pressures.

Appendix A:

Relation between b and α in torsional shear test

The magnitude of the intermediate principal stress is often indicated by the value of b which is defined as:

$$b = \frac{\sigma_2 - \sigma_3}{\sigma_1 - \sigma_3} \qquad \text{(A-1)}$$

For the torsional shear test on hollow cylinder specimens with the same internal and external cell pressure, the value of b is related to the angle of σ_1 to vertical, α.
Fig.A-1 shows the state of stress in an element of the hollow cylindrical torsional shear specimen.

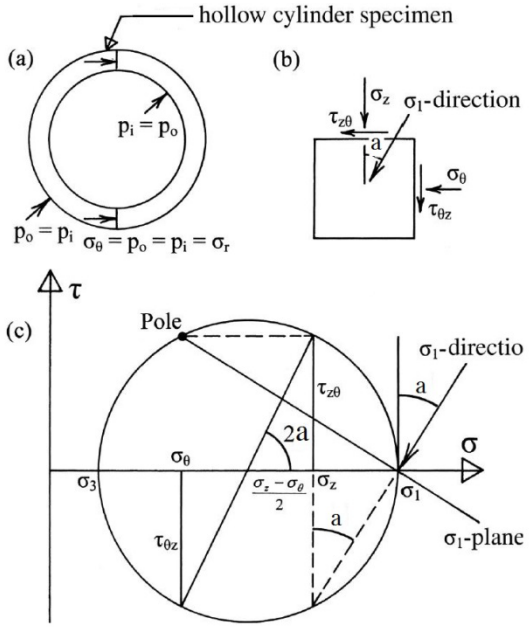

Fig. A-1. (a) and (b) stress conditions in torsional shear tests; (c) determination of inclination of major principal stress.

By the pole method it could be seen that the major principal stress is inclined at α, and

$$\tan(2\alpha) = \frac{2\tau_{z\theta}}{(\sigma_z - \sigma_\theta)} \tag{A-2}$$

Computation for the major and minor principal stresses is:

$$\begin{Bmatrix}\sigma_1\\ \sigma_3\end{Bmatrix} = \frac{\sigma_z + \sigma_\theta}{2} \pm \sqrt{\tau_{z\theta}^2 + \frac{(\sigma_z - \sigma_\theta)^2}{4}} \tag{A-3}$$

Both σ_1 and σ_3 act in the plane of the wall. Hence, σ_2 is perpendicular to the wall and equal to the cell pressure. Also, equilibrium in the cylinder wall requires that the normal stress in the wall is equal to the cell pressure σ_r. Thus, $\sigma_2 = \sigma_r = \sigma_\theta$.

By substituting the principal stresses in Eq. A-1 into the normal stresses in Eq. A-3:

$$b = \frac{\sigma_\theta - \left(\frac{\sigma_z + \sigma_\theta}{2} - \frac{\sigma_z - \sigma_\theta}{2}\sqrt{1 + \frac{4\tau_{z\theta}^2}{(\sigma_z - \sigma_\theta)^2}}\right)}{2 * \frac{\sigma_z - \sigma_\theta}{2}\sqrt{1 + \frac{4\tau_{z\theta}^2}{(\sigma_z - \sigma_\theta)^2}}} \tag{A-4}$$

By Eq. A-2,

$$b = \frac{-(\sigma_z - \sigma_\theta) + (\sigma_z - \sigma_\theta)\sqrt{tan^2 2\alpha + 1}}{2 * (\sigma_z - \sigma_\theta)\sqrt{tan^2 2\alpha + 1}} \tag{A-5}$$

As

$$tan2\alpha = \frac{2tan\alpha}{1 - tan^2\alpha} \tag{A-6}$$

Then Eq. A-5 turns to

$$b = \frac{-1 + \sqrt{\frac{4tan^2\alpha}{(1 - tan^2\alpha)} + 1}}{2 * \sqrt{1 + \frac{4tan^2\alpha}{(1 - tan^2\alpha)^2}}} \tag{A-7}$$

which is

$$b = \frac{-1 + tan^2\alpha + \sqrt{1 + 2tan^2\alpha + tan^4\alpha}}{2\sqrt{1 + 2tan^2\alpha + tan^4\alpha}} \tag{A-8}$$

finally

$$b = \frac{tan^2\alpha}{1 + tan^2\alpha} = sin^2\alpha \tag{A-9}$$

Therefore, the relationship between b and α in a torsional shear test with the same inner and outer cell pressure could be clarified by Eq. A-9.

Appendix B:

Shear band under fixed direction of σ_1

1. No-pipe-specimen:

(a) (b)

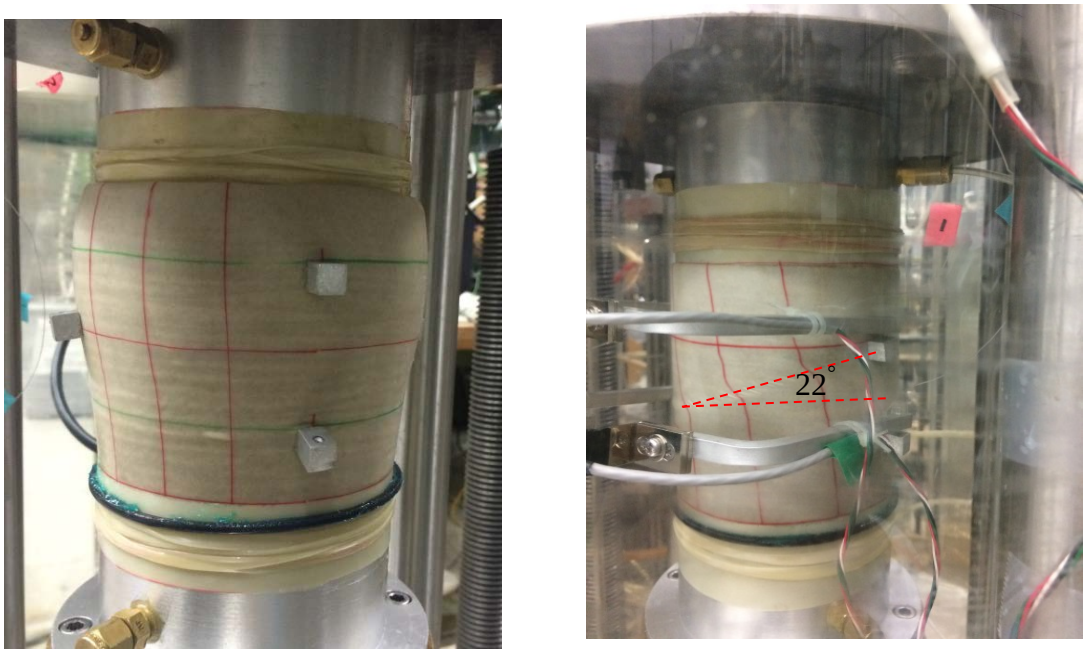

Fig. B-1 Shear band in No-pipe-specimen for (a) $\alpha = 0^{\circ}$ and (b) $\alpha = 45^{\circ}$

2. Vertical-pipe specimen:

(a)

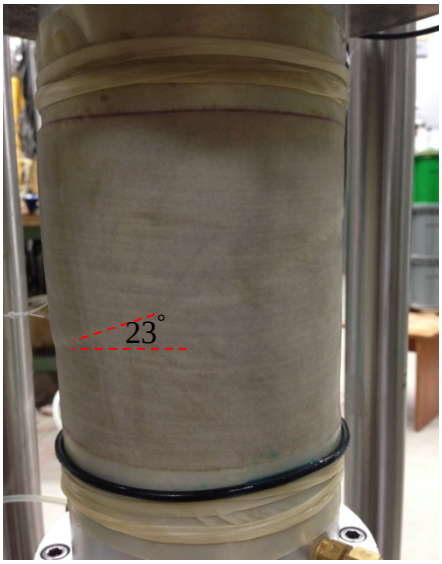

(b)

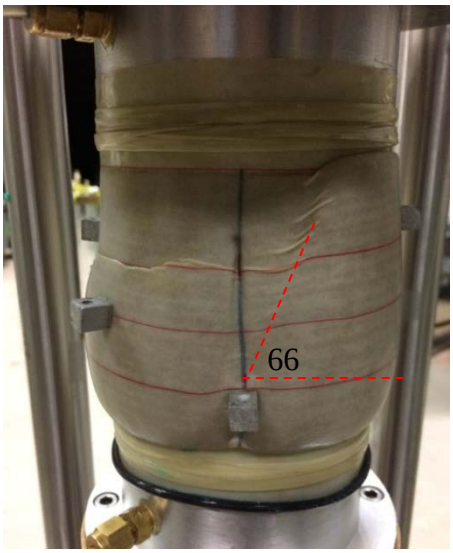

(c)

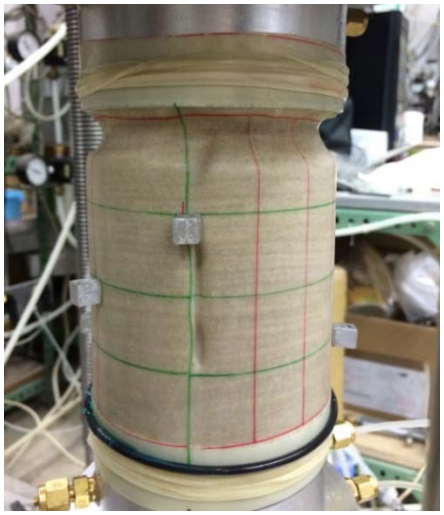

Fig. B-2 Shear band in Vertical-pipe-specimen for (a) $\alpha = 0^{\circ}$, (b) $\alpha = 45^{\circ}$ and (c) $\alpha = 90^{\circ}$

3. Horizontal-pipe-specimen

(a)

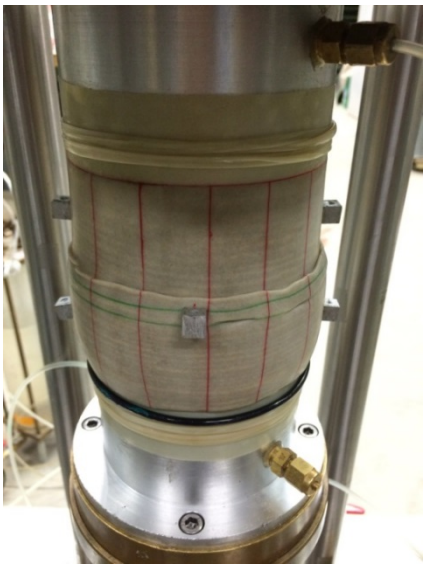

(b)

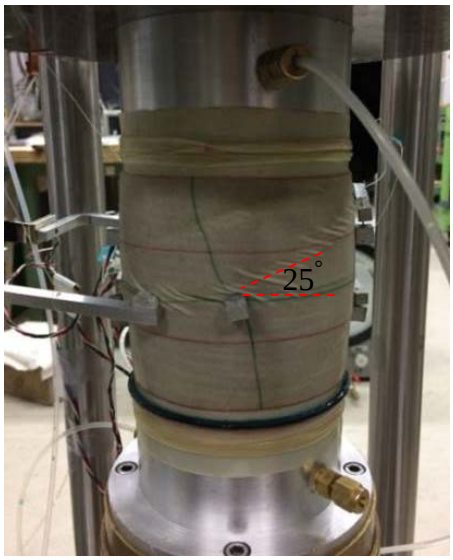

(c)

(d)

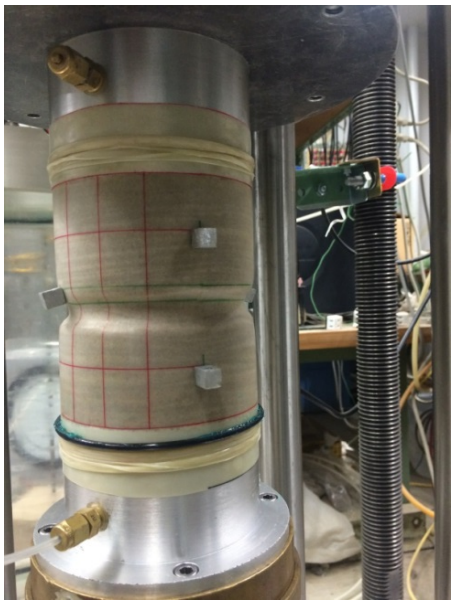

Fig. B-3 Shear band in Horizontal-pipe-specimen for (a) $\alpha = 0^{\circ}$, (b) $\alpha = 45^{\circ}$, (c) $\alpha = 60^{\circ}$ and (d) $\alpha = 90^{\circ}$